How To Search for Axion Dark Matter with MADMAX (MAgnetized Disk and Mirror Axion eXperiment)

A Survey of Systematic Uncertainties and Design Opportunities
in Dielectric Haloscopes:
Theory, Simulation and Proof of Principle Setup

Stefan Knirck

Technischen Universität München
Fakultät für Physik

Max-Planck-Institut für Physik
(Werner-Heisenberg-Institut)

How To Search for Axion Dark Matter with MADMAX (MAgnetized Disk and Mirror Axion eXperiment)

Stefan Paul Nikolas Knirck

Vollständiger Abdruck der von der Fakultät für Physik der Technischen Universität München zur Erlangung des akademischen Grades eines

Doktors der Naturwissenschaften (Dr. rer. nat.)

genehmigten Dissertation.

Vorsitzender:	Prof. Dr. B. Gabrecht
Prüfer der Dissertation:	1. Priv.-Doz. Dr. B. Majorovits
	2. Prof. Dr. P. Fierlinger

Die Dissertation wurde am 14.04.2020 bei der Technischen Universität München eingereicht und durch die Fakultät für Physik am 22.06.2020 angenommen.

to
the numerous COVID-19
victims and heros

Abstract

The QCD Axion is an excellent dark matter candidate, while originally introduced to explain CP conservation in strong interactions. Axions could be detected using their conversion to photons at boundaries between materials of different dielectric constants in a strong magnetic field. Combining many such surfaces (booster), one can enhance this conversion significantly using constructive interference and resonances (boost factor). The proposed 'MAgnetized Disk and Mirror Axion eXperiment' (MADMAX) containing approximately 80 high dielectric disks with 1.25 m diameter in a 9 T magnetic field could probe the well-motivated mass range of 40–400 μeV, a range which is at present inaccessible by existing cavity searches. Previous studies rely on an idealized lossless 1D model of the setup and lack experimental verification. This work hence validates the concept under more realistic boundary conditions using simulations along with an experimental setup and thereby derives important implications from systematic uncertainties on the boost factor.

To this end, we upgrade the previous 1D calculations to a numerically efficient three dimensional description of the system. We investigate diffraction, near fields as well as axion-velcity effects. We derive central implications for experimental design. We find that for the considered benchmark system the disks need a dielectric loss below $\tan\delta \sim 2 \times 10^{-4}$, be tilted less than 100 μm over their diameter and have a flatness better than 2 μm root-mean-square. Moreover, crucial parameters for antenna and magnet design are deduced. We also make suggestions on how to optimize the design with respect to 3D effects to maximize sensitivity in the final setup.

In addition, we explore the calibration and optimization process of the boost factor using reflectivity measurements. In order to validate the concept experimentally, we present a proof of principle booster consisting of a copper mirror and up to five sapphire disks. The mechanical accuracy, calibration of unwanted reflections and the repeatability of a basic tuning algorithm are investigated. The electromagnetic response in terms of the group delay predicted by the models is sufficiently realized in our setup. The boost factor frequency and amplitude repeatability of the tuning is at the percent level, and would have negligible impact on sensitivity.

Besides, we discuss how axion haloscopes can be made directionally sensitive to the axion velocity distribution. This would not only lead strong evidence for its nature as dark matter, but also enable a new era of 'axion astronomy'.

In summary, this work lays out one of the first coherent studies of systematic effects for MADMAX and design requirements therein. The presented results form the basis for a full understanding of the MADMAX booster and its corresponding systematic uncertainties, which is crucial for a successful run of the experiment. This work is also applicable to other haloscope experiments ranging from dish antennas, other dielectric haloscopes to even neutron star observations.

Zusammenfassung

Das QCD Axion ist ein exzellenter Dunkle Materie Kandidat, der auch CP Erhaltung in der starken Wechselwirkung erklären würde. Axionen können detektiert werden durch ihre Umwandlung zu Photonen and Grenzflächen zwischen verschiedenen Dielektrika in starken Magnetfeldern. Indem man viele solcher Flächen kombiniert (Booster), kann die Umwandlung signifkant verstärkt werden durch konstruktive Interferenz und Resonanzen (Boostfaktor). Das vorgeschlagene "MAgnetized Disk and Mirror Axion eXperiment" (MADMAX) enthält etwa 80 dielektrische Platten mit 1.25 m Durchmesser in einem 9 T Magnetfeld und könnte den gut motivierten Massenbereich von 40–400 μeV testen. Bisherige Studien basieren auf einem idealisierten, verlustfreiem 1D Modell des Aufbaus und es fehlt eine experimentelle Umsetzung. Daher validiert diese Arbeit das Konzept unter realistischeren Randbedinungen mit Simulationen und einem experimentellen Aufbau. Dabei werden wichtige Implikationen für systematische Unsicherheiten des Boostfaktors abgeleitet.

Dazu generalisieren wir die bisherigen Rechnungen zu einer numerisch effizienten dreidimensionalen Beschreibung. Wir studieren Diffraktions, Nahfeld- sowie Axion-Geschwindigkeits-Effekte. Die dieletrische Platten im untersuchten Vergleichssystem müssen dielektrische Verluste von weniger als $\tan\delta \sim 2 \times 10^{-4}$ aufweisen, weniger als 100 μm über ihren Durchmesser verkippt sein und eine Ebenheit besser als 2 μm (mittlere quadratische Abweichung) besitzen. Darüber hinaus folgern wir zentrale Parameter für Antennen- und Magnet-Entwicklung. Außerdem schlagen wir vor, wie die Sensitivität im Hinblick auf 3D Effekte weiter optimiert werden kann.

Darüber hinaus untersuchen wir den Kalibrations- und Optimierungsprozess des Boostfaktors mit Reflektivitätsmessungen. Zur experimentellen Validierung präsentieren wir einen Demonstator-Aufbau, der aus einem Spiegel und bis zu fünf Saphirplatten besteht. Die mechanische Genauigkeit, Kalibration unerwünschter Reflektionen und Wiederholbarkeit eines einfachen Tuning-Algorithmus werden untersucht. Die elektromagnetische Antwort im Hinblick auf die von Modellen vorhergesagte Gruppenlaufzeit ist ausreichend realisiert. Die Boostfaktorfrequenz und -amplitude sind auf dem Prozentlevel reproduzierbar, was vernachlässigbaren Einfluss auf die Sensitivität hätte.

Daneben diskutieren wir Axion-Haloskope, welche auf die Geschwindigkeitsverteilung von Axion sensitiv sind. Solch ein Aufbau könnte nicht nur prüfen, ob ein detektiertes Axion sich auch wie Dunkle Materie verhält, er würde auch eine neue Ära der "Axionenastronomie" einläuten.

Zusammenfassend legt diese Arbeit eine der ersten koheränten Studien systematischer Effekte in MADMAX und der Designanforderungen daraus dar. Die präsentierten Ergebnisse bilden die Basis für ein vollständiges Verständnis des MADMAX Boosters, unerlässlich für eine erfolgreichen Umsetzung. Diese Arbeit ist anwendbar auf andere Haloskope, wie Dish-Antennas, andere dielektrische Haloskope bis hin zu Neutronenstern-Beobachtungen.

Publications

Many of the results presented in this thesis led to publications [1–4],

[1] *"Directional axion detection,"*
S. Knirck, A. J. Millar, C. A. J. O'Hare, J. Redondo and F. D. Steffen,
JCAP 11 (2018) 051, arXiv:1806.05927,

[2] *"A new experimental approach to probe QCD axion dark matter in the mass range above 40 μeV,"*
P. Brun *et al.* [MADMAX Collaboration],
Eur. Phys. J. C 79, 186 (2019), arXiv:1901.07401,

[3] *"A First Look on 3D Effects in Open Axion Haloscopes,"*
S. Knirck, J. Schütte-Engel, A. Millar, J. Redondo, O. Reimann, A. Ringwald and F. Steffen,
JCAP 08 (2019) 026, arXiv:1906.02677,

[4] *"A first proof of principle booster setup for the MADMAX dielectric haloscope"*,
J. Egge, S. Knirck, B. Majorovits, C. Moore, O. Reimann,
Eur. Phys. J. C 80, 392 (2020), arXiv:2001.04363,

* *"3D Effects in Dielectric Haloscopes,"*
S. Knirck, J. Schütte-Engel, *et al.* (in preparation).

and also contributed to conference proceedings and other reports [5–7].

In addition, the author's research work at the Max-Planck-Institute for Physics comprised the co-supervision of various interns and Master's students, and thus contributed to the following two Master thesis [8, 9],

[8] *"Investigation of Loss Effects Influencing the Sensitivity of the Magnetized Disc and Mirror Axion Experiment - MADMAX,"*
A. Partsch, Master thesis, Munich, 2018,

[9] *"Electromagnetic Properties of the Proof of Principle Booster Setup for the MADMAX Experiment,"*
J. Egge, Master thesis, Munich, 2018.

Hence, some of the content and argumentation within this thesis overlap with the results presented in these papers and thesis.

In particular, chapter 3 presents the author's original contributions to [1]. In addition, the text and figures in sections 6.1, 6.2, 8.1, 8.2, 8.3.2 in large parts follow closely [3] which the author wrote in close collaboration together with Jan Schütte-Engel (JSE) [10]. Therefore large parts of the text in these sections were formulated together with JSE. Original results from JSE are cited as [10] within the respective sections. Finally, text and figures in chapters 9 – 11, 14 in part closely follow [4] which was also originally written by the author.

Acknowledgments

This thesis would be impossible without the support and commitment of many people. First of all, I would like to express my gratitude to my supervisor Béla Majorovits for his kindness and generosity, who always had time for my concerns and gave me the freedom to do independent research. In addition, I wish to thank Frank Steffen to be my mentor and support my theoretical studies. Besides, I am grateful to Peter Fierlinger for his interest in my work and to bring in an independent view as an external expert.

The presented results profited in large amounts from numerous stimulating discussions with Olaf Reimann. His inventive and pragmatic approach always brings in a fresh breeze. Moreover, it has been a true pleasure to work together with Javier Redondo. Much of this work is inspired by his passion for physics and his creativity. I also acknowledge Alexander Schmidt for many interesting discussions and his great hospitality.

In addition, I am glad for the fruitful collaboration with Alexander Millar and Ciaran A. J. O'Hare. It was also fun to work together with Jan Schütte-Engel on simulations, which benefited from his eye for details. Continuing the work of Christopher Moore enabled me to obtain the experimental results presented in this thesis. Besides, I enjoyed valuable discussions with Chang Lee and Xiaoyue Li. Among all the above are many other members from the MADMAX collaboration, but also the GERDA, LEGEND and theoretical astroparticle group at the Max-Planck-Institute for which this page is simply too short to mention everyone. The discussion with all these people was truly motivating and much of their work is directly related to the studies presented here. At this point, special thanks belongs to my students Dongju (Kota) Chang, Jacob Egge, Moahan Murugappan and Alexander Partsch for their commitment and contributions. It has been delighting and fun to work with all of them.

Moreover, I profited from the IMPRS EPP (International Max-Planck Research School for Elementary Particle Physics) program, which allowed me to grow and learn in various seminars, workshops and block courses. I also emphasize my appreciation for the efforts of all members of the Max-Planck-Institute for Physics, including engineers and administration, who did everything in their power to support the scientific goals of the group without too many bureaucratic obstacles.

Finally, many of the people mentioned above have also become friends over the years. They are among Aksel Alpay, Martin Barth, Bernhard Klein, Oliver Plaul, Edoardo Vitagliano, and many others, whom I thank for the good time spent together. Last but not least, I express my deep gratitude to my family for their great support. In particular, I thank my wife for her endless dedication and to give me our young daughter Yuna, because it is that what empowers me to excel myself: their unconditional love and happiness in their eyes.

Contents

Conventions

In this work we use natural units $\hbar = c = 1$ and Lorentz-Heaviside convention with the fine-structure constant $\alpha = e^2/4\pi$ with e the elementary charge, unless denoted otherwise. When we refer to velocities, we like to write down the factor c for clarity. Note that in this units also the vacuum permittivity ϵ_0 is unity. For convenience, unless the time-dependency is denoted explicitly, we will use complex, time-harmonic fields (also called phasors) for all fields, i.e., we explicitly leave out the time dependency of all fields and assume it to be $\exp(-i\omega t)$. The physical fields are obtained from the phasors by multiplying with this factor and taking the real part.

We denote the complex conjugate of any quantity x with a star, i.e., x^*, and $\hat{\boldsymbol{e}}_y$ is the unit vector in y-direction.

Finally, since in dielectric haloscopes the relevant electric fields are essentially polarized in the same direction than the external magnetic field, we will sometimes only refer to the scalar quantities E and B_e instead of the vectors $\boldsymbol{E}, \boldsymbol{B}_e$. This implies that the vectors point in y-direction and have magnitude E or B_e, respectively.

Part I

Motivation

Chapter 1

The Dark Matter Axion

Many astrophysical observations are indicating the existence of cold dark matter (CDM) – a non-radiating and weakly interacting massive component of the universe [11]. It makes up $\sim 27\,\%$ of the total energy density in our universe [12], and is expected to form halos around galaxies giving rise to a local CDM density around Earth at the order of $\rho \sim 0.45\,\mathrm{GeV\,cm^{-3}}$ with abundant astrophysical uncertainty, cf. e.g. [13–16]. While axions have been originally proposed to explain combined charge and parity conservation in strong interactions [17–19], they have been found to also be an excellent candidate particle to make up CDM [20–30].

Hence, there is great interest in building experiments to directly detect axion dark matter, for a review cf. [31–33]. In this thesis we discuss the realization of a promising new concept to directly detect galactic axions: the dielectric haloscope [34]. Let us first briefly review axions, their cosmological production and the local CDM velocity distribution, as these topics give important implications for direct detection. For a more comprehensive review cf. e.g. [32,35] for axion physics and [1] for the local dark matter velocity distribution.

The QCD Axion

The Lagrangian of strong interactions contains a term which violates charge and parity (CP) conservation, given by

$$\mathcal{L}_{\bar{\theta}} = -\frac{\alpha_s}{8\pi}\,\bar{\theta}\,G^a_{\mu\nu}\widetilde{G}^{a\mu\nu}\,, \tag{1.1}$$

where α_s is the strong coupling constant, $\bar{\theta} \in (-\pi, \pi)$ is an angular constant and $G^a_{\mu\nu}$ is the gluonic field strength tensor with its dual $\widetilde{G}$. Such a CP-violating term would manifest itself for example in an electric dipole moment of the neutron $d_\mathrm{n} \propto \bar{\theta}$ [36]. However, measurements constrain $|d_\mathrm{n}| < 3 \times 10^{-13} e\,\mathrm{fm}$ [37–40] with the electron charge e, which implies

$$|\bar{\theta}| < 2 \times 10^{-10}. \tag{1.2}$$

In fact, $\bar{\theta}$ is the sum of two contributions, one from the θ-angle defining a gauge invariant QCD vacuum, another from the common phase of the quark-mass matrix. Thus, it is extremely surprising that these two contributions cancel out so precisely: the so called strong CP-problem.

One elegant solution introduced in [41, 42] realizes that the vacuum energy density of QCD is minimized for $\bar{\theta} = 0$. Thus, by promoting $\bar{\theta}$ to a field, $\bar{\theta} \to a(\boldsymbol{x}, t)/f_a$ with the axion decay

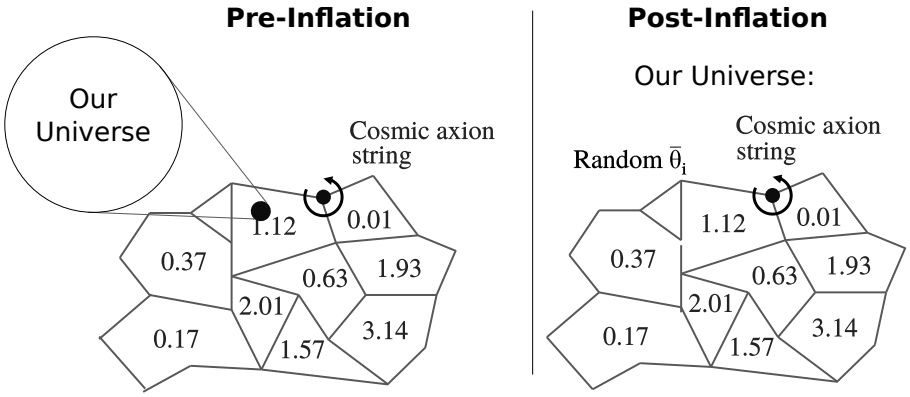

Figure 1.1: Schematic sketch of different axion dark matter production scenarios: in the left scenario Peccei-Quinn (PQ) symmetry breaking happens before cosmic inflation, such that a patch with a single, homogeneous initial misalignment angle $\bar{\theta}_i$ is inflated to be our whole observable universe. In the right scenario PQ symmetry breaking happens after inflation leading to much more inhomogeneous initial conditions. Adapted from [46].

constant f_a, this field can dynamically relax to zero. This corresponds to a new global $\mathrm{U}(1)_{\mathrm{PQ}}$ symmetry, called Peccei-Quinn (PQ) symmetry, spontaneously broken at energy scale f_a. Excitations of this new field represent a new pseudo-Nambu-Goldstone boson: the axion [43, 44], while its mass today is given by [45]

$$m_a \approx 5.7\,\mu\mathrm{eV}\left(\frac{10^{12}\,\mathrm{GeV}}{f_a}\right). \tag{1.3}$$

Axion Cosmology

Since the initial misalignment angle $\bar{\theta}_i$ at the time of Peccei-Quinn (PQ) symmetry breaking determines the initial amplitude of the oscillations in the axion field, it sets the energy density in the axion field. Hence, the observed dark matter abundance gives the required axion mass. Thus, the cosmological production of the observed dark matter abundance of axions depends on whether the PQ symmetry is broken before or after cosmic inflation, outlined in figure 1.1. At the time of symmetry breaking causally disconnected patches of the universe have independent initial $\bar{\theta}_i$. If the symmetry breaking happens before inflation, inflation will expand one of these patches to be the whole observable universe today. Since $\bar{\theta}_i$ is unknown, the axion mass m_a is relatively unconstrained below $m_a \lesssim 10^{-2}\,\mathrm{eV}$ [33]. In the post-inflationary symmetry breaking scenario one has to perform a complicated average over the inhomogeneous initial conditions giving rise to axion domains walls and cosmic strings. This scenario restricts the axion mass to roughly $25\,\mu\mathrm{eV} \lesssim m_a \lesssim 1\,\mathrm{meV}$ [25, 26, 29, 47–50]. In addition, the inhomogeneous initial conditions lead to additional dark matter substructure in the form of dense axion dark matter clumps, so called axion 'miniclusters'. For more details on these objects, see e.g. [32, 51, 52].

The Local Dark Matter Velocity Distribution

Apart from the local CDM density, the CDM velocity distribution is important for direct detection, and, as we will see later, axion direct detection experiments may even be able to measure this

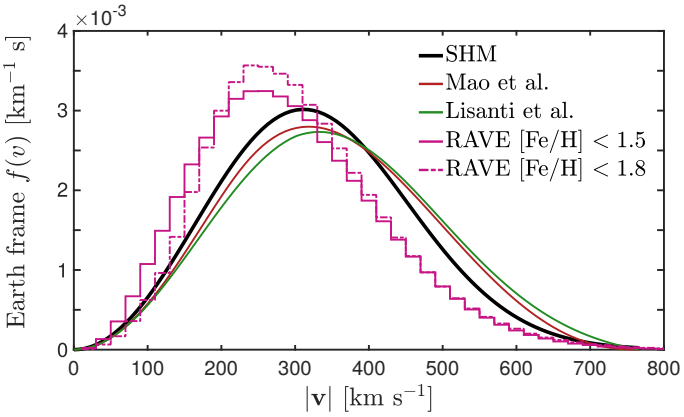

Figure 1.2: Local dark matter speed distribution. The SHM is shown as a bold black line, the fitting functions of Mao et al. [53] as a red line and Lisanti et al. [54] as a green line. The speed distribution obtained from measurements of RAVE stars for two different metallicities [55] is shown in purple. Adapted from [56].

velocity distribution. The model most commonly used is a spherically symmetric isothermal halo: the standard halo model (SHM) [57]. Its velocity distribution in the lab frame is given by

$$f(\boldsymbol{v}) = \frac{1}{(2\pi\sigma_v^2)^{3/2}} \exp\left(-\frac{|\boldsymbol{v}-\boldsymbol{v}_{\rm lab}|^2}{2\sigma_v^2}\right) \frac{\Theta\left(v_{\rm esc}-|\boldsymbol{v}|\right)}{N_{\rm esc}}\,, \tag{1.4}$$

where $\boldsymbol{v}_{\rm lab}$ is the lab velocity in galactic coordinates with $|\boldsymbol{v}_{\rm lab}| \sim 220\,\mathrm{km\,s^{-1}}$, $\sigma_v \sim 156\,\mathrm{km\,s^{-1}}$ is the velocity dispersion, Θ is the Heaviside theta function, $v_{\rm esc} \sim 600\,\mathrm{km\,s^{-1}}$ is the galactic escape velocity [58] and $N_{\rm esc}$ is a normalization constant. Clearly, this velocity distribution is oversimplified. While N-body simulations, e.g. [59, 60], and results from stellar surveys [55, 61] point to necessary modifications of this simplified picture, as shown in figure 1.2, the SHM is a good benchmark to compare different direct detection experiments.

Moreover, there exists substructure within the CDM halo. For example, streams, cf. e.g. [62–64], can comprise an additional component on top of the above velocity distribution with rather narrow velocity dispersion, i.e., add additional peaks to the spectrum [65]. A stream can be parameterized analogous to the Maxwellian distribution above as

$$f_{\rm str}(\boldsymbol{v}) = \frac{1}{(2\pi\sigma_{\rm str}^2)^{3/2}} \exp\left(-\frac{|\boldsymbol{v}-\boldsymbol{v}_{\rm str}-\boldsymbol{v}_{\rm lab}|^2}{2\sigma_{\rm str}^2}\right)\,, \tag{1.5}$$

where $\boldsymbol{v}_{\rm str}$ is the velocity of the stream in galactic coordinates and $\sigma_{\rm str} \sim \mathcal{O}(10\,\mathrm{km\,s^{-1}})$ is the velocity dispersion of the stream. Besides streams, other possible substructures have been discussed in literature, such as dark disks [66]. In the dark disk scenario the dark matter would be comoving with the frame of the Solar rotation around the galactic center, which would enhance the local velocity distribution at low speeds. Finally, axion miniclusters could be tidally disrupted by stars in our galaxy and form a network of streams with much smaller radii than the streams discussed above [67, 68]. For a direct detection experiment these 'ministreams' would show up as strong temporary enhancements over time scales of hours to days.

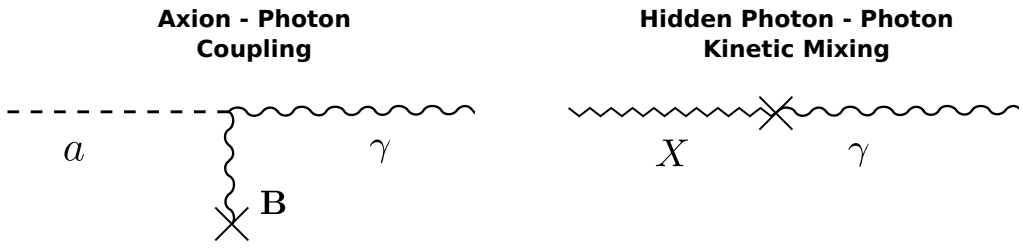

Figure 1.3: Feynman graph of the conversion of an axion-like particle to a photon under an external magnetic field (Primakoff effect) as proposed by Sikivie [69], (left), and the analogous process for a hidden photon kinetically mixing with the photon (right).

Axion Phenomenology for Direct Detection

Let us now consider how to detect axions. The low-energy effective Lagrangian leads to an interaction of the axion with two photons, given by

$$\mathcal{L}_{a\gamma} = -\frac{g_{a\gamma}}{4}\, a\, F_{\mu\nu}\widetilde{F}^{\mu\nu} = g_{a\gamma}\, a\, \boldsymbol{E}\cdot\boldsymbol{B}, \tag{1.6}$$

where $g_{a\gamma}$ is the axion-photon coupling constant, $\boldsymbol{E}$ is the electric field, and $\boldsymbol{B}$ the magnetic field. The axion-photon coupling constant is given by [45],

$$g_{a\gamma} = \frac{\alpha}{2\pi}\,\frac{C_{a\gamma}}{f_a} \approx 2.0\times 10^{-14}\,\mathrm{GeV}^{-1}\left(\frac{m_a}{100\,\mu\mathrm{eV}}\right) C_{a\gamma}, \tag{1.7}$$

where $C_{a\gamma}$ is a model-dependent constant usually assumed to be of order one. For the KSVZ [70,71] and DFSZ [72, 73] benchmark axion models $|C_{a\gamma}|$ is ~ 1.9 and ~ 0.7, respectively.

While the solution to the strong CP-problem is a compelling motivation for the QCD axion, treating $g_{a\gamma}$ as a free parameter independent of QCD leads to so-called axion-like particles (ALPs). In this case there is no fixed relation between $g_{a\gamma}$ and f_a. Thus, limits on axions and ALPs are often compared in the plane axion-photon coupling $g_{a\gamma}$ vs. axion mass m_a.

The coupling to photons can be tested using the Primakoff effect, shown in figure 1.3 (left), by providing one of the photons with an external magnetic field, and observing the conversion of axions to photons as suggested by Sikivie [69]. This process is analogous to the kinetic mixing of hidden photons with photons [74]. In fact, considering the strength of the kinetic mixing parameterized by χ, the conversion probability of a hidden photon to photon is the same than the conversion probability for an axion to a photon under the external magnetic field $\boldsymbol{B}$, when replacing $\chi \to g_{a\gamma}|\boldsymbol{B}|/m_a$. For more details on the phenomenology of hidden photons we refer the reader to e.g. [75, 76].

Notice an important consequence for direct detection from energy conservation. As we have discussed above, CDM moves non-relativistically with a velocity of $v \sim 10^{-3}\,c$ in the lab frame and hence the energy of axion CDM particles is given to very good approximation by their rest mass m_a. Therefore, due to energy conservation, the (angular) frequency $\omega = 2\pi\nu$ of the converted photons directly resembles the mass of the dark matter particle, while the frequency linewidth is given by the velocity distribution and thus $\Delta\nu_a \sim 10^{-6}\nu$.

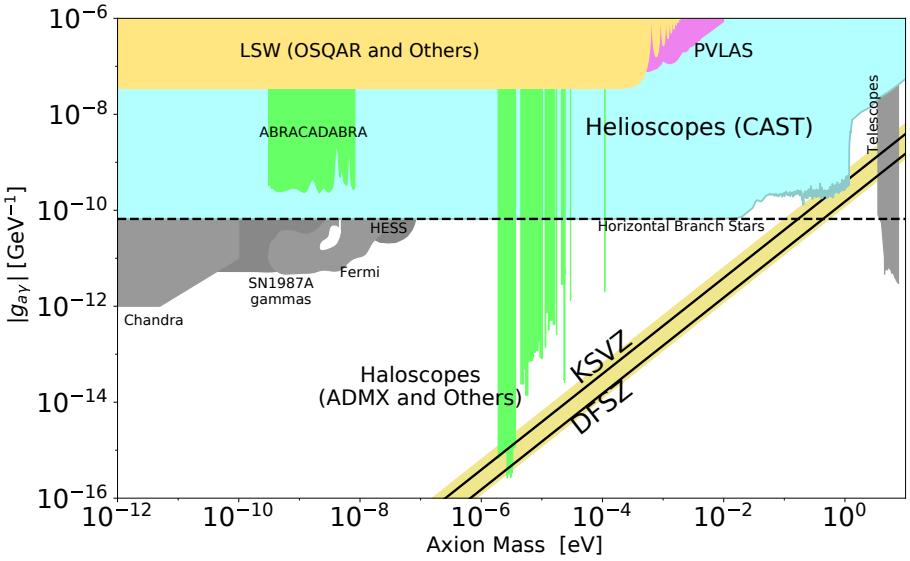

Figure 1.4: Exclusion limits on axion-like particles in the plane photon-coupling $g_{a\gamma}$ against mass m_a, reprinted from [77]. The light green regions are excluded by direct detection experiments, the upper yellow region are excluded by light-shining-through-wall experiments, the purple region is excluded by searches for vacuum magnetic birefringence, the upper blue regions are excluded by helioscope experiments probing the axion flux from the Sun, and the gray regions are excluded by astronomical observations. The diagonal ocher band indicates the range of typical QCD axion models such as KSVZ and DSFZ. For more details see [77].

Axion Detection Landscape

A comprehensive review of most recent limits for axion-like particles, as well as a summary on current constraints also on hidden photons, can be found in [77]. Here we summarize the essentials. The limits on axion-like particles in the plane $(g_{a\gamma}, m_a)$ are shown in figure 1.4. The various colored regions correspond to exclusion limits from different experimental efforts, while the diagonal ocher band denotes the region where the QCD axion is expected. The width of this band depends on predictions for $C_{a\gamma}$ from different models. Searches for vacuum magnetic birefringence (VMB), light-shining through-a-wall (LSW) and helioscopes [35, 78] probe the combination of the inverse Sikivie process and the Sikivie process: While axions are first produced either inside a strong magnetic field in the lab or within the Sun, they can reconvert to photons in a magnetic field in the lab. These photons are afterwards detected. Thus, these experiments probe all axion masses smaller than the energy of the initial photons, which makes them sensitive to a broad range of axion masses. However, for the expected mass range of axion dark matter below $\sim$ meV, these experiments lack sufficient sensitivity in $g_{a\gamma}$ to reach the QCD axion band.

This caveat can be overcome by haloscope experiments aiming to directly detect axions in the local CDM halo. These approaches rely on the conversion of galactic axions to photons using the Primakoff process, which can be resonantly enhanced by providing a high-Q resonant cavity whose resonance frequency is matched to the axion mass [69, 79]. Most notably, the ADMX collaboration has excluded parts of the QCD axion band with this approach [80], but also other efforts such as HAYSTAC [81] provide some of the most sensitive limits. Clearly, the downside

of this approach is the fact that the cavity needs to be tuned to the axion mass, which leads to a rather narrow sensitivity for different axion masses. In addition, higher axion masses lead to higher resonance frequencies and thus smaller photon wavelengths. Therefore, at higher masses one needs to reduce volume of resonant cavities to still match the wavelength of the converted photons. In addition, the quality factor of resonant cavities roughly scales inversely with the surface-to-volume ratio of the cavity. Both effects decrease sensitivity for higher masses. This fact roughly limits this approach to $\lesssim 40\,\mu\text{eV}$, unfortunately just about the lower end of the mass range preferred by the post-inflation symmetry breaking scenario. Hence, a variety of different concepts to generalize the cavity setup to use higher modes in larger volumes have been proposed and are being prototyped, such as cavities with multiple coupled cells, e.g. pizza cavities [82] or RADES [83], cavities with dielectrics, e.g. [84, 85], or simply the idea to scan in parallel with multiple separate cavities, e.g. ORGAN [86].

An alternative approach to cavity setups is the dish antenna [76]. Placing a metal mirror inside a strong magnetic field, CDM axions can convert to photons on its surface, generating an emitted power of $\sim 10^{-27}\,\text{W}\,\text{m}^{-2}$ for a magnetic field of 10 T, independent of the axion mass. While this allows for a broadband measurement also at high masses, for square-meter-scale mirror sizes and 10 T magnetic fields the emitted power is still not enough to reach competitive sensitivies with realistic setups. The recently proposed dielectric haloscope [34, 87–89] brings together both approaches by placing multiple dielectric disks in front of such a metal mirror (booster). In this case, each dielectric disk coherently emits electromagnetic radiation, which can interfere constructively within the setup and excite resonances between the dielectric disks. These two effects give rise to the power boost factor β^2 which is defined as the power emitted by the dielectric haloscope and a dish antenna of the same surface area. Calculations [34] indicate that this approach could indeed be sensitive to the QCD axion in the mass range motivated by the post-inflationary symmetry breaking scenario.

This led to the foundation of the MADMAX (MAgnetized Disk and Mirror Axion eXperiment) collaboration perusing to realize such a dielectric haloscope [2]. This thesis contributes to this effort. Thus, in the next chapter, we review the dielectric haloscope concept in more detail, discuss the MADMAX sensitivity goals and introduce the physics challenges which we are going to tackle within this thesis.

In short. The QCD axion is a very well-motivated candidate for cold dark matter and also explains the absence of CP-violation in strong interactions. Large parts of the allowed parameter space for axions remain unconstrained. In particular, the scenario in which the PQ symmetry is broken after inflation prefers a mass range unexplored by any direct detection experiment so far. Dielectric haloscopes, such as MADMAX, are a promising concept to explore this range.

Chapter 2

The Dielectric Haloscope

In order to understand the dielectric haloscope in more detail, we first briefly review axion-electrodynamics and the boost factor. This also lays the analytical basis for the calculations presented later on. Afterwards, we sketch the baseline design and sensitivity prospects for MADMAX and introduce the challenge of quantifying boost factor uncertainties tackled in this work.

2.1 Experimental Concept

Axion Electrodynamics

The axion de Broglie wavelength is $\lambda_{\mathrm{dB}} = 2\pi/(m_a v) \sim 10\,\mathrm{m}$ due to their non-relativistic velocity $v \sim \mathcal{O}(10^{-3})$ and small mass. Comparing the local CDM abundance $\rho_a \sim 0.45\,\mathrm{GeV\,cm^{-3}}$ with the axion mass $m_a \sim 100\,\mu\mathrm{eV}$, one finds for the local number density of axions $\sim 5 \times 10^{21} \lambda_{\mathrm{dB}}^{-3}$. Therefore, it is sufficient to treat CDM axions as a classical field and we may just solve the classical equations of motion following from the axion-photon interaction in (1.6). Further assuming a constant, static external magnetic field $\mathbf{B}_{\mathrm{e}}$, the axion modifies Maxwell equations by adding axion-induced effective charge and current densities [90, 91], leading to the so-called axion-Maxwell equations. Explicitly,

$$\epsilon \boldsymbol{\nabla} \cdot \boldsymbol{E} = \rho + \rho_a\,, \tag{2.1a}$$

$$\boldsymbol{\nabla} \times \boldsymbol{H} - \epsilon \dot{\boldsymbol{E}} = \boldsymbol{J} + \boldsymbol{J}_a\,, \tag{2.1b}$$

$$\nabla \cdot \boldsymbol{B} = 0, \tag{2.1c}$$

$$\nabla \times \boldsymbol{E} + \dot{\boldsymbol{B}} = 0, \tag{2.1d}$$

$$\ddot{a} - \boldsymbol{\nabla}^2 a + m_a^2 a = g_{a\gamma} \boldsymbol{E} \cdot \boldsymbol{B}_{\mathrm{e}}\,, \tag{2.1e}$$

with

$$\rho_a = -g_{a\gamma} \boldsymbol{B}_{\mathrm{e}} \cdot \boldsymbol{\nabla} a, \tag{2.1f}$$

$$\boldsymbol{J}_a = g_{a\gamma} \boldsymbol{B}_{\mathrm{e}} \dot{a}, \tag{2.1g}$$

where ρ and $\boldsymbol{J}$ are the electric charge density and current respectively, $\boldsymbol{E}$ and $\boldsymbol{B}$ the electric and magnetic field, ϵ the dielectric constant and $\boldsymbol{H} = \mu^{-1}\boldsymbol{B}$ the macroscopic magnetic field, while

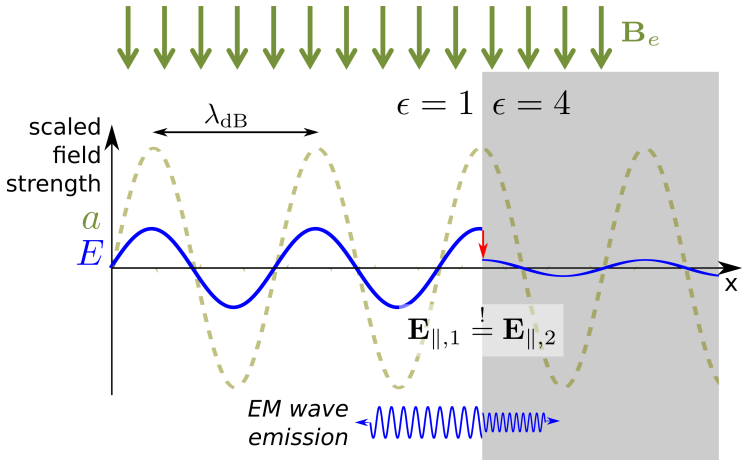

Figure 2.1: Sketch of axion-photon conversion in the classical field picture. The vertical axis corresponds to scaled field strengths, the horizontal axis is a spatial coordinate. In an external magnetic field $\boldsymbol{B}_e$ (denoted by the green arrows) the axion field a (dashed green line) sources an axion-induced electric field $\boldsymbol{E}_a$ (solid blue line) given in equation (2.3). This field follows the spatial dependency of the axion field and is inversely proportional to the dielectric constant ϵ, which leads to a discontinuity (red arrow) at the boundary of a dielectric (gray area). It is compensated by electromagnetic (EM) waves emitted from the boundary (blue waves on the bottom, shifted downwards for clarity).

in the following we assume $\mu = 1$. The refractive index is thus $n = \sqrt{\epsilon}$. Here $\boldsymbol{H}$ is without the contribution of $\boldsymbol{B}_\mathrm{e}$ and $\boldsymbol{J}$ respectively without the current needed to generate $\boldsymbol{B}_\mathrm{e}$. Plugging equation (2.1d) into equation (2.1b) after taking the time derivative of the latter, we arrive at the modified wave equation

$$-\nabla^2 \boldsymbol{E} + \nabla(\nabla \cdot \boldsymbol{E}) + \partial_t^2 \epsilon \boldsymbol{E} = \partial_t \boldsymbol{J}_a. \tag{2.2}$$

Let us for now assume $\boldsymbol{B}_\mathrm{e}$ to be constant, and $a \propto \exp(-i m_a t)$ spatially constant which corresponds to the zero-velocity limit of the axion. Then, this equation is trivially solved by the so-called axion-induced electric field

$$\boldsymbol{E}_a(t) = -\frac{g_{a\gamma} \boldsymbol{B}_\mathrm{e}}{\epsilon}\, a(t) \quad \sim \quad 1.6 \times 10^{-12}\ \mathrm{V/m}\ \frac{B_\mathrm{e}}{10\ \mathrm{T}}\ \frac{|C_{a\gamma}| f_\mathrm{DM}^{1/2}}{\epsilon}, \tag{2.3}$$

where f_DM is the fraction of CDM made up by axions.

Further, the homogeneous Maxwell equations are unchanged. Thus, the usual electromagnetic boundary conditions for $\boldsymbol{E}$ and $\boldsymbol{H}$ fields remain, i.e., on boundaries of two media with different dielectric constant ϵ their component parallel to the boundary must be continuous. However, equation (2.3) suggests a jump of the axion-induced electric field on such a boundary. In order to fulfill all axion-Maxwell equations, electromagnetic waves must be emitted from the boundary compensating this discontinuity [76], as sketched in figure 2.1. Their amplitudes are

$$E_1^\gamma = +\Delta E^a\, \frac{\epsilon_2 n_1}{\epsilon_1 n_2 + \epsilon_2 n_1}, \quad E_2^\gamma = -\Delta E^a\, \frac{\epsilon_1 n_2}{\epsilon_1 n_2 + \epsilon_2 n_1}, \quad H_{1,2}^\gamma = -\Delta E_a\, \frac{\epsilon_1 \epsilon_2}{\epsilon_1 n_2 + \epsilon_2 n_1}, \tag{2.4}$$

with $\Delta E_a = (E_{a,2} - E_{a,1})$ is the difference of the axion-induced field in both media and $n_i = \sqrt{\epsilon_i}$ the refractive indices of the media. Assuming that the external magnetic field $\boldsymbol{B}_e$ is parallel to

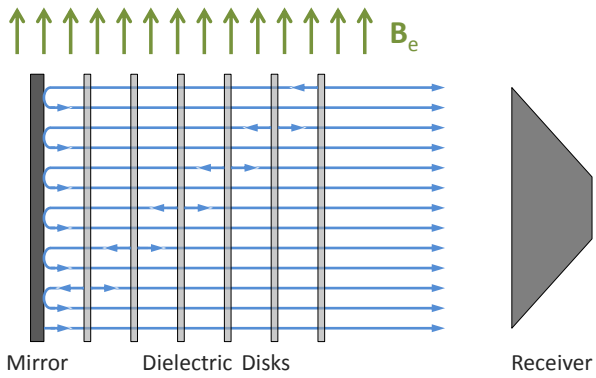

Figure 2.2: MADMAX idea: Each interface coherently emits electromagnetic radiation due to the presence of the axion field. Depending on the axion mass and the disk placements these may interfere constructively and 'boost' the emitted power compared to a single mirror setup by $4-5$ orders of magnitude. Taken from [34].

the boundary, this leads to an emitted power from the boundary of

$$P_\gamma = 3.3 \times 10^{-27}\,\mathrm{W} \left(\frac{B_\mathrm{e}}{10\ \mathrm{T}}\right)^2 \left(\frac{A}{1\,\mathrm{m}^2}\right) f(\epsilon_1, \epsilon_2)\, C_{a\gamma}^2\, f_\mathrm{DM}\,. \tag{2.5}$$

where A is the interface area between the dielectrics and typically $f(\epsilon_1, \epsilon_2) \leq 1$, depending on the dielectrics. If one uses only a perfect mirror ($\epsilon = \infty$) in vacuum this gives $f(\infty, 1) = 1$, where this approach is known as the dish antenna haloscope [76].

Power Boost

By employing many dielectric disks in a strong magnetic field $\mathbf{B}_\mathrm{e}$, each surface emits this radiation coherently, as long as the axion coherence length guaranteed by its de Broglie wavelength $\lambda_\mathrm{dB} \sim 10^3\lambda$ (with the photon wavelength λ) is greater than the size of the setup. By placing the disks accordingly, those contributions may interfere constructively while also internal reflections may resonantly enhance the emission of electromagnetic waves, both leading to a total emission much higher than what would be expected from a single surface. The power boost factor β^2 is defined as the ratio between the power emitted by the booster and the power emitted by a single perfect mirror. Notice that β^2 is a function of frequency ν and can be manipulated in practice by changing the disk positions. If not denoted otherwise, the term power boost factor, or sometimes just boost factor, refers to the power boost factor curve as a function of frequency. Moreover, in this thesis we call the assembly of dielectric disks in front of a metal mirror within the external magnetic field 'booster', while the dielectric haloscope always comprises the full experiment, including the cryogenic housing, the antenna and the receiver. The total power emitted by the booster is

$$P_\gamma(\nu) = 1.6 \times 10^{-22}\,\mathrm{W} \left(\frac{\beta^2(\nu)}{5 \times 10^4}\right) \left(\frac{B_\mathrm{e}}{10\,\mathrm{T}}\right)^2 \left(\frac{A}{1\,\mathrm{m}^2}\right) \left(\frac{\rho_a}{0.45\,\mathrm{GeV/cm}^3}\right) C_{a\gamma}^2\,. \tag{2.6}$$

Note that within this thesis we will take 3D effects and the coupling to an antenna into account for the calculation of the boost factor, where applicable. In practice, the power boost factor β^2

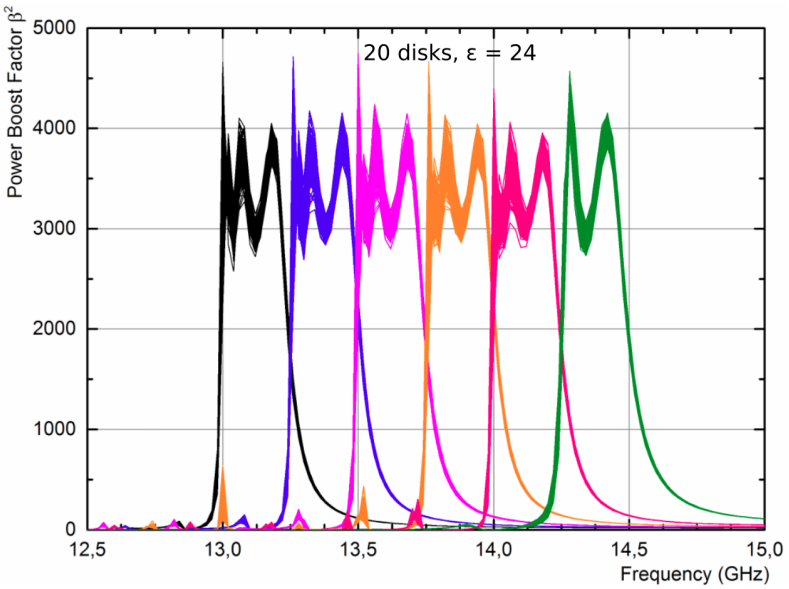

Figure 2.3: Example broadband boost factors covering a boost factor bandwidth of 250 MHz for 20 $LaAlO_3$disks, $\epsilon = 24$ and $d = 1\,\text{mm}$, for a set of six different disk positions corresponding to the different colors. In each case the positions are randomly varied with a standard deviation of $15\,\mu\text{m}$ and plotted on top of each other. Adapted from [2].

is hence defined as the emitted power, after taking above effects into account, compared to the total power emitted by an ideal mirror with the same area as predicted from 1D calculations. We sometimes also refer to the 'amplitude boost factor' $|\beta|$, which is the square root of the power boost factor and in 1D corresponds directly to the enhancement of the electric field compared to an ideal mirror. It is not to be confused with the (power) boost factor amplitude, which we use to quantify the maximum of the boost factor curve.

By optimizing the dielectric disk distances the frequency response of the boost factor can be controlled. Generally, the boost factor is large at frequencies where the disk distances are around $\sim \lambda/2$, with the photon wavelength λ. Besides the frequency position, it is relevant to also consider the frequency bandwidth (in the following just bandwidth) $\Delta\nu_\beta$ in which the boost factor is maximized (boost factor bandwidth). For larger bandwidths a larger variance in the disk distances is required. For a broadband scan over various frequencies, i.e., axion masses m_a, a boost factor curve similar to a top-hat response is ideal. By numerically optimizing the disk positions, one can find such solutions approximately, as shown for example figure 2.3. For each boost factor curve the positions of the disks were randomly varied with a standard deviation of $15\,\mu\text{m}$ and plotted on top of each other.

Importantly, the area under the power boost factor curve $\int \beta^2\,\mathrm{d}\nu$ is approximately conserved when changing the disk positions (area law) and proportional to the number of dielectric disks. While for integrating over $0 \leq \nu \leq \infty$ this holds exactly, it is still a good approximation in the region containing the main peak. Therefore one can trade bandwidth with power boost by changing disk positions, but not simultaneously gain in both. We will review this and other important properties of the boost factor in some more detail later in chapter 4.

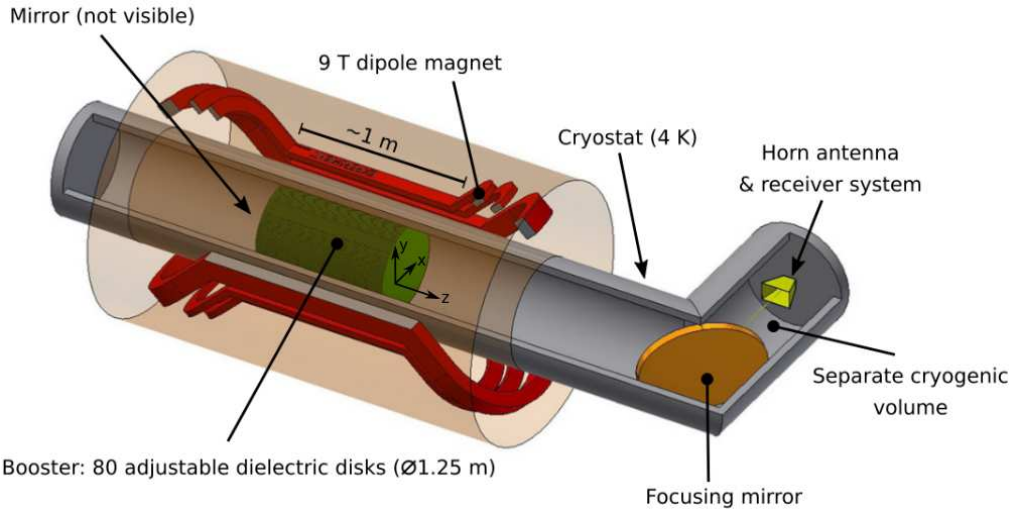

Figure 2.4: Baseline design of the MADMAX experiment: The magnet coils are shown as red racetracks. The booster consists of the mirror (copper disk at the far left) and 80 dielectric disks and is shown in green. Its emitted power is steered by a focusing mirror onto a horn antenna (yellow) connected to a cryogenic preamplifier inside a separate cryostat. Not to scale. Adapted from [96].

Besides MADMAX this concept is also found in other experimental proposals to search for axion-like particles. Among them are ORPHEUS [92, 93] and DALI [94] which are designed for similar mass ranges as MADMAX. In addition, the LAMPOST experiment [95] uses a similar approach in the $\sim$ eV (optical) range.

2.2 The MADMAX Experiment

Based on the idea of the dielectric haloscope the MADMAX collaboration was founded in October 2017 with the goal to search for QCD axions in the mass range between 40 μeV (10 GHz) and 400 μeV (100 GHz). A detailed description of the status of the project and recent achievements can be found in [2, 96]. Here we summarize the essentials relevant for this work.

Baseline Design

The baseline design of MADMAX is outlined in figure 2.4. The booster consists out of a mirror and around $N_{\text{disk}} \sim 80$ dielectric lanthanum aluminate ($LaAlO_3$, $\epsilon \approx 24$) disks with a thickness of $d \sim 1\,\text{mm}$ and a diameter of $\varnothing \approx 1.25\,\text{m}$ in a $B_\text{e} = 9\,\text{T}$ magnetic field ($B^2A = 100\,\text{T}\,\text{m}^2$). Notice, that the length of the booster is $L_b \sim N_{\text{disk}}(\lambda/2 + d)$, i.e., 1.4 m around 10 GHz and 30 cm at 100 GHz. This requires a unique dipole magnet with a strong field and a large bore, never built before, which is currently under development. The booster is housed in vacuum within a 4 K cryostat surrounded by the dipole magnet. The emitted electromagnetic radiation is focused by another mirror onto an antenna connected to a receiver system (not shown). We refer to the focusing mirror together with the antenna as the optical system.

Before going to the full-scale experiment, the MADMAX collaboration strives to build a smaller

prototype, to explicitly test the mechanical concept, demonstrate the feasibility of the experimental approach and eventually also obtain first physics results on axion-like particles with a reduced sensitivity in $g_{a\gamma}$. This prototype is intended to be operated within the MORPURGO magnet at CERN, which provides a 1.6 T dipole field, around 1/6 of the magnetic field of the full-scale system. The prototype booster is going to house 20 disks, i.e., 1/4 of the number of disks used for the final experiment which are a factor 1/4 smaller in diameter ($\varnothing = 30\,\mathrm{cm}$). We will refer to this setup as the 'MADMAX prototype' throughout this thesis.

If not denoted otherwise, we chose our coordinate system such that the dielectric disks ideally lay in the xy-plane, sometimes instead parameterized in polar coordinates (r, ϕ), and are orthogonal to the z-direction. $r = 0$ corresponds to the center of the disks. For the different studies it is instructive to put the origin $z = 0$ at different points as defined in the respective chapters. We often refer to the 'front disk' of the booster, which is the disk placed at the highest value of z and thus most close to the focusing mirror. If not stated otherwise, the external magnetic field with strength B_e is always assumed to point in y-direction.

Achieving the Goal Sensitivity

Numerical 1D calculations show that for the full-scale MADMAX (80 $LaAlO_3$ disks) a power boost factor of $\beta^2 \sim 5 \times 10^4$ may be achieved over a bandwidth of $\Delta\nu_\beta = 50\,\mathrm{MHz}$ at $\nu = 20\,\mathrm{GHz}$, leading to the emitted power of $P_{\mathrm{sig}} \sim 1.6 \times 10^{-22}\,\mathrm{W}$ quoted above. In order to distinguish such a tiny signal from thermal and electronic background noise, the power in a single frequency bin $\Delta\nu$ (receiver resolution) is integrated for a time τ, giving a signal-to-noise ratio according to the Dicke radiometer equation [97, 98]

$$\frac{S}{N} = \frac{P_{\mathrm{sig}}}{k_B T_{\mathrm{sys}}} \sqrt{\frac{\tau}{\Delta\nu}}, \tag{2.7}$$

where k_B is the Boltzmann constant and T_{sys} is the total system noise temperature arising from thermal and electronic noise. The MADMAX collaboration has demonstrated the operation of a detection system with $T_{\mathrm{sys}} \approx 5\,\mathrm{K}$ at $\sim 20\,\mathrm{GHz}$ using a commercial HEMT amplifier [99]. Note that in future there is room for further improvement of the noise temperature using, for example, traveling wave parametric amplifiers, which may potentially push the noise temperature down close to the quantum limit, i.e., $\sim 1\,\mathrm{K}$ at 20 GHz, cf. e.g. [100]. Here we take the total system noise temperature to be 8 K to also account for noise contributed by the booster. For a discovery experiment, the receiver resolution should be smaller than the axion linewidth, i.e., $\Delta\nu \approx 10^{-6}\nu$. In this case, a signal of $1 \times 10^{-22}\,\mathrm{W}$ is seen with a signal-to-noise ratio of $S/N = 4$ after $\tau = 4\,\mathrm{days}$. Also notice that the currently available detection system provides a bandwidth of 50 MHz (receiver bandwidth). Thus, we take this value as the benchmark boost factor bandwidth in this thesis.

Let us review the sensitivity of the proposed MADMAX setups based on these assumptions. To summarize, this estimate assumes that a power boost factor of $\beta^2 \sim 5 \times 10^4$ over a bandwidth of $\Delta\nu_\beta \sim 50\,\mathrm{MHz}$ can be achieved with 80 $LaAlO_3$ disks with a diameter of 1.25 m in a 9 T magnetic field, providing a power of $\sim 1 \times 10^{-22}\,\mathrm{W}$. Here for the receiver a detection efficiency of 80 % and a measurement time of 4 days, system noise temperature of 8 K and required signal-to-noise ratio of $S/N = 4$ for each frequency band are assumed. The resulting MADMAX sensitivities for CDM axions and hidden photons with a mass in the range $40\,\mu\mathrm{eV}$ to $400\,\mu\mathrm{eV}$ using the

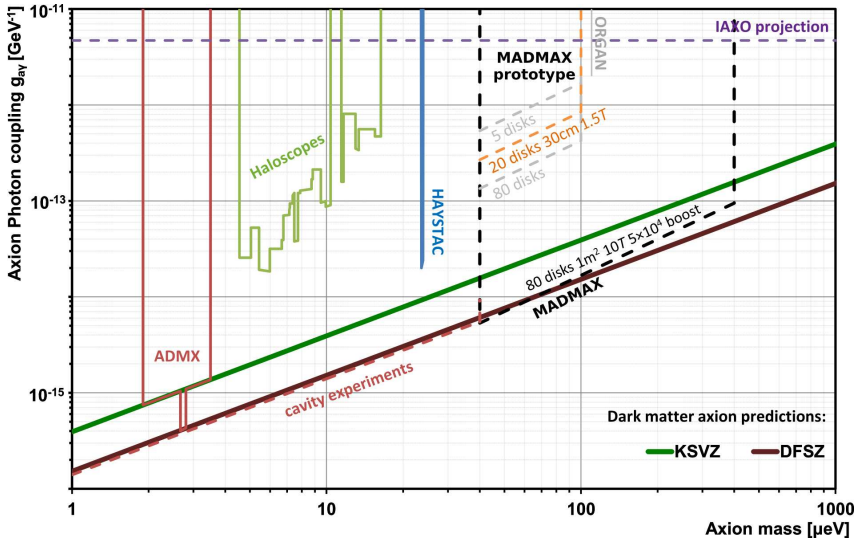

Figure 2.5: Projected MADMAX sensitivities for CDM axions and axion-like particles on the axion-photon coupling $g_{a\gamma}$ against axion mass m_a. The couplings expected from the DFSZ and KSVZ are shown as solid green and red diagonal lines. For the MADMAX projections, a setup with 80 dielectric disks each with a diameter of 1.25 m and a magnetic field of 9 T parallel to the disk surfaces has been assumed, as well as setups with 5 and 20 disks both with a disk diameter of 30 cm in a 1.5 T magnetic field. We also show the expected sensitivity range for future cavity experiments and IAXO [35], together with existing limits from ADMX [80, 101], other haloscope experiments [33], from HAYSTAC [81] and ORGAN [86]. Adapted from [2].

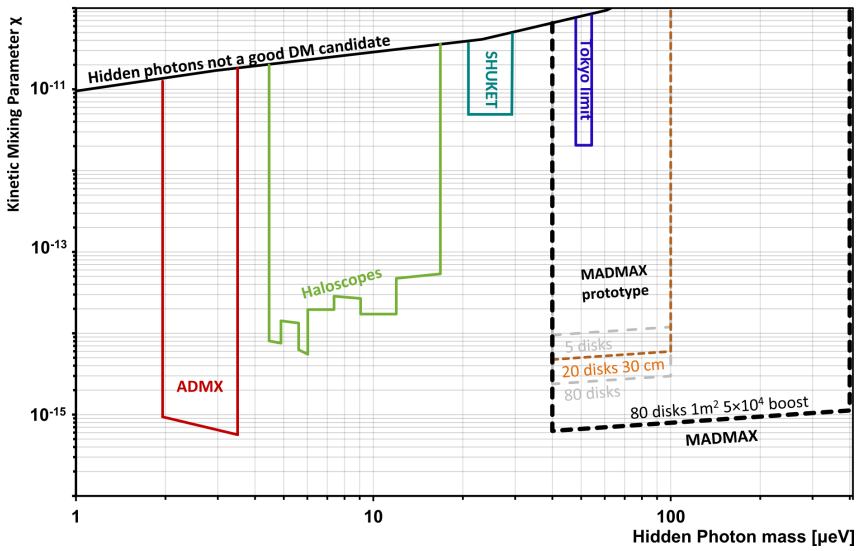

Figure 2.6: Projected sensitivities for hidden photons on the kinetic mixing parameter χ against hidden photon mass. For the MADMAX projections the assumptions are analogous to figure 2.5. The projected sensitivities are compared to existing limits from ADMX and other haloscope experiments for hidden photon searches from [102] and from dish antenna experiments, i.e., an experiment in Tokyo [103] and SHUKET [104]. The area above the black line represents the parameter space where hidden photons are not a good dark matter (DM) candidate [102]. Adapted from [2].

above assumptions and the Dicke equation (2.7) are shown in figures 2.5 and 2.6, respectively. A significant part of the parameter space predicted for CDM axions in the post-inflationary PQ scenario could be probed. Also a parameter space consistent with hidden photons as CDM could be probed down to $\chi \lesssim 10^{-15}$. If one conservatively estimates the time to readjust the disks with one day in which no signal can be integrated, a single 50 MHz bandwidth can be scanned within 5 days, i.e., the range between 40 μeV and 120 μeV could be scanned in around 5 years [2, 34].

Notice that these estimates are very sensitive to the detailed underlying assumptions, and therefore just give a rough estimate of the potential reach of a haloscope experiment. Here we have for example conservatively taken 1×10^{-22} W instead of the full 1.6×10^{-22} W (approximately to the power that would be provided by $\rho_a \sim 0.3\,\mathrm{GeV\,cm^{-3}}$ instead of $\rho_a \sim 0.45\,\mathrm{GeV\,cm^{-3}}$), which however roughly halves the scan rate.

The Systematic Uncertainty on the Power Boost Factor

Obviously, it is critical for the operation of any dielectric haloscope to understand the systematic uncertainties of the expected signal strength and its coupling to the detection system. While for the antenna and receiver system this task has been performed many times before in radio astronomy, the dominant sources of systematic uncertainty on the power boost factor remain to be determined. In addition, the 1D calculations mentioned above have been conducted using an idealized lossless 1D model, which for example does not account realistic flatness of the dielectric disks or the fact that the out-propagating power from the booster needs to be received by an

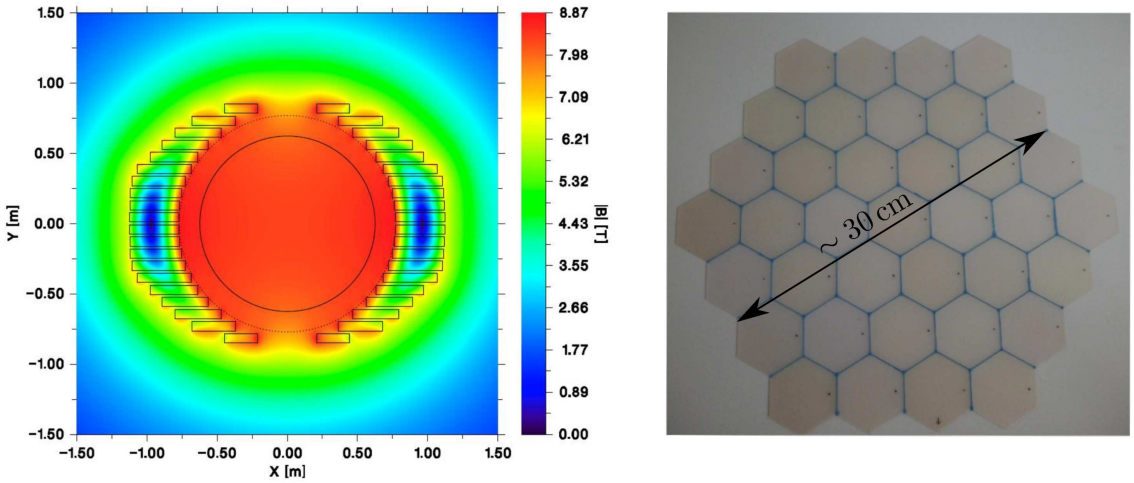

Figure 2.7: **Left:** Map of the external magnetic field parallel to the dielectric disks from one of the current magnet designs for the final-scale MADMAX boosters [105]. **Right:** Lanthanum aluminate disk made by gluing together commercially available wavers. Both taken from [96].

antenna matched to the right beam shape. Quantifying the uncertainty on the power boost factor becomes in particular important, if one realizes that the power boost factor is a quantity that cannot be directly measured and thus needs to be constrained from correlated quantities. In this thesis we therefore conduct one of the first rigorous studies to explore the systematic uncertainty of the power boost factor.

We will start our survey purely with simulations in part III. To this end, we first extend the calculations from the 1D model with magnetic field inhomogeneities and losses. This will already lead to decisive consequences for magnet design and operation of the dielectric haloscope. However, in a realistic dielectric haloscope various 3D effects may be relevant. These include diffraction losses and effects from charge accumulation at the disk rims, but also the emitted beam shape. In addition, realistic magnetic fields are not perfectly homogeneous, such as the one from the envisioned MADMAX magnet shown in figure 2.7 (left). Thus, the tolerable inhomogeneities have to be quantified. Moreover, the fact that the transverse axion-velocity is non-zero unlike assumed above has to be taken into account. Finally, the dielectric disks themselves are not perfectly flat, can be slightly tilted and may even be glued together from multiple small patches. The latter is the current baseline concept for the disk design in MADMAX and a first Lanthanum aluminate disk has been made following this concept, as displayed in figure 2.7 (right). Thus, we will introduce and validate various methods to efficiently perform 3D axion-electrodynamics calculations. Afterwards, we present our results from simple systems, such as an idealized single disk, to complicated boosters with the non-ideal boundary conditions sketched above. As a result, we constrain antenna parameters and tolerable disk inaccuracies such as transverse thickness variations. Finally, we show how the boost factor and its uncertainty can be constrained using reflectivity measurements on the booster and taking the 3D effects above into account.

Apart from simulation, we demonstrate the feasibility of a small-scale dielectric haloscope with a proof of principle experimental setup in part IV. After exploring systematic uncertainties on reflectivity measurements, we use the method to constrain the boost factor described before,

to determine the repeatability of disk alignment in terms of the power boost factor uncertainty.

We close with a sensitivity estimate for small-scale proof of principle setups comparable with the setup described above, and a concluding discussion of the major results in part V.

However, before facing the experimentalists' problems that the world has more than one spatial dimension and other obstacles, we invite the reader in the following part to join us on a theoretical excursus of what could be the future of axion physics after a detection.

In short. The axion induces emitted radiation from dielectric interfaces under a strong magnetic field. When combining multiple dielectric interfaces (dielectric haloscope) the emission can be enhanced using constructive interference and resonances between the interfaces (power boost factor). We presented the design and sensitivity goals for the MADMAX dielectric haloscope, and sketched important, but previously unaccounted systematic effects which potentially reduce the power boost factor and hence motivate the studies presented hereafter.

Part II

Theoretical Excursus

Chapter 3

Directional Axion Detection

In axion haloscopes the energy of the (massless) detected photons corresponds directly to the rest mass of the axion plus a contribution from the momentum of the axion. For CDM axions with a velocity of $v \sim 10^{-3}\,c$ the latter is $\sim v^2 \sim \mathcal{O}(10^{-6})\,c^2$ times smaller than the contribution from the rest mass. Nevertheless, the power spectrum of the converted photons directly corresponds to a measurement of the velocity distribution of the detected axions. This is a natural property of all major axion haloscopes, including MADMAX. Thus, after the detection of the axion, haloscope experiments will quickly be able probe the CDM velocity distribution [106, 107].

Interestingly though, the cross-section of axion haloscopes can be designed to exhibit a directional velocity dependency. This would allow us to measure quantities of the velocity distribution in the different components of the axion velocity vector $\boldsymbol{v}$. The measured distribution would for example be daily and annually modulated, which allows for the measurement of the peculiar velocity of the Sun in the galactic rest frame. In addition, local streams and miniclusters crossing the path of the solar system could be directly measured. Hence, the detection of a CDM axion would not only be a breakthrough in particle physics, it would also usher in a new era in which the axion itself would become a new messenger of astrophysics allowing for a precise probe of the local dark matter halo.

In this chapter we will briefly review how axion haloscopes can acquire a directional sensitivity in section 3.1. Based on this, we will develop a general formalism to calculate the changes to the measured power spectrum of these haloscopes in section 3.2. In section 3.3 we eventually derive requirements on the experimental sensitivity in an analytical statistical framework in order to deduce astrophysical parameters of the CDM velocity distribution.

3.1 Velocity Sensitive Axion Haloscopes

The axion field can be expanded in a sum of plane waves,

$$a(\boldsymbol{x}, t) = a_0 \exp\left[-i(m_a t - \boldsymbol{p}\cdot\boldsymbol{x})\right], \tag{3.1}$$

where $\boldsymbol{p}$ is the axion momentum related to the de Broglie wavelength λ_{dB} of the axion as $|\boldsymbol{p}| = 2\pi/\lambda_{\mathrm{dB}}$. As usual, in the non-relativistic limit the momentum is directly given by the velocity as $\boldsymbol{p} = \boldsymbol{v}/m_a$. Hence, a directional axion haloscope thus must be sensitive to the spatial phase

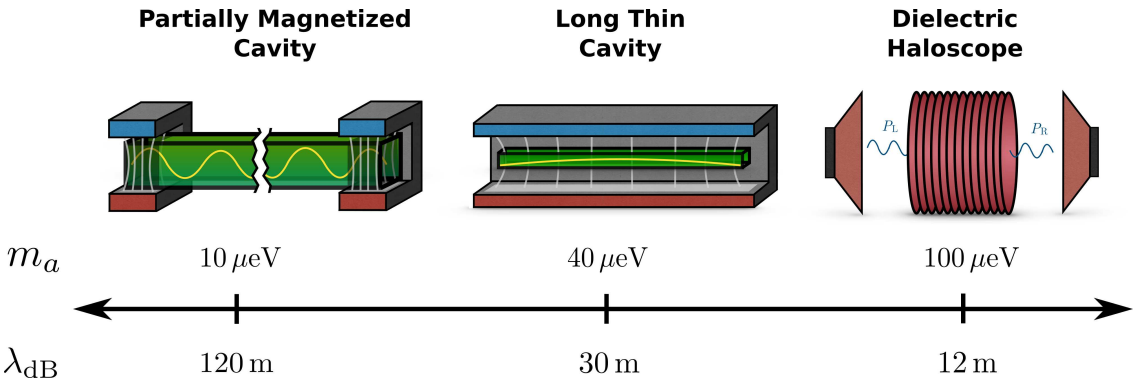

Figure 3.1: Schematic illustration of different approaches for directionally sensitive axion haloscopes together with their preferred mass range and the corresponding axion de Broglie wavelength. For masses around $\sim 10\,\mu$eV one can use a long, partially magnetized cavity operating at a higher mode, at intermediate masses $\sim 40\,\mu$eV an elongated cavity [108] and at higher masses $\sim 100\,\mu$eV a dielectric haloscope [91]. For clarity the magnetic field is not shown for the dielectric haloscope, where it also stretches over all dielectric disks. Figure adapted from [1].

differences of the axion-field. This can be done, by probing the corresponding phase differences of the axion-induced electric field, cf. equation (2.3). Figure 3.1 shows three concepts to do this. The first concept uses an elongated cavity at a high mode number, where only the ends of the cavity are magnetized. Thus, the axion-induced field excites both ends with a different phase. Hence, the overlap between the axion-induced field and the resonant mode, usually dubbed form factor, will be reduced for higher velocities along the cavity axis, and thus the output power is reduced. This concept is suited for axion de Broglie wavelengths which are still significantly larger than the size of a realistic setup since the overlap is reduced already for a small phase difference. For axion smaller de Broglie wavelengths, but still larger than the size of the setup, one can use a similar concept. Here one magnetizes the full elongated cavity and uses the fundamental mode [108]. Phase differences of the axion-induced field over the length of this cavity again reduce the form factor. For the mass range relevant for MADMAX and above, including experiments like LAMPOST [95], one can extend the dielectric haloscope concept by distributing the dielectric layers over the length scale of an axion de Broglie wavelength [91]. For more details on the feasibility of these concepts and explicit calculations of the form factors, see also [1].

In this work we consider a general expansion of the form factor up to second order in the axion velocity v_z along the velocity-sensitive axis of the experiment

$$C(\boldsymbol{v}) = 1 - \mathcal{G}(v_z), \quad \mathcal{G}(v_z) = g_\ell v_z + g_q v_z^2, \tag{3.2}$$

where g_ℓ and g_q are the expansion coefficients and we take the experiment to be velocity sensitive in z-direction only. In general, an experiment can have velocity-dependency in all three different spatial directions, in which $\mathcal{G}$ would be a sum over all directions. Notice that the resonant modes in the first two cavity concepts above are standing waves, which are symmetric under inversion of the velocity-sensitive axis $z \to -z$. Thus, these setups cannot distinguish the sign of the axion velocity in z-direction v_z, and, more generally, these experiments can only have a form factor quadratic in v_z, i.e., they have $g_\ell = 0$. In contrast, the dielectric haloscope can be open to both sides, and

hence distinguish between modes which radiate more towards the left or the right. Therefore, it can be sensitive to the sign of v_z and also exhibit a linear response in v_z. In the following we will discuss experiments with a linear response $g_\ell \neq 0, g_q = 0$ (ℓ-type) and a quadratic response $g_\ell = 0, g_q \neq 0$ (q-type) separately. From the linearity of the considered equations, it will be clear that the fully general results are sums of the respective specific results.

We point out that the above expansion must break down when $C(\boldsymbol{v}) < 0$, since output powers cannot be negative. In this thesis we consider typical experiments with $g_\ell = 100c^{-1}$, $g_q = 10^5 c^{-2}$, where this happens for velocities higher than $v_z \sim 10^{-2}c$, one order of magnitude above relevant CDM velocities $\sim 10^{-3}c$.

3.2 Effect on the Power Spectrum

Our goal is to calculate the corrections to the power spectrum $\mathrm{d}P/\mathrm{d}\omega$ measured by an axion experiment due to the directional velocity effect. A non-relativistic CDM axion with mass m_a and momentum $\boldsymbol{p} = m_a \boldsymbol{v}$ converts to photons with frequency $\omega(\boldsymbol{v}) = \sqrt{m_a^2 + \boldsymbol{p}^2} \approx m_a + \frac{1}{2} m_a |\boldsymbol{v}|^2$ due to energy-conservation. Hence, in a frequency bin $\mathrm{d}\omega$ at frequency ω, any axion-experiment receives the power where the velocity matches the above condition. However, the velocity-dependent correction of the form factor $\mathcal{G}(\boldsymbol{v})$, changes the amount of power one can extract for a particular velocity $\boldsymbol{v}$. Since the form factor is a sum of a non-directional and directional part, also the power spectrum splits up into a sum of these two parts and is given by

$$\begin{aligned} \frac{\mathrm{d}P}{\mathrm{d}\omega}(t) &= P_0 \frac{\mathrm{d}v}{\mathrm{d}\omega} \left(\int v^2 \, f(\mathbf{v}; t) \, \mathrm{d}\Omega_v - \int v^2 \mathcal{G}(\mathbf{v}) \, f(\mathbf{v}; t) \, \mathrm{d}\Omega_v \right) \Big|_{|\mathbf{v}| = v(\omega)} && (3.3) \\ &\equiv P_0 \frac{\mathrm{d}v}{\mathrm{d}\omega} \Big(f[v(\omega); t] - f_{\mathcal{G}}[v(\omega); t] \Big) , && (3.4) \end{aligned}$$

where P_0 is the total power received without any directional sensitivity, i.e., $\mathcal{G} = 0$ and f is the velocity distribution in the lab frame. The integrals run over all solid angles $\mathrm{d}\Omega_v$ on a shell fulfilling the above energy-conservation condition and in the last line we define the geometry-weighted speed-distribution $f_{\mathcal{G}}$.

We may now calculate the corrections to the power spectrum due to the directional velocity sensitivity. With the shortcut $p = \mathrm{d}P/\mathrm{d}\omega$, and defining the corrections Δ as the relative difference between the directional sensitive power spectrum $p_{\mathrm{dir.}}$ and the same power spectrum without directional sensitivity $p_{\mathrm{non-dir.}}$ (i.e., setting $\mathcal{G} = 0$), we find

$$\Delta_\ell(\omega, t) \equiv \frac{p_{\mathrm{dir.}} - p_{\mathrm{non-dir.}}}{p_{\mathrm{non-dir.}}} = -\frac{f_{\mathcal{G}}[v(\omega); t]}{f[v(\omega); t]} = -\frac{g_\ell \int v_z \, f(\boldsymbol{v}; t) \, \mathrm{d}\Omega_v}{\int f(\boldsymbol{v}; t) \, \mathrm{d}\Omega_v} \Bigg|_{|\mathbf{v}| = v(\omega)} = -g_\ell \langle v_z(\omega, t) \rangle_{\Omega_v} , \tag{3.5}$$

for linearly dependent experiments, and

$$\Delta_q(\omega, t) \equiv \frac{p_{\mathrm{dir.}} - p_{\mathrm{non-dir.}}}{p_{\mathrm{non-dir.}}} = -\frac{f_{\mathcal{G}}[v(\omega); t]}{f[v(\omega); t]} = -\frac{g_q \int v_z^2 \, f(\boldsymbol{v}; t) \, \mathrm{d}\Omega_v}{\int f(\boldsymbol{v}; t) \, \mathrm{d}\Omega_v} \Bigg|_{|\mathbf{v}| = v(\omega)} = -g_q \langle v_z^2(\omega, t) \rangle_{\Omega_v} , \tag{3.6}$$

for those with quadratic dependence. We now evaluate these integrals for the Maxwellian velocity distribution f in equation (1.4). We parameterize the alignment of the lab axis $\hat{\mathbf{e}}_z$ with respect to the lab velocity $\boldsymbol{v}_{\mathrm{lab}}$ with the polar angles $(\theta_{\mathrm{lab}}, \Phi_{\mathrm{lab}})$ where we take $\hat{\mathbf{e}}_z$ to be the north pole,

i.e., $\angle(\mathbf{v}_{\rm lab}, \hat{\boldsymbol{e}}_z) \equiv \theta_{\rm lab}$. We can assume $\Phi_{\rm lab} = 0$ without loss of generality, since the velocity distribution projected on $\hat{\mathbf{z}}$ looks for all $\Phi_{\rm lab}$ the same. We also neglect the escape-velocity cutoff in the velocity distribution, since the contribution for the power spectrum should be negligible. We find for the different types of experiments

$$\ell - \text{type} : \Delta_\ell(\omega, t) = -g_\ell \ \zeta_\ell(\omega) \ \cos[\theta_{\rm lab}(t)], \tag{3.7}$$

$$q - \text{type} : \Delta_q(\omega, t) = -g_q \ \left\{\zeta_{q1}(\omega) + \zeta_{q2}(\omega) \ \cos^2[\theta_{\rm lab}(t)]\right\}, \tag{3.8}$$

where the coefficients $\zeta_{\ell,q1,q2}$ are functions that depend only on ω and parameters $\sigma_v, v_{\rm lab}$ of the velocity distribution. Explicitly,

$$\zeta_\ell(\omega) = v(\omega) \coth\left(\frac{v(\omega) v_{\rm lab}}{\sigma_v^2}\right) - \frac{\sigma_v^2}{v_{\rm lab}}, \tag{3.9}$$

$$\zeta_{q1}(\omega) = \frac{\sigma_v^2}{v_{\rm lab}} \ \zeta_\ell(\omega), \tag{3.10}$$

$$\zeta_{q2}(\omega) = v(\omega)^2 - 3\zeta_{q1}(\omega). \tag{3.11}$$

These quantities in general also depend on time, since $v_{\rm lab}$ has time-dependence. For short enough integration times less than a day, we can treat $v_{\rm lab}$ as constant. Moreover, for a respective alignment of the experiment, the time dependent terms $\theta_{\rm lab}(t)$ in equations (3.7) and (3.8) dominate. Note, that we can treat a stream in the same way by just replacing $\sigma_v \to \sigma_{\rm str}$, $\mathbf{v}_{\rm lab} \to \mathbf{v}_{\rm lab} + \mathbf{v}_{\rm str}$ and redefining $\theta_{\rm lab}$ accordingly, cf. equation (1.5). Due to the linearity of the involved integrals, if $\mathcal{G}$ is a sum of contributions from different axes of the experiment, the above result holds in general by simply adding up all corrections from all axes with each different $\theta_{\rm lab}^{x,y,z}$ depending on the axes.

Figure 3.2 shows the modulations of the power spectrum for different cases. The blue lines show the power spectrum of an equivalent experiment without directional sensitivity, while the orange shaded regions show the range of the modulation in an experiment with directional sensitivity. The upper panels correspond to parameters similar to the power spectrum of the SHM ($v_{\rm lab} = \sigma_v = 220\,\mathrm{km\,s^{-1}}$), while the lower panels correspond to parameters similar to a recently discovered stream in the solar neighborhood dubbed 'S1 stream' [64] ($|\boldsymbol{v}_{\rm lab} + \boldsymbol{v}_{\rm stream}| = 520\,\mathrm{km\,s^{-1}}$, $\sigma_v = 20\,\mathrm{km\,s^{-1}}$). The left panels correspond to linear experiments with $g_\ell = 100\,c^{-1}$, the right panels correspond to quadratic experiments with $g_q = 10^5\,c^{-2}$. These are of the same order than the benchmark values for realistic experiments assumed in [1].

Let us now gain some more intuition from this analytical result. First of all, all ζ approach 0 for $\boldsymbol{v} \to 0$, since $x\coth(x)$ approaches 1 for small x. This is expected, since $\mathcal{G}(0) = 0$ by definition. Moreover, all coefficients are positive. Thus, in the ℓ-type experiment the power spectrum can be both increased or decreased depending on time, while for the q-type experiment the power spectrum is always decreased, as we can see in figure 3.2. This is intuitive, since the geometry factor with a positive g_q only reduces the received power. For the q-type experiments the coefficient ζ_{q1} appears as a constant power reduction in the correction. It is proportional to the dispersion of the velocity distribution σ_v and thus vanishes for a stream with low velocity dispersion, as can be seen in the lower right panel in figure 3.2. A large dispersion corresponds to multiple velocities the experiment 'sees' during a single measurement of the power spectrum. For the ℓ-type these average out, since the negative and positive velocities affect the power in the opposite way. For the q-type, however, there is no distinction between sign and all non-zero velocities reduce the power, i.e., the

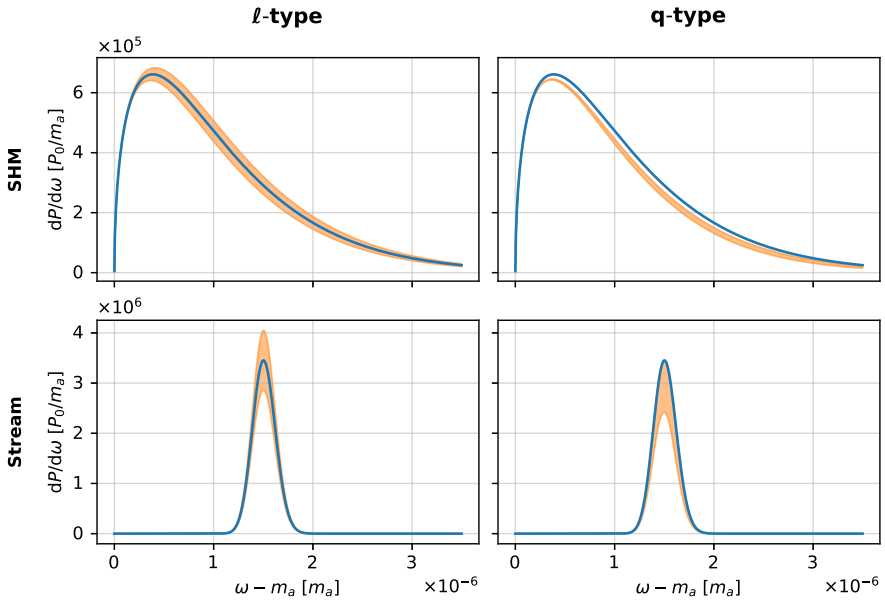

Figure 3.2: Modulation of the power spectrum received by a generic axion-experiment. The blue lines show the power spectrum without any directional sensitivity. The orange shaded regions show the maximum modulation range for a linearly-sensitive experiment with $g_\ell = 100\,c^{-1}$ (left) and a quadratically-sensitive experiment with $g_q = 10^5\,c^{-2}$ (right). The upper panels show the effect on the power spectrum if the CDM velocity distribution follows the SHM. The lower panels show the effect if the CDM velocity distribution is given by a stream similar to the S1 stream [64]. In reality one expects a linear superposition of both.

dispersion leads to a minimum reduction of the received power. Lastly, for the ℓ-type experiment the modulation goes with $\cos\theta_{\rm lab}$ while for the q-type one it goes with $\cos^2\theta_{\rm lab}$. Hence, for a linearly rotating $\theta_{\rm lab}$, the frequency at which the power spectrum modulates is doubled for the q-type experiment compared to the ℓ-type experiment. This is easily understood by remembering that the q-type experiment does not distinguish between positive and negative velocities, e.g. sees twice the same distribution of absolute velocities per day, while the ℓ-type experiment is sensitive to the sign of v_z.

3.3 Framework for Analytical Sensitivity Estimates

The above formalism enables us to calculate the changes to the power spectrum for a general velocity-sensitive experiment. In order to actually measure these changes and possibly infer parameters of the velocity distribution, one has to compare the changes to the signal-to-noise ratio of the measured power spectrum given by the Dicke radiometer equation (2.7). In this section we therefore employ a likelihood approach, which will enable to extract general requirements for observation time or, conversely, required system noise temperature to resolve these modulations in the power spectrum.

We assume we have measured a total number of $N_t = t_{\rm obs}/\Delta t$ power spectra, where $t_{\rm obs}$ is

the total observation time and Δt the time required to acquire a single spectrum, and for each power spectrum we measured $N_\omega = \Delta\Omega/(2\pi\Delta\nu)$ frequency bins, where $\Delta\Omega$ is the bandwidth of the full recorded spectrum and $\Delta\omega = 2\pi\Delta\nu$ the bandwidth of a single bin. In reality we measure the integrated power in these frequency bins, i.e., we can measure $P_{ij}^{\mathrm{obs}} \simeq \Delta\omega\,[\mathrm{d}P(\omega_i, t_j)/\mathrm{d}\omega]$.

Statistical Framework

Let us now assume a model $\mathcal{M}(\Theta)$ with free parameters Θ predicting the measured power spectrum to follow $P_{ij}^{\mathrm{exp}}(\Theta)$. In our case, Θ will be the free parameters of the model including all information on the velocity distribution and its modulation as seen by the experiment. Then, we expect the measured power spectrum P_{ij}^{obs} according to the radiometer equation (2.7) to be normal distributed around the expected value with a standard deviation of

$$\sigma_N = k_B T_{\mathrm{sys}} \sqrt{\frac{\Delta\nu}{\Delta t}}. \tag{3.12}$$

The likelihood of measuring a particular set of power spectra P_{ij}^{meas} assuming the model $\mathcal{M}(\Theta)$ can thus be expressed as

$$\mathcal{L}(P_{ij}^{\mathrm{obs}}|\mathcal{M}(\Theta)) = \prod_{ij} \frac{1}{\sqrt{2\pi\sigma_N^2}} \exp\left\{ \frac{-\left[P_{ij}^{\mathrm{obs}} - P_{ij}^{\mathrm{exp}}(\Theta)\right]^2}{2\sigma_N^2} \right\}. \tag{3.13}$$

To test a model $\mathcal{M}_1$ against a null-hypothesis $\mathcal{M}_0$, we consider the likelihood ratio

$$\Lambda = \frac{\max_{\Theta_1} \mathcal{L}(P|\mathcal{M}_1, \Theta_1)}{\max_{\Theta_0} \mathcal{L}(P|\mathcal{M}_0, \Theta_0)}, \tag{3.14}$$

where we compare the models with the set of parameters Θ such their respective likelihood is maximized, i.e., they describe the data best. According to Wilks' theorem the test statistic $D = -2\ln\Lambda$ is $\chi^2_{\mu_1-\mu_0}$-distributed for a large set of measurements, where the degree of freedom for the χ^2-distribution is given by the difference of free parameters $\mu_1 - \mu_0$ between the two models [109]. A given set of measured data then gives D_{obs} from which the p-value can be calculated by integrating $\chi^2_{\mu_1-\mu_0}$-distribution from D_{obs} to infinity.

Therefore, we could estimate the sensitivity of a particular experiment with a Monte Carlo approach, i.e., by generating a large set of simulated measurements. One would then infer the median of D_{obs} from the simulated ensemble, which would give the expected p-value for detection of e.g. the modulation. Here we follow a more analytic approach using Asimov data, i.e., we use data that follows exactly the prediction of model $\mathcal{M}_1$, instead. This means, we set $P_{ij}^{\mathrm{obs}} = P_{ij}^{\mathrm{exp}}(\Theta_1)$. Thus, the likelihood for the model $\mathcal{M}_1$ is set to one. Assuming the model $\mathcal{M}_1$ is correct, one can show that for a large set of measurement points (i, j) this procedure gives the median value of the distribution of D one would obtain with the Monte Carlo approach described above [110].

Measuring Modulations

Besides the parameters of the velocity distribution $(v_{\mathrm{lab}}, \sigma_v)$, which we assume to be constant in time (see above), we need to parameterize the temporal oscillation of θ_{lab}. We thus rewrite

$$\cos(\theta_{\mathrm{lab}}) \approx c_0 + c_1 \cos(\omega_d t + \phi), \qquad \text{with } |c_0| + |c_1| < 1, \tag{3.15}$$

where ω_d is the frequency of the daily or annual modulation, respectively. The parameters c_0, c_1, ϕ are given by astrophysics, i.e., the earth spinning and rotating around the Sun [1]. We compare the model including the modulation $\mathcal{M}_1$ with a model without modulation $\mathcal{M}_0$

$$\mathcal{M}_0: \quad P_{ij} = P_0 \Delta\omega f(\omega_i), \quad \Theta = \{P_0, v_{\text{lab}}, \sigma_v\}\,, \tag{3.16}$$

$$\mathcal{M}_1: \quad P_{ij} = P_0 \Delta\omega [f(\omega_i) - f_{\mathcal{G}}(\omega_i, t_j)], \quad \Theta = \{P_0, v_{\text{lab}}, \sigma_v, c_0, c_1, \phi\}\,, \tag{3.17}$$

where $f(\omega) = f[v(\omega)], f_{\mathcal{G}}(\omega, t) = f_{\mathcal{G}}[v(\omega), t]$. When computing the test statistic D for these models using Asimov data the unmodulated speed distribution $f[v(\omega)]$ drops out and we are left with an integral over the correction $f_{\mathcal{G}}(\omega, t)$ given by

$$D = \sum_{i,j} \left[\frac{\int_{\text{bin}} P_0 f_{\mathcal{G}}(\omega_i, t_j)\, \mathrm{d}\omega}{\sigma_N} \right]^2 . \tag{3.18}$$

Assuming that the frequency and time bin sizes are small enough and our data contain most of the signal peak, we can approximate the sum with an integral

$$D \approx \frac{\Delta\omega}{\Delta t} \int_0^{t_{\text{obs}}} \mathrm{d}t \int_{m_a}^{\infty} \mathrm{d}\omega \, \left[\frac{P_0 f_{\mathcal{G}}(\omega, t)}{\sigma_N} \right]^2 . \tag{3.19}$$

While for the linear-type experiment we want to resolve the modulation, we consider two cases for the quadratic-type experiment, where we are either just interested in resolving the offset of the power spectrum or its modulation, assuming we know the offset. We then find for the test statistics in these cases

$$\ell-\text{type}: \quad D_\ell \approx \frac{\Delta\omega}{\Delta t} \int_0^{t_{\text{obs}}} \mathrm{d}t \int_{m_a}^{\infty} \mathrm{d}\omega \, \left[\frac{g_\ell\, P_0 f(\omega)\, \zeta_\ell(\omega)\, \cos\theta_{\text{lab}}(t)}{\sigma_N} \right]^2 , \tag{3.20}$$

$$q-\text{type (offset)}: \quad D_{q1} \approx \frac{\Delta\omega}{\Delta t} \int_0^{t_{\text{obs}}} \mathrm{d}t \int_{m_a}^{\infty} \mathrm{d}\omega \, \left[\frac{g_q\, P_0 f(\omega)\, \zeta_{q1}(\omega)}{\sigma_N} \right]^2 , \tag{3.21}$$

$$q-\text{type (modulation)}: \quad D_{q2} \approx \frac{\Delta\omega}{\Delta t} \int_0^{t_{\text{obs}}} \mathrm{d}t \int_{m_a}^{\infty} \mathrm{d}\omega \, \left[\frac{g_q\, P_0 f(\omega)\, \zeta_{q2}(\omega)\, \cos^2\theta_{\text{lab}}(t)}{\sigma_N} \right]^2 . \tag{3.22}$$

The full test statistic for the q-type experiment can be obtained as a sum of all those when replacing $\zeta_\ell \to \zeta_{q1}\zeta_{q2}$ in equation (3.20). Neglecting this term leads to a slightly too small D and thus underestimates the sensitivity of a given experiment. Notice that the integrands are separable functions in ω and t, i.e., the integrals split up in a product of two integrals over ω and t, respectively.

Let us first consider the linear-type experiments. Inserting the astrophysical parameters of the velocity distribution and lab velocity, we find explicitly

$$D_\ell \approx 2\pi \left(\frac{P_0}{k_B T_{\text{sys}}} \right)^2 g_\ell^2\, \mathcal{I}_\omega^\ell\, \mathcal{I}_t^\ell\,, \tag{3.23}$$

where the integrals $\mathcal{I}_{\omega,t}^\ell$ are given by

$$\mathcal{I}_\omega^\ell = \frac{\sqrt{\pi}\left(2v_{\text{lab}}^2 - \sigma_v^2\right) \operatorname{erf}\left(\frac{v_{\text{lab}}}{\sigma_v}\right) + 2\sigma_v v_{\text{lab}} \exp\left(-\frac{v_{\text{lab}}^2}{\sigma_v^2}\right)}{4\pi v_{\text{lab}} \sigma_v} \frac{1}{m_a}\,, \tag{3.24}$$

$$\mathcal{I}_t^\ell = \Big[{c_0}^2 t + \frac{{c_1}^2 t}{2} + \frac{2c_0 c_1 \sin(\omega_d t + \phi)}{\omega_d} + \frac{{c_1}^2 \sin(\omega_d t + \phi)\cos(\omega_d t + \phi)}{2\omega_d} \Big]_0^{t_{\text{obs}}} . \tag{3.25}$$

Notice, importantly, that $\mathcal{I}_\omega^\ell$ contains a factor $1/m_a$. It comes from the fact that we integrate the square of the distribution[1] $f(\omega)$. For daily modulations the oscillatory and phase-offset terms can be neglected for long enough measurement times, giving

$$\mathcal{I}_t^\ell \approx \left({c_0}^2 + \frac{1}{2} {c_1}^2 \right) t_{\rm obs} \,. \tag{3.26}$$

For a stream with small velocity dispersion $\sigma_v \equiv \sigma_{\rm str} \ll |\boldsymbol{v}_{\rm lab} - \boldsymbol{v}_{\rm str}|$, we can in addition approximate the integral over frequencies

$$\mathcal{I}_\omega^\ell \approx \frac{2|\boldsymbol{v}_{\rm lab} - \boldsymbol{v}_{\rm str}|^2 - \sigma_{\rm str}^2}{4\sqrt{\pi}|\boldsymbol{v}_{\rm lab} - \boldsymbol{v}_{\rm str}|\sigma_{\rm str}} \frac{1}{m_a}. \tag{3.27}$$

Analogously we find for the full test statistic of the quadratic experiments

$$D_q = 2\pi \left(\frac{P_0}{k_B T_{\rm sys}} \right)^2 g_q^2 \left(\mathcal{I}_\omega^{q1} \mathcal{I}_t^{q1} + \mathcal{I}_\omega^{q2} \mathcal{I}_t^{q2} + \mathcal{I}_\omega^{q12} \mathcal{I}_t^{q12} \right) , \tag{3.28}$$

where the '$q1$' terms arise from the offset term $\propto \zeta_{q1}$ and the the '$q2$' terms arise from the offset term $\propto \zeta_{q2}$. From the offset we get

$$\mathcal{I}_\omega^{q1} = \left(\frac{\sigma_v^2}{v_{\rm lab}} \right)^2 \mathcal{I}_\omega^\ell \,, \tag{3.29}$$

$$\mathcal{I}_t^{q1} = t_{\rm obs}. \tag{3.30}$$

Since the offset is independent of the modulation, $\mathcal{I}_t^{q1}$ does not depend on c_0, c_1 and ϕ. In contrast, the modulation terms are

$$\mathcal{I}_\omega^{q2} = \frac{\sqrt{\pi}\left(-4\sigma_v^2 v_{\rm lab}^2 + 4v_{\rm lab}^4 + 3\sigma_v^4\right) \mathrm{erf}\left(\frac{v_{\rm lab}}{\sigma_v}\right) + \exp\left(-\frac{v_{\rm lab}^2}{\sigma_v^2}\right)\left(4\sigma_v v_{\rm lab}^3 - 6\sigma_v^3 v_{\rm lab}\right)}{8\pi\sigma_v v_{\rm lab}} \frac{1}{m_a} \,, \tag{3.31}$$

$$\begin{aligned} \mathcal{I}_t^{q2} = & \Bigg[\left(\frac{3c_1^4}{8} + 3c_1^2 c_0^2 + c_0^4 \right) t \\ & + \left(\frac{4c_1 c_0^3}{\omega_d} + \frac{3c_1^3 c_0}{\omega_d} \right) \sin(t\omega_d + \phi) + \left(\frac{3c_1^2 c_0^2}{2\omega_d} + \frac{c_1^4}{4\omega_d} \right) \sin\left[2(t\omega_d + \phi)\right] \\ & + \frac{c_1^3 c_0}{3\omega_d} \sin\left[3(t\omega_d + \phi)\right] + \frac{c_1^4}{32\omega_d} \sin\left[4(t\omega_d + \phi)\right] \Bigg]_0^{t_{\rm obs}} . \end{aligned} \tag{3.32}$$

The mixing term can be expressed in terms of previously calculated integrals as

$$\mathcal{I}_\omega^{q12} \mathcal{I}_t^{q12} = 2 \int_0^{t_{\rm obs}} \mathrm{d}t \int_{m_a}^\infty \mathrm{d}\omega \; \zeta_{q1}(\omega) \zeta_{q2}(\omega) \left[f(\omega) \cos(\theta_{\rm lab}) \right]^2 \tag{3.33}$$

$$= 2 \frac{\sigma_v^2}{v_{\rm lab}^2} \; \mathcal{I}_\omega^{q2} \; \mathcal{I}_t^\ell \,. \tag{3.34}$$

Notice that we can employ the same approximations as before, i.e., if we approximate over several days we have for the modulation

$$\mathcal{I}_t^{q2} \approx \left(\frac{3c_1^4}{8} + 3c_1^2 c_0^2 + c_0^4 \right) t_{\rm obs} \,, \tag{3.35}$$

[1] Consider:

$$\int_{m_a}^\infty f(\omega)^2 \, \mathrm{d}\omega = \int_{m_a}^\infty \left(\frac{\mathrm{d}v}{\mathrm{d}\omega} f(v) \right)^2 \mathrm{d}\omega = \frac{1}{m_a} \int_0^\infty \frac{f^2(v)}{v} \, \mathrm{d}v.$$

and in the case of a stream ($\sigma_v \equiv \sigma_{\rm str} \ll |\boldsymbol{v}_{\rm lab} - \boldsymbol{v}_{\rm str}|$) we find

$$\mathcal{I}_\omega^{q2} \approx \frac{\sqrt{\pi}\left(-4\sigma_{\rm str}^2|\boldsymbol{v}_{\rm lab} - \boldsymbol{v}_{\rm str}|^2 + 4|\boldsymbol{v}_{\rm lab} - \boldsymbol{v}_{\rm str}|^4 + 3\sigma_{\rm str}^4\right)}{8\pi\sigma_{\rm str}|\boldsymbol{v}_{\rm lab} - \boldsymbol{v}_{\rm str}|}\frac{1}{m_a}\,. \tag{3.36}$$

Let us briefly compare how the test statistics scale with the total power P_0, the system noise temperature $T_{\rm sys}$, the measurement time $t_{\rm obs}$, the axion linewidth $\Delta\nu_a \propto m_a$ and the parameters of the experiment g_ℓ, g_q with our intuition. Assuming sufficiently long integration time over more than a full modulation and taking the square root of the test statistics in equations (3.23) and (3.28) we find after inserting the relevant integrals

$$\sqrt{D_{\ell,q}} \propto \left(\frac{g_{\ell,q}P_0}{k_B T_{\rm sys}}\right)\sqrt{\frac{t_{\rm obs}}{\Delta\nu_a}}\,. \tag{3.37}$$

Notice that this is in full analogy to the Dicke radiometer equation (2.7), just as expected. The change in power due to the velocity sensitivity is always linear in $g_{\ell,q}$ according to equation (3.2), i.e., it reappears here as a constant factor in front of P_0, as well. Turning to the parameters of the velocity distribution, we see that the parameters c_0 and c_1 only appear in the time integrals and only in the nominator, cf. equations (3.25) and (3.32). This is intuitive, since only measuring over a certain time can reveal the modulation in time. In addition, large modulation parameters c_0 and c_1 lead to a larger test statistic, i.e., a more significant modulation signal, as expected. In turn, the unmodulated parameters $v_{\rm lab}$ and σ_v of the velocity distribution essentially modify the shape of the power spectrum but were assumed not to change with time. Thus, they only appear in the frequency integrals, cf. equations (3.24), (3.29) and (3.31).

To obtain a better intuition on how the test statistics depends on $v_{\rm lab}$ and σ_v, we plot the required system noise temperatures for a realistic linear-type experiment and quadratic-type experiment in figure 3.3 as a function of these parameters. Assuming we want to achieve a p-value of 0.3 % (corresponding to $\sim 3\sigma$-level), we require for the test statistic $D \approx 14$. Note that after the axion is found, it is much easier to build very sensitive experiments to see the signal from axion-photon conversion. Therefore, we consider $P_0 \sim 10^{-21}\,\mathrm{W}$ to be a roughly realistic assumption for the total power output. We also assume the experiment is positioned such that $c_0 \approx 0$, $c_1 \approx 0.7$. The dotted circle denotes the SHM. The area below the horizontal dotted line ($\sigma_v = 25\,\mathrm{km\,s^{-1}}$) roughly corresponds to the realistic area for streams. We see that system temperatures of a few Kelvin are sufficient to resolve the modulations. We also notice that for low lab velocities, corresponding to a dark disk scenario, the sensitivity to modulation parameters would disappear, since the orientation of the lab $\theta_{\rm lab}$ with respect to the lab velocity is undefined for $\boldsymbol{v}_{\rm lab} = 0$. On the other hand, this is irrelevant for the offset in a q-type experiment, where we see again that it essentially scales with the dispersion of the velocity distribution σ_v as discussed above, i.e., it disappears for a stream. In contrast, the dispersion reduces the modulations, since more velocities are 'seen' during the time Δt of a single power spectrum measurement. Thus, the sensitivity for modulations goes down as one increases σ_v. More detailed calculations of the sensitivity for realistic experiments based on the test statistics above for different components of the velocity distribution have been performed by our collaborators, see [1].

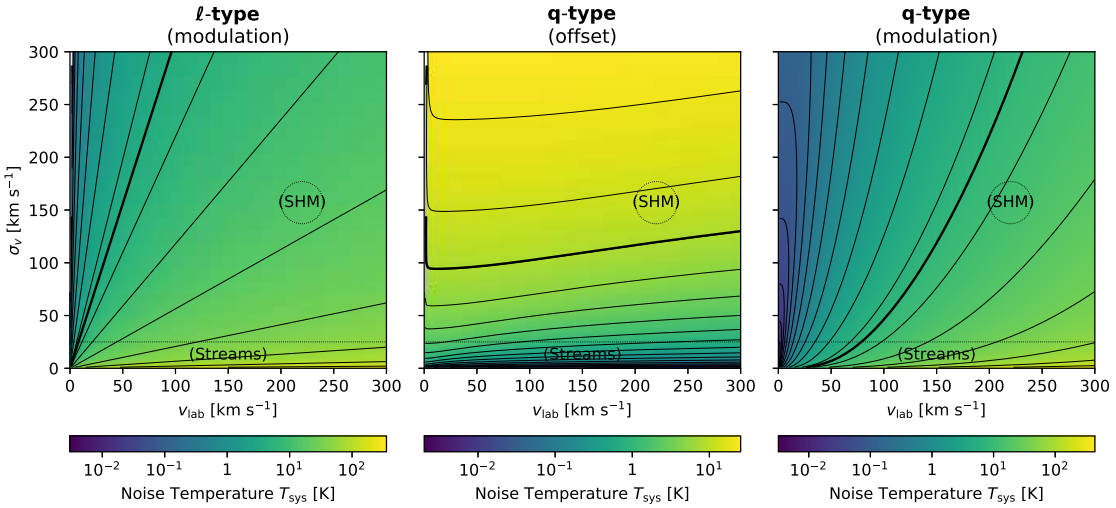

Figure 3.3: Required noise temperature T_{sys} to be sensitive to daily modulations after one month of measurement with a p-value of 0.3 % as a function of the parameters from the velocity distribution. Assuming the experiment provides $P_0 \sim 10^{-21}\,\mathrm{W}$ and is positioned such that for the modulation signal we have $c_0 \approx 0$, $c_1 \approx 0.7$. The lines denote identical required system noise temperatures. The bold line corresponds to 4 K. The dotted circle denotes the SHM, while the viable range for streams is indicated by a horizontal dotted line. More details cf. main text.

Parameter Constraints

Until now we have only determined a test statistic to quantify how significant a measurement of the change to the power spectrum would be. Once there is evidence for the modulation, one would in addition be interested to infer the parameters of the modulation c_0, c_1, ϕ itself. This would allow us to compare them with astrophysical expectations to confirm once more that the signal origin is the dark matter halo. Moreover, one could even do 'axion astronomy,' i.e., use this method to measure for example the Solar velocity in the galactic frame.

The uncertainty on a parameter measurement can be estimated by considering the unmaximized likelihood radio

$$d(\Theta) = 2 \ln \frac{\mathcal{L}(P|\mathcal{M}_1,\, \Theta)}{\mathcal{L}(P|\mathcal{M}_0,\, \Theta)}\,, \tag{3.38}$$

where if Θ only contains the parameters of interest, $\max_\Theta d(\Theta) = D$. The uncertainty on a model parameter $\vartheta \in \Theta$ can be estimated from the curvature of d around the value $\hat{\vartheta}$ that maximizes the likelihood under $\mathcal{M}_1$

$$\sigma_\vartheta^{-2} = -\frac{1}{2} \frac{\partial^2}{\partial \vartheta^2} d\big|_{\vartheta=\hat{\vartheta}}\,. \tag{3.39}$$

For a daily modulation we are interested in the set $\Theta = \{c_0, c_1, \phi\}$. The other parameters are treated as known, which is a reasonable assumption because they can already be extracted from an experiment without directional sensitivity. If the true parameters are θ_{true}, we may compute d for the Asimov data set giving

$$d(\Theta) = -\sum_{i,j} \chi^2_{ij,\,1}(\Theta) + \sum_{ij} \chi^2_{ij,\,0}\,, \tag{3.40}$$

where

$$\chi^2_{ij,\,1}(\Theta) \equiv \left[\frac{\int_{\text{bin}} P_0\{f_{\mathcal{G}}(\omega_i,\, t_j \,|\, \Theta) - f_{\mathcal{G}}(\omega_i,\, t_j \,|\, \Theta_{\text{true}})\}\,\mathrm{d}\omega}{\sigma_N}\right]^2 \tag{3.41}$$

$$\chi^2_{ij,\,0} \equiv \left[\frac{\int_{\text{bin}} P_0 f_{\mathcal{G}}(\omega_i,\, t_j \,|\, \Theta_{\text{true}})\,\mathrm{d}\omega}{\sigma_N}\right]^2 . \tag{3.42}$$

Before we were only interested in the second summand, since the likelihood maximization makes the first one 0. However, here only the first one depends actually on Θ, and the second term vanishes when taking the derivative with respect to any $\vartheta \in \Theta$. For the linear-type experiment we find

$$d(\Theta) \approx \frac{\Delta\omega}{\Delta t}\int_0^{t_{\text{obs}}}\mathrm{d}t\int_0^{\infty}\mathrm{d}\omega\ \left[\frac{P_0 f(\omega) g_\ell\,\zeta_\ell(\omega)\,\{\cos(\theta_{\text{lab}})|_\Theta - \cos(\theta_{\text{lab}})|_{\Theta_{\text{true}}}\}}{\sigma_N}\right]^2 , \tag{3.43}$$

which involve the same integrals over ω that have already been introduced in computing D. We find for the uncertainty

$$\sigma_\vartheta^{-2} = -\,\pi\left(\frac{P_0}{k_B T_{\text{sys}}}\right)^2 g_\ell^2\,\mathcal{I}_\omega^\ell\,\frac{\partial^2 d_t}{\partial\vartheta^2}\bigg|_{\Theta=\Theta_{\text{true}}} , \tag{3.44}$$

with the derivatives of the time integral d_t given by

$$-\frac{\partial^2 d_t}{\partial c_0^2}\bigg|_{\Theta_{\text{true}}} = 2t_{\text{obs}} \tag{3.45}$$

$$-\frac{\partial^2 d_t}{\partial c_1^2}\bigg|_{\Theta_{\text{true}}} = t_{\text{obs}} - \frac{\sin(2\phi_{\text{true}})}{2\omega_d} + \frac{\sin\left[2(t_{\text{obs}}\omega_d + \phi_{\text{true}})\right]}{2\omega_d} \tag{3.46}$$

$$-\frac{\partial^2 d_t}{\partial \phi^2}\bigg|_{\Theta_{\text{true}}} = {c_{1,\text{true}}}^2\left(t_{\text{obs}} + \frac{\sin(2\phi_{\text{true}})}{2\omega_d} - \frac{\sin\left[2(t_{\text{obs}}\omega_d + \phi_{\text{true}})\right]}{\omega_d} + \frac{\sin\left(2t_{\text{obs}}\omega_d + 2\phi_{\text{true}}\right)}{2\omega_d}\right) . \tag{3.47}$$

The offset in the quadratic-type experiments is insensitive to any of the parameters Θ. The modulation for the quadratic-type experiments leads more lengthy terms, analogous to (3.45)–(3.47). For large times t_{obs} the oscillatory terms again are negligible and we arrive at

$$-\frac{\partial^2 d_t}{\partial c_0^2}\bigg|_{\Theta_{\text{true}}} \approx (8c_{0,\text{true}}^2 + 4c_{1,\text{true}}^2)\,t_{\text{obs}} , \tag{3.48}$$

$$-\frac{\partial^2 d_t}{\partial c_1^2}\bigg|_{\Theta_{\text{true}}} \approx (4c_{0,\text{true}}^2 + 3c_{1,\text{true}}^2)\,t_{\text{obs}} , \tag{3.49}$$

$$-\frac{\partial^2 d_t}{\partial \phi^2}\bigg|_{\Theta_{\text{true}}} \approx c_{1,\text{true}}^2(4c_{0,\text{true}}^2 + c_{1,\text{true}}^2)\,t_{\text{obs}} . \tag{3.50}$$

Including the offset term ends exactly as above since it does not depend on Θ, so it cancels out in the first summand of d. This is as expected, since a known offset should not alter the significance at which the parameters of an oscillation can be inferred. Again checking how the result scales we see

$$\sigma_\vartheta^{-1} \propto \left(\frac{g_{\ell,q} P_0}{k_B T_{\text{sys}}}\right)\sqrt{\frac{t_{\text{obs}}}{\Delta\nu_a}} \tag{3.51}$$

behaves analogous to the naive expectation from Dicke's radiometer equation (2.7). Also notice that the uncertainty in ϕ scales always inversely to the amplitude of the modulation as c_1.

This dependency is also expected, because for unmodulated signal ($c_1 = 0$) the phase is undefined and unmeasurable.

Based on the formalism derived above, our collaborators have derived more detailed requirements and resultant expected sensitivities for directional sensitive axion experiments to astrophysical parameters. For more details see [1].

In short. We have derived an analytical formalism for the modulation of the power spectrum from axion-photon conversion of a general directionally sensitive axion haloscope. Using frequentist statistics and Asimov data we have derived analytical formulae for experimental sensitivity on these parameters, analogous to the radiometer equation (2.7). This work thus provides a basis for axion astronomy in the post-detection era of an axion-like particle.

Part III

Simulating MADMAX

Chapter 4

1D Models Review

In section 2.1 we have argued that the emission of axion-induced radiation from the disks occurs in order to compensate the discontinuity of the axion-induced electric field at the surface of dielectrics. By combining many such boundaries one can constructively interfere the emission from all boundaries. In addition, each emission from a particular surface can interfere constructively with itself when it is internally reflected within the booster, which corresponds to an additional resonant enhancement of the power emitted by the haloscope. In this chapter we lay out different formalisms to actually calculate the electromagnetic fields in the haloscope, and thereby the boost factor, reflectivity and transmissivity of the system.

All formalisms have in common that we start with the general 1D solution to the axion-Maxwell-equations. We consider regions r within the dielectric haloscope with the same dielectric constant ϵ_r and magnetic field B_r, cf. figure 4.1. In each region the electric field E and magnetic field strength H take the form

$$E_r(z) = \quad R_r \exp(+i\omega n_r z) + L_r \exp(-i\omega n_r z) + (E_a)_r, \tag{4.1}$$

$$H_r(z) = n_r \left[R_r \exp(+i\omega n_r z) - L_r \exp(-i\omega n_r z)\right], \tag{4.2}$$

where R_r, L_r are complex-valued amplitudes of the fields in each region, n_r is the refractive index of region r, and $(E_a)_r$ is the axion-induced field in region r as defined in equation (2.3). For convenience we define

$$A_r \equiv \frac{B_r}{B_{\mathrm{e,max}}\epsilon_r}, \quad E_0 \equiv \frac{(E_a)_r}{A_r}, \tag{4.3}$$

where $B_{\mathrm{e,max}}$ is the maximum external magnetic field in the haloscope. E_0 is the amplitude of the axion-induced field in vacuum at the point of the maximum magnetic field. The task is to find the coefficients L_r, R_r, such that the electromagnetic fields solve all boundary conditions between any two regions r and $r-1$ of the haloscope, given by

$$E_r(z_r) = E_{r-1}(z_r), \qquad H_r(z_r) = H_{r-1}(z_r), \tag{4.4}$$

where the boundary between region r and $r-1$ is at z_r.

We will first review transfer matrices [89, 111] to solve all boundary conditions simultaneously. To gain a better qualitative understanding, we will employ a ray tracing approach. These two

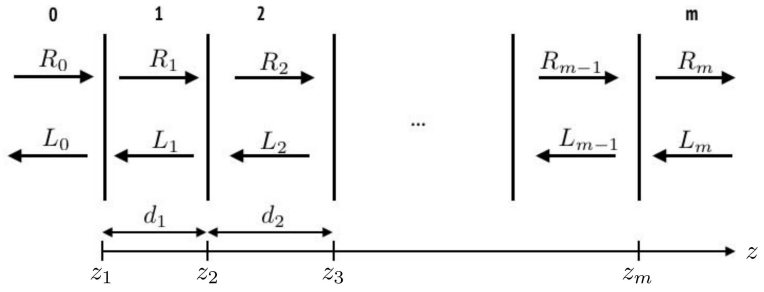

Figure 4.1: Parametrization of left- and right-propagating waves with amplitudes R_r and L_r in our system of different regions with different dielectric constants ϵ_r and length d_r. Adapted from [89].

approaches are later generalized to 3D in chapter 6. After briefly discussing alternatives, we review some important consequences directly following from these models. They will play a role in the understanding of systematic effects on the boost factor in later chapters.

4.1 Transfer Matrix Formalism

We follow the derivation in [89]. After inserting the general solutions described in equations (4.1) and (4.2), the boundary conditions in equations (4.4) can be expressed in terms of the coefficients (R_r, L_r) in each region as

$$\begin{pmatrix} R_m \\ L_m \end{pmatrix} = \mathsf{G}_{m-1}\mathsf{P}_{m-1} \begin{pmatrix} R_{m-1} \\ L_{m-1} \end{pmatrix} + \mathsf{S}_{m-1} \begin{pmatrix} E_0 \\ E_0 \end{pmatrix}. \tag{4.5}$$

Here we have defined the transfer matrices

$$\mathsf{G}_r = \frac{1}{2n_{r+1}} \begin{pmatrix} n_{r+1}+n_r & n_{r+1}-n_r \\ n_{r+1}-n_r & n_{r+1}+n_r \end{pmatrix}, \qquad \text{(Reflection / Transmission)} \tag{4.6}$$

$$\mathsf{P}_r = \begin{pmatrix} e^{+i\delta_r} & 0 \\ 0 & e^{-i\delta_r} \end{pmatrix}, \qquad \text{(Propagation)} \tag{4.7}$$

$$\mathsf{S}_r = \frac{A_{r+1} - A_r}{2}\,\mathbb{1}, \qquad \text{(Axion-Induced Fields)} \tag{4.8}$$

and $\delta_r = \omega n_r d_r$ is the phase depth of region r. Iteratively applying equation (4.5) gives the rightmost fields in region m in terms of the leftmost fields in region 0 as

$$\begin{pmatrix} R_m \\ L_m \end{pmatrix} = \mathsf{T}_0^m \begin{pmatrix} R_0 \\ L_0 \end{pmatrix} + \sum_{s=1}^{m} \mathsf{T}_s^m \mathsf{S}_{s-1} \begin{pmatrix} E_0 \\ E_0 \end{pmatrix} \tag{4.9}$$

$$\equiv \mathsf{T} \begin{pmatrix} R_0 \\ L_0 \end{pmatrix} + \mathsf{M} \begin{pmatrix} E_0 \\ E_0 \end{pmatrix}, \tag{4.10}$$

with a transfer matrix between regions a and b with $b < a$

$$\mathsf{T}_b^a = \mathsf{G}_{a-1}\mathsf{P}_{a-1}\mathsf{G}_{a-2}\mathsf{P}_{a-2} \ldots \mathsf{G}_{b+1}\mathsf{P}_{b+1}\mathsf{G}_b\mathsf{P}_b, \quad \mathsf{T}_a^a = \mathbb{1}. \tag{4.11}$$

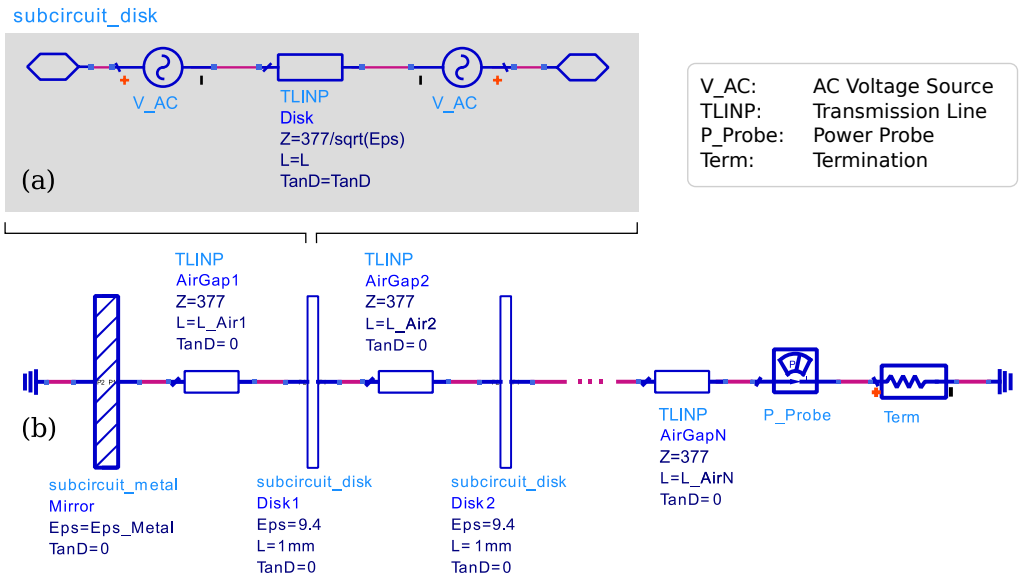

Figure 4.2: One-dimensional (1D) model representation in *Advanced Design System (ADS)* [112]. 'Z' is the impedance in Ω, 'Eps' is the dielectric constant, 'L' is the length, and 'TanD' is the loss tangent of the respective element. (a) Model of a dielectric disk ('subcircuit_disk'). The discontinuity of the axion-induced field on the disk surfaces is implemented with voltage sources ('V_AC'). The copper mirror ('subcircuit_metal') is modeled analogous. (b) Booster model combining many dielectric disks. The mirror sub-circuit is analogous to the disk.

The power boost factor is obtained when considering the rightmost (leftmost) outgoing amplitude as $\beta^2 = |R_m/E_0|^2$ ($\beta^2 = |L_0/E_0|^2$), requiring no inwards propagating waves $R_0 = L_m = 0$. Solving equation (4.9) under these conditions gives

$$L_0 = -\mathsf{T}[2,2]^{-1}\left(\mathsf{M}[2,1] + \mathsf{M}[2,2]\right) E_0, \tag{4.12a}$$

$$R_m = \left\{\mathsf{M}[1,1] + \mathsf{M}[1,2] - \mathsf{T}[2,2]^{-1}\left(\mathsf{M}[2,1] + \mathsf{M}[2,2]\right)\mathsf{T}[1,2]\right\} E_0. \tag{4.12b}$$

The transmissivities and reflectivities are obtained without the axion contribution and again setting the respective opposite inward propagating wave to zero. This gives

$$\mathcal{T}_L = \mathsf{T}[1,1] - \mathsf{T}[1,2]\mathsf{T}[2,2]^{-1}\mathsf{T}[2,1]\,, \qquad \mathcal{T}_R = \mathsf{T}[2,2]^{-1}\,, \tag{4.13}$$

$$\mathcal{R}_L = -\mathsf{T}[2,2]^{-1}\mathsf{T}[2,1]\,, \qquad \mathcal{R}_R = +\mathsf{T}[1,2]\mathsf{T}[2,2]^{-1}\,, \tag{4.14}$$

where $\mathcal{T}_L$ is the transmissivity from left to right, $\mathcal{T}_R$ the transmissivity from right to left, $\mathcal{R}_L$ the reflectivity from the left side and $\mathcal{R}_R$ the reflectivity from the right side.

Such 1D transfer matrices are implemented in circuit simulators such as *Advanced Design System (ADS)* [112] or the open-source pendant *Qucs* [113]. An example of how this can be done in ADS is shown in figure 4.2. In a circuit simulator the discontinuity corresponds to a voltage drop between transmission-lines and can therefore be modeled using voltage sources at the disk surfaces. We will make use of ADS in the experimental part of this thesis.

In order to numerically calculate the boost factor, reflectivity or transitivity of a booster, transfer matrices are very efficient, since we simply have to evaluate above equations. However, it

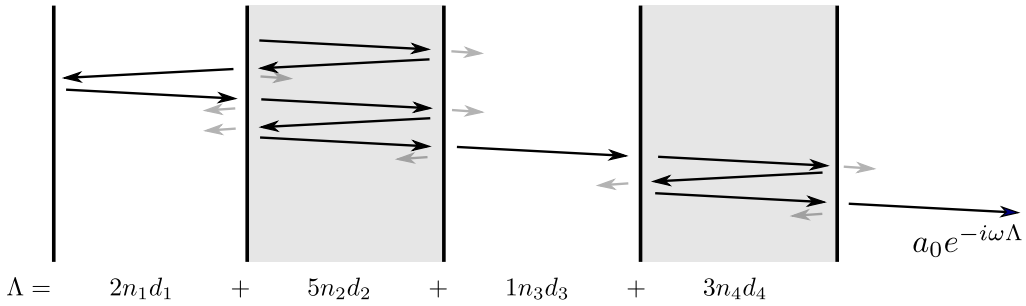

Figure 4.3: One arbitrary example ray traced throughout the dielectric haloscope. The total optical length Λ of the ray is a sum of integer multiples of the various optical lengths $n_r d_r$ of the different regions r. The amplitude a_0 is determined by the axion-induced emission at the boundary where the ray originates and the reflection- and transmission coefficients during propagation. Here the angle of the rays is only for illustration purpose and has no physical meaning.

is difficult to gain a more intuitive understanding of crucial properties of the haloscope with this formalism. Therefore, we briefly discuss some alternatives below.

4.2 Ray Tracing

Ray tracing is a way to iteratively find a solution that fulfills the boundary conditions at all interfaces by tracing all possible paths (rays) electromagnetic radiation can take within the system. Consider the interface between regions 1 and 2 and a wave impinging from region 1. For this wave the reflection coefficient $\mathcal{R}_s$ and transmission coefficient $\mathcal{T}_s$ are then

$$\mathcal{R}_s = \frac{n_1 - n_2}{n_1 + n_2}, \qquad \mathcal{T}_s = 1 + \mathcal{R}_s, \tag{4.15}$$

which follows directly from equation (4.4). We now may follow a wave through its way throughout the system. In each region it acquires a phase $\exp(-i\omega\Lambda_r)$ with the optical length of that region $\Lambda_r = n_r d_r$. We apply reflection and transmission coefficients at each boundary and continue following the reflected and transmitted waves separately. Each time we split up a ray, we fulfilled the boundary condition at the respective interface. Thus, the sum of the fields from all rays fulfills all boundary conditions.

The power boost factor can be calculated following all rays q emitted from different boundaries until they leave the system at one side and summing up as

$$\beta^2(\omega) = \left| \sum_q a_q e^{-i\omega\Lambda_q} \right|^2, \tag{4.16}$$

where a_q is the product of all reflection and transmission coefficients ray q encounters until it leaves the system and Λ_q is the total optical length of ray q. Figure 4.3 illustrates how to obtain the summand for one specific example ray. Notice that there exist infinitely many paths through the system, such that the sum runs over infinitely many rays q.

Obviously, this approach has a close relation to the Fourier transform of the amplitude boost factor in time domain, if the refractive indexes do not depend on frequency. The Fourier transform

of the amplitude boost factor is

$$\beta(t) = \sum_q a_q \delta(t - \Lambda_q), \tag{4.17}$$

i.e., tracing rays is the same as following a δ-pulse through the system and simply histogram the times the pulse spends inside the system.

4.3 Other Formalisms

We will use the above two formalisms for most arguments on the 1D model within this thesis. Nevertheless, there are other approaches of calculating electromagnetic fields in such a setup. While these are not explicitly used for the calculations in this thesis, let us briefly consider the alternatives below.

In cavity experiments one usually calculates the fields $\boldsymbol{E}_m(\boldsymbol{x})$ of the modes m of the cavity. These fulfill the classical axion-free Maxwell equations for the considered frequency respecting the boundary conditions of the cavity. The axion-induced field $\boldsymbol{E}_a$ acts as a source and excites these modes such that their field is much larger than $\boldsymbol{E}_a$ on resonance. The output power is therefore proportional to a form factor C given by the *overlap integral* [69, 79]

$$C = \frac{\left| \int \boldsymbol{E}_a^* \cdot \boldsymbol{E}_\mathrm{m} \, \mathrm{d}V \right|^2}{\int |\boldsymbol{E}_a|^2 \, \mathrm{d}V \int |\boldsymbol{E}_m|^2 \, \mathrm{d}V}. \tag{4.18}$$

A similar overlap integral formalism can also be used to calculate the power boost factor of a dielectric haloscope. In this case one needs to insert for $\boldsymbol{E}_m$ the electromagnetic fields excited by a signal reflected on the dielectric haloscope, which are again those fulfilling the classical Maxwell equations while respecting the boundary conditions of the haloscope. For more details see [89,114].

Lastly, another way to calculate the reflectivity is by considering instead the impedance $Z = E/H$ of the system, which can be compared to the free space impedance of $Z_0 \approx 377\,\Omega$. The reflection coefficient between two systems of impedances Z_1, Z_2 is then for example

$$\mathcal{R} = \frac{Z_2 - Z_1}{Z_2 + Z_1}. \tag{4.19}$$

For more see *impedance transformation* or *impedance matching* in e.g. [115].

4.4 Important Consequences

4.4.1 Transparent and Resonant Case

As an example, it is straightforward to calculate the reflectivity of a single disk, given by

$$\mathcal{R}_\mathrm{disk} = \frac{(n^2 - 1) \sin\delta}{i\, 2n \cos\delta + (n^2 + 1) \sin\delta}, \tag{4.20}$$

where n is its refractive index and $\delta = \omega n d$ its phase depth. For thicknesses corresponding to phase depths $\delta = 0, \pi, 2\pi, \ldots$ the disk does not reflect any electromagnetic radiation, i.e., is transparent; while for $\delta = \pi/2, 3\pi/2, \ldots$ the disk becomes maximally reflective. Using the ray tracing picture we can gain an intuitive understanding of this result, cf. figure 4.4. For $\delta = \pi$ all transmitted rays

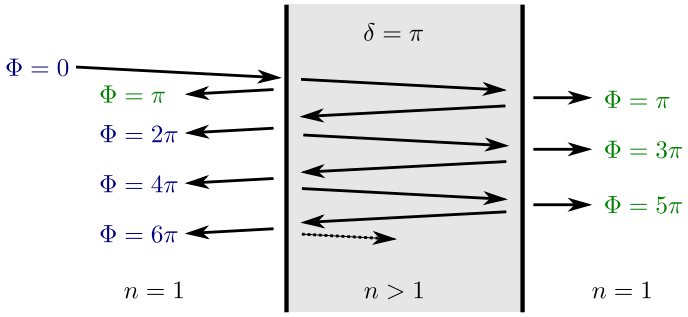

Figure 4.4: Rays traced through a disk of phase depth π. Φ denotes the phases of the outgoing waves, same colors interfere constructively.

interfere constructively. Changing δ away from this value will change their relative phases and thus only reduce the transmissivity of the disk.

In a many disk system one can now place the disks at distances to coherently add up the signal for frequencies at which they are transparent [88] (transparent case) or make the system maximally resonant at frequencies where they are maximally reflective (reflective case). In fact the combination of both effects allows for the broadband boost factors for MADMAX. These two configurations correspond to the most extreme operational settings of the booster. Therefore, it will be instructive to study some of the systematic effects described in later chapters at those extreme ends.

4.4.2 Area Law

The are law [34, 89] states the following: If considering a sufficiently wide frequency range, the area under the power boost factor curve $\int \beta^2 d\omega$ remains approximately constant when changing the lengths of the different regions d_r when integrating over a sufficiently large frequency range.

We can use the ray tracing formalism to gain an intuitive understanding of this important law. If all regions are lossless we can rewrite the power boost factor in equation (4.16) as a sum of the powers contributed by the individual rays and interference terms

$$\beta^2 = \sum_q |a_q|^2 + \sum_{\substack{p,q \\ p \neq q}} a_q a_p^* e^{-i\omega(\Lambda_q - \Lambda_p)}. \tag{4.21}$$

We assume that the refractive indices do not depend on frequency, i.e., a_q is approximated to be constant with frequency. When integrating over frequency the first term in equation (4.21) remains, because it is independent of frequency. However, the second term oscillates with frequency. For different rays with different optical lengths, the second term sums up to zero as soon as we integrate over a large enough frequency interval (ω_1, ω_2). In other words the number of frequencies at which the two rays interfere constructively or destructively is approximately the same, so the interference term averages out. We therefore have

$$\int_{\omega_1}^{\omega_2} \beta^2 \, \mathrm{d}\omega \approx (\omega_2 - \omega_1) \sum_q |a_q|^2 . \tag{4.22}$$

The power of a single ray $|a_q|^2$ does not depend on the lengths of the different regions d_r and just on the reflection and transmission coefficients. Therefore, the area under the power boost factor curve

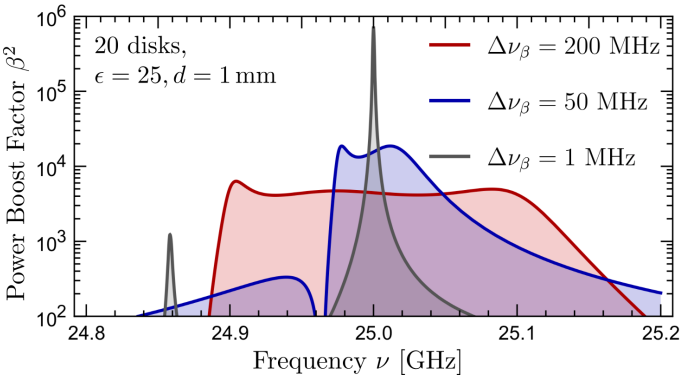

Figure 4.5: Illustration of the area law for 3 different example configurations of different bandwidths $\Delta\nu_\beta$ for a 20 $LaAlO_3$ disk system. $\int \beta^2 d\nu$ is roughly constant for different spacing configurations. When decreasing the boost factor bandwidth $\Delta\nu_\beta$ the boost factor amplitude increases accordingly. Adapted from [34].

is constant when changing the lengths d_r. It is given by an incoherent sum over the integrated powers contributed by all rays. Since every dielectric interface contributes axion-induced emitted rays of a certain integrated power, the incoherent sum is proportional to the number of interfaces. A more rigorous proof of these statements following a similar idea is given in [89].

For dielectric haloscopes like MADMAX this has two important consequences: One may trade power boost factor amplitude with boost factor bandwidth and vice versa by changing the positions of the dielectric disks. This property is illustrated in figure 4.5. In addition, when tuning the boost factor to cover a fixed frequency range, the power boost factor amplitude is approximately proportional to the number of magnetized dielectric disks used. Notice that it is not possible to align the disks to achieve any desired shape. Therefore, always some of the area will be at frequencies which cannot be covered by the receiver bandwidth and thus not used for the axion search. More importantly, as we will see in section 5.4, losses in the system dictate a minimal bandwidth below the area law does not hold anymore. In addition, 3D effects may reduce the usable area under the boost factor curve, cf. chapter 8.

4.4.3 Correlation Between Boost Factor and Reflectivity

In sections 4.1 to 4.3 it became apparent various times, that there exist correlations between the reflectivity and the power boost factor. In section 4.1 we see in equations (4.12) to (4.14) that the denominator of the left-going boost factor amplitude, $\mathsf{T}[2,2]$, is the same as the denominator of the reflectivity from the left side. Therefore, both may have poles (resonances) at the same frequency. In addition, we can consider rays of a reflected signal in terms of ray tracing in section 4.2. After a ray impinges onto a surface which is emitting axion-induced electromagnetic radiation at the same frequency, it splits up into the same set of rays as the rays describing the axion-induced radiation with a fixed phase difference. Thus it interferes the same way with itself as the axion-induced emission. Moreover, the overlap integral formalism directly calculates the boost factor from correlating the axion-induced field with the field configuration of a reflected signal within the booster. These mathematical observations suggest that the reflectivity of the dielectric haloscope

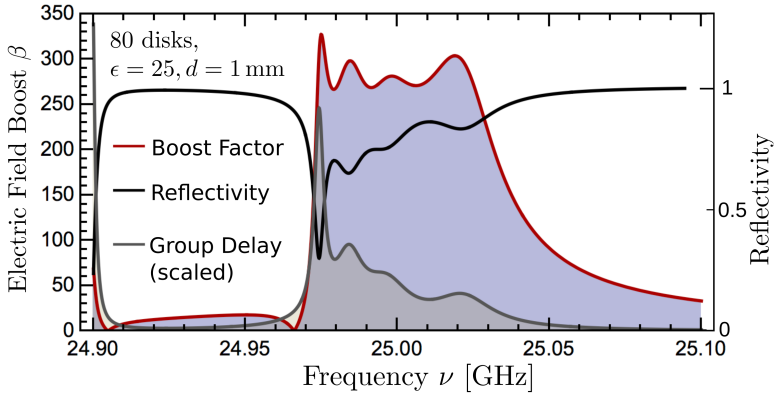

Figure 4.6: Amplitude boost factor (red) for a 80 $LaAlO_3$ disk system optimized for a bandwidth of 50 MHz. We also show the magnitude of the reflectivity (black) and the group delay (gray). The absolute reflectivity has been obtained assuming a loss of $\tan\delta \sim$ few $\times\, 10^{-4}$. Adapted from [91].

is correlated to the boost factor.

While the boost factor cannot be measured directly, a measurement of the reflectivity can be compared to expectations from simulation to infer the boost factor and to guide the tuning of the dielectric haloscope when adjusting the disk positions. In an ideal lossless dielectric haloscope with a mirror at the end like in MADMAX the magnitude of the reflectivity will always be unity. Therefore, it is more feasible to use the phase Φ of the reflectivity rather than its absolute magnitude. In practice we use the group delay

$$\tau_g = -\frac{d\Phi}{d\omega}. \tag{4.23}$$

Qualitatively, the group delay can be understood as the mean retention time of reflected photons within the booster. Thus, peaks in the group delay frequency spectra map out resonances. An example for the correlation between boost factor and group delay is shown in figure 4.6. In this figure we compare group delay and boost factor for a set of 80 disks in front of a perfect mirror aligned such that a boost factor with a bandwidth of 50 MHz is obtained. The absolute reflectivity is calculated assuming a non-zero dielectric loss of $\tan\delta \sim$ few $\times\, 10^{-4}$. For more details on loss cf. section 5.4.

Such a boost factor calibration is limited by the systematic uncertainties in simulations, i.e., the need of the simulation to cover all relevant effects, as discussed in section 8.6. In addition, it is limited by the uncertainties on the measurement of the reflectivity itself, as discussed in part IV of this thesis.

Chapter 5

Results from the 1D Model

In the previous chapter we have introduced the 1D model and derived properties of an idealized 1D system. In this chapter we will survey systematic effects from inhomogeneous magnetic fields, disk mispositioning and losses. We briefly review how to obtain optimized boost factors in section 5.1. Afterwards we address spatial inhomogeneities of the axion-induced field $\propto \boldsymbol{B}_e\, a$. A non-zero axion velocity alters the spatial phase of the axion-field a as previously studied in [1, 91]. For MADMAX these effects have been found to be negligible, therefore they are not discussed hereafter. In contrast, the impacts of inhomogeneous magnetic fields $\boldsymbol{B}_e$ along z are of central importance for MADMAX and are discussed in section 5.2. In addition, systematic effects on the propagation of electromagnetic waves inside the system may affect the boost factor. These include phase errors due to variation of the disk thicknesses, dielectric constants and mispositioning as briefly addressed in section 5.3, and most importantly losses as discussed in section 5.4.

5.1 Optimizing Boost Factors

In general we seek optimal disk positions such that the boost factor is maximized within a given frequency bandwidth $\Delta\nu_\beta$. This can be achieved using any optimization algorithm minimizing the cost function

$$C = -\min_\nu \left[\beta^2(\nu) | \nu \in (\nu_0, \nu_0 + \Delta\nu_\beta)\right]. \tag{5.1}$$

The results presented in this chapter are obtained using the Nelder-Mead algorithm [116], but other algorithms can be used as well, such as genetic [89, 117], simulated annealing [118], Monte Carlo Markov chains [119], gradient descent [120] and others. Investigating different algorithms may open the possibility of speeding up the convergence in future.

Figure 5.1 shows power boost factors for 20 (left) and 80 (right) $LaAlO_3$ disks at three different example bandwidths obtained from our optimizations. The disk positions for these ideal configurations are used as initial guesses for the optimizations in the sections below. One can clearly see the behavior expected from the area law introduced in section 4.4.2: The area under the power boost factor curve stays approximately constant when changing the disk positions. In addition, it is approximately proportional to the number of disks, i.e., the 80 disk power boost factors are roughly four times larger than the ones from the 20 disk calculations. Moreover, sharp peaks in the boost factor curve correspond to a more resonant behavior. Therefore, the 80 disk

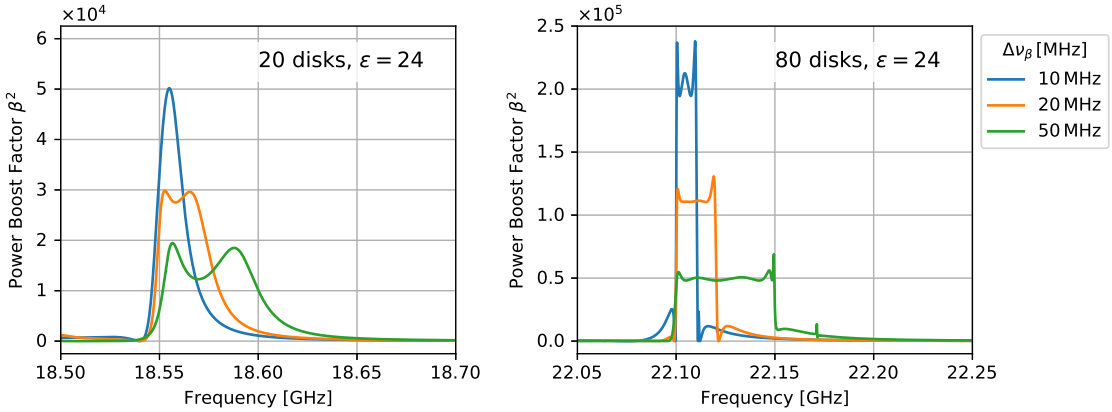

Figure 5.1: Example boost factors for a system with 20 (left) and 80 (right) $LaAlO_3$ disks ($\epsilon = 24$) for three different bandwidths ($\Delta\nu_\beta = 10, 20$ and $50\,\mathrm{MHz}$).

boost factors curves can be adjusted closer to a top-hat shape. On the other hand, for 20 disks at a bandwidth of around 10 MHz the shape starts to become more comparable to a Lorentzian.

These optimizations still assume an idealized system. Indeed, if the system suffers from the systematics described below, the optimal disk positions to obtain a mostly top-hat shaped boost factor may change. In practice, we will have some information on the magnetic field inhomogeneity or losses in the system, which we can include into the model and reoptimize the disk spacings to again increase the boost factor in the desired frequency range. In particular, we may assume that there exists a procedure to independently derive the boost factor, e.g. by a reflectivity measurement on the booster. This would allow us to run this optimization in the final setup rather than in the simulation only, i.e., to optimize the measurement-inferred boost factor with the real disk positions as parameters. How this can be realized is investigated in more detail later in section 8.6 and part IV of this thesis.

5.2 Magnetic Field Inhomogeneity

One may think of situations in which the axion-induced emissions from some dielectric disks only interferes destructively thereby lowering the boost factor [121]. Nevertheless, these disks would still contribute to resonantly enhance the emissions from the other disks. In this case, it may seem advantageous not magnetizing these disks to increase the achievable boost factor. In this section we will test this hypothesis. Thereby, we will also derive homogeneity requirements for the magnetic field along the z-axis, which are important for magnet design.

We consider two different configurations for the final MADMAX setup with 80 disks: In the first one the magnetic field stretches over the mirror and N dielectric disks but steeply drops off and is set to zero for the remaining $80 - N$ disks facing the antenna side. The steep magnetic field gradient in such a case would cause additional axion-induced radiation. We neglect this radiation here, in order to just see the contribution from explicitly "turning off" the emission from particular disks. Hence, this tests the initial hypothesis most directly. Neglecting the magnetic field gradient is justified in realistic setups where the magnetic field would be much more smooth and drop off

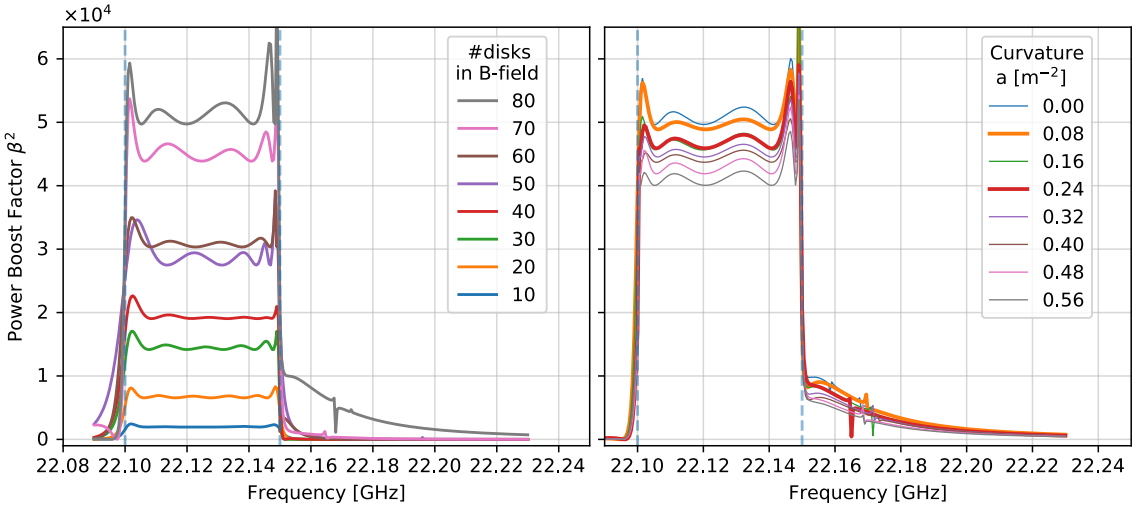

Figure 5.2: Optimized boost factors for a 80 disk configuration with modified magnetic fields. We show cases with only a number of disks magnetized (left) and with a magnetic field dropping smoothly over the booster extent $\propto -az^2$ (right). The blue dashed lines indicate the boundaries of the frequency range in which the power boost factor was maximized during the optimizations. The cases on the right with $a = 0.08\,\mathrm{m}^{-2}$ (orange) and $a = 0.24\,\mathrm{m}^{-2}$ (red) correspond to benchmark designs from the magnet builders [105].

at least over a few disks; more on such gradients cf. e.g. [3, 122, 123] and section 8.1. The second configuration is motivated by the actual design of the magnet. The magnet design aims for a homogeneous magnetic field inside of a large symmetric magnet bore. Thus, the magnetic field can be approximated as

$$B_y(z) = B_0 \left[1 - az^2 - \mathcal{O}(z^4)\right], \tag{5.2}$$

where B_0 is the maximum magnetic field and a is a curvature parameter for the inhomogeneity. This has been explicitly tested with simulated magnetic fields provided by the magnet builders [105]. Reducing the physical length of the magnet increases the curvature parameter a, where the two benchmark designs considered by the magnet builders correspond to $a = 0.08\,\mathrm{m}^{-2}$ for a magnet with $\sim 2\,\mathrm{m}$ straight section and $a = 0.24\,\mathrm{m}^{-2}$ for one with only $\sim 1\,\mathrm{m}$ straight section. Therefore, relaxing homogeneity constraints in z-direction may save a significant amount of conductor material and hence magnet cost.

Since the magnetic field distribution in the setup will be known, it can be taken into account during the disk position optimization. In order to estimate the effect on the power boost factor, we therefore reoptimize the disk positions for the various different magnetic field configurations, such that the boost factor is maximized in the same frequency interval. Figure 5.2 shows the results of finding such optimal boost factors for those configurations, while we show in figure 5.3 the reduction of the area under the boost factor curve as a function of disk number or curvature parameter a, respectively. Note that the obtained results from these optimizations depend on the convergence of the optimizer. Therefore, it may always be possible to find better boost factors when running the optimizer again.

The case in which we only consider the radiation from the first N disks is shown on each figure

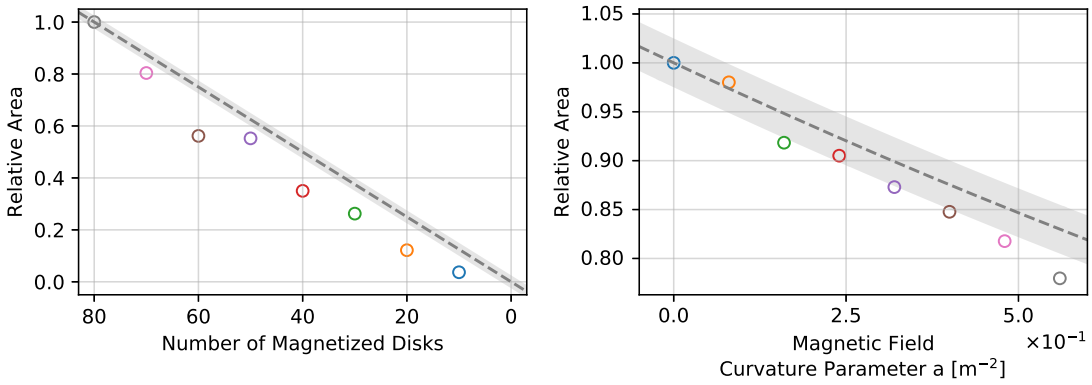

Figure 5.3: Relative area reduction under the boost factor curve as a function of magnetized disks (left) or curvature parameter a (right), respectively. The different colors correspond to the different boost factors shown in figure 5.2. The gray dashed line shows the estimates from the reduction of $\int B^2 dz$. The gray areas indicate deviations of $\pm 2.5\,\%$ (absolute).

on the left. Clearly the achievable area under the boost factor curve is reduced when less disks are magnetized. The area is approximately proportional to the number of magnetized disks, i.e., disks that actually contribute axion-induced radiation. This indicates no benefit from a shorter magnet for the power boost factor. However, for realistic magnetic fields the decrease in boost factor due to a shorter straight section of the magnet may be acceptable, as shown on the right of figure 5.3. Nevertheless, also in this case a reduction of the boost factor is observed when decreasing the magnetic field for the outer disks. The presented calculation assumes that the booster is aligned such that the mirror is at $z = 0$, i.e., the mirror is in the center of the magnet. However, analogous results have been obtained placing the booster at other places. Ideally, the booster is centered within the maximum magnetic field (see below).

To understand this result, notice that the interference-argument for a shorter magnetic field mentioned initially in this chapter only holds for a fixed frequency, since interference is frequency dependent. However, we are actually interested in maximizing the boost factor over a range of frequencies. While calculations show that indeed the boost factor can be increased at a fixed frequency when magnetizing less disks, this does not hold for the area under the boost factor curve. In the sense of the area law as described in section 4.4.2, when calculating the area under the boost factor curve, we integrate over some frequency interval, and therefore over different relative phases of the signals emitted from the different disks. This corresponds to the incoherent sum of integrated powers contributed from each disk. If we reduce the power contributed from a specific disk, the area is expected to be reduced by the corresponding amount.

Since the power scales with the magnetic field squared, the area under the boost factor curve is expected to be proportional to the mean quadratic field over the booster, i.e.

$$\int \beta^2(\nu)\,\mathrm{d}\nu \propto \int_{\text{booster}} B_y^2(z)\,\mathrm{d}z. \tag{5.3}$$

The estimate from this scaling is indicated by the gray dashed lines in figure 5.3. The optimized boost factors do not strictly follow the predicted behavior, most likely due to the fact that the

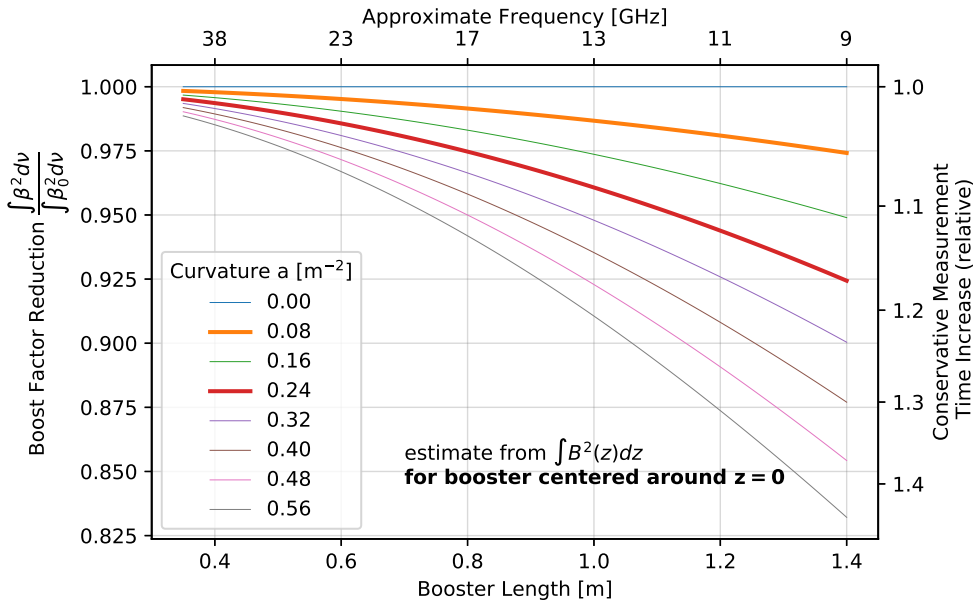

Figure 5.4: Estimated reduction of the power boost factor for different smoothly decreasing magnetic fields $B_y(z)$ in equation (5.2) as a function of the length of the booster L_b, for the final MADMAX setup with 80 disks. Each length corresponds to approximately a frequency to tune the haloscope to if the disk spacings are approximately half a photon wavelength. The measurement time reduction is conservatively estimated by assuming that only the amplitude, but not the bandwidth of the boost factor is reduced.

optimizer might not have converged fully to the global minimum. Nevertheless, we find that this estimate approximates the order of magnitude reduction of the area under power boost factor well. This has also been checked for lower frequency and lower boost factor bandwidth scenarios as well as for different placement of the booster along the z-axis.

Figure 5.4 shows this estimate for a booster which is centered around the maximum of the magnetic field in order to maximize the achievable power boost factor. The reduction in power boost factor due to the magnetic field inhomogeneity is plotted as a function of booster length. The reduction in power boost factor amplitude can be translated to a naive increase in measurement time according to Dicke's radiometer equation, cf. equation (2.7), in order to still achieve the same sensitivity. Even for the lowest frequencies, i.e., a very long booster, the boost factor reduction only gives a increase of 20 % in measurement time for a magnetic field with $a = 0.24\,\mathrm{m}^{-2}$. This estimate is conservative, because one could imagine to reoptimize the boost factors to have the same amplitude but a reduction in bandwidth, instead. In this case, the scan rate is reduced proportionally to the bandwidth reduction, rather than proportional to the square of the amplitude reduction as suggested by Dicke's equation. Though, in contrast to the above conservative estimate, such a linear scaling would correspond to the most optimistic scenario, since the minimal bandwidth is limited by losses, cf. section 5.4, and decreasing the boost factor bandwidth increases the readjustment time of the system in addition.

In short. No evidence for a direct benefit in terms of a constant or even better power boost factor from making the magnet shorter is found in this study. While it is true that at a single frequency a higher boost factor can be achieved with not magnetizing all disks, the area under β^2 could not be increased by a magnetic field stretching over a shorter range in theses studies. We find that a shorter magnet always reduces the area under the boost factor curve, roughly proportional to the reduction in the mean squared magnetic field $\propto \int B^2(z)\,\mathrm{d}z$. As a result of this study, this relation has been included in the magnet figure of merit for the magnet designers.

Realistic simulated B-field maps show that the B-field drops approximately quadratically along the longitudinal axis of the booster, parameterized with the magnetic field curvature parameter a. A design with $a = 0.24\,\mathrm{m}^{-2}$ is expected to reduce the boost factor by less than 10% if the booster can be always placed in the center of the booster. This increases the measurement time by less than 20 %.

5.3 Phase Depth Errors

Adjusting the phase depths of the individual regions of the haloscope $\delta_r = \omega n_r d_r$ allows for constructively interfering the emissions from various disks and the resonant enhancement in the desired frequency range. Variations in the thickness or (effective)[1] dielectric constant therefore alter the boost factor. Thus, this ultimately defines the precision at which the distances between the disks need to be adjustable when optimizing the boost factor. This important topic has been studied previously [2, 89, 121, 124]. Therefore, we will only briefly review and confirm their main results and give some intuitive interpretation.

In [89] it was argued that the needed disk position standard deviation σ_d is bound by

$$\sigma_d \ll \frac{\lambda}{2\pi\sqrt{\beta}} \approx 200\,\mu\mathrm{m}\left(\frac{10^4}{\beta^2}\right)^{1/4}\left(\frac{25\,\mathrm{GHz}}{\nu}\right). \tag{5.4}$$

Numerical studies [2, 121, 124] typically show that at least one to two orders of magnitude less than the quoted value of $200\,\mu$m is required. As an example we show the effect of a $1\,\mu$m, $3\,\mu$m and $10\,\mu$m positioning precision for the benchmark boost factors with 50 MHz bandwidth for both the 20 and 80 disk cases in figure 5.5.

Notice that in the estimate of [89] above the needed precision only scales inversely to the forth order on the power boost factor. The numerical results for 20 and 80 disks show that a similar accuracy is needed for 20 and 80 disks. In particular, for both cases an accuracy of $\sim 3\,\mu$m is needed for deviations from the idealized case of $\lesssim 10\%$. This may be counter-intuitive at first glance, since more disks can naively make the system more resonant, which makes phase errors more important. However, relative errors on the phase depth directly correspond to relative errors on the resonance frequency. This is obvious e.g. for a minimal dielectric haloscope with only one slim disk and a mirror. Here the distance d between the disk and mirror directly defines the resonance frequency

$$\nu \approx \frac{c}{2d}, \tag{5.5}$$

[1] Various 3D effects discussed later can be seen as effectively changing the dielectric constant.

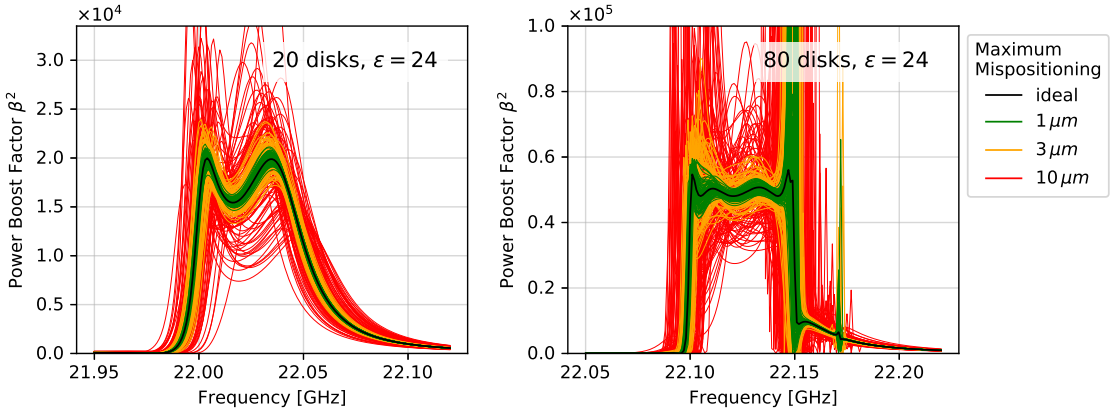

Figure 5.5: Effect of disk misalignments on the power boost factor for the 20 disk MADMAX prototype (left) and 80 disk MADMAX full-scale experiment (right). The black line denotes the idealized case without any mispositioning. The lines in various colors correspond to randomly realigned disks, where the misalignments have been sampled from a uniform distribution with the maximum for each color as defined in the legend.

with the speed of light c. Since the 20 and 80 disk boost factors are tuned to cover the same frequency bandwidth, the relative frequency error for the resonances that make up the boost factor are the same. Therefore, the relative phase errors we may allow for are the same. Another way of seeing this is by considering the Fourier transform of the amplitude boost factor. A boost factor bandwidth in frequency domain $\Delta\nu_\beta$ requires the amplitude boost factor to stretch over a range $\propto \Delta\nu_\beta^{-1}$ in time domain, i.e., defines how long the signal must propagate on average through the booster before being detected. These are the same if the chosen bandwidth is the same, regardless of the actual disk number. Therefore, phase errors affect the boost factor in both cases in a similar way.

In short. Disk position and disk thickness inaccuracies cause phase errors. Numerical 1D calculations show that for a boost factor bandwidth of 50 MHz both for 20 and 80 disks an accuracy of $\sim 3\,\mu$m is needed to leave the boost factor unchanged at a level of $\lesssim 10\%$.

5.4 Losses

For the design of the MADMAX booster it is important to know the order of magnitude of tolerable losses that have an impact on the boost factor to set design goals for the dielectric disks. Therefore, we seek for an approximate parametrization of loss effects to the achievable power boost factor in this section. We will first review the definition and consequences of dielectric losses. Based on this we will derive an analytical equation to quantify their effect on the boost factor in dielectric haloscopes for the transparent case as introduced in section 4.4.1. We then compare this parametrization to a set of numerical calculations for more realistic boost factors. This leads us eventually to a parametrization of loss effects depending on disk number, boost factor bandwidth and frequency.

Dielectric Losses

Dielectric losses are quantified using the usual loss tangent defined as

$$\tan\delta \equiv \frac{\operatorname{Im}\epsilon}{\operatorname{Re}\epsilon}. \tag{5.6}$$

With non-zero loss, the refractive index $n = \sqrt{\epsilon\mu}$ becomes complex, i.e., for small δ we have $n \approx |n|(1 + i\delta/2)$. The amplitude of a propagating wave is then damped according to

$$|E(z)| = |E(z=0)| \exp\left(-\tfrac{\delta}{2}|n|\omega z\right). \tag{5.7}$$

Of course, this does not only apply if the losses are actual dielectric losses, but δ can parameterize any kind of continuous loss mechanism in the system that exponentially damps the electric field along z. This will be useful in later chapters, where we will use this to compare these studies to the expected loss from 3D effects. Since in this parametrization the dielectric constant of a lossy medium has a finite imaginary part, also the reflectivity between two media, in particular its phase, will be affected, cf. equation (4.15). In a resonator this corresponds to a phase error, slightly shifting the resonance in frequency. This can be used to measure $\tan\delta$ [125]. In a dielectric haloscope like MADMAX we can compensate these phase errors to some extent by realigning the disks. The amplitude reduction, however, cannot be compensated. This is therefore the dominating effect considered here.

Analytical Ansatz

It is instructive to first study the transparent case, i.e., a configuration where the disk thickness is chosen such that the disks are effectively transparent as introduced in section 4.1. Afterwards we generalize this to more resonant configurations. Considering an electromagnetic wave in the transparent case passing through N disks (or air gaps) with a dielectric loss of $\tan\delta$ and thickness d, the amplitude of this wave is damped according to equation (5.7) by a factor of $\exp\left(-N\frac{\delta}{2}|n|\omega d\right)$. Each disk emits a left- and right-moving wave. Assume we have a mirror on the left side. Then, the left-moving emission from disk i gets transmitted through $i-1$ disks (air gaps) until it is reflected on the mirror and then transmitted through all N disks (air gaps) again until it propagates out of the booster. The right-moving emission only propagates through $N-i$ disks (air gaps). In the transparent case it is always possible to align all dielectric disks such that their contributions interfere constructively. Therefore adding up all emissions constructively, the power boost factor is given by the squared sum of all these amplitudes. Therefore, the boost factor reduction is

$$\frac{\beta_\delta^2}{\beta_0^2} = \left|\frac{1}{2N}\sum_{i=1}^{N}\left\{\exp\left[-(N+i-1)\tfrac{\delta}{2}|n|\omega d\right] + \exp\left[-(N-i)\tfrac{\delta}{2}|n|\omega d\right]\right\}\right|^2 \tag{5.8}$$

$$= \frac{1}{4N^2}\left|\frac{1-\exp(-N\delta|n|\omega d)}{1-\exp(-\frac{\delta}{2}|n|\omega d)}\right|^2 \tag{5.9}$$

$$\gtrsim \exp(-N\delta\,|n|\omega d). \tag{5.10}$$

where β_δ^2 is the boost factor with loss and β_0^2 is the boost factor without loss. The consistency of equation (5.9) with numerical 1D calculations has been confirmed in [8]. The approximation in equation (5.10) corresponds to each emission passing on average through N disks.

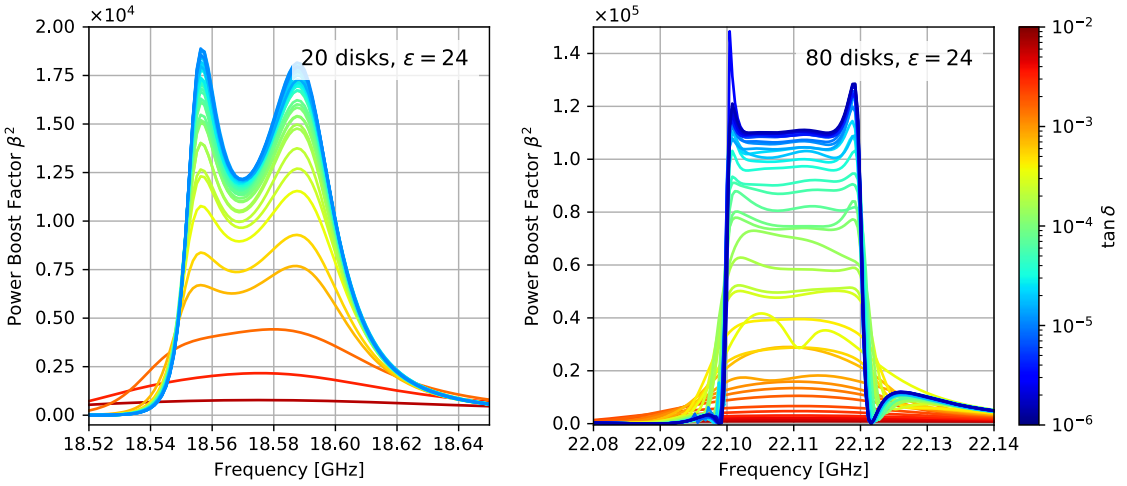

Figure 5.6: Effect of dielectric loss on the achievable power boost factor, for the MADMAX prototype (left) and the final MADMAX setup (right). Each curve shows the boost factor after varying the disk spacings in the 1D model to obtain the optimal boost factor in a example bandwidth of 50 MHz (prototype) or 20 MHz (full scale MADMAX), as described in section 5.1.

In general we are not in the transparent case, i.e., the disks have a phase depth such that they have some reflectivity. Therefore, we also have to take into account paths throughout the system which experience reflection from the disks. Each such path can be seen as a random walk through the system. If the reflectivity is $\frac{1}{2}$, the average walked distance is the square root of the number of steps, analogous to the well-known Brownian motion. Therefore, we need to pass through $\sim N^2$ disks before leaving a block of N disks [126]. In our case the reflectivity can be different, and we still have to take into account interference. Nevertheless, this suffices as a motivation to use the same formalism as above, but considering an effective number of disks N_{eff} any boosted signal experiences before leaving the system. For realistic boost factors the task of parameterizing losses therefore reduces to finding the average total optical length in the lossy medium. It is given by the effective number of disks as a function of boost factor bandwidth, frequency and number of disks.

Numerical Survey

In order to obtain this parametrization we numerically study more realistic configurations. To this end, we assume a $\tan\delta$ value and then find disk alignments of N disks that give an optimized boost factor in a given bandwidth $\Delta\nu_\beta$, as described in section 5.1. Considering various loss tangents in the range of $\tan\delta = 10^{-6} \ldots 10^{-2}$, we can fit the result with equation (5.9) and infer N_{eff}. In order to deduce the bandwidth dependence we consider various bandwidths in the range of $\Delta\nu_\beta = 2.5\,\text{MHz} \ldots 500\,\text{MHz}$. To derive the frequency dependence for the MADMAX prototype we consider boost factors at frequencies of $\sim 18\,\text{GHz}$ and $\sim 24\,\text{GHz}$ for 20 disks. Lastly, to get an idea how this behaves for the full MADMAX experiment, we do the same also for 80 disks at a frequency of $\sim 22\,\text{GHz}$.

The result of the boost factor calculations for the prototype and a 50 MHz bandwidth, as well as for the full scale MADMAX but a 20 MHz bandwidth are shown as examples in figure 5.6. Other

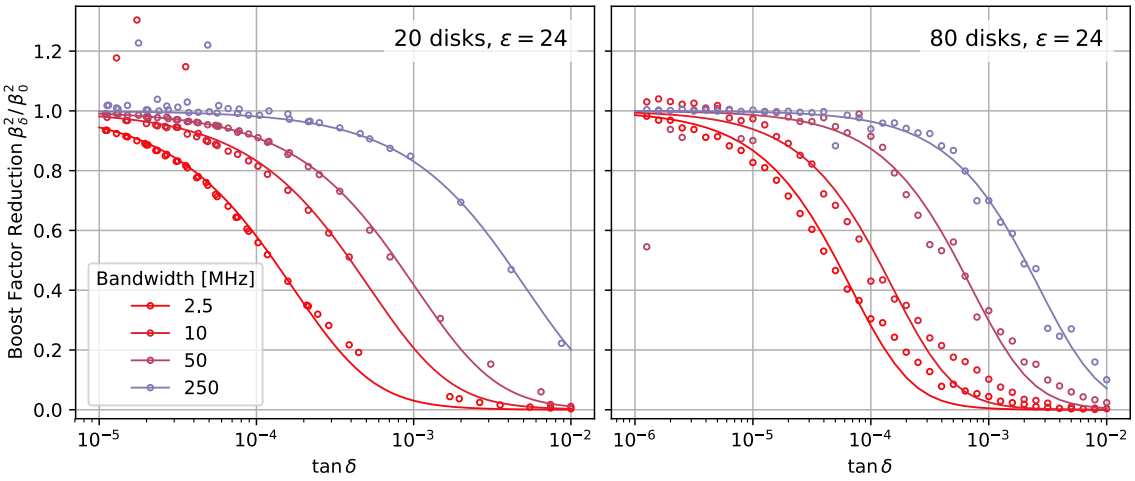

Figure 5.7: Reduction of the power boost factor minimum in the optimized bandwidth as a function of dielectric loss, for four example boost factor bandwidths and 20 disks at $\sim 18\,\mathrm{GHz}$ (left) and 80 disks at $\sim 22\,\mathrm{GHz}$ (right). The circles denote the results from the aforementioned optimizations, the straight lines are curve fits to those points using equation (5.9) (exact for the transparent case) using an effective number of disks N_{eff} as the only free parameter.

results are analogous. We see that even for higher losses $\tan\delta > 10^{-4}$ almost box-shaped boost factors may be achieved. In addition, substructures of the boost factor curve tend to smooth out for higher losses, which can be understood in the same sense as a reduction of the quality factor Q in resonators. However, here the effect of the boost factor reduction is dominating compared to this smoothing.

We take the minimum of the power boost factor curve in the respective frequency range as the achievable power boost factor amplitude. The reduction of this amplitude compared to the ideal power boost factor amplitude for four different example bandwidths is shown in figure 5.7. Each circle denotes the result of a single disk position optimization for that particular $\tan\delta$ and $\Delta\nu_\beta$. The outliers occur, if the optimization converges to a different (local) minimum than the ideal boost factor, or if the solution for higher loss is smoothed out such that the minimum of the boost factor curve with loss actually lies above the minimum of the lossless curve. The lines correspond to curve fits using equation (5.9) where we take the number of disks as the free parameter. We see that this parameterizes sufficiently the dependency on the dielectric loss that we need to estimate. Moreover, we see that the order of magnitude of δ which is relevant for the boost factor is approximately the same for 20 and 80 disks. Again, this might be surprising since one may think that losses become more relevant for a system with more disks.

In figure 5.8 we examine the bandwidth dependency of the fit parameter N_{eff} for all studied cases. Each point corresponds to the result from fitting a set of optimizations with the same bandwidth $\Delta\nu_\beta$ but different loss tangents as described before. The results are consistent with our previous estimate at a fixed bandwidth in [8]. The green (blue) dashed line shows a power-law fit for all 20 (80) disk points. We see that for the prototype the frequency dependency is small compared to the statistical uncertainties when fitting N_{eff}. In addition, we obtain a similar bandwidth dependency for N_{eff} for 80 disks.

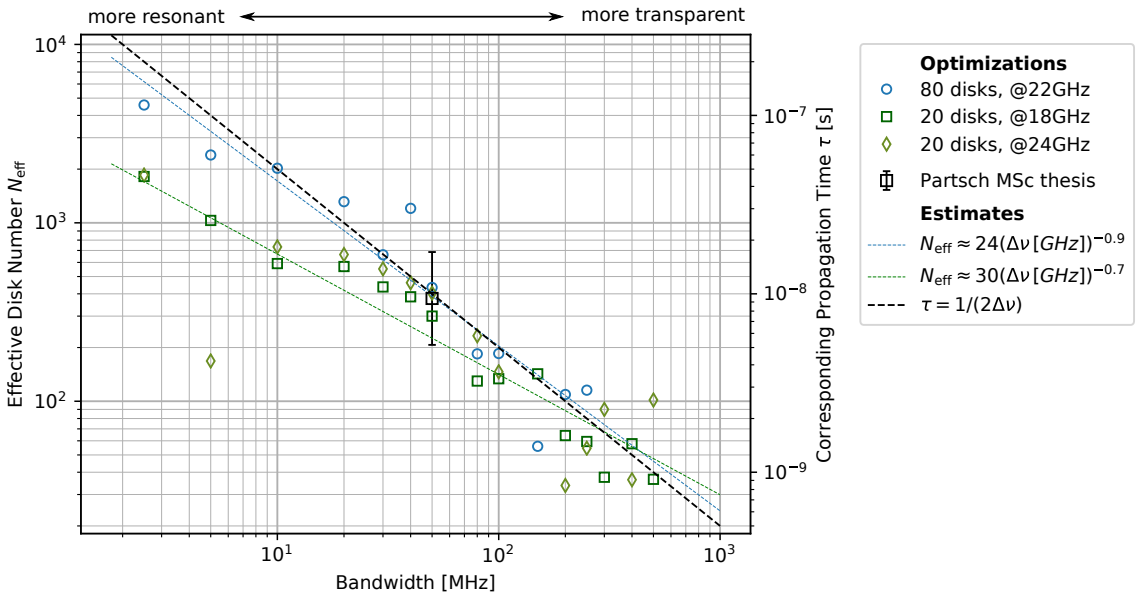

Figure 5.8: Effective disk number as a function of boost factor bandwidth, obtained from the fits exemplified in figure 5.7. The data points correspond to the results from the fits for a 20 disk system (green) at two different frequencies (squares for 18 GHz, diamonds for 24 GHz), and for a 80 disk booster (blue circles). The black square and errorbar denotes the result from our older estimate in [8]. The green (blue) dashed line is a power-law fit to the 20 (80) disk data points. The secondary axis shows the time a signal propagating through N_{eff} disks spends in the lossy regions at 20 GHz. Estimating it with the inverse boost factor bandwidth as described in the text gives the black dashed line.

Parametrization

We can understand this result by realizing that for a signal that in frequency domain has some width $\Delta\nu_\beta$ the width in time domain τ must obey $\tau\Delta\nu \geq \frac{1}{2}$, independently of how many disks are actually installed. Taking this time as the propagation time in the booster, we can estimate the corresponding phase depth in lossy regions, which equals $N_{\text{eff}}|n|\omega d$. This estimate is shown as the black dashed line in figure 5.8. Explicitly this gives the desired parametrization of N_{eff} as

$$N_{\text{eff}} \sim \left(\frac{\nu}{\Delta\nu}\right)\left(\frac{\pi}{|n|\omega d}\right), \tag{5.11}$$

independent of the actual disk number N. Notice that a change of the refractive index n has no direct effect on N_{eff}, as long as one remains the phase depth of the lossy regions $|n|\omega d$ approximately the same. Therefore, the same $\tan\delta$ affects the power boost factor the same way for different boosters with different dielectric constants. Plugging this estimate into the approximation in equation (5.10) and requiring the reduction of the boost factor to be less than 10 %, we can derive a critical bandwidth

$$\Delta\nu_{\text{crit}} \sim 20\,\text{MHz}\left(\frac{\delta}{10^{-4}}\frac{\nu}{20\,\text{GHz}}\right). \tag{5.12}$$

For bandwidths above the critical bandwidth the area law holds. For smaller bandwidths losses dominate. The critical bandwidth is approximately independent on the number of disks and the real part of the dielectric constant of the disks.

In short. Losses such as a dielectric loss ($\tan\delta$) modify the area law, i.e., the achievable area under the power boost factor curve is not constant with bandwidth, but rapidly decreases when going below a critical bandwidth. The critical bandwidth is found to be approximately $\sim 20\,\text{MHz}\,(\tan\delta/10^{-4})$ at the frequency range for the prototype around 20 GHz, independent of the number of disks in the haloscope.

Chapter 6

3D Models

The results discussed until now rely on the 1D model of the booster, which holds if the disks are extended infinitely in radius and are perfectly flat and homogeneous. These assumptions are not realized in the experimental setup. In this chapter we therefore discuss three independent methods to numerically solve the wave-equation (2.2) in three dimensions with more complicated boundary conditions. We are mostly only interested in the solution around at fixed frequencies since the axion field oscillates at a very sharp frequency $m_a(1+\mathcal{O}(10^{-6}))$. Therefore, we consider simulations in frequency domain, where for each fixed frequency a separate simulation is performed and the time dependency of all fields is simply $\exp(-i\omega t)$. Recall that the wave-equation (2.2) then takes the form

$$-\nabla^2 \boldsymbol{E} + \nabla(\nabla \cdot \boldsymbol{E}) - (n\omega)^2 \boldsymbol{E} = -i\omega \boldsymbol{J}_a. \tag{6.1}$$

Of course it is also possible, to solve the wave-equation (2.2) in time domain [127, 128]. However, in order to resolve e.g. a resonance over a smaller frequency band, one typically needs to run the simulation for more time steps, while in each step these approaches accumulate additional numerical error.

Table 6.1 gives an overview over the methods considered here. We start with Finite Element Methods (FEM) in section 6.1, which is suited to simulate electromagnetic fields in any 3D geometry without any restricting assumptions on the wave-equation, albeit numerical discretization and convergence. If one assumes no net charges $\rho = \nabla \cdot \boldsymbol{E} = 0$, the wave-equation simplifies significantly and the Recursive Fourier Propagation method in section 6.2 can be applied. Lastly one can decompose the fields into a set of orthogonal eigenmodes, as introduced in section 6.3. This will not only provide a very efficient method for calculating and parameterizing fields in a dielectric haloscope but also offers some intuitive understanding of 3D effects. At last in section 6.4 we will briefly point out how an antenna included into the system can be treated.

6.1 Finite Element Methods (FEM)

We can explicitly solve equation (6.1) for complex geometries numerically with finite element methods (FEM) [129]. FEM decompose the problem into a set of a finite number of cells ("mesh"). Imposing the boundary conditions between cells results in a matrix equation which is solved

numerically. An example for a mesh is shown in figure 6.1. In order to resolve the wave structure sufficiently, the mesh needs to consist of at least 5 to 10 cells per photon wavelength. This holds in particular for media where a dielectric constant decreases the wavelength. Here a finer mesh is required, such as e.g. for the dielectric disk which is located at $z \sim 0.2\,\mathrm{m}$ in figure 6.1. The results obtained in this thesis are obtained with the open-source package Elmer [130, 131] (VectorHelmholtz module). They are compared to results obtained with the commercially available COMSOL Multiphysics ® [132] (wave-optics module) from our collaborators [3, 10]. Using two different FEM tools enables us to cross-check results obtained with both tools and to possibly disentangle systematics from the different algorithms or meshes from physical effects.

Previous axion-electrodynamics studies [82, 133, 134] for cavity setups aim to find modes of closed cavities. In the case of dielectric haloscopes like MADMAX we are faced with open situations, which requires absorbing boundary conditions. Therefore in Elmer we use Robin boundary conditions to describe an open system

$$\boldsymbol{n} \times \nabla \times \boldsymbol{E} - \alpha\, \boldsymbol{n} \times (\boldsymbol{n} \times \boldsymbol{E}) = g \quad \text{on } \Gamma, \tag{6.2}$$

with $\boldsymbol{n}$ the normal vector on the simulation boundary Γ and $\alpha = ik, g = 0$ (impedance boundary

Method	Assumptions	Benchmark Time
Finite Elements (FEM)	◦ 3D mesh ($\lesssim \lambda/5$) fine enough	$\sim 1\,\mathrm{year}$
	◦ numerical convergence	(Elmer)
	• azimuthal symmetry (only 2D3D approach)	$\sim 30\,\mathrm{min}$ (2D3D-COMSOL [10])
Recursive Fourier Propagation	◦ 2D discretization ($\lesssim \lambda/2$) sufficient	$\sim 5\,\mathrm{s}$
	◦ number of iterations sufficient	(own implementation)
	• $\nabla \cdot \boldsymbol{E} = 0$	
	• radiation at $r > R$ absorbed	
	• $\boldsymbol{B}_e \sim$ const. on length scales λ	
Mode Matching	• (number of) modes sufficient to approximate field	$\lesssim 1\,\mathrm{s}$ (own implementation)
	modes in our implementation:	
	• $\nabla \cdot \boldsymbol{E} = 0$	
	• $\boldsymbol{E}(r > R) = 0$ for dielectric disks	
	• $\boldsymbol{B}_e \sim$ const. on length scales λ	

Table 6.1: Overview of various methods considered here to solve the axion-Maxwell equations for dielectric haloscopes in 3D, and their core numerical (◦) and physics (•) assumptions. The benchmark time denotes the order of magnitude calculation time of the boost factor for a minimal dielectric haloscope (single disk and mirror) with a diameter of $\varnothing = 20\,\mathrm{cm}$ and Sapphire disks at a frequency of 10 GHz calculated on a single CPU (clock rate $\sim 2\,\mathrm{GHz}$). More details cf. sections 6.1 through 6.3.

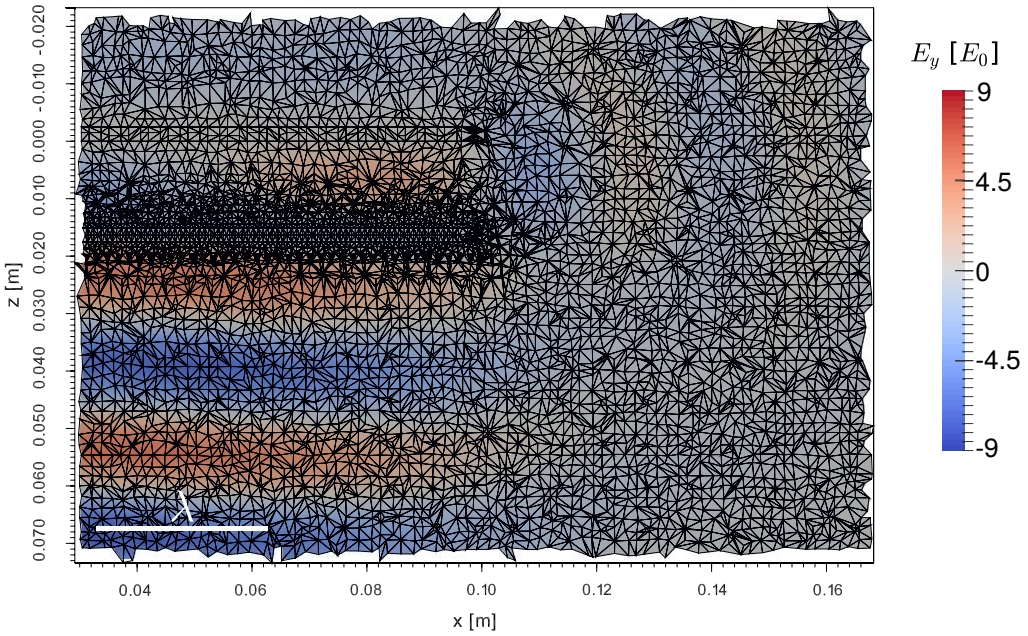

Figure 6.1: Subset of an example mesh for a minimal dielectric haloscope, which consists of a circular perfect mirror at $z = 0$ and a dielectric disk of thickness 0.25 cm around half wavelength away from the mirror, i.e. at $z \approx 1.5\,\text{cm}$, as considered in section 8.3.2. The colors denote the result for E_y at a fixed instant of time obtained with Elmer.

conditions) [135]. One can show that this only works for plane waves impinging the boundary with a spatial frequency k orthogonal to the boundary, i.e. waves impinging under other angles will experience some unwanted reflectivity. Therefore, perfectly matched layer (PML) boundary conditions [132, 136] are used in COMSOL, which absorb a large amount of impinging radiation also under a large incidence angle. A comparison and discussion of different boundary conditions for electromagnetic FEM solvers can be found for example in [137].

FEM can handle 3D geometries which have typical length scales of a few wavelengths in all three spatial dimensions. In this case both direct and iterative solvers may be used. In Elmer for example we obtain the 3D solution always by using a tuned "Biconjugate Gradient Stabilized" iterative solver [135, 138, 139], while in COMSOL direct solvers have been used [132, 140]. While iterative solvers may suffer from insufficient convergence, a direct solver directly calculates the solution to the matrix system. On the other hand a direct solver is much more memory intensive and therefore computationally more demanding. Due to the numerical complexity of FEM, it is hard to use this method for a full 3D simulation of a larger system than a single disk and mirror, as we will see explicitly in section 8.3.2.

As pointed out by [3, 10], in order to reduce the size of the computational problem by one dimension one can exploit the azimuthal symmetry ("2D3D approach"). Even if the external magnetic field is polarized in y-direction, we can decompose all fields as a sum of azimuthally symmetric fields as

$$\boldsymbol{E} = \tilde{\boldsymbol{E}}^{+} e^{i\phi} + \tilde{\boldsymbol{E}}^{-} e^{-i\phi}, \tag{6.3}$$

where $\tilde{\boldsymbol{E}}^{\pm}$ have no ϕ-dependency. Analogous to the superposition of left-circular and right-circular

fields [141] the sum of the two $\tilde{\boldsymbol{E}}^{\pm} = (-\hat{\boldsymbol{e}}_\phi \pm i\hat{\boldsymbol{e}}_r)e^{im\phi}$ is polarized in y-direction. Since the wave equation (6.1) is linear we can solve it for each $\tilde{\boldsymbol{E}}^{\pm}$ separately and afterwards sum up the results. This strategy is used for example in the context of the simulation of radial symmetric antennas [142] as well. For more details on this method cf. [3]. This method has been implemented using COMSOL for multi-disk systems by our collaborators [10].

6.2 Recursive Fourier Propagation

In order to reduce the effort to solve the full wave equation, we can assume that there are no net charges, i.e., $\rho = \nabla \cdot \boldsymbol{E} = 0$, while an external current $\boldsymbol{J} \neq 0$ is still possible. This ansatz neglects near fields generated by any induced charge distributions. In this case equation (6.1) simplifies to

$$-\nabla^2 \boldsymbol{E} - (\omega n)^2 \boldsymbol{E} = -i\omega \boldsymbol{J}_a. \tag{6.4}$$

We can now treat all three components of $\boldsymbol{E}$ as independent scalar fields, since all three components decouple in (6.4). Such a scalar diffraction theory is applicable if the optical system is much larger than the photon wavelength of the propagating fields [143]. In addition, the fields are required to propagate along one preferred axes. The optical size of a dish antenna is given by the dish diameter, while for a dielectric haloscope the optical size is given by the diameter of the mirror and dielectric disks. In the proposed dielectric haloscopes such as MADMAX [2,34] and LAMPOST [95] as well as in dish antenna experiments such as BRASS [144] this condition will be fulfilled. We will elaborate the validity of this assumption in some more detail in section 8.2.1 on the example of a dish antenna.

First we find a specific solution to the inhomogeneous equation (6.4). For haloscope experiments like MADMAX spatial gradients of $\boldsymbol{J}_a$ are small on the length scale of a photon wavelength λ, since the axion field changes length scales of its de Broglie wavelength $\lambda_{\mathrm{dB}} \sim 10^3\lambda$ and the external magnetic field is approximately constant over the size of the experiment. In this case the first term in equation (6.4) can be neglected and the solution is simply the axion-induced field $\boldsymbol{E}_a$ as introduced already in equation (2.3). The homogeneous part of equation (6.4) is solved by plane waves fulfilling the photon dispersion relation $|\boldsymbol{k}| = \omega n$. The full solution before introducing boundary conditions is therefore a Fourier series plus the axion-induced field

$$\boldsymbol{E}(\boldsymbol{x}) = \int_{\mathbb{R}^3} \hat{\boldsymbol{E}}(\boldsymbol{k}) e^{i\boldsymbol{k}\cdot\boldsymbol{x}} \frac{\mathrm{d}k^3}{(2\pi)^3} + \boldsymbol{E}_a(\boldsymbol{x}), \tag{6.5}$$

which is fully analogous to equation (4.1) in 1D. As for 1D, the task is to find the appropriate plane waves $\hat{\boldsymbol{E}}_r(\boldsymbol{k})$ in any region r of the haloscope that compensate the discontinuity of $\boldsymbol{E}_a(\boldsymbol{x})$ across all the boundaries of the dielectrics.

Due to the photon dispersion relation, it is sufficient to know the fields on a xy-slice to calculate how they propagate along z. Let $E(x, y; 0)$ be the field in y-direction at $z = 0$ without the axion-induced field, then the propagated field is [143, 145]

$$E(x, y; z) = \mathcal{F}^{-1}\left\{\mathcal{F}[E(x, y; 0)](k_x, k_y) \exp[ik_z(k_x, k_y)z]\right\}, \tag{6.6}$$

where $\mathcal{F}$ denotes the two dimensional Fourier transformation in x and y directions and where $k_z(k_x, k_y)$ is given by the photon dispersion relation

$$k_z(k_x, k_y) = \pm\sqrt{(\omega n)^2 - k_x^2 - k_y^2}, \tag{6.7}$$

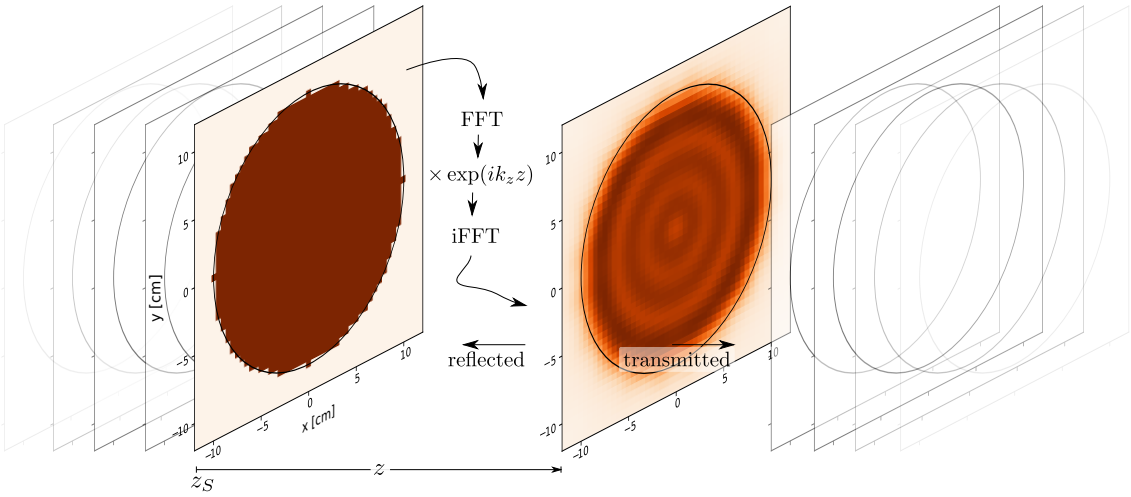

Figure 6.2: Illustration of the recursive Fourier propagation approach. The field on the left surface in brown is given and propagated to the next surface by applying equation (6.6). The propagation consists of a Fourier transformation of the initial field and a backtransformation which is taking into account the phase factor $\exp(ik_z z)$. The implementation can be done with the fast Fourier transformation (FFT) algorithm and the corresponding inverse (iFFT). We also illustrate that the fields are defined on a discretized grid over the different slices. The approach takes into account diffraction phenomena arising from the finite size disks. Repeating the propagation recursively and applying reflection and transmission coefficients at each slice, a 3D multilayer system can be calculated.

where the sign determines the propagation direction. Therefore, in comparison to the 1D case, where the phase evolves as $e^{i\omega n z}$, the phase evolves more slowly as $e^{ik_z z}$ in 3D.

Small tilts or thickness inhomogeneities of the disks cause small distance deviations $\Delta z(x, y)$ when arriving at the interface at distance z, giving

$$E(x, y; z) \to E(x, y; z) \exp[ik_0 \Delta z(x, y)], \quad k_0 = \omega n, \tag{6.8}$$

where in particular for relative tilts γ_x around the x-axis and γ_y around the y-axis between the interfaces

$$\Delta z(x, y) = \gamma_y x + \gamma_x y. \tag{6.9}$$

Here we have assumed $k_0 \approx k_z$. Since k_0 is always slightly larger than k_z, this does only overestimate the effects due to the thickness variation of the disks. Assuming the leading order effect of small variations $\Delta n(x, y)$ are also phase differences, we can estimate their effects simply by considering the according phase shifts corresponding to the same relative thickness inhomogeneity, i.e.,

$$\frac{\Delta n(x, y)}{n} \mathrel{\hat{=}} \frac{\Delta z(x, y)}{z}. \tag{6.10}$$

In order to compute the 3D fields for a dielectric haloscope, this approach can be recursively applied to propagate the radiation emitted from the individual interfaces in the system to compensate the discontinuity in the axion-induced field $\boldsymbol{E}_a$. Since the boundary conditions on the

disk surface are the same in 1D and 3D, the amplitudes of the emitted radiation fields are directly given by the corresponding equations in 1D, cf. equation (2.4), but including the transverse spatial dependency for all quantities. The full response of the booster can be calculated by tracing these fields analogous to the ray-tracing strategy discussed in section 4.2 through the system until they leave it, as sketched in figure 6.2. The full procedure is

- Considering the fields $E(z_1)$ emitted at z_1, the fields at the opposite interface $E(z_2)$ are obtained using the Fourier approach with equation (6.6).
- At the next surface the fields $E(z_2)$ outside of the disk radius $r > R$ are set to zero.
- $\mathcal{T}E(z_2)$ is transmitted and $\mathcal{R}E(z_2)$ is reflected, where $\mathcal{R}$ is the complex reflectivity and $\mathcal{T} = (1 + \mathcal{R})$ the complex transmissivity of the surface as seen from the region through which we just propagated.
- Repeating the above for N iterations between all interfaces and adding up all fields outside, converges to the out-propagating fields for large N.

For our implementation, the reflectivity of the interface in the third step is taken from the 1D model, cf. equation (4.15), which holds for plane waves under a normal incident angle. Other angles could be accounted for by making $\mathcal{R}(k_x, k_y)$ dependent on the transverse momenta. However, $\mathcal{R}$ only depends at second order on the incident angle (see "Fresnel equations," e.g., in [143]). Since electromagnetic fields propagate essentially along the booster axis in dielectric haloscopes, assuming normal incidence is a good approximation in our case. Moreover, this procedure assumes that the plane waves in equation (6.5) are still approximate solutions inside the dielectric disk and all fields propagating outside of the disk radius are being absorbed. This is justified, considering that the fields over-shining the disks are not reflected and therefore not resonantly enhanced like the fields inside the disk radius. The validity of this approximation for MADMAX has also been investigated in a recent Bachelor's thesis [146].

Note that one can store fields at all layers simultaneously and sum up the reflected and transmitted fields at each layer after each iteration step, such that the numerical complexity grows linear with the number of iteration steps and layers. We use the fast Fourier transformation (FFT) algorithm. In addition, this approach also requires only a discretization in x and y dimensions with grid spacings according to the Nyquist theorem of $\approx \lambda/2$, and thus makes this method numerically efficient.

6.3 Mode Matching

In the previous chapter we have decomposed the electromagnetic fields into the homogeneous free-space solutions of the wave equation (6.4), which are plane waves. In this section, we start with the solutions inside the dielectric disks, and will decompose all fields into a coherent sum of those.

To begin with, consider a dielectric waveguide, i.e., a cylinder of dielectric material with radius R surrounded by vacuum. In the limit for large radii $R \gg \lambda$ and large dielectric constant $\epsilon \gg 1$, we obtain a disk of the dielectric haloscope. In this limit the fields drop to zero at the boundary of the waveguide. This can be intuitively understood in 2D by considering the momentum of a plane

wave $\exp[i(k_z z + k_x x)]$ essentially propagating in z-direction inside the waveguide, i.e., $k_z \approx n\omega$. For the transverse spatial frequency k_x of this wave we have according to equation (6.7)

$$k_x = \pm\sqrt{(n\omega)^2 - k_z^2}. \tag{6.11}$$

Inside the waveguide we have $k_z < n\omega$, hence k_x is real. Outside, k_z needs to be the same than inside in order to match the boundary condition on the waveguide walls at $x = \pm R$ for all z. However, outside the refractive index is $n = 1$. We have $k_z > \omega$, since before we assumed $k_z \approx n\omega$ with $n \gg 1$. Hence, $k_x \sim \pm in\omega$ is imaginary and the field is exponentially damped in x-direction $\sim \exp(-n\omega|x|)$ and thus effectively zero outside the waveguide. To match the electromagnetic boundary conditions at $x = R$, the fields therefore have to drop to zero towards the boundary. This argument generalizes in 3D and radial coordinates. For more details see for example [147, 148]. Assuming again $\nabla \cdot \boldsymbol{E} = 0$, the solutions to each component of $\boldsymbol{E}$ in the wave equation (6.4) under this boundary condition give the field inside the disk. These solutions are the waveguide eigenmodes illustrated in figure 6.3 and given by

$$E_{m\ell}(r,\phi) = \mathcal{N}_{m\ell} J_\ell(k_{c,m\ell} r) e^{i\ell\phi} \quad , \quad J_m(k_{c,m\ell} R) = 0, \tag{6.12}$$

where $m > 0, \ell$ are discrete mode indices, $\mathcal{N}_{m\ell}$ is a normalization factor such that $\int_{\mathbb{R}^2} |E_{m\ell}|^2 \mathrm{d}A = 1$, J_ℓ are the Bessel function of the first kind of order ℓ and $k_{c,m\ell}$ is the transverse spatial frequency or transverse momentum. Notice that $k_{c,m\ell}$ is determined by the radius of the disk under the boundary condition that the fields drop to zero at the rims of the disk on the right of equation (6.12). As $k_{c,m\ell}$ appears in front of the the radius r, its inverse corresponds the transverse length scale on which the field distribution of the mode changes. These modes are orthogonal and complete in the sense that we can expand any field distribution inside the disks into a set of those modes. Most importantly, they are *eigen*modes inside the disks, i.e., they propagate independently along z-direction within the disks as

$$E(r,\phi,z) = \sum_{m,\ell} e_{m\ell} E_{m\ell}(r,\phi) e^{ik_{z,m\ell} z} \quad , \quad k_{z,m\ell} = \sqrt{k_0^2 - k_{c,m\ell}^2}, \tag{6.13}$$

where $e_{m\ell}$ are the coefficients for the mode expansion and $k_0 = n\omega$. Notice that the longitudinal momenta $k_{z,m\ell}$, sometimes also referred to as the propagation constant, determines the phase velocity $v_{p,m\ell} = \omega/k_{z,m\ell}$ of the different modes, which in general is not the same for different modes. In free space these modes in general do not propagate independently anymore, since they are no more solutions of the scalar wave equation under the new boundary conditions. Since they are orthogonal, we still can expand any field into these modes, but during propagation they 'mix' with each other, i.e.,

$$E(r,\phi,z) = \sum_{m,\ell,m',\ell'} P_{m\ell}^{m'\ell'}(z)\ e_{m'\ell'}\ E_{m\ell}(r,\phi), \tag{6.14}$$

with $e_{m'\ell'}$ the coefficients of the mode expansion at $z = 0$ and the linear map $P_{m\ell}^{m'\ell'}$ between the modes. It is given by

$$P_{m\ell}^{m'\ell'}(z) = \int_{\mathbb{R}^2} E_{m\ell}^*(r,\phi) \cdot E_{m'\ell'}^p(r,\phi;z)\, \mathrm{d}A, \tag{6.15}$$

where $E_{m'\ell'}^p(r,\phi;z)$ is the field of the mode (m',ℓ') after propagating for a distance z. The propagated fields E^p in free space can be obtained with equation (6.6). Indeed, equations (6.14)

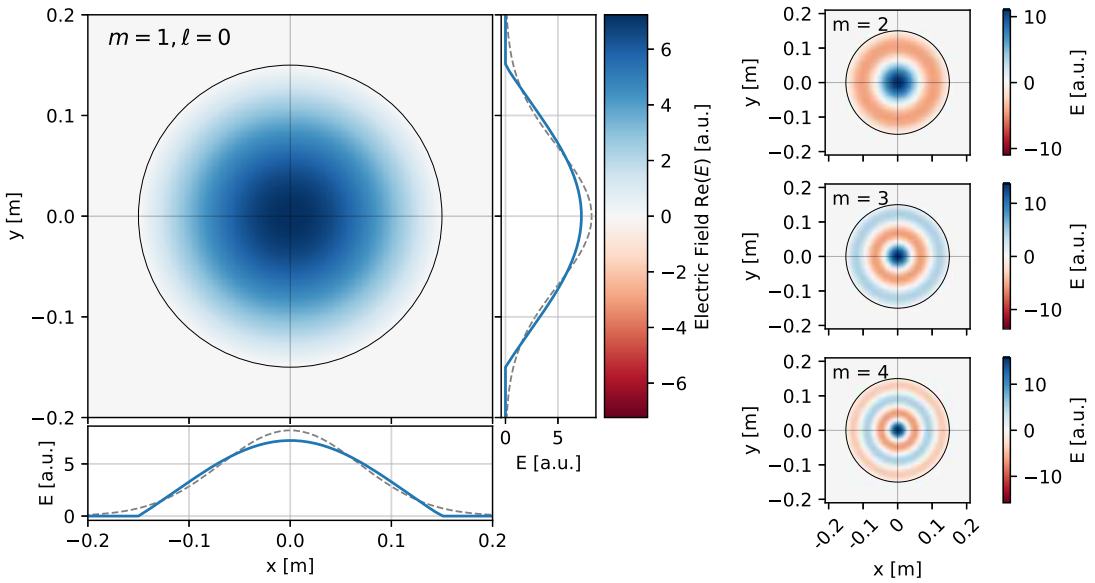

Figure 6.3: Modes of the circular dielectric haloscope. **Left:** Fundamental mode $n = 1$. Main panel: Spatial field distribution. Side and bottom panels: Fields along the x and y-axis (blue straight lines) and fields corresponding to a Gaussian beam [149] with a beam waist of $w_0 \approx 10\,\mathrm{cm}$ (gray dashed lines). **Right:** Same as main panel on the left, but for higher modes.

and (6.15) hold generally for all media with any boundary condition, but P is diagonal inside an ideal disk, i.e., $P = \mathrm{diag}\left[\exp(\pm i k_{z,m\ell} z)\right]$, such that one obtains equation (6.13).

To include the axion in this formalism, we expand the axion-induced field in a sum of the modes, i.e.,

$$E_a(r,\phi,z) = \mathcal{N}_a \sum_{m,\ell} \eta_{m\ell} E_{m\ell}(r,\phi), \tag{6.16}$$

$$\Rightarrow \quad \eta_{m\ell} = \frac{1}{\mathcal{N}_a} \int_{\mathbb{R}^2} E^*_{m\ell}(r,\phi) \cdot E_a(r,\phi,z)\,\mathrm{d}A, \tag{6.17}$$

with the normalization of the axion-induced field $\mathcal{N}_a \equiv \int |E_a(\boldsymbol{x})|^2 \mathrm{d}A$. Notice that equation (6.17) is analogous to (6.15). The coupling coefficients $\eta_{m\ell}$ define the amplitude at which the axion-induced electric field excites the modes describing the emitted radiation from the individual dielectric interfaces. We call the square of the coefficients $|\eta_{m\ell}|^2$ coupling efficiency of the axion-induced electric field to the mode (m,ℓ). In general, the coupling coefficients depend on z. However, if not stated otherwise, we assume a spatially constant external axion-induced field and a spatially constant external magnetic field, which also makes the coupling coefficients independent of z.

We can now generalize the one dimensional transfer matrix formalism for dielectric haloscopes in [89], to higher dimensions using these modes. This can be done by having mode coefficients for the left- and right-moving fields in each region, i.e., $L = (\cdots l_{m\ell} \cdots)^T$, $R = (\cdots r_{m\ell} \cdots)^T$ become $\hat{m}(2\hat{\ell}+1)$-dimensional vectors when considering the modes $m = 1 \ldots \hat{m}, \ell = -\hat{\ell} \ldots \hat{\ell}$. Analogous, for the axion-induced field we make the replacement $E_0 \to E_0(\cdots \eta_{m\ell} \cdots)^T$. The transfer matrices

	Axion Coupling	Propagation			
		$\varnothing = 30\,\mathrm{cm}$		$\varnothing = 1.2\,\mathrm{m}$	
Mode	$\lvert\eta\rvert^2$	k_c	δ_d	k_c	δ_d
$n = 1$	69 %	$16\,\mathrm{m}^{-1}$	$\sim 2 \times 10^{-5}$	$4\,\mathrm{m}^{-1}$	$\sim 2 \times 10^{-7}$
$n = 2$	13 %	$37\,\mathrm{m}^{-1}$	$\sim 1 \times 10^{-4}$	$9\,\mathrm{m}^{-1}$	$\sim 1 \times 10^{-6}$
$n = 3$	5 %	$58\,\mathrm{m}^{-1}$	$\sim 2 \times 10^{-4}$	$14\,\mathrm{m}^{-1}$	$\sim 4 \times 10^{-6}$
$n = 4$	3 %	$79\,\mathrm{m}^{-1}$	$\sim 5 \times 10^{-4}$	$20\,\mathrm{m}^{-1}$	$\sim 6 \times 10^{-6}$
$n = 5$	2 %	$100\,\mathrm{m}^{-1}$	$\sim 7 \times 10^{-4}$	$25\,\mathrm{m}^{-1}$	$\sim 1 \times 10^{-5}$
$n = 6$	1 %	$121\,\mathrm{m}^{-1}$	$\sim 1 \times 10^{-3}$	$30\,\mathrm{m}^{-1}$	$\sim 2 \times 10^{-5}$
		...			

Table 6.2: Properties of the most important modes for a dielectric haloscope as foreseen for the MADMAX prototype (disks $\varnothing = 30\,\mathrm{cm}$) and final scale experiment (disks $\varnothing = 1.2\,\mathrm{m}$). $|\eta|^2$ denotes the coupling of the uniform axion field to the mode, k_c its transverse momentum, and δ_d the diffraction loss parameter between the dielectric disks as defined in the main text.

become explicitly

$$\mathsf{G}_r = \frac{1}{2n_{r+1}} \begin{pmatrix} (n_{r+1}+n_r)I & (n_{r+1}-n_r)I \\ (n_{r+1}-n_r)I & (n_{r+1}+n_r)I \end{pmatrix}, \qquad \text{(Reflection / Transmission)} \tag{6.18}$$

$$\mathsf{P} = \begin{pmatrix} P & 0 \\ 0 & P^{-1} \end{pmatrix}, \qquad \text{(Propagation)} \tag{6.19}$$

$$\mathsf{S}_r = \frac{A_{r+1} - A_r}{2}\,\mathbb{1}, \qquad \text{(Axion-Induced Fields)} \tag{6.20}$$

where here the entries of the matrices are sub-matrices in the vector space of the mode coefficients, i.e. I is the $\hat{m}(2\hat{\ell}+1)$-dimensional identity matrix. With these definitions the equations (4.12), (4.13) and (4.14) for the boost factor, reflectivity and transmission directly hold in 3D.

For dielectric haloscopes like MADMAX this formalism is particularly beneficial. To understand this, consider the fundamental properties of these modes, summarized in table 6.2. Firstly, the axion-induced field essentially only excites lower modes; indeed the the coupling efficiency to the fundamental mode is 69 % and for the first four modes $\sum_{m\leq 4} |\eta_{m\ell}|^2 = 90\,\%$. Secondly, as will be shown explicitly later, the modes turn out to be approximate eigenmodes of the whole booster ('eigenmode approximation'), i.e., when only considering the relevant modes with $m = 1, 2, 3, 4; \ell = 0$ even for disks with 30 cm diameter at 20 GHz the mixing between these modes, i.e., $|P_{m\ell}^{m'\ell'}|$ for $(m, \ell) \neq (m', \ell')$, is $\lesssim 8 \times 10^{-4}$. So unless the system is tuned to be very resonant, the mixing can be neglected, and we find

$$P_{m\ell}^{m'\ell'} \approx \exp\left(ik_{z,m\ell}z - \tfrac{1}{2}\delta_{\mathrm{d},m\ell}k_{z,m\ell}z\right)\mathbb{1}_{m\ell}^{m'\ell'}, \quad \text{(eigenmode approximation)} \tag{6.21}$$

where δ_d is a diffraction loss parameter, and all modes propagate essentially independently. If, on the contrary, the system is tuned to be very resonant for a specific mode, the difference in k_z for the other modes will make them rapidly dephase, i.e. make all other modes irrelevant. When inserting

the eigenmode approximation in (6.21) into the transfer matrix formalism all modes decouple, i.e., the result for each mode can be obtained by an independent 1D calculation. In particular, if the antenna is coupled to only one eigenmode, a 1D model is sufficient to describe the whole system including the antenna; for more on the antenna coupling see below. We will investigate the validity of the eigenmode approximation in section 8.3.1, and in section 8.3 and later this understanding will also provide an intuitive, but still quantitative explanation of the observed effects.

Notice that this method can in principle be applied for any complete, orthogonal set of independent waveguide modes describing the propagation of electromagnetic fields inside the dielectric disks. Thus, one can use instead vectorized fields, setting aside the approximation of zero net charge $\nabla \cdot \boldsymbol{E}$, and modes which do not strictly fall to zero at the rims of the dielectric disks that could account also for propagation around the disks. More details are outlined in literature such as [147, 148].

6.4 Including an Antenna

Let us briefly review the basics of receiving the signal coming from the booster with an antenna. According to the reciprocity theorem [150], if we know the transmission from antenna A to antenna B it will be the same if antenna B is used as the sender and A as the receiver. The antennas considered here, when used as a sender, are excited by a scalar voltage U_A. The radiation from the antenna is fully described by a 2D field distribution (beam shape) $\boldsymbol{E}_\mathrm{A}(x, y)$. Due to the theorem of reciprocity for any beam which is impinging this antenna, it can only receive fields following the same beam shape.

Mathematically we can decompose any beam $\boldsymbol{E}_\mathrm{B}$ in a sum of the antenna beam $\boldsymbol{E}_\mathrm{A}$ and an orthogonal residual beam $\boldsymbol{E}_\mathrm{R}$. The inner product of $\boldsymbol{E}_\mathrm{A}$ with $\boldsymbol{E}_\mathrm{B}$ then gives the coefficient for the antenna beam in this decomposition. It is given by the so-called coupling integral

$$c = \frac{\int \boldsymbol{E}_\mathrm{A}^* \cdot \boldsymbol{E}_\mathrm{B} \,\mathrm{d}A}{\sqrt{\int |\boldsymbol{E}_\mathrm{A}|^2 \,\mathrm{d}A \int |\boldsymbol{E}_\mathrm{B}|^2 \,\mathrm{d}A}}, \tag{6.22}$$

where the integrals are typically taken over the antenna aperture, but may be taken over any infinite spatial slice both beams propagate through.[1] Note that this is fully analogous to equations (6.17) and (6.15). $|c|^2$ is called the coupling efficiency or power coupling coefficient of the antenna and determines how much power can be extracted from a specific beam. We will use the coupling efficiency later to quantify how well two beam shapes match, and also refer to it as 'matching ratio'.

The power in the residual beam $\boldsymbol{E}_\mathrm{R}$ is not received by the antenna. It depends on the geometry of the antenna and surroundings what happens with this power. If it is focused well onto the physical antenna aperture one may assume it is reflected. However, if it for example has significant non-zero fields outside of the physical aperture of the antenna, one could place absorbers there to absorb this part of residual fields.

In addition, we remark that apart from the coupling efficiency of the antenna to a specific beam shape $\boldsymbol{E}_\mathrm{R}$, it typically has an intrinsic reflection coefficient, arising for example from the coupling of the antenna waveguide to a coaxial cable.

[1] This can be easily seen considering their propagation from one slice to the other according to equation (6.6).

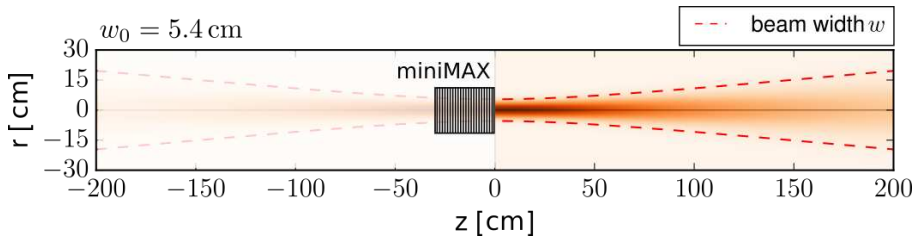

Figure 6.4: Example Gaussian beam with $\lambda = 1.6\,\mathrm{cm}$ ($\nu = 19\,\mathrm{GHz}$) focused on a spot of size $w_0 = 5.4\,\mathrm{cm}$. The orange shading sketches the intensity distribution of the beam. The red dashed line indicates the beam width $\pm w(z)$. In this thesis, we assume antennas that produce Gaussian beams focused on the front disk of the booster, as schematically indicated here for the MADMAX prototype ('miniMAX'). Adapted from [154].

Gaussian Beams

The fundamental mode of the booster has a coupling efficiency of 97% with a Gaussian beam. Gaussian beams are obtained as the fundamental mode of propagation in free space considering azimuthal symmetry and the paraxial approximation [149, 151]. Moreover, it is a standard task for antenna builders to provide Gaussian beam antennas and Gaussian quasi-optics [152, 153]. Therefore, we will consider Gaussian beams for the antenna beam in this thesis. Such a beam is given by

$$\boldsymbol{E}\,(r,z) = \frac{w(z)}{w_0}\exp\left[-\frac{r^2}{w^2(z)} + i\frac{kr^2}{R(z)} + i\tan^{-1}\frac{z}{z_0}\right]\exp\left(-ikz\right)\hat{\boldsymbol{e}}_y \tag{6.23}$$

with the radial distance from the beam axis $r = \sqrt{x^2+y^2}$, the wavenumber $k = 2\pi/\lambda$ and

$$w(z) = w_0\sqrt{1+\left(\frac{z}{z_0}\right)^2} \quad ; \quad R(z) = z\left[1+\left(\frac{z_0}{z}\right)^2\right] \quad ; \quad z_0 = \frac{\pi {w_0}^2}{\lambda}, \tag{6.24}$$

where $w(z)$ is the beam width equal to two standard deviations of the Gaussian intensity distribution, $R(z)$ is the curvature radius of the beam, and z_0 is called the Rayleigh length and determines the range within which the beam width does not open by more than a factor of $\sqrt{2}$. We show an example for a Gaussian beam in figure 6.4.

Ellipsoidal mirrors can be used to map Gaussian beams onto each other. This is the benchmark method proposed for the MADMAX optics [153]. Notice that the needed diameter of such an ellipsoidal mirror placed far away ($z \gg z_0$) from the beam waist can be determined by the opening angle or divergence θ of the Gaussian beam, explicitly given by

$$\theta = \lim_{z\to\infty}\frac{w(z)}{z} = \frac{1}{\pi}\frac{\lambda}{\omega_0} \approx 3^\circ\left(\frac{10\,\mathrm{cm}}{\omega_0}\right)\left(\frac{20\,\mathrm{GHz}}{\nu}\right). \tag{6.25}$$

The radius of the mirror is typically required to be three times the beam width $\omega(z)$, i.e., the mirror should cover an opening angle of 6θ. More details including coupling integrals between Gaussian beams can be found in [149, 151, 152].

Chapter 7

Validation of 3D Models

In the previous chapter we have outlined methods to solve the axion-Maxwell equations under typical boundary conditions for haloscope experiments. It is important to ensure numerical convergence and correct implementation of the physics for these methods. In this chapter we briefly lay out how we do this in the framework of this thesis. Later, within chapter 8 we will compare the results of the different methods for different specific setups. This will inform us about the validity of the physics assumptions of the different numerical methods.

7.1 Finite Element Methods

Ensuring convergence of finite element methods and iterative solvers for large linear systems is a scientific topic on its own [140]. The output of the Elmer software offers a convergence parameter h [155], which corresponds to the error $h = |Ax - b|/|b|$, when solving the linear system $Ax = b$ for the vector x, where the matrix A and vector b encode our physical problem. While generally smaller values are better, the order of magnitude one can achieve in h can heavily dependent on the studied case. It is therefore only useful to compare results of simulations with the same or similar boundary conditions to each other.

We can, however, check the self-consistency of the FEM solution. A prime example is the density of mesh points. If the mesh is fine enough to approximate gradients on the mesh well, the solution does not change when decreasing the maximum distance of mesh points $\Delta x_{\max}$. As an example we present the calculation of a rectangular waveguide with dimensions $L_x = 3\lambda$ in x-direction, $L_y = \lambda$ in y-direction and a length of $L_z = 40\,\text{cm}$ in z-direction at a frequency of 10 GHz. Inside the waveguides we assume an external magnetic field

$$\boldsymbol{B}_e(\boldsymbol{x}) = B_0 \sin^2\left(\frac{\pi x}{L_x}\right) \cos^2\left(\frac{\pi z}{L_z}\right) \Theta\left(\frac{L_z}{2} - z\right) \hat{\boldsymbol{e}}_y, \tag{7.1}$$

with the Heaviside step function Θ, i.e., the field smoothly drops to zero over half of the length of the waveguide. The waveguide is closed at $z = 0$, where the discontinuity of the axion-induced field leads to emission of electromagnetic radiation inside the waveguide. For a sufficiently fine meshes the power propagating inside the waveguide needs to be independent of the mesh. To explicitly confirm this, we performed this calculation using 5 different values for $\Delta x_{\max} \leq \lambda/10$, as shown on the left of figure 7.1. The power and its numerical uncertainty is calculated by integrating

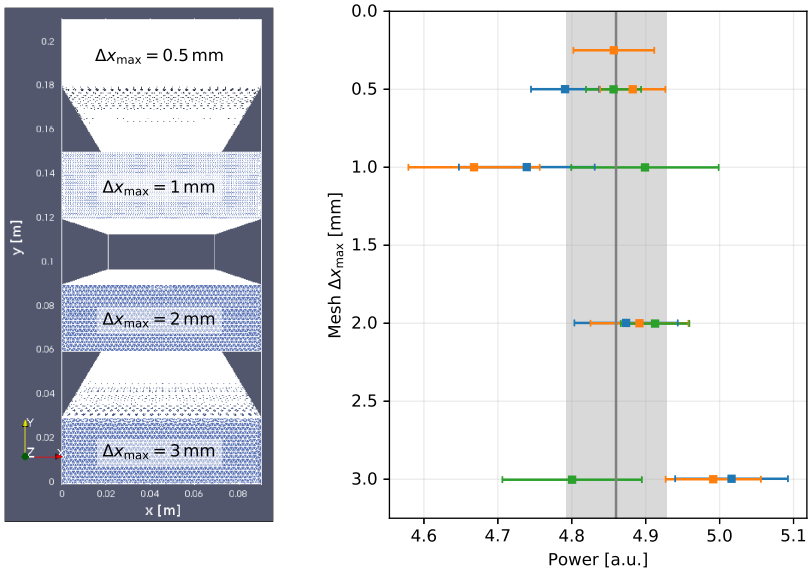

Figure 7.1: Simulation of the same waveguide but with different meshes, controlled by the maximum distance between mesh points $\Delta x_{\max}$. **Left:** Front-view of meshes corresponding to four different waveguides with different $\Delta x_{\max}$. The waveguide on the top has the most dense mesh with $\Delta x_{\max} = 0.5\,\mathrm{mm} = \lambda/60$, while the waveguide on the bottom has the most sparse mesh with $\Delta x_{\max} = 3\,\mathrm{mm} = \lambda/10$. **Right:** Power propagating within the waveguides for different $\Delta x_{\max}$. The three different colors correspond to three different simulations described in the text. The vertical gray line indicate the mean value, the band corresponds to one standard deviation. The power emitted from all waveguides is consistent within numerical uncertainties.

the Pointing flux over different transverse slices of the waveguide. We show the results of these calculations on the right of figure 7.1. The blue data points correspond to one simulation with 4 identical waveguides but with different meshes placed beneath each other as shown in the figure. The orange data points correspond to the same simulation but adding another waveguide with an even finer mesh. The green data points correspond to the same simulation but without leaving spaces between the waveguide. We see that these changes in boundary conditions and $\Delta x_{\max}$ lead to small differences in the FEM results, consistent within numerical uncertainties.

To show that a FEM solution indeed matches the analytical result, one needs to do a direct comparison with analytical solutions for cases where this is possible. We will do this for free space, a dish antenna setup and a single dielectric disk at the beginning of the next chapter.

7.2 Recursive Fourier Propagation

Since the Recursive Fourier Propagation method follows the electric fields analogous to the 1D ray tracing approach, after N iterations, the out-propagating waves have propagated over a total optical length $\Lambda_{\mathrm{tot}} \sim Nd$, where d is the average distance between the disks. This corresponds to a signal in frequency domain $\sim \exp(-iN\omega d)$. Therefore, in order to resolve frequency dependencies

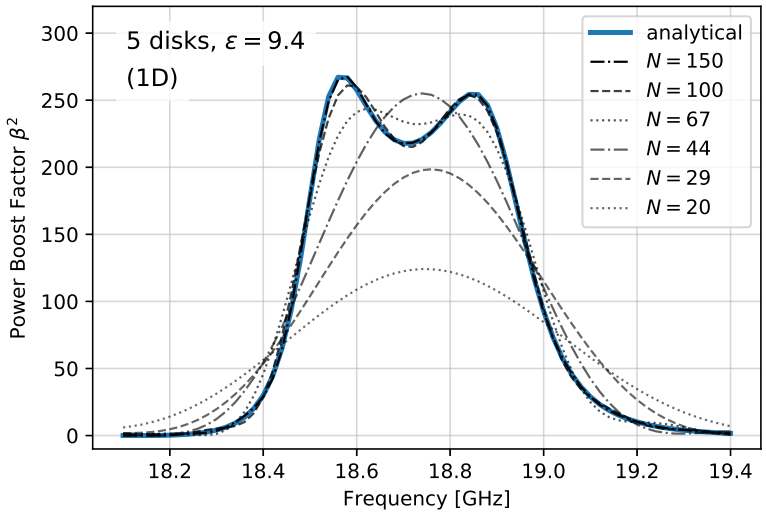

Figure 7.2: Convergence of numerical 1D ray tracing solutions (black) to the exact analytical result (blue) for a booster with 5 sapphire disks in front of a mirror adjusted for a boost factor bandwidth of $\sim 500\,\mathrm{MHz}$. The different line styles correspond to a different setting of maximum iterations N.

with a resolution $\Delta\nu$, we need

$$N \gtrsim \frac{1}{\Delta\nu\, d} \sim 4 \times 10^3 \left(\frac{1\,\mathrm{MHz}}{\Delta\nu}\right)\left(\frac{1.5\,\mathrm{cm}}{d}\right). \tag{7.2}$$

We show the convergence of the numerical 1D ray tracing implementation to the analytical result in figure 7.2. Here we consider a booster with 5 sapphire disks, similar than the one considered in part IV of this thesis, tuned for a boost factor that covers a bandwidth of 500 MHz. This result is obtained using the exact same code than the 3D calculations using Recursive Fourier Propagation, but only using a single point in x and y direction. According to equation (7.2) we need more than 10 iterations to resolve structures in the boost factor curve over $\Delta\nu = 500\,\mathrm{MHz}$ and more than 100 iterations to resolve 50 MHz. The numerical results confirm this estimate. Notice that running for fewer iterations than needed has the same effect as an effective loss, i.e., the area under the boost factor curve is generally reduced. In addition, this reduces the quality factor of internal resonances within the simulation, which in turn corresponds to smoothing out the boost factor curve.

In the following 3D calculations we always checked first that the corresponding 1D ray tracing calculation with N iterations agrees up to percent level with the analytical solution. Since the three-dimensional system has diffraction loss, we expect it to be less resonant. Thus, for simplicity, we can take the same number of N iterations also for the 3D calculations, while we usually use around one order of magnitude more iterations than required by equation (7.2). In principle, one can also check for convergence by requiring that the changes to the results after a number of steps are below a threshold. This needs to be done with great care, since on resonance each ray may only contribute a small field, but the constructive interference of many small contributions can be significant.

Besides numerical convergence, we have checked that our implementation correctly reproduces diffraction expected from a Gaussian beam and refraction between two different media up to numerical noise. As expected, this is the case, if the discrimination in x and y dimensions has grid spacings smaller or equal to $\lambda/2$.

7.3 Mode Matching

Numerical errors from the Mode Matching calculation described in section 6.3 arise from various steps during the calculation. First of all, it is important to calculate the free space propagation matrix P with high enough accuracy. In our implementation, the fields of the modes after a single propagation are calculated with the same implementation as we use for the Recursive Fourier Propagation method above, i.e., a grid in x and y directions with a spacing finer than half a photon wavelength is needed. Next, the numerical error from computationally multiplying and solving the transfer matrices in higher dimensions may be relevant. For the low number of modes considered in this thesis the dimension of the involved matrices is $\mathcal{O}(30)$. This is much lower than for other numerical applications like FEM where this can be orders of magnitude higher. Thus, a multitude of efficient algorithms exist [155–158] leading to numerical errors mainly from floating point inaccuracies in our case. These are orders of magnitude below the percent scale, i.e., can be safely neglected for our purposes.

The dominating additional error in this calculation arises from the assumption that the considered modes are sufficient to approximate the fields inside the booster. Naively, if the length scale $k_{c,m\ell}^{-1}$ of the highest considered mode defines the length scales the simulation can resolve in transverse direction. We can explicitly check that the number of considered modes is sufficient, by running the same calculation with a different number of considered modes. If all major contributing modes are taken into account, the result in the considered frequency range does not change significantly.

We show the result for such an example calculation in figure 7.3. Here we consider the same 20 disk booster with a predefined transverse thickness variation of the dielectric disks over transverse length scales of $\xi = 35\,\mathrm{mm}$ as discussed in more detail later in section 8.4.3. The different colored areas denote the total axion-induced power emitted by the booster within a certain mode. The red line denotes the total power expected from a calculation using Recursive Fourier Propagation. The red dashed line shows the same power times antenna coupling. The blue line shows the power times antenna coupling obtained from Mode Matching. We see that when more ℓ modes are taken into account the result converges towards the result from Recursive Fourier Propagation. While the total emitted power only changes on the $\sim 10\,\%$ level when increasing $\hat{l}$, the power that couples to the antenna almost differs by a factor of 2 between $\hat{l} = 0$ and $\hat{l} = 3$. While the axion essentially does not excite $\ell \neq 0$ modes, the mixing between the modes makes them relevant. The result with $\hat{\ell} = 3$ is sufficiently converged against the result from Recursive Fourier Propagation and adding higher modes to the calculation does not significantly change the result. Notice that the length scale of the highest considered mode $k_{c,43}^{-1} \approx 18\,\mathrm{mm}$ is slightly below the length scale of considered thickness variations of $\xi = 35\,\mathrm{mm}$.

For the numerical Mode Matching calculations presented in this thesis we usually only consider length scales larger or equal $\xi = 35\,\mathrm{mm}$ and therefore usually consider $\hat{m} = 4, \hat{l} = 3$, unless denoted

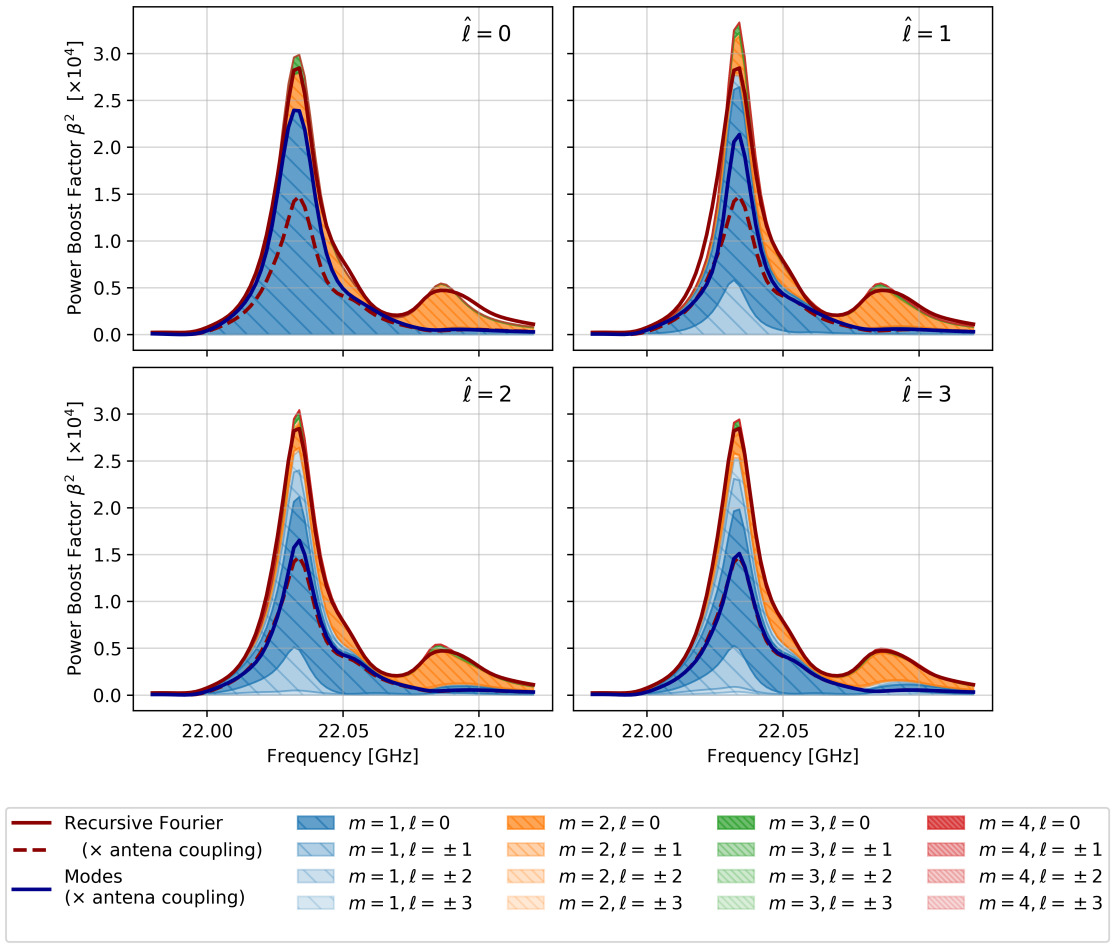

Figure 7.3: Convergence of Mode Matching method when including higher modes. We show an example simulation for a booster with deformed disks for $\hat{m} = 4$ and $\hat{l} = 0 \dots 3$ (top left to bottom right). In this particular example we used thickness variations at a scale of $\sigma = 10\,\mu$m and transverse length scale $\xi = 35\,$mm for a 20 disk ($\epsilon = 24$) booster with diameter $\varnothing = 30\,$cm as for the envisioned MADMAX prototype. For more details cf. section 8.4.3.

otherwise. Moreover, than more resonant a system is, than less modes are typically required, since only a subset of modes matches the resonant condition in a given frequency range. We will see this explicitly in section 8.3. For these reasons, it is sufficient to use the same number of modes when going from 20 to 80 disks, if the considered boost factor bandwidth and the considered inaccuracies, such as the scale of thickness variations, remain unchanged.

Chapter 8

Results from the 3D Models

In the following we will concentrate on the simulation of axion haloscopes streching over multiple photon wavelengths $\sim (5-100)\,\lambda$ using the methods described above. We will start with simple situations, such as free space and a single dielectric disk and successively go to more complex situations to finally arrive at a full picture of the MADMAX dielectric haloscope. While for free space and a single disk the Mode Matching picture is less useful, FEM calculations fail to be efficient for large-scale boosters with asymmetric boundary conditions such as axion velocity or disk tilts. Hence, going to larger setups, each step will allow us to use different approximations and methods and use these cases to cross-check the above methods with each other. Our central goal is to study the impacts of going to finite-size disks for a dielectric haloscope like MADMAX in general, and in particular to obtain requirements of engineering accuracies of the booster.

We will start with a free space situation in section 8.1, where we explicitly show that the axion-induced field $\boldsymbol{E}_a$ which is proportional to the external magnetic field $\boldsymbol{B}_e$ as defined in equation (2.3) already solves the axion-Maxwell equations. We then turn our attention to different general dish antenna setups consisting of a single disk in an external magnetic field in section 8.2, including for the first time a non-ideal dielectric disk glued together from two patches. In each case we will focus on three major effects: the modification of the power boost factor in 3D, diffraction of the emitted radiation and charge $\nabla \cdot \boldsymbol{E} \neq 0$ accumulating on the disk surfaces. The latter is neglected by the Fourier Propagation and Mode Matching methods. In section 8.3 we eventually generalize our study to dielectric haloscope consisting of multiple dielectric layers. We first check the eigenmode approximation introduced in section 6.3, and afterwards study a minimal dielectric haloscope with only one dielectric disk and a mirror. This example will demonstrate that neglecting charge effects from $\nabla \cdot \boldsymbol{E} \neq 0$ for dielectric haloscopes is indeed justified.

Armed with this general understanding, we will describe major changes on the power boost factor from 3D effects expected for MADMAX haloscopes with ideal dielectric disks in section 8.3.3. This will lead to important design parameters for the optical system of MADMAX. Afterwards, we consider non-ideal boosters and obtain central requirements for the experimental design such as the required transverse magnetic field homogeneity, allowed disk tilt or roughness, in section 8.4.

At the end, in section 8.6, we will expand on these findings by surveying the possibility of calibrating the boost factor using reflectivity measurements on the booster.

8.1 Axion-Induced Field in Free Space

As we have argued in section 6.2, it is easy to see that the axion-induced field $\boldsymbol{E}_a$ in equation (2.3) approximately solves the wave-equation (6.1) in free space, since in the case when $\boldsymbol{J}_a$ changes over length scales much larger than a wavelength the derivative terms in the wave-equation are negligible. In this section we explicitly show the validity of this approximation using FEM. This will also allow us to survey the numerical error of the FEM solvers.

Specifically, with free space we refer to a vacuum domain, only containing CDM axions and a static magnetic field. More precisely we assume that the external magnetic field $\boldsymbol{B}_e$ changes over scales larger than the Compton wavelength of the axion, which suppresses effects due to the inhomogeneity of the B-field [122]. In practice it is only possible to set current densities inside the simulation domain of a FEM simulation. Setting the external magnetic field to constant over the whole simulation domain, it is still effectively set to zero outside, and therefore has a steep drop at the boundary. In this case the derivative terms in the wave-equation lead to additional axion-induced emissions from the boundary. To avoid these gradient effects, we let $\boldsymbol{B}_e$ smoothly drop to zero towards the boundaries in all our FEM simulations, such that the first derivative at the boundary is zero and the drop stretches over a few λ. Specifically, let us take for now

$$\boldsymbol{B}_e(\boldsymbol{x}) = \sin^2\left(\frac{\pi x}{L_x}\right)\sin^2\left(\frac{\pi y}{L_y}\right)\sin^2\left(\frac{\pi z}{L_z}\right)\hat{\boldsymbol{e}}_y, \tag{8.1}$$

inside the simulation domain $[0, L_x] \times [0, L_y] \times [0, L_z]$, with $L_x = L_y = 9\lambda$, $L_z = 20\,\mathrm{cm} \approx 6.7\lambda$ and zero outside at a frequency of $\nu = 10\,\mathrm{GHz}$. For simplicity we have chosen the external B-field in equation (8.1) such that it is non-physical, i.e., it has a small divergence $\nabla \cdot \boldsymbol{B}_e \neq 0$.

The full analytical solution for this situation has been deduced from our collaborators using the theory of retarded potentials [10, 123, 159]. Here one starts again with the axion-induced field as a first estimate of the solution. Now, instead of neglecting the derivative terms in the wave-equation, they can then be treated as source terms for additional electromagnetic radiation emitted from places of strong gradients ('radiative correction').

We show a comparison between the results from different methods in figure 8.1. The retarded potential solution gives the fields shown in (a) as explicitly been obtained by [10]. Notice that by eye the electric fields approximately follow the same $\sin^2$ spatial dependency than the external magnetic field in equation (8.1). Figure 8.1 (b) shows the radiative correction, obtained when subtracting the axion-induced field from the full analytic solution. Although the external magnetic field drops only over a few photon wavelengths, the radiative correction is about two orders of magnitude smaller than the axion-induced field. This explicitly confirms that assuming a constant magnetic field for haloscope experiments is valid as long as the magnetic field only drops over large length scales. The 1D models, as well as the Recursive Fourier Propagation and Mode Matching methods in this thesis make use of this assumption. Comparing the axion-induced field with our FEM result using Elmer, as described below, leads to the same conclusion.

We show the subtraction of the analytical solutions from the results obtained from our collaborators in COMSOL in figure 8.1 (c) [10] and the same but for our result using Elmer in figure 8.1 (d). In addition to COMSOL and Elmer using different meshes, we further verify the independence on the chosen absorbing boundary condition by using different boundary conditions for the two solvers, i.e., impedance boundary conditions in Elmer and PML boundary conditions

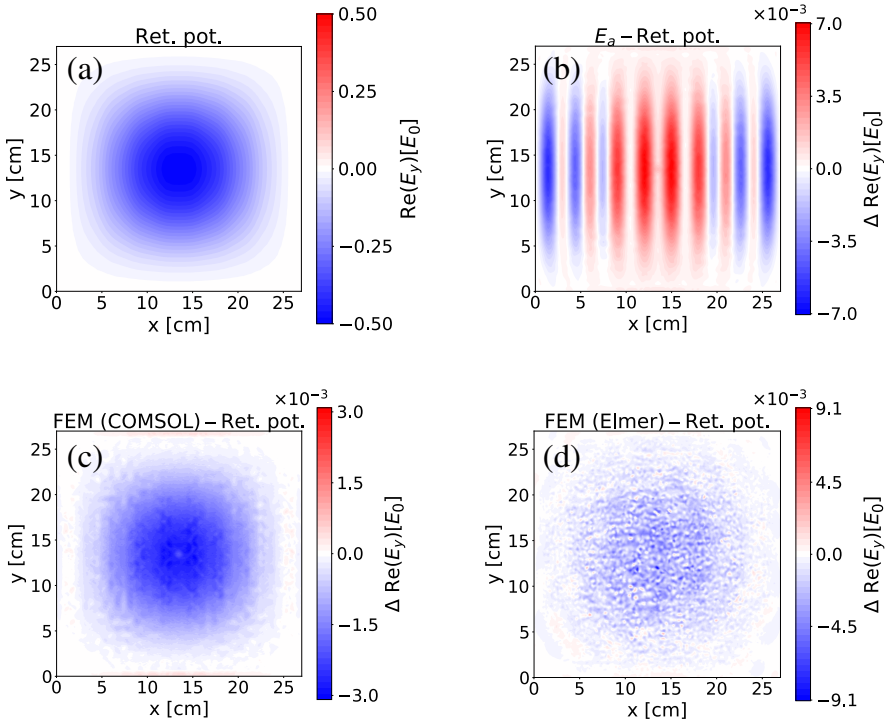

Figure 8.1: Assuming a CDM axion background field for $m_a \approx 40\,\mu$eV and an external B-field pointing in y-direction as given in equation (8.1), the real part of the resulting E_y field at $z = 15\,$cm is shown in panel (a) as obtained with the method of retarded potentials (ret. pot.) derived in [10], whereas the other panels show the respective differences to this result. (b) shows the difference of the retarded potential result in (a) to the case when the radiative corrections are neglected, i.e., to the axion-induced field $\boldsymbol{E}_a$ in equation (2.3). (c) shows the difference to the COMSOL simulation from [10] and (d) the difference to our Elmer simulation. The considered simulation domain is a box with $9\lambda \times 9\lambda \times 6.7\lambda$ extent and the frequency of the axion-induced field is 10 GHz as given by the assumed m_a value.

in COMSOL, as introduced in section 6.1. Since the radiative correction shown in figure 8.1 (b) does not reappear, we conclude that both solvers calculated the radiative correction $\sim \mathcal{O}(10^{-3})E_0$ correctly. Even smaller systematics remain, which are most likely attributed to boundary conditions not perfectly resembling free space. While the numerical noise in COMSOL is smaller than the radiative correction, it can be as large as the radiative correction in Elmer thus dominating over other systematics. The order of magnitude of these systematics and numerical deviations is below the percent level and is thus negligible for our purposes. This gives us confidence that our FEM simulation approaches are working as required.

When the distribution of electromagnetic fields is shown in the following, the axion-induced field is subtracted for clarity, such that only in-principle detectable propagating fields remain.

In short. The axion-induced field $\boldsymbol{E}_a$ approximately solves the axion-Maxwell equations in free space situations where the external magnetic field changes over length scales larger than the photon wavelength λ.

8.2 General Dish Antennae

The dish antenna has already been considered in the idealized 1D setup with a PEC of infinite transverse extent [76, 89]. Here, we study a 3D setup with a PEC of finite transverse extent. We later generalize this study to a dielectric disk and a dielectric disk made from two halves glued together. If applicable, we will compare the emitted power with the corresponding result from 1D calculations. In addition, going to 3D now allows us for the first time within this thesis to study diffraction effects of the emitted electromagnetic radiation. Moreover, we will look at changes in the near field of the disk due to charges, i.e., challenge the approximation $\rho = \nabla \cdot \boldsymbol{E} = 0$.

8.2.1 Perfect Mirror

Let us first consider explicitly a circular perfectly electrical conductor (PEC) with a diameter of $\varnothing = 12\,\text{cm} = 4\lambda$ at $z = 0$ within constant external B-field $\boldsymbol{B}_e = B_0 \hat{\boldsymbol{e}}_y$ over the whole PEC at a frequency of 10 GHz. We chose a circular disk diameter which is much smaller than in the planned full size haloscopes such as MADMAX, since smaller diameter for a given axion mass are more prone to 3D finite size effects, which we investigate here.

The total emitted power is trivially given by the size of the PEC. Hence, we begin with a study diffraction effects and then look at near field effects below.

Diffraction

In figure 8.2 we show the emitted electromagnetic radiation in terms of the electric field of the PEC. We compare the results obtained from the FEM solution to Fourier Propagation. Using Fourier Propagation, cf. equation (6.6), one finds for the E-field of the emitted electromagnetic wave analytically [10, 160]

$$E_y(r, z) = E_0 \int_0^\infty e^{i\sqrt{\omega^2 n^2 - k_r^2} z} J_0(r k_r) J_1(k_r R) R \, \mathrm{d}k_r. \tag{8.2}$$

The x and z components of the fields $E_{x/z}$ of the emitted electromagnetic wave are zero, because we assume a constant external B-field over the PEC which is polarized in y direction only. Notice the different color scale in panel (c) of figure 8.2 to make the differences at the $10 - 20\,\%$ level visible. The results show that the Fourier approach can describe the E-field of the propagating electromagnetic wave well in the forward direction. The largest differences at the level of 25 % between the Fourier approach and the FEM solution are at the rims of the PEC.

Taking the limit $z \to \infty$ we can derive the opening angle θ into which the axion-induced signal is radiated. It is typically defined by the first minimum of the diffracted E-field in momentum space, cf. integrand in equation (8.2), which gives [160]

$$\tan\theta \approx 1.22 \frac{\lambda}{2R} \approx 38 \times 10^{-3} \left(\frac{1\,\text{m}}{2R}\right) \left(\frac{40\,\mu\text{eV}}{m_a}\right). \tag{8.3}$$

This angle is indicated as dashed lines in figure 8.2. Although above equation strictly only holds far away from the disk, we see that fields outside this angle are typically below the 10 % level when compared to the axion-induced field. This shows explicitly that diffraction effects decrease with larger radii and axion masses. Therefore, dish antennas and dielectric haloscopes are limited

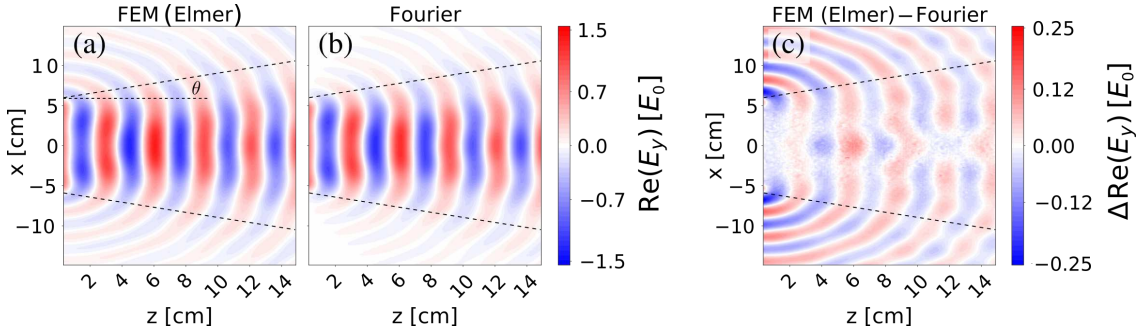

Figure 8.2: Simulated electric fields for a single circular PEC located at $z = 0$ with a diameter of 12 cm in the CDM axion field and assuming an external magnetic field pointing in y-direction. Real part of the y-component of the E-field in the xz-plane at $y = -2.5\,\text{cm}$, at a frequency of 10 GHz, i.e., $m_a \approx 40\,\mu\text{eV}$, corresponding to a wavelength of the propagating electromagnetic fields of 3 cm. (a) shows the FEM solution, where we have subtracted the axion-induced field since we are only interested in the emitted fields described by the Fourier approach. The results from the Fourier approach as explicitly obtained by our collaborators in [10] are shown in panel (b). Panel (c) shows the difference between the results shown in panels (a) and (b). The largest difference is observed at the rims of the circular PEC. The dashed lines indicate the opening angle into which the radiation is emitted as estimated from equation (8.3).

towards lower axion masses by diffraction effects. A more quantitative study calculating the amount of power than can be received by a finite surface at varying distances to the PEC obtained from our collaborators can be found in [3, 10]. It leads to consistent results.

Near Fields

In figure 8.2 we observe that the Fourier approach describes well the far field behavior of the y component of the emitted electromagnetic waves. The difference between FEM and Fourier approach is below 10% in the far field. The largest differences between Fourier approach and FEM are observed at the rims of the circular PEC. Here additional radiation appears on the sides of the PEC. Within this thesis we will refer to the fields not described by the Fourier approach as near fields. For a more complete analytical understanding we have to take into account the vectorial nature of the E-field and boundary charges at the rims of the dish antenna.

The vectorial nature of the emitted E-field was neglected in the scalar Fourier approach by assuming zero net charge $\nabla \cdot \boldsymbol{E} = 0$ in deriving equation (6.6). However, the axion-induced field drives the electrons in the PEC up and down such that at the boundary of the PEC the charges accumulate. This physical picture can be confirmed by explicitly calculating the net charge $\rho = \nabla \cdot \boldsymbol{E}$ from the result of our FEM calculations on the disk surface, as shown in figure 8.3 (left). This charge distribution leads to electric fields also in the x and z components. We show the x component of the electric field at $z = 10\,\text{cm}$ in figure 8.3 (right). The characteristic cross-pole field pattern can be understood when one imagines an E-field pointing from the positive charges towards the negative charges. For example, the x-component of the electric field is 0 along the axis $x = 0$ since the charge distribution is symmetric when mirrored at this axis. At a distance of 10 cm also this effect is at the 10 % level compared to E_0.

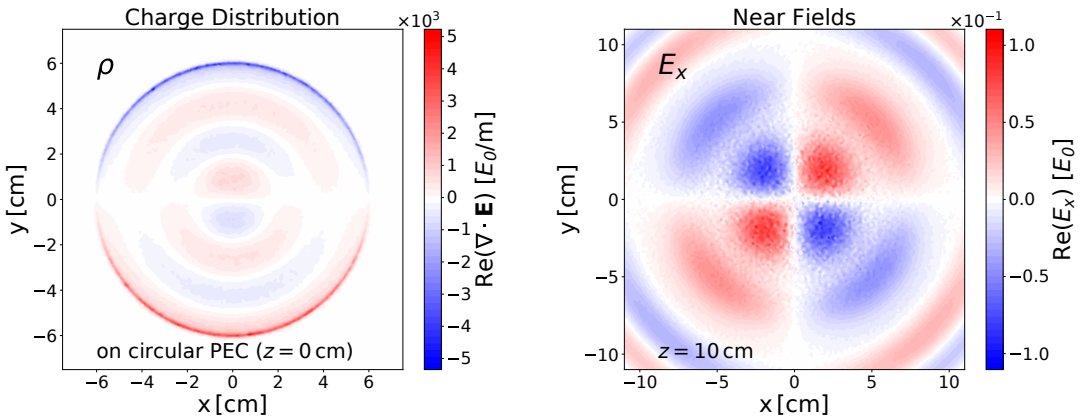

Figure 8.3: Near field effects of a single circular PEC with diameter of 12 cm obtained with a FEM simulation (Elmer), at 10 GHz, i.e., $m_a \approx 40\,\mu$eV, and external magnetic field pointing in y-direction. **Left:** Charge distribution on the circular PEC. **Right:** E_x fields 10 cm $\approx 3.3\lambda$ from the circular PEC away.

The effects from allowing $\nabla \cdot \boldsymbol{E} \neq 0$ are taken into account in more sophisticated analytical solutions, given by the *vector Kirchhoff diffraction formula* [143] and *Stratton-Chu formula* [161]. Comparing the FEM results to these analytical solutions, also the x and z components of the electric field can be described. For an explicit comparison from our collaborators cf. [10].

In dielectric haloscopes like MADMAX near field effects and boundary charges may be important, because the dielectric disks are typically separated by a distance of around half a wavelength. However, observe that the charges mainly appear at the rims of the disk, where the fields of the first few eigenmodes of a corresponding dielectric waveguide with the same diameter would drop to approximately zero, i.e., not excite those charges. The influence of the near fields and boundary charges among diffraction in the context of a minimal dielectric haloscope is discussed more closely in section 8.3.

In short. Simulations confirm that diffraction effects for a dish antenna scale inversely with the size of the dish antenna and axion mass, as expected. In addition, charge accumulating at the rims of the dish causes additional electromagnetic wave emissions from the rims (near fields).

8.2.2 Dielectric Disk

The most simple setup containing more than one boundary between media with different dielectric constants ϵ is a dielectric disk. In this section we assume a circular disk of a diameter of $\varnothing = 4\lambda = 12$ cm, dielectric constant $\epsilon = 9$ (sapphire) for varying thicknesses d_ϵ. First, we compare the total emitted power, reflectivity and transmissivity of a dielectric disk in FEM directly with the 1D model. Analogous to the previous section, we aim for understanding diffraction and near field effects by compare the diffraction pattern of the dielectric disk obtained from FEM and Recursive Fourier Propagation.

Boost Factor and Reflectivity

For a single dielectric disk the emitted axion-induced power, reflectivity and transmissivity are the primary output of the 1D model. Comparing those to the 3D results thus directly tests the validity of the 1D model when going to 3D and disks with finite sized transverse extent. Note that while we are mostly interested in the axion-induced power, the reflection or transmission of a test signal may be used to calibrate the correct alignment of the setup, cf. section 8.6 and part IV of this thesis.

For the reflection and transmission coefficients, a Gaussian beam as introduced in section 6.4 with a beam waist of $w_0 = 5\,\mathrm{cm}$ focused on the front surface of the dielectric disk was assumed. In Elmer the Gaussian beam was forced to propagate into the system by using the Robin boundary conditions from equation (6.2) and setting g such that the Gaussian beam fulfills the boundary condition. The respective power is obtained by integrating the flux $\int \bar{\boldsymbol{S}} \cdot d\mathbf{A}$ at the front and back simulation domain boundaries, where $\bar{\boldsymbol{S}}$ is the time averaged Poynting vector. Numerical errors can be evaluated by varying the integration surface and are below one percent of the maximal output power. A few percent of power is radiated to the outside of the finite integration surface in the 3D FEM simulations. We estimate this non-captured power with the Fourier approach and correct the obtained values respectively.

We compute the emitted axion-induced power (power boost factor β^2) in full 3D with Elmer. Corresponding COMSOL result was obtained by our collaborators [10]. While Elmer solves the vectorized Helmholtz equation in 3D, azimuthal symmetry is exploited in COMSOL (2D3D approach), see section 6.1. Figure 8.4 shows the different emitted powers against disk phase depth $\delta_\epsilon = n\omega d_\epsilon$ compared with the 1D model result. The results agree within 10% with the 1D model. Figure 8.5 shows reflectivity and transmissivity which are within 5% of the 1D model results. Similar results are obtained for the phase of the emitted fields.

As we deliberately choose a small disk diameter of only two wavelengths, if deviations from the 1D model are to be found at all, they would be found at small diameter close to a photon wavelength λ. Diffraction will cause phase shifts inside the disk compared to the 1D case and power loss to the sides, while the near fields of each surface may directly affect the emission from the other surface. The approximate match even for a disk with 4λ diameter is encouraging, since haloscope experiments like MADMAX aim for much larger disk radii. For disks with $R \gg \lambda$ one expects these effects to be less dominant as demonstrated in the previous section.

Diffraction

We use Recursive Fourier Propagation introduced in section 6.2 to compute the diffraction pattern of a single dielectric disk. Figure 8.6 shows the diffraction patterns at 10 GHz ($m_a \approx 40\ \mu\mathrm{eV}$) for a circular dielectric disk with a diameter of $\varnothing = 4\lambda = 12\,\mathrm{cm}$, $\epsilon = 9$ and a thickness of $d_\epsilon = 5\,\mathrm{mm}$, i.e., a phase depth of $\delta_\epsilon = \pi$. We compare the result for the real part of the E_y-field obtained with the full 3D FEM with the one from Recursive Fourier Propagation for $N = 25$ iterations. This particular result was obtained with a specific implementation for a single disk from our collaborators [10]. We find that the simple propagation approach matches the fields far away from the disk well, analogous to the result obtained previously for a perfect mirror in section 8.2.1. In the region around the rims of the disk we find the largest discrepancies. As we have seen already

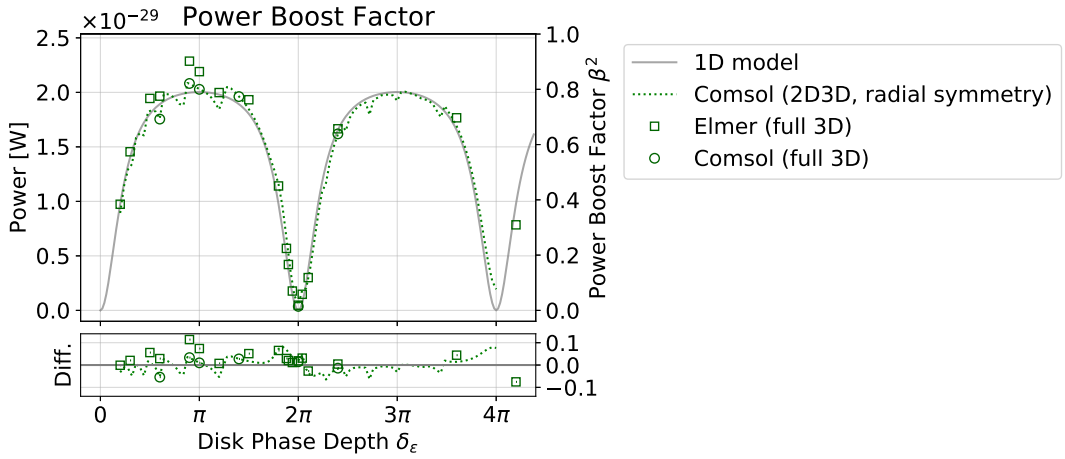

Figure 8.4: Power boost factor β^2 of a single dielectric disk against disk phase depth $\delta_\epsilon = n\omega d_\epsilon$ where d_ϵ is the disk thickness. We consider a single circular dielectric disk with diameter $\varnothing = 4\lambda$, $\epsilon = 9$, at 10 GHz, i.e., $m_a \approx 40\,\mu$eV, assuming $|C_{a\gamma}| = 1$ and $B_e = 10\,$T. We show the power obtained in Elmer (squares) and COMSOL (circles) in 3D and by using 2D azimuthal symmetry in COMSOL (green dotted line), compared with the result from the 1D model (solid gray line). The COMSOL results have been obtained by our collaborators, see [10]. The lower panel shows the difference with respect to the 1D model result in terms of power boost factor β^2. Numerical uncertainties are on the percent level and thus smaller than the size of the data points.

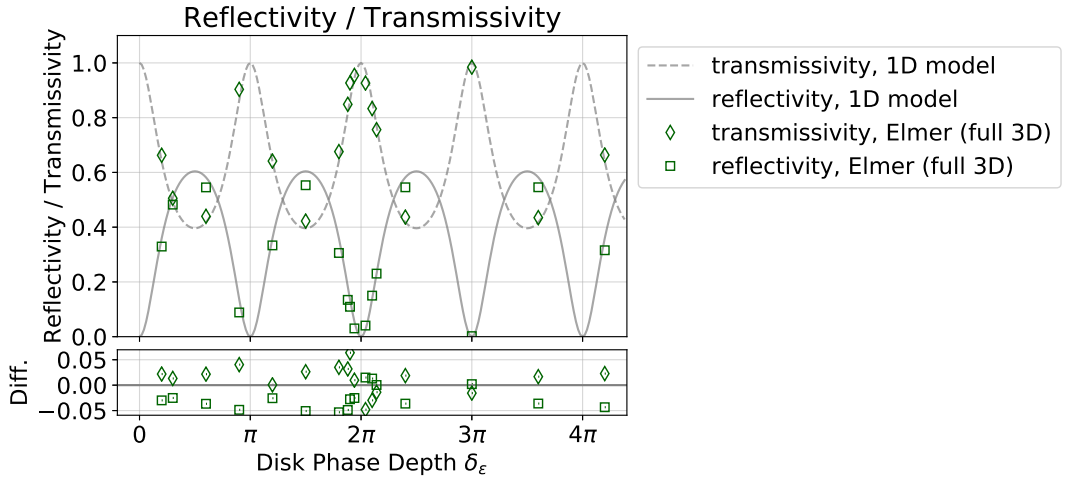

Figure 8.5: Reflectivity (squares) and transmissivity (diamonds) of a single dielectric disk against disk phase depth $\delta_\epsilon = n\omega d_\epsilon$ where d_ϵ is the disk thickness, analogous to figure 8.4. These results are obtained with Elmer for a Gaussian beam with waist $w_0 = 5$ cm at the disk. The reflectivity from the 1D model is indicated by solid gray line and the transmissivity from the 1D model by the dashed gray line. The disk is transparent for phase depths of integer multiples of π. The lower panel shows the respective differences with respect to the 1D model result. The lower panel shows the difference with respect to the 1D model result in terms of power boost factor β^2. Numerical uncertainties are on the percent level and thus smaller than the size of the data points.

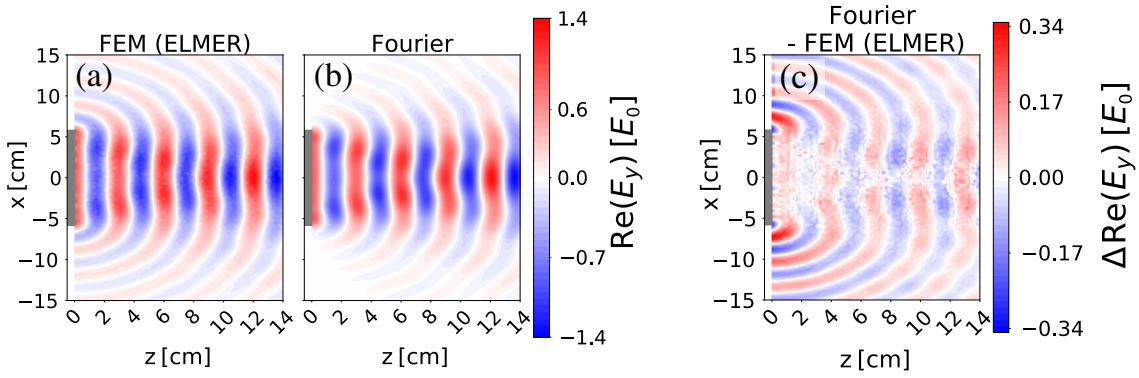

Figure 8.6: Real part of the E_y-field for a circular dielectric disk with $\epsilon = 9$ and phase depth $\delta_\epsilon = \pi$, i.e., with thickness $d_\epsilon = 5\,\text{mm}$ at 10 GHz, i.e., $m_a \approx 40\,\mu\text{eV}$ for an external magnetic field pointing in y-direction. We show the fields in the xz-plane, analogous to the case of a PEC in figure 8.2. Panel (a) shows our FEM solution after subtraction of the axion-induced field, panel (b) the result obtained with the recursive Fourier propagation approach for $N = 25$ iterations as explicitly obtained by our collaborators in [10], and panel (c) the difference between (a) and (b).

in the previous section, this can be understood in terms of the charge distributions at the rims of the disk neglected by the Recursive Fourier Propagation. In addition, the disk has an interface to vacuum also at its rims. Therefore, it emits axion-induced radiation in radial directions at angles where the interface of the rim gets parallel to the external magnetic field. We thus can conclude, that there exist additional near fields at the 30 % level compared to the axion-induced field around the rims of the disks. We will discuss their impact on dielectric haloscopes later in section 8.3.3.

In short. The power emitted from a dish antenna consisting of a dielectric disk with a diameter of four photon wavelength approximately matches the expectation from 1D calculations. The spatial distribution of the emitted field reveals analogous diffraction and near field effects as observed for the mirror in the previous section.

8.2.3 Tiled Disk

To obtain sufficiently large disks for dielectric haloscopes like MADMAX one approach is to glue many smaller patches of dielectric material together. Here we aim for studying their impact the emitted power, diffraction patterns and near field effects studied in the previous sections.

Due to the non-trivial geometry such a change of boundary conditions has only been studied with FEM within this thesis. We consider circular disks with a diameter of $\varnothing \approx 6.7\lambda \approx 20\,\text{cm}$ and a slit with a width of $\lambda/10 = 3\,\text{mm}$, cf. figure 8.7. For MADMAX first dielectric disks have been glued together with much narrower slit widths [162], i.e., the value we assume is conservative. We explore the cases of a PEC and a sapphire disk with a vacuum slit, as well as a sapphire disk with a slit filled with a epoxy. The dielectric constant of the epoxy was taken to be $\epsilon = 5$, which is around the expected value for example for *Stycast 2850FT* [163], and $\tan\delta = 10^{-3}$. For each of these cases we consider slits parallel and orthogonal to the polarization of the axion-induced field $\boldsymbol{E}_a$. We choose to place the horizontal (vertical) slit not exactly in the center of the disk but slightly displaced such that its lower edge (its left edge) lies at the center of the disk. This means

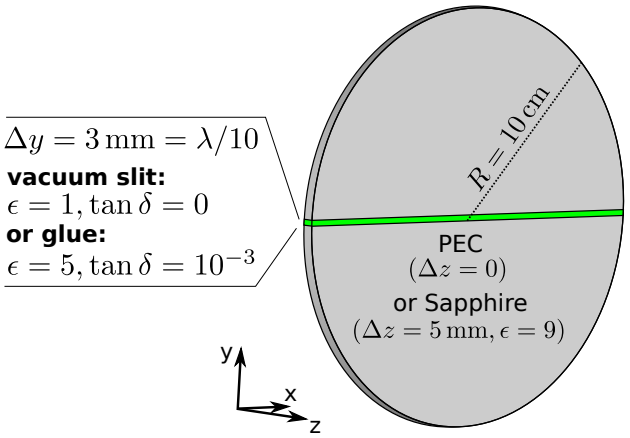

Figure 8.7: Case definition for simulations with tiled disks. We consider either an infinitesimal thin PEC or a $\lambda/(2n) = 5\,\mathrm{mm}$ thick sapphire disk, each with a vertical/horizontal slit filled with either vacuum or glue with $\epsilon = 5$ and $\tan\delta = 10^{-3}$ inside an external magnetic field pointing in y-direction.

that the disk is not separated symmetrically to break possible degeneracies due to symmetry.

Boost Factor

Figure 8.8 shows the calculated power emitted by the various tiled disks introduced above compared to the powers emitted by an untiled PEC and by an untiled sapphire disk, as obtained with Elmer in 3D. We first compare the Elmer results for the power output of the untiled PEC/disk to corresponding results from the 1D model and observe deviations at the 10% level as in the previous section in figure 8.4. As discussed above, they are likely attributed to diffraction and near field effects. Since we use the same mesh and solver for all tiled disk cases considered here, systematics numerical uncertainties are expected to be the same for all compared tiled disks. Therefore, comparing them to each other is valid although the absolute deviation from the 1D model result is larger.

Now turning our attention to the comparison between the various tiled disks, note that the slit considered here reduces the surface area emitting axion-induced electromagnetic waves by $\approx 2\%$. This seems to lead to a power-reduction of around the same order compared to the untiled disks as can be seen in figure 8.8. For the sapphire disk with a horizontal glue filled slit the power is not significantly reduced because the surface of the dielectric glue ($\epsilon = 5$) emits electromagnetic waves as well. However, if the slit with the glue is placed parallel to the applied external magnetic field, the boundary condition on the electric field between the glue and the sapphire may constrain possible propagation modes, inhibiting the emission again.

Notice that the results indicate no additional adverse effects on the emitted power rather than from the area reduction, as one may suspect from additional diffraction or near field effects described below. This is encouraging, since a reduction of emitted power at the order of the relative area covered by gluing slits would not significantly affect the experimental sensitivity, even for multiple slits.

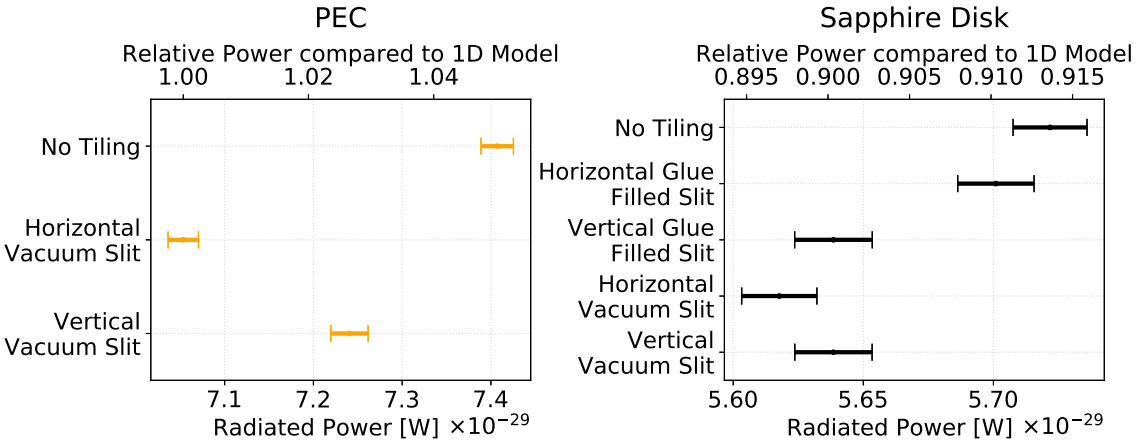

Figure 8.8: Power emitted from untiled disks compared to various different tiled disks, at 10 GHz, i.e., $m_a \approx 40\,\mu\text{eV}$, assuming $|C_{a\gamma}| = 1$ and an external magnetic field $B_e = 10\,\text{T}$ pointing in the y-direction (vertical). The power deviation from the untiled disks roughly matches the naive expectation from the reduction of the size of the emitting surface area of around 2%.

Diffraction

Besides the amount of total power emitted by the disk, it is important to consider the direction into which this power is emitted. This determines how it can be received in the case of a dish antenna and how it will propagate within a dielectric haloscope.

Figure 8.9 shows the diffraction pattern of the studied tiled dielectric disks in comparison to the one of an untiled disk in terms of the total Poynting flux in z-direction at a distance of $z = 7.5\,\lambda$ away from the dielectric disk. The patterns are shown at a distance of $7.5\,\lambda = 22.5\,\text{cm}$ away from the disk in the polarization direction of the axion-induced field $\boldsymbol{E}_a$. The slight asymmetries reflect that the gluing position is not exactly in the center of the disk as mentioned above. More importantly, the diffraction pattern is suppressed with respect to the untiled case by $\approx$ 20% at low radii.

At large distances different transverse momenta separate spatially, since they propagate at different angles away from the disk. Therefore, the reduction of the diffraction pattern at low radii indicates that low transverse momenta k_x, k_y are suppressed by the tiling. It is consistent with the naive expectation that a slit or gluing spot in the disk inhibits large transverse wavelengths, corresponding to aforementioned low momentum modes. Note that it is not trivial to implement these effects in the Recursive Fourier Propagation method for the diffraction patterns presented above, since now the 3 regions of the disk (upper half, lower half and glue) have to be treated separately with appropriate boundary conditions.

Due to the dispersion relation, cf. equation (6.7), such a suppression of low traverse momenta, effectively increases the longitudinal momentum of the propagating wave in a dielectric haloscope. Therefore, a change due to tiling might cause an additional phase shift compared to the 1D model, which may affect the boost factor. In addition, if the power is radiated at higher transverse momenta, this increases the diffraction loss. Lastly, it obviously changes the beam shape within the dielectric haloscope, which has implications on antenna design.

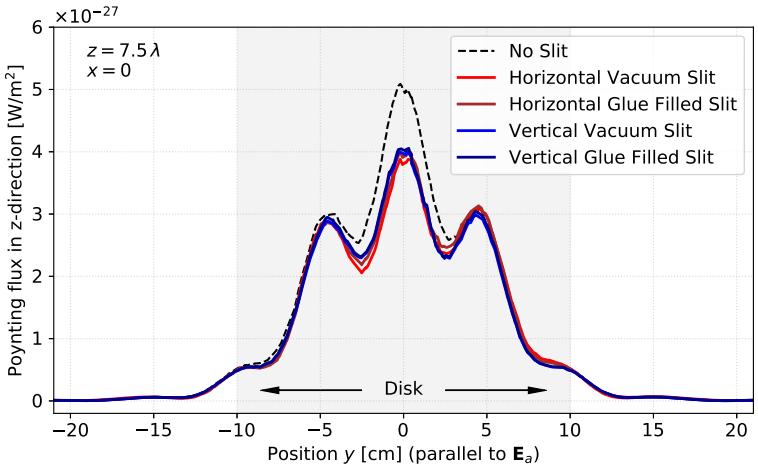

Figure 8.9: Diffraction pattern in terms of Poynting flux along z-direction of different tiled sapphire disks compared to an untiled sapphire disk at a distance $z = 7.5\,\lambda = 22.5\,\text{cm}$, at 10 GHz, i.e., $m_a \approx 40\,\mu\text{eV}$, assuming $|C_{a\gamma}| = 1$ and an external magnetic field $B_e = 10\,\text{T}$ pointing in the y-direction (vertical) as obtained with Elmer. The gray area indicates the extent of the dielectric disk ($\varnothing \approx 6.7\lambda \approx 20\,\text{cm}$).

Near Fields

Figure 8.10 shows the effect of the tiling on the polarization charges of a dielectric disk. It is apparent that the polarization charge distributions over the whole disk become asymmetric just due to the small asymmetry of the tiling. These asymmetries mainly manifest in different surface wave patterns on both sides of the disks seen as spatial oscillations of $\rho = \nabla \cdot \boldsymbol{E}$. This again may impact the emitted wave from a tiled disk in momentum space, as discussed in the previous section. In addition, we see additional polarization charge accumulations along the slit when the disk is horizontally separated, just as naively expected. The effects of these additional charge accumulations cancel out in the far field but may contribute to the near fields of the disk. In the case of a glue filled slit these changes are more moderate due to the smaller difference in dielectric constant. The effect of tiling is expected to be less relevant for larger disks with larger tiles.

In short. Tiling reduces the emitted power of a dielectric disk consistent with the expected amount from reducing the surface area of the dielectric disk. It further changes the diffraction pattern, suppressing lower transverse momenta at the order of $\sim 20\%$ in our example, as well as near fields due to additional net charge near the slit between tiles.

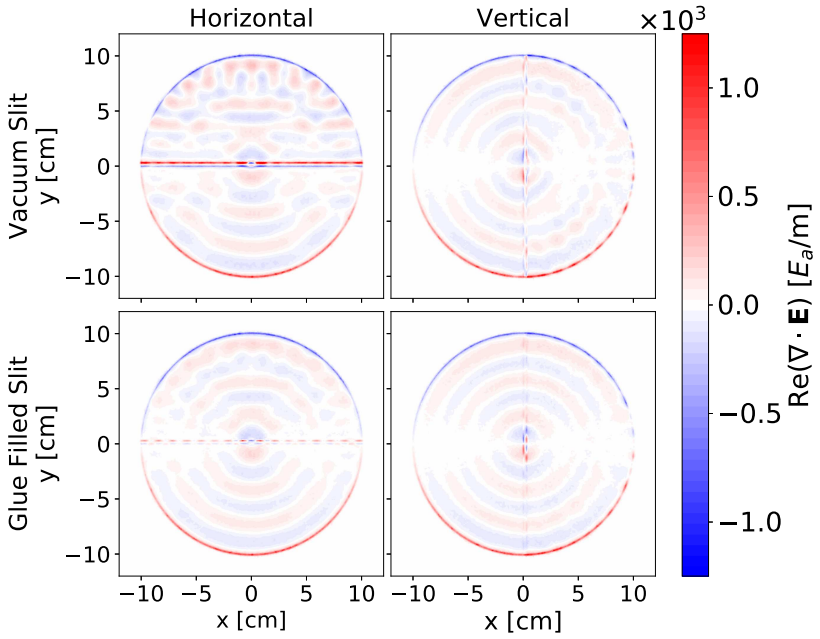

Figure 8.10: Polarization charge distributions $\rho = \nabla \cdot \mathbf{E}$ on various tiled sapphire disks (horizontal/vertical slit filled with vacuum/glue) with diameter $\approx 6.7\lambda \approx 20\,\text{cm}$, at 10 GHz, i.e., $m_a \approx 40\,\mu\text{eV}$, for an external magnetic field pointing in y-direction. The small asymmetry induced by the slit affects mainly surface wave propagation.

8.3 Idealized Boosters

In the previous sections we have studied the axion-induced electromagnetic emission from a mirror and a circular dielectric disk separately in the presence of a strong external B-field. In this section we will make the step to dielectric haloscopes, first combining a single dielectric disk and a mirror and later extending our study to full scale boosters like foreseen for MADMAX.

8.3.1 Eigenmode Approximation

In the end of section 6.3 we have argued that the eigenmodes of a dielectric disk are also approximate eigenmodes of an (ideal) dielectric haloscope (eigenmode approximation). In practice this means that for an ideal system each eigenmode propagates independently from each other throughout the whole booster. The numerical results we present hereafter, indeed do not rely on this approximation. However, it is very helpful to understand the behavior of ideal finite-size boosters in 3D. Thus, in this section we will explicitly verify this approximation. Here we consider only an ideal booster with perfectly flat, parallel and untiled disks. To obtain the approximate eigenmodes of the booster, indeed all three numerical approaches can be used, as outlined below.

Remember that the booster eigenmodes, as well as their propagation through a single disk or air gap, do not depend on the number disks installed in the dielectric haloscope but only on the transverse boundary conditions of the disks, i.e., their diameter. Thus, the following numerical schemes do not assume a specific disk number.

Mode Matching

The waveguide eigenmodes $E_{m\ell}$ introduced at the beginning of section 6.3 are not eigenmodes of free space. Thus, following the definition of the mode-mixing matrix P in equation (6.15) will lead to non-zero off diagonal elements for the propagation in the free space gaps between the dielectric disks. However, if these off-diagonal elements are small, then the waveguide eigenmodes $E_{m\ell}$ are still approximate free space eigenmodes in the gaps between the disks, and thus eigenmodes of the whole booster. Figure 8.11 shows the absolute values of the entries in the mixing matrix for up to mode $m = 5, \ell = 2$ for the MADMAX prototype (disk diameter $\varnothing = 30\,\mathrm{cm}$). To quantify numerical errors, we show the mixing matrix without any propagation on the left, i.e., the mixing matrix of the set of modes with itself. Analytically it is given by the orthogonality of the modes, i.e., $P_{m\ell}^{m'\ell'} = \int E_{m\ell}^* E_{m'\ell'}\,\mathrm{d}A = \delta_{m\ell}^{m'\ell'}$ and thus fully diagonal. Numerical errors cause off-diagonal entries at the order of $\sim 10^{-5}$. We show the mixing-matrix for $\lambda = 1.5\,\mathrm{cm}$ and propagation through a $\lambda/2$ gap on the right. Due to symmetry we expect the $\ell \neq 0$ modes are not excited. The axion-induced field couples mostly to the modes $m = 1, 2, 3, 4, 5; \ell = 0$, i.e., $\sum_{m\leq 5} |\eta_{m\ell}|^2 > 90\,\%$. For those lower modes the entries $|P_{m\ell}^{m'\ell'}|$ for $(m, \ell) \neq (m', \ell')$, are smaller than $\sim 1 \times 10^{-3}$ (corresponding to $|P_{m\ell}^{m'\ell'}|^2 \sim -60\,\mathrm{dB}$ as in figure 8.11), if only considering couplings between the fundamental mode and any mode $m \leq 5$ it is smaller than $\sim 1 \times 10^{-4}$ ($|P_{m\ell}^{m'\ell'}|^2 \sim -80\,\mathrm{dB}$). For a disk diameter of 1.2 m the mixing between any modes with $m = 1, 2, 3, 4, 5; \ell = 0$ is even smaller than $\sim 2 \times 10^{-5}$ ($|P_{m\ell}^{m'\ell'}|^2 \sim -97\,\mathrm{dB}$).

Of course, it is not sufficient for the mixing to be small. Since we are building a resonator one may expect the mixing effects to be resonantly enhanced at a particular frequency. A mixing

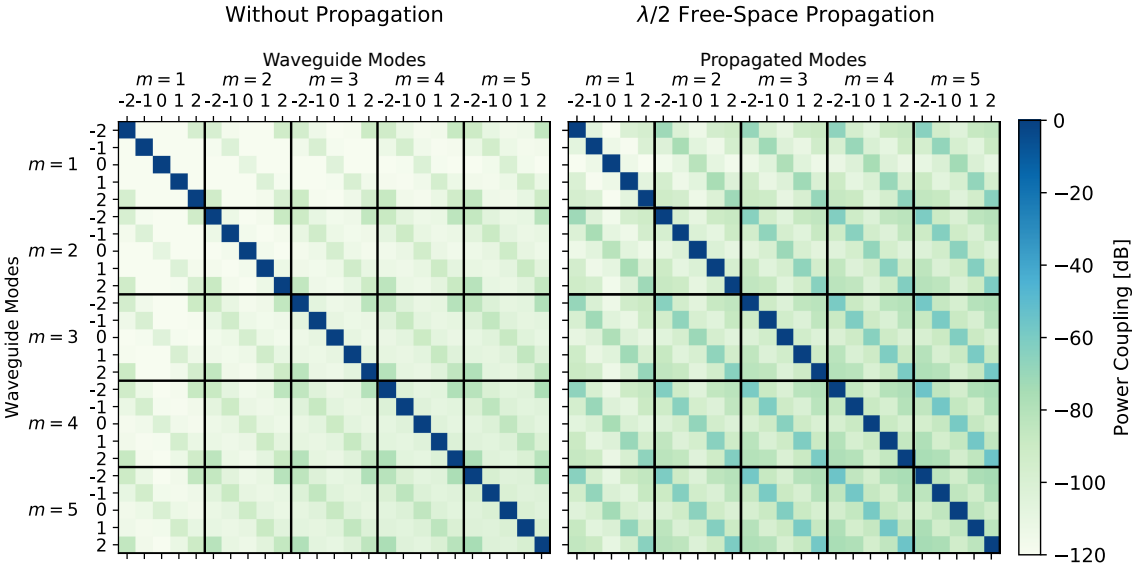

Figure 8.11: Result of a numerical calculation of the mode mixing matrix elements $|P_{ml}^{m'l'}|^2$ for the modes with themselves (left) and after a propagation of $\lambda/2$ in free space (right). For the MADMAX prototype setup, i.e. $\varnothing = 30\,\text{cm}$, and at a frequency of 20 GHz. The sub-blocks are the mixing matrices for a fixed m.

$|P_{m\ell}^{m'\ell'}|$ for $(m,\ell) \neq (m,\ell)$ is comparable to a loss mechanism, since it leads to the diagonal elements to be reduced as $|P_{m\ell}^{m\ell}| \sim 1 - \frac{1}{2}|P_{m\ell}^{m'\ell'}|$. So the effect of $|P_{m\ell}^{m'\ell'}| \neq 0$ can be compared with a $\tan\delta$ of the order $|P_{m\ell}^{m'\ell'}|/\pi$. Comparing with the acceptable loss in section 5.4, we see that the effect of the mode mixing for the ideal system considered here, is indeed negligible for a benchmark bandwidth of 50 MHz.

For the results presented in this thesis using the Mode Matching method, the matrix P is directly implemented as described in section 6.3. Therefore, those results do not rely on the eigenmode approximation, but can be understood in terms of it.

Recursive Fourier Propagation

Using the Fourier Propagation technique, we can actually define an arbitrary beam shape within the booster and monitor it as it would be propagating throughout the booster. In the following we discuss such a calculation and see how it can be used to determine the eigenmodes of the booster. Here we assume that alternating between propagation through free space gaps and disks is sufficient to determine the eigenmodes as described below. Each propagation step then consists of a propagation through one free space region of length $\Delta z = \lambda/2$ and successively propagation through one $LaAlO_3$ disk with a thickness of $\Delta z = 1\,\text{mm}$. A general beam in the booster of course does not strictly alternate between disk and free space, but since it can be reflected from an interface, it can stay inside the same disk or air gap multiple times. We discuss the implications of this simplifications later below. We start with the axion-induced beam shape emitted from a single disk, i.e., a homogeneous field $E(r < R) = \text{const}$.

The result of this approach is shown in figure 8.12. The upper panel shows how the beam shape changes during the propagation through the booster. The middle panel shows the coupling

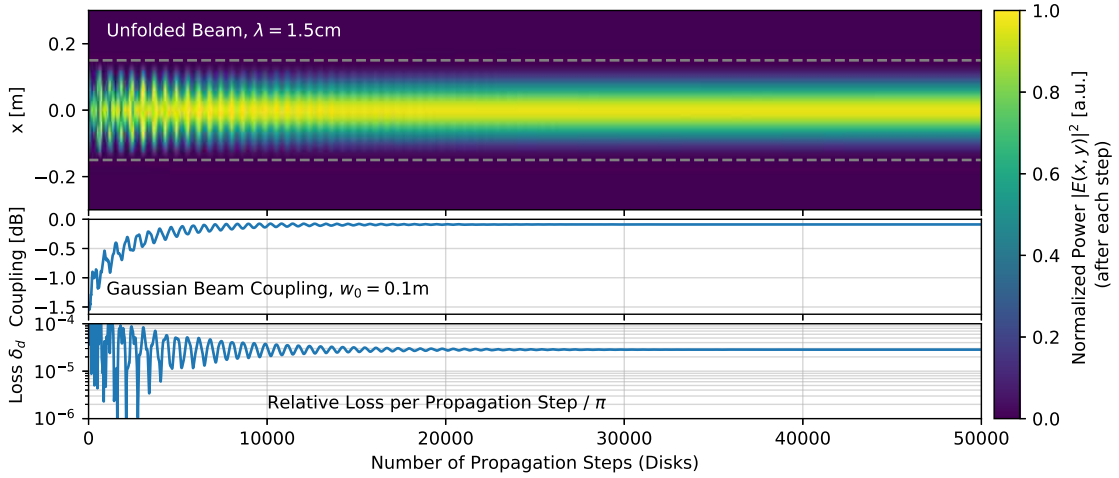

Figure 8.12: Beam propagating in each propagation step though a $\lambda/2$ free space gap and successively through 1 mm dielectric disk at 20 GHz. The upper panel shows the beam shape at $y = 0$ in the xz-plane as a function of propagation steps. It is normalized after each propagation step such that the maximum of the squared electric field is 1, in order to show the change in beam shape. The middle panel shows the coupling efficiency of the beam to a Gaussian beam shape with $w_0 = 10\,\text{cm}$. The lower panel shows the relative power lost in each propagation step over the phase depth between the disks, which directly gives the effective diffraction loss δ_d.

efficiency of the beam to a Gaussian beam with 10 cm beam waist. The lower panel shows the diffraction loss δ_d defined analogous to a $\tan\delta$ as in section 6.3, so it is obtained dividing the relative loss with the phase depth of the free space gap. We can clearly see that after $\sim 20 \times 10^3$ propagation steps the beam shape does not change anymore, i.e., the system maps the beam to itself, which is the definition of an eigenmode. Therefore, we can extract this eigenmode, by simply letting the propagation numerically run until it converges. Notice that the initial beam shape is explicitly not an eigenmode of the system. While the beam shape is still changing during propagation, it is obviously not yet an eigenmode of the system, but can be understood in terms of a coherent sum of eigenmodes. Since the eigenmodes have different diffraction losses, the relative power contained in a certain mode changes during propagation. Therefore, eventually only the eigenmode with the lowest diffraction loss survives.

If we assume that the beam shape is always a coherent sum of eigenmodes, we can extract the other eigenmodes in the following way. Suppose after $\hat{N}$ propagation steps the beam shape is given by the eigenmode $\tilde{m}$, because all other eigenmodes have higher diffraction loss. Then we can decompose the beam shape at previous steps N into a sum of the field of this eigenmode $E_{\tilde{m}}$ and a residual beam shape E_R, such that

$$E(N) = c_{\tilde{m}} E_{\tilde{m}} + E_R(N), \tag{8.4}$$

where $c_{\tilde{m}}$ is a complex number, all fields depend on x and y and $\int dA\, E^*_{\tilde{m}} E_R(N) = 0$. By definition we have $E_R(\hat{N}) = 0$, but at an earlier propagation step the residual beam is then dominated by the eigenmode $\tilde{m} + 1$. It is then given by the residual beam shape after for example half the

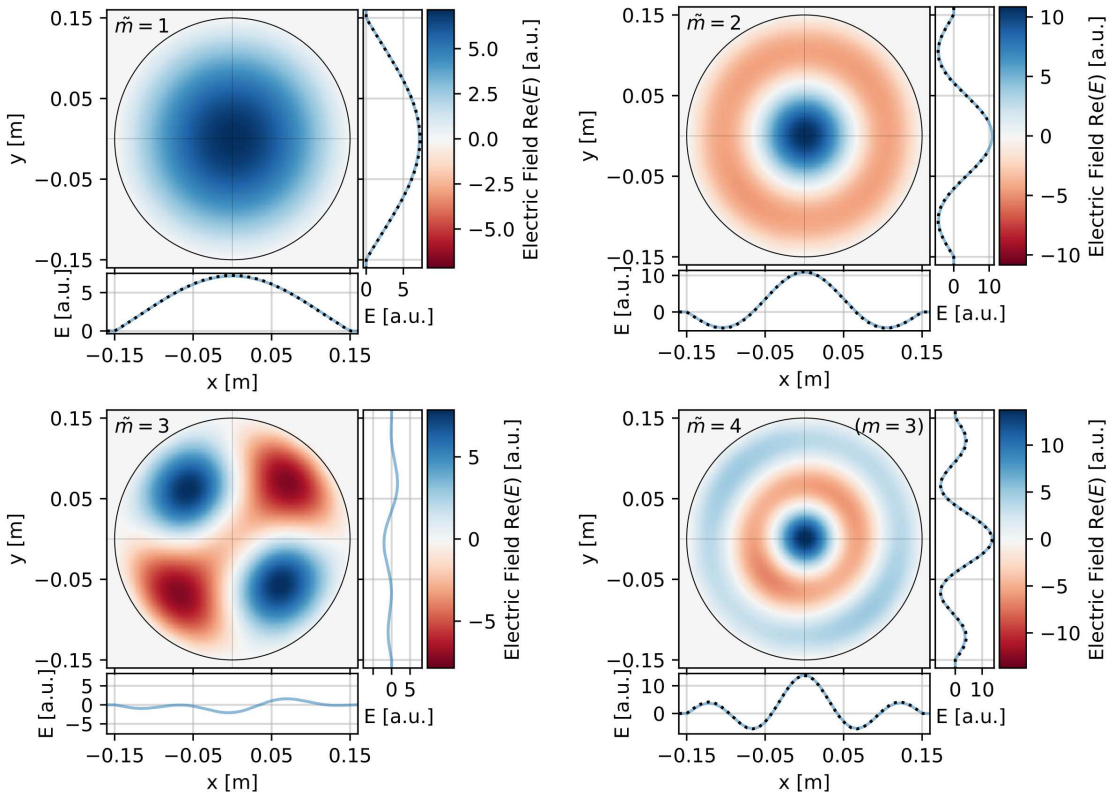

Figure 8.13: Modes obtained using Fourier Propagation. The main panels show the modes $\tilde{m} = 1 \ldots 4$. The sub-panels show cuts along the x- and y-axes. The light blue curve corresponds to the numerical result from Fourier Propagation. The black dotted curve laying on top of the blue curve shows the fields of the corresponding waveguide mode obtained analytically in section (6.3). More details, cf. text.

propagation steps

$$E_{\tilde{m}+1} \equiv \mathcal{N} E_R(\hat{N}/2), \tag{8.5}$$

where $\mathcal{N}$ is a normalization constant. By iterating this procedure we can obtain the relevant eigenmodes of the system.

Figure 8.13 shows the first four modes obtained with this method. The main panels show the electric field distribution of the fields, while the side-panels show cuts along the x and y-axes. We show the modes as light blue lines and compare them with the waveguide modes introduced in section 6 shown as black dotted lines. The latter lay on top of the light blue lines, i.e., the differences are small. To quantify this, we summarize the properties of the modes analogous to table 6.2 in table 8.1. We see that the eigenmodes obtained with this method are mostly consistent with the dielectric waveguide modes. The small differences at the percent level are indeed expected, since we know that the dielectric waveguide modes are only approximate eigenmodes of the booster, as described above. Nevertheless, for sensitivity estimates but in particular also for our qualitative understanding of the system, these differences are small. Notice that the mode $\tilde{m} = 3$ does not exhibit azimuthal symmetry although the disks are azimuthally symmetric. The reason for this

	Axion Coupling	Propagation		Waveguide Mode
Mode	$\lvert\eta\rvert^2$	k_c	δ_d	Matching
$\tilde{m}=1$	71 %	$16\,\mathrm{m}^{-1}$	$\sim 3\times10^{-5}$	99.9 %
$\tilde{m}=2$	13 %	$37\,\mathrm{m}^{-1}$	$\sim 1\times10^{-4}$	99.4 %
$\tilde{m}=3$	3×10^{-5}	$35\,\mathrm{m}^{-1}$	$\sim 1\times10^{-4}$	—
$\tilde{m}=4$	5 %	$57\,\mathrm{m}^{-1}$	$\sim 3\times10^{-4}$	97 %
		...		

Table 8.1: Properties of the most important eigenmodes of a dielectric haloscope with disk diameter 30 cm, as foreseen for the MADMAX prototype, i.e., disk diameter $\varnothing = 30\,\mathrm{cm}$, as obtained with Fourier Propagation. $|\eta|^2$ denotes the coupling of the uniform axion field to the mode, k_c its transverse momentum, and δ_d the diffraction loss parameter between the dielectric disks as defined in the text. The waveguide mode matching is defined as the coupling efficiency between the beam shape of the obtained mode and the dielectric waveguide modes considered in the previous section.

mode to appear here is, that the spatial discretization of the disk happens in Cartesian coordinates. This choice of coordinates breaks the azimuthal symmetry of the disk, i.e., the border of the disk does not correspond to a perfect circle anymore. This causes a small coupling of the uniform axion-induced field to this mode within the simulation. Since the coupling is much below the percent level, it is irrelevant for the boost factor calculations. This also shows that for the lower booster eigenmodes the position of the rim of the disk has to be only exact on length scales of $\sim \lambda/2$ (discretization of the grid for the Fourier Propagation method).

Lastly, we point out that analogous results have been obtained for the eigenmodes of a booster with disk diameter of 1 m. Here the match with the dielectric waveguide modes is an order of magnitude better. In this case the mode breaking azimuthal symmetry ($\tilde{m} = 3$ above) has not been observed. This is expected, since for the $\varnothing = 1\,\mathrm{m}$ disk the spatial discretization at the order of $\sim \lambda/2$ describes the circular shape of the disk much better than for $\varnothing = 30\,\mathrm{cm}$.

At last, let us review the assumptions we have made. Initially we assumed that it is sufficient to alternate between the same free space gap and a disk. This is of course a very specific choice. Therefore the calculation has been repeated using randomized disk spacings and order of disk and free space propagation. The differences in terms of the coupling efficiency between the fundamental mode from this result and the result above are at the permil level. Higher modes are more difficult to extract since the randomization of the steps tends to increases numerical noise. The higher eigenmodes therefore have to be extracted at an earlier propagation step. Extracting the second eigenmode at propagation step ~ 4500, we find that it agrees within 98 % coupling efficiency with the initial result, and for the third eigenmode at propagation step ~ 2300 we find 92 % while here distortions due to numerical noise appear.

Moreover, we assumed that there exist higher eigenmodes $\tilde{m} > 1$, i.e., so far it was only shown that $\tilde{m} = 1$ is an eigenmode. One can show that all extracted modes are in fact approximate eigenmodes by doing the same numerical calculation but starting with the beam shape of an arbitrary mode $E_{\tilde{m}>1}$ and checking that the beam shape is unchanged during propagation. The

way we have extracted the eigenmodes suffers, however, from the fact that at all propagation steps all eigenmodes are still present, but just strongly suppressed with respect to the strongest one. Thus, when extracting an the mode $\tilde{m}+1$, it will contain a strongly suppressed contribution from mode $\tilde{m}$. Therefore, starting with the mode $\tilde{m}+1$, one expects spurious parts of the lower eigenmodes to dominate again after a number of propagation steps. Doing this kind of calculation, indeed reveals that the beam shape remains constant for the higher modes for the expected number of propagation steps. This confirms, that they are indeed approximate eigenmodes of the booster. The error due to this approximation, i.e., the small contribution of other spurious eigenmodes when obtaining a specific eigenmode,

FEM

In FEM we can calculate the fields in specific booster configurations. Above we have observed a beam as it propagates through the booster. We can construct an analogous procedure, which only looks at the output beam of the booster, by considering different boosters from the transparent case to the resonant case and observing how the emitted beam shape changes once one goes to more resonant configurations. If the system is sufficiently resonant, the different propagation constants of the modes shifts the resonance frequencies of the different modes with respect to each other, i.e., only a single mode is resonantly enhanced at a given frequency, with the fundamental mode at the lowest frequency. We present such a calculation with a more detailed explanation for a single disk and mirror ('minimal dielectric haloscope') in the following section.

In short. We have numerically demonstrated that the dielectric waveguide modes introduced in section 6 are approximate eigenmodes of an ideal dielectric haloscope with finite sized dielectric disks.

8.3.2 Single Disk and Mirror

It is instructive to consider a minimal dielectric haloscope consisting of a mirror and a single dielectric disk before going to full-sized dielectric haloscopes with multiple disks. Here we directly compare all three methods introduced in section 6 for the first time. This will allow us to most directly check that near field effects from net charges $\nabla \cdot \boldsymbol{E} \neq 0$ are negligible for ideal dielectric haloscopes. In addition, we will be able to understand the behavior of this haloscope in terms of the eigenmode approximation discussed above.

Boost Factor

Both a single PEC surface (dish antenna) and a single dielectric disk are limited in the amount of generated power. In terms of the boost factor β^2, which describes the emitted power compared to the power emitted by a single PEC in the 1D model, both are limited to be below one. We now turn our attention to dielectric haloscopes with a single dielectric disk and a PEC ('minimal dielectric haloscope'), which can provide already boost factors greater than one.

In order to study how the properties of such a setup change in 3D, let us first recap the basic properties of such a setup in 1D [89]. In figure 8.14 (a) we show a sketch of such a minimal dielectric haloscope. For the further discussion we will use the phase depths $\delta_v = \omega d_v$ and $\delta_\epsilon = n\omega d_\epsilon$, where d_v is the vacuum distance between disk and mirror and d_ϵ the thickness of the disk and $n = \sqrt{\epsilon}$

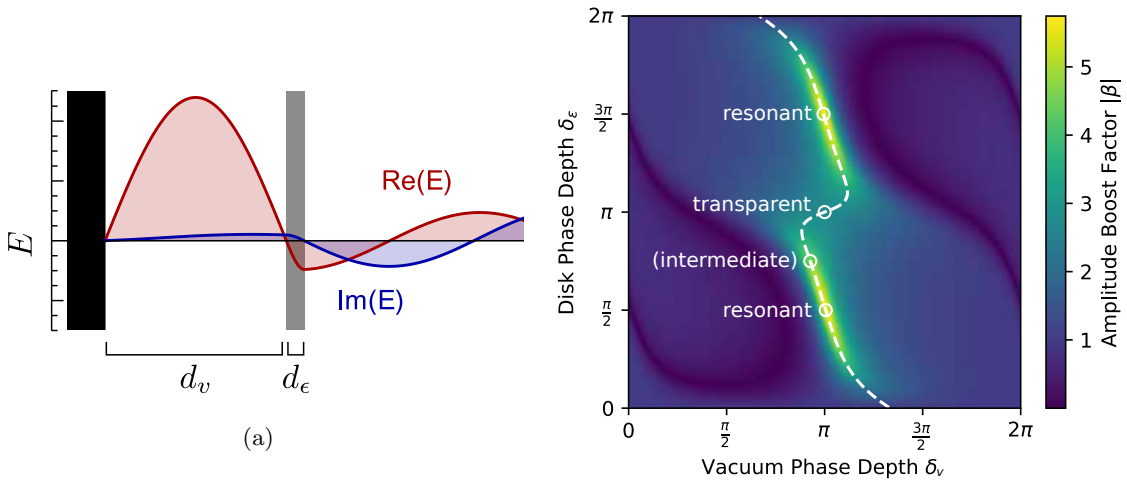

(a) (b)

Figure 8.14: (a) Real and imaginary part of the emitted E-field in a minimal dielectric haloscope setup, which consists vacuum gap with phase depth $\delta_v = d_v\omega$ between a PEC mirror and a dielectric disk of phase depth $\delta_\epsilon = nd_\epsilon\omega$ [89]. (b) Amplitude boost factor $|\beta|$ as a function of δ_v and δ_ϵ for the minimal dielectric haloscope as obtained in the 1D model. We indicate maximally resonant, transparent and intermediate cases as discussed in the main text. The considered 3D simulations sweep along the parameter space indicated by the dashed line, i.e., for each disk phase depth the vacuum phase depth is optimized to obtain the maximal boost factor.

its refractive index. In figure 8.14 (b) we show the boost amplitude from the 1D calculation as a function of δ_v and δ_ϵ, where the white dashed line marks for each δ_ϵ the optimal δ_v such that the boost factor is maximized. As depicted in the figures the optimal phase depth for this setup is around $\delta_v \approx \pi$. Putting the dielectric disk one wavelength further away from the PEC does not change the situation in the 1D model, hence the boost factor is in general periodic and maximal at around $\delta_v \approx \pi + 2\pi n, n \in \mathbb{N}$. $\delta_v \approx \pi$ corresponds to a distance between disk and mirror of $\sim \frac{\lambda}{2}$. In the resonant case ($\delta_\epsilon = \frac{\pi}{2}$ and $\delta_v \approx \pi$) the boost factor reaches its global maximum and the minimal dielectric haloscope is most resonant. This can be understood physically, since for $\delta_\epsilon = \frac{\pi}{2}$ the reflectivity of the dielectric disk is maximal (see figure 8.5). In the transparent case ($\delta_\epsilon = \pi$) the reflectivity of the dielectric disk is zero in 1D, but we still get a boost factor which is larger than one due to constructive interference of the axion-induced emissions from the PEC mirror and dielectric disk. The case at $\delta_\epsilon = \frac{3\pi}{4}$ between resonant and transparent case is denoted as intermediate case in the following.

In the following we will generalize this setup to compute the E-fields and the boost factors for the minimal dielectric haloscope in 3D. The disk and PEC in the considered minimal dielectric haloscope have both a diameter of $\varnothing \approx 6.6\lambda \approx 20\,\text{cm}$. We consider dielectric disks with $\epsilon = 4$ and $\epsilon = 9$. Sapphire disks ($\epsilon = 9$) with this size are actually also used in the proof of principle setup studied in part IV of this thesis. This is smaller than what is envisioned for the MADMAX prototype (30 cm) and final stage experiment (1 m). Here we only consider simulations at 10 GHz ($m_a \approx 40\,\mu\text{eV}$), while the envisioned search range of MADMAX reaches from 10 GHz up to 100 GHz ($m_a \approx 400\,\mu\text{eV}$). The small diameter and frequency considered here are conservative and, as

discussed for the dish antenna in section 8.2.1, diffraction effects for larger radii and frequencies as envisioned in the final MADMAX setup are expected to be less dominant. We performed simulations with all methods introduced in chapter 6. The setup is considered in full 3D in Elmer with two geometries of the surrounding simulation domain in order to check the consistency of the results when changing the domain. Geometry I uses a simulation domain with a size $L_x, L_y \sim 25\lambda$, $L_z \sim 12\lambda$ and geometry II with size $L_x, L_y \sim 17\lambda$, $L_z \sim 20\lambda$, i.e., the second domain is more narrow in x and y-direction but also more long in z-direction. In addition, we consider the 2D3D FEM result making use of azimuthal symmetry from our collaborators [10]. The simulations using Recursive Fourier Propagation have been done with $N = 200$ iterations. In the Mode Matching method we take into account modes until $\hat{m} = 10$ while it is not necessary to consider any mode breaking azimuthal symmetry, i.e., $\hat{l} = 0$.

In figure 8.15 we compare the boost factor from the 1D model to the 3D calculations. Specifically, we show the boost factor as a function of δ_ϵ, while each δ_ϵ has previously been optimized in the 1D model to maximize the boost factor. The comparisons are done for three different situations corresponding to two different refractive indices $n = 4$ and $n = 9$ and two different vacuum phase depths $\delta_v \approx \pi$ and $n \approx 3\pi$. In all situations the 3D calculations show a boost factor reduction with respect to the idealized 1D calculation as expected. We find the largest boost factor reduction for the resonant cases, i.e., at $\delta_\epsilon = \frac{\pi}{2}, \frac{3\pi}{2} \cdots$ to be around 25 % for a sapphire disk. In these cases the reflectivity of the dielectric disk is maximal (see e.g. figure 8.5) which makes the system more resonant. While going to more resonant configurations, dephasing effects from the different phase velocities of the modes become more dominant. Thus the resonant enhancement in the sense of the power boost factor does not happen for the higher booster eigenmodes which have a longitudinal momentum not matching the resonance condition. This leads to the observed reduction in the power boost factor compared to 1D. Comparing the simulations for $\epsilon = 9$ and $\epsilon = 4$, we see that in the latter case the power reduction is less dominant, which is expected since a dielectric disk with $\epsilon = 4$ has a smaller reflectivity than a disk with $\epsilon = 9$ and therefore makes the system less resonant. Comparing further the $\epsilon = 4$ cases with $\delta_v \approx \pi$ and 3π, we see that the power boost is reduced for the larger vacuum gap. This is only evident from the 3D solutions and not from the 1D solution, where the power boost is the same. Since an electromagnetic wave traveling for some distance is diffracted over a larger area if the distance is increased, cf. section 8.2.1, the larger (3π) gap between disk and mirror leads to more diffraction losses in the system as expected.

Let us now discuss the comparison between the various 3D methods in figure 8.15. We first consider the results from the diffraction-only calculations neglecting boundary charge effects. The results from Mode Matching are shown as red dashed lines and the results from Recursive Fourier Propagation as yellow dashed lines. While for $\epsilon = 9$ both results are consistent on the percent level, the Mode Matching method typically predicts around $\sim 5\,\%$ less emitted power for $\epsilon = 4$. This is expected from higher modes not taken into account by the calculation. The sum of the coupling efficiencies of the first ten modes to the axion-induced field is 96 %, compatible with the observed differences. When going to more resonant systems ($\epsilon = 9$) this effect disappears, since higher modes are not resonant anymore. In fact, we will see that for the MADMAX boost factors considered in the next section it is sufficient to consider modes up to $\hat{m} = 5$.

We now turn our attention to the results from the full 3D calculations including the boundary charges. The full 3D COMSOL result which has been obtained from our collaborators by making

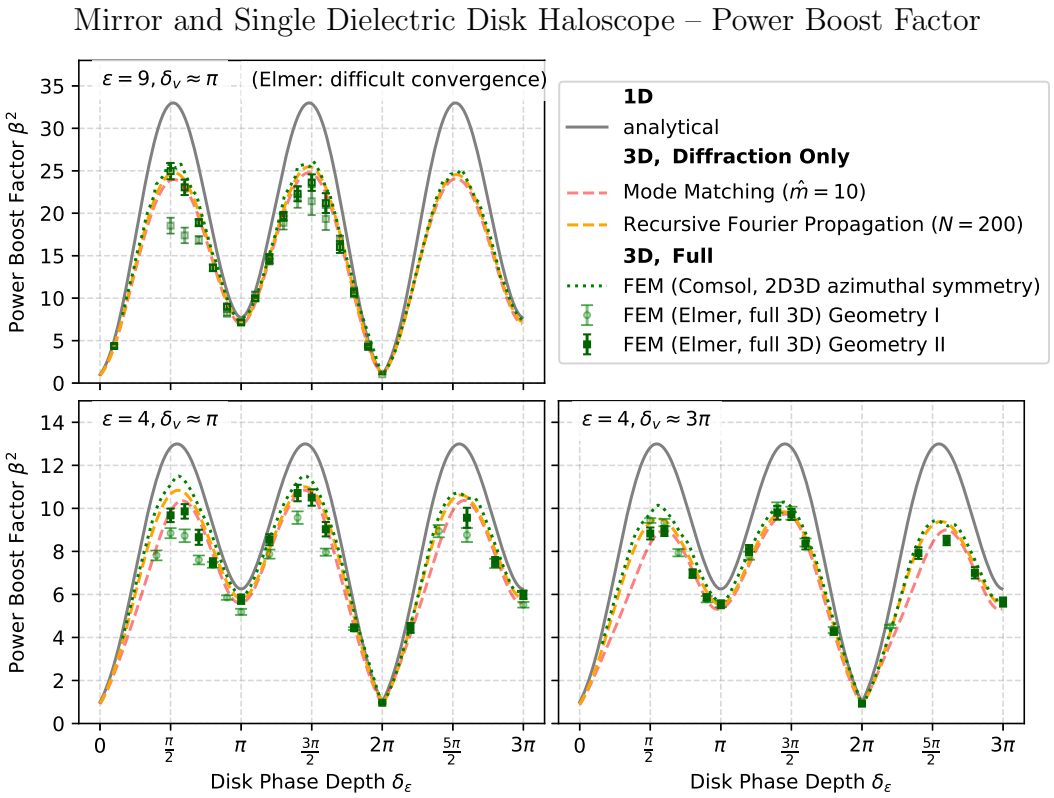

Figure 8.15: Power boost factor β^2 as a function of the disk phase depths $\delta_\epsilon = \omega n d_\epsilon$ for the minimal dielectric haloscope shown in figure 8.14 at 10 GHz ($m_a \approx 40\,\mu$eV) and for $\epsilon = 9$ (top) and 4 (bottom). The disk is considered at vacuum phase distances to the PEC mirror of $\delta_v \approx \pi$ (left) and 3π (right) at which β^2 is maximized in the 1D model. Both disk and PEC mirror have an identical diameter of $\varnothing \approx 6.7\lambda \approx 20$ cm. We show our 3D results obtained with various methods introduced in section 6 in comparison to analytically obtained 1D results. The 2D3D FEM results with COMSOL (green dotted lines) have been obtained by [10]. The power boost factor is consistently reduced compared to the 1D model for resonant configurations, i.e., around $\delta_\epsilon = \pi/2$, $3\pi/2$, and $5\pi/2$. When we get good convergence of the full 3D FEM calculations, i.e., self-consistent results, all 3D methods give results consistent to within a few percent.

use of azimuthal symmetry (2D3D approach) [10] is shown as dotted green lines, while the Elmer results are shown as green squares. Comparing the full 3D Elmer simulation and the 3D COMSOL simulation making use of the azimuthal symmetry (2D3D approach) shows significant deviations for $\delta_v \approx \pi$. Note that the boost factor is still most reduced in the resonant case for the full 3D solution obtained by Elmer. The error bars in figure 8.15 show the self-consistency of the simulation result in terms of the outgoing power integrated over different xy-slices and different quadrants of the simulation domain. For a vacuum phase depth of about π the Elmer calculations have trouble to converge. While in previous chapters the convergence parameter (introduced in section 7.1) in Elmer was always around or below $h \lesssim 10^{-7}$, for a sapphire disk haloscope the convergence parameter did not reach below $\lesssim 10^{-4}$, for a $\epsilon = 4$ disk it varied between $10^{-1} - 10^{-9}$ depending on geometry and disk phase depth. In addition, the Elmer results are inconsistent with up to 30 % differences between geometry I and geometry II. When increasing the distance of the dielectric disk and mirror by one wavelength (figure 8.15 (right)), the results from both geometries become consistent and confirm the other 3D results. Hence, this shows the limitations of a full 3D FEM simulation in Elmer for large geometries, which can be overcome by assuming azimuthal symmetry (2D3D approach) and reducing the problem by one dimension, as described in section 6.1. On the other hand, when the full 3D FEM calculations converge, our results explicitly confirm the results obtained assuming azimuthal symmetry (2D3D approach) in COMSOL or just taking diffraction (Recursive Fourier Propagation, Mode Matching) into account.

At last, we comment on the differences between the diffraction-only and full-3D calculations. While the first are based on a scalar diffraction theory the latter take into account boundary charges. Since the distance of the disk and PEC is around $\frac{\lambda}{2}$ and $\frac{3}{2}\lambda$, one may expect that near field effects can play a major role. Nevertheless, apart from the Elmer results suffering from the numerical shortcomings discussed above, the comparison between different methods explicitly shows that these effects cause deviations at the level of few percent in terms of the emitted power of the minimal dielectric haloscope.

Beam Shape and Modes

Let us now explicitly look at the beam shape generated by the minimal dielectric haloscope in order to study diffraction and near field effects of the system more thoroughly. This will not only allow us to understand the behavior in terms of booster eigenmodes, but is also important to aid antenna design to receive the emitted power from such a system in an optimal way.

Figure 8.16 shows how the emitted beam shape changes as a function of δ_ϵ. The beam shape acquires more substructure when going from resonant to the transparent case. Furthermore we see that for the resonant case the beam is concentrated more in the center, while we observe more substructure for the transparent case. We can understand this by considering the modes contributing the emitted beam shape, as outlined in the middle of figure 8.16. The different hatched colored regions correspond to the power contributed by different modes $m, \ell = 0$. Notice that modes $\ell \neq 0$ do not contribute due to symmetry. Only the fundamental mode $m = 1$ follows a similar boost factor curve as expected from the 1D model, i.e., the resonant enhancement of the higher modes compared to the fundamental mode is suppressed when comparing e.g. $\delta_\epsilon = \pi/2$ and $\delta_\epsilon = \pi$. This is expected, since the propagation constant k_z of the higher modes is smaller and making their longitudinal wavelength longer. However, for a resonance, half a wavelength

must fit between the dielectric disk and the mirror ($\delta_v \sim \pi$, cf. figure 8.14). The lowest mode has a propagation constant closest to the one from the 1D calculation, i.e., it fits the resonance condition best. On the other hand the fundamental mode couples to the axion-induced field with an efficiency of $|\eta|^2 \sim 70\,\%$. Thus, the total emitted power is reduced on resonance by this efficiency. Note that this is not a dissipative loss mechanism of the system, but simply due to the fact that only a subset of the modes can be boosted.

We have compared the radiation patterns obtained above with the Recursive Fourier Propagation and FEM in terms of the matching ratio between two beams defined in section 6.4. While Mode Matching and Recursive Fourier Propagation results have a matching ratio better than 96%, their matching ratio with the FEM solutions is typically above 85%. Here we see again that the impact from near field and boundary charge effects on the y-component of the emitted electric fields has small $\sim \mathcal{O}(10\,\%)$ impact on the sensitivity of such a minimal dielectric haloscope. In addition, this is supported by looking at the details of the beam shape: In section 8.2.1 we saw that additional x and z-components at the order of $\sim \mathcal{O}(10\,\%)$ of the axion-induced E-field arise due to near field effects and boundary charges. There, the electric field had a steep discontinuity at the rim of the disk. Here the relevant lower modes all drop off to zero near the outer boundary of the dielectric disk, which implies that net charges from these modes are also much smaller than for the dish antenna, i.e., $\rho = \nabla \cdot \boldsymbol{E} \approx 0$. Therefore, we expect the x and z-components of the E-field to be below the $\mathcal{O}(10\,\%)$ level. This can be confirmed by looking at the FEM solutions of these fields. An example is shown in figure 8.17 where we show the full field distribution for $\delta_\epsilon = \frac{3}{4}\pi$. Here we show the result obtained with COMSOL from our collaborators [10], since they converged much better and have less numerical noise than the Elmer results as discussed above. The results from Elmer lead to consistent conclusions. The x and z-components of the E-fields is about a factor 10 smaller than the y-components, i.e., the effect on the emitted power (quadratic in the E-field) is at the percent level. This confirms that boundary charges and near fields do affect the fields inside the minimal dielectric haloscope, but they are not boosted because they do not fulfill the resonance condition and hence are smaller than the E_y-fields. Finally, let us mention that we observe in the x-component (z-component) a characteristic quadrupole (dipole) structure that we already observed in the case of a single PEC, cf. section 8.2.1. The structure comes from the boundary charge fields and near fields which are now emitted from every disk and superimposed in the end. Notice that the amplitude is, however, at the order $\lesssim \mathcal{O}(10\,\%)E_y$, i.e., modifies the emitted power at the level of of 1 % which is irrelevant for sensitivity.

In short. In a minimal dielectric haloscope containing a single disk and a mirror with a diameter of around 7λ only the fundamental mode is efficiently boosted by the system in 3D. Since the axion-induced field only has a coupling efficiency of 70 % to the fundamental mode, the boost factor is reduced by up to this factor compared to the 1D calculation. Moreover, calculations for the power boost factor of a minimal dielectric haloscope with a single disk and mirror agree within few percent in terms of the total emitted power for the different numerical methods discussed in section 6. This implies, that near field effects from net charges are negligible for sensitivity.

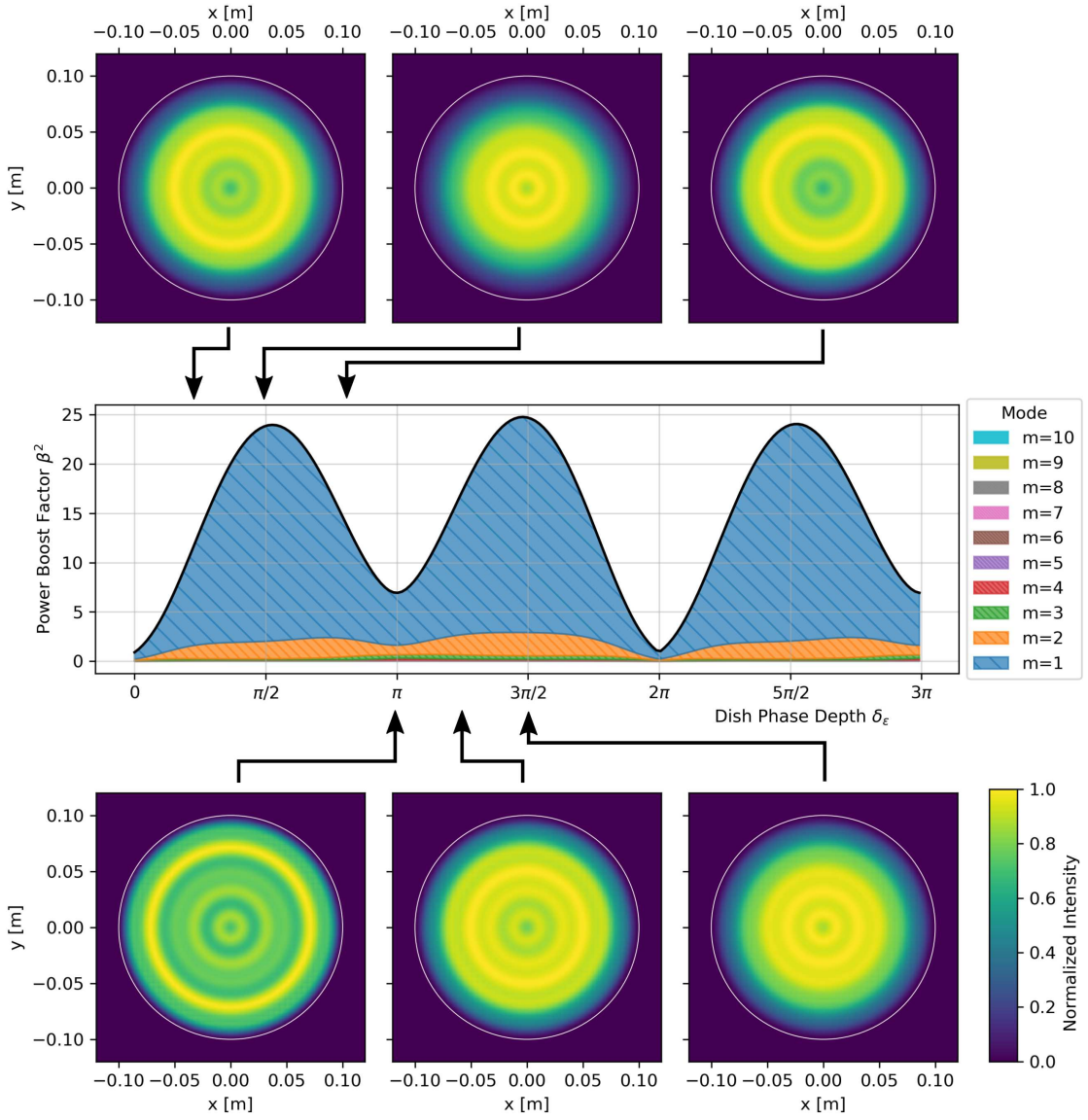

Figure 8.16: Beam shape and mode decomposition of the out-propagating electromagnetic wave from the minimal dielectric haloscope. The central panel shows the total power emitted as a function of disk phase depth δ_ϵ and optimized vacuum phase depth analogous to figure 8.15, but calculated only with the Mode Matching method. The different hatched regions correspond to the power contributed by different modes m, $\ell \neq 0$ modes are not excited due to symmetry. The upper and lower sub-panels show the intensity distribution at the front surface of the dielectric disk for different phase depths as indicated by the arrows.

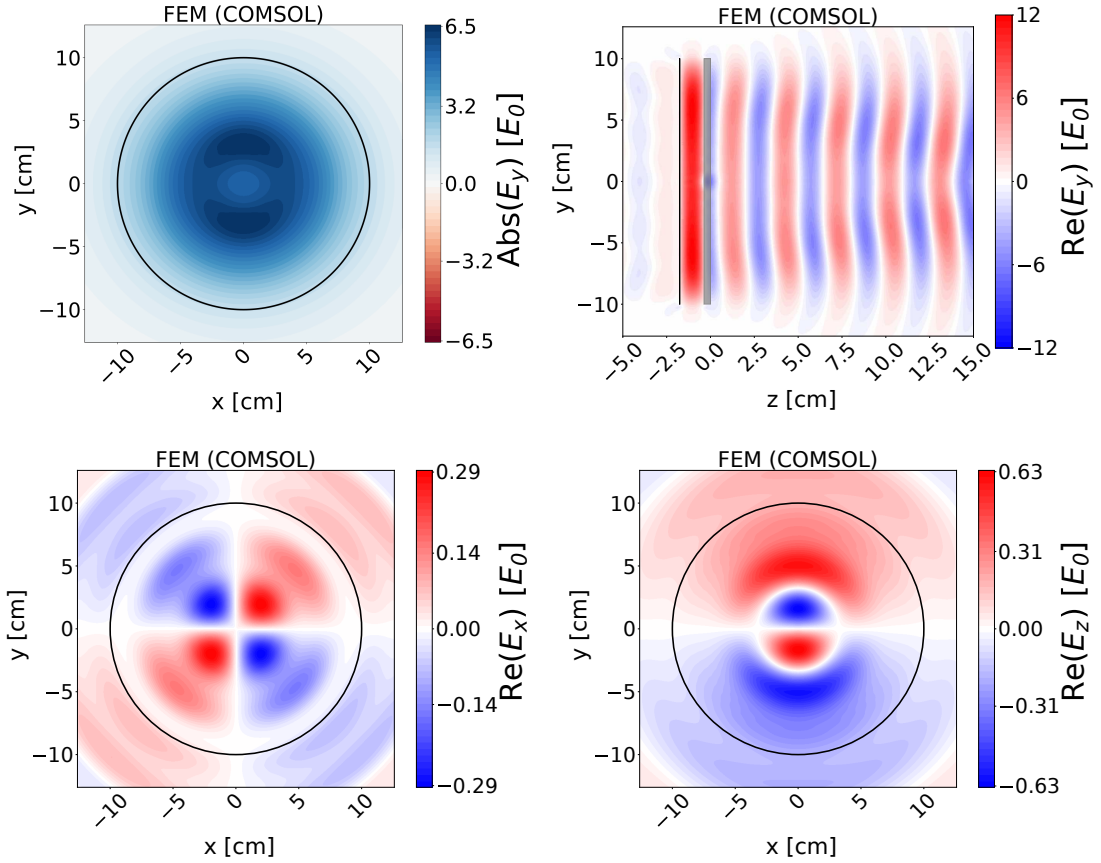

Figure 8.17: Beam shape for the minimal dielectric haloscope at $\delta_\epsilon = \frac{3}{4}\pi$ obtained with COMSOL from our collaborators [10]. On the top we show the y-component of the E-field in the xy-slices (left) and zy-slices (right). On the bottom we show the x-component (left) and the z-component (right) of the E-field in xy-slices. The xy-slices are evaluated 14 cm away from the minimal dielectric haloscope and the zy-slices are evaluated at $y = 0$ cm. The considered frequency is 10 GHz, i.e., $m_a \approx 40\,\mu$eV, and the external magnetic field points in y-direction.

8.3.3 MADMAX Boosters

Let us now make the step to full dielectric haloscopes with more than one dielectric disk. We will first only look at results obtained with the Mode Matching method and explicitly confirm them below by comparing them to the other methods. We consider an idealized but three-dimensional booster with finite extended disks, which are however still perfectly flat and parallel. We consider a booster of 20 lanthanum aluminate disk ($\epsilon = 24$) with 30 cm diameter disks as foreseen in the MADMAX prototype, and a 80-disk system with 100 cm diameter disks as foreseen in the final MADMAX setup. Figure 8.18 shows power boost factors for the MADMAX prototype for different bandwidths. Figure 8.19 shows the same for the final MADMAX setup, but only for a benchmark bandwidth of 50 MHz. Power boost factors from a 1D calculation are shown as gray dashed lines. Since all modes are orthogonal, the total power emitted in the 3D case is given by the sum of the power contributed by the different modes, each denoted by differently colored hatched regions. The power which can be coupled to a Gaussian beam antenna is denoted as thick blue lines. In addition, to the right of each boost factor we show the beam shape corresponding to the frequency indicated by the vertical dashed marker on the left. At frequencies where only the fundamental mode contributes, the beam shape directly corresponds to the fundamental mode. In contrast, if higher modes contribute, the beam shape is given by a respectively weighted coherent sum of the field distributions from the different modes, cf. e.g. equation (6.13).

First notice that all boost factors are shifted to higher frequencies compared to the 1D calculations. This is easily understood considering the phase evolution of the different modes along the booster. Due to their transverse momentum k_c the propagation constant k_z is smaller than in 1D, as given by equation (6.13). This situation corresponds to a longer longitudinal wavelength $\lambda_z = 2\pi/k_z$. Therefore, in order to have the same resonant behavior as in 1D one needs to decrease the longitudinal wavelength again by going to slightly higher frequencies. Analytically one finds for small transverse momenta $k_c \ll k_z$ that the frequency shift is given by

$$\Delta\nu \approx \frac{1}{8\pi^2}\frac{k_c^2}{\nu} \approx 13\,\mathrm{MHz}\left(\frac{k_c}{16\,\mathrm{m}^{-1}}\right)^2\left(\frac{22\,\mathrm{GHz}}{\nu}\right), \tag{8.6}$$

where the example of 13 MHz corresponds to the $m = 1$ mode for the prototype booster. Since higher modes have higher transverse momenta, the shift is more pronounced for higher modes. Also remember that the transverse momentum is inversely proportional to the disk diameter, cf. equation (6.12), giving $\Delta\nu \propto \varnothing^{-2}$, i.e., larger disks quadratically suppress the frequency shift. This is clearly seen, when considering the boost factor for the final-sized MADMAX booster with $\varnothing = 1$ m shown in figure 8.19. Because each mode propagates essentially independently through the system as shown in section 8.3.1, no matter to which bandwidth the boost factor is tuned, for a fixed disk diameter the different modes always appear at the same frequency shifts relative to each other for different boost factor bandwidths. This can be explicitly seen in figure 8.18 when comparing the calculations for different bandwidths to each other.

Now considering the power emitted by the system, we see again that in 3D the boost factor is reduced compared to the 1D calculations. For the MADMAX prototype in figure 8.18 we see that the second mode is already shifted by around 50 MHz. Thus, for boost factor bandwidths smaller or equal to the shift we essentially only get the power contributed by the first mode within one boost factor bandwidth. Since this mode couples to $\sim 70\,\%$ (independent of disk diameter) to

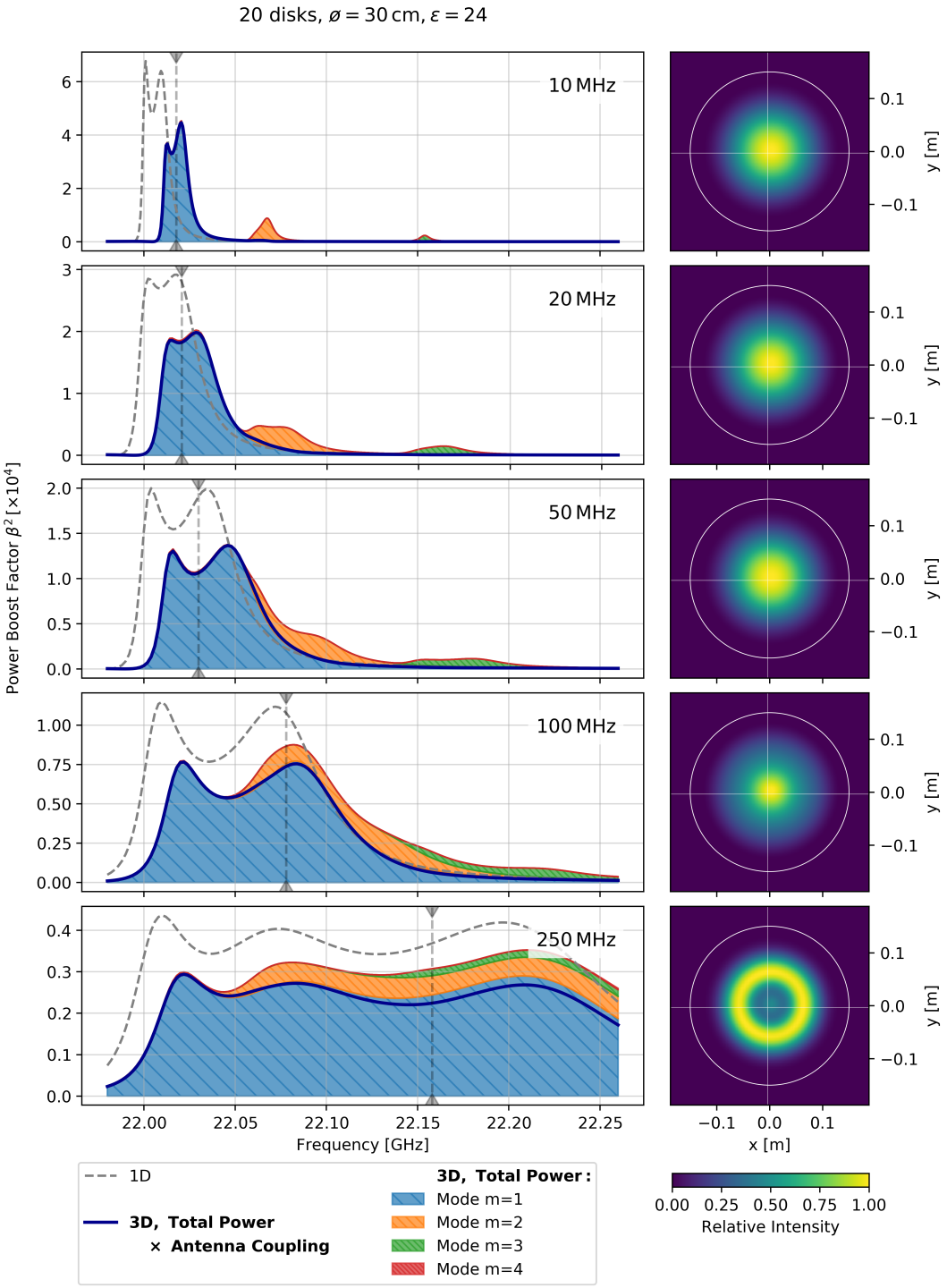

Figure 8.18: **Left:** Ideal boost factors for MADMAX prototype (20 $LaAlO_3$ disks, ø = 30 cm) considering the finite size of the dielectric disks, for different boost factor bandwidths at around 22 GHz. The 1D result is shown as gray dashed lines. The contribution to the total power boost factor from different modes is denoted as differently colored regions. The total power multiplied with the antenna coupling of an antenna receiving a Gaussian beam with $w_0 \sim 10$ cm at the front disk of the booster is denoted as bold dark blue lines. **Right:** Beam shapes at the front disk corresponding to the frequency indicated by the vertical gray dashed markers on the left.

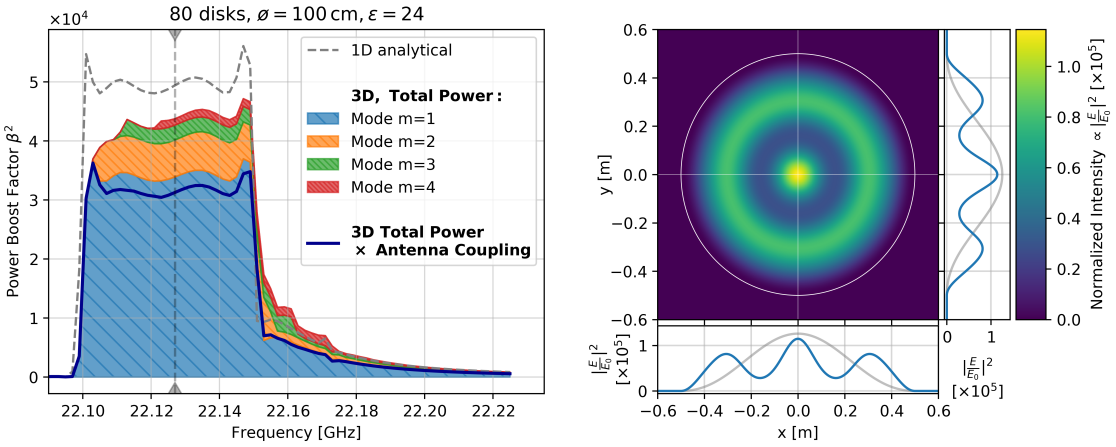

Figure 8.19: **Left:** Ideal boost factor for the full-scale MADMAX (80 $LaAlO_3$ disks, ø = 1 m) considering the finite size of the dielectric disks, for a boost factor bandwidth of 50 MHz at around 22 GHz. The result of the 1D analytical calculation is shown as gray dashed lines. The contribution to the total power boost factor from different modes is denoted as differently colored regions. The total power multiplied with the antenna coupling of an antenna receiving a Gaussian beam with $w_0 \sim 30$ cm at the front disk of the booster is denoted as a bold dark blue line. **Right:** Beam shape at the front disk corresponding to the frequency indicated by the vertical gray dashed marker on the left. The sub-panels show cuts along the x and y-axis of the booster beam shape (blue line) and the contribution from the fundamental mode (gray line).

the axion field, the boost factor is reduced by the same factor compared to 1D. Therefore, this effect has to be understood as a reduced coupling efficiency (form factor) of the system to the axion field and not as a dissipative (diffraction) loss. Instead of actually losing power somewhere during propagation, the higher modes are resonant at different frequencies and are thus simply not boosted by the system at the frequency considered. Indeed, the diffraction loss of the first mode arising from the finite disk size in this case is smaller than $\delta_d \sim 10^{-5}$ (see table 6.2) which is negligible. This of course may not hold anymore including the geometrical inaccuracies considered later in section 8.4.3.

Lastly, we have to consider how to couple the power leaving the booster with an antenna into a receiver. As shown in figure 6.3 (left) the fundamental mode has a 97% matching ratio with a Gaussian beam with a waist of $w_0 \sim D/3$ with D the diameter of the disks. We therefore consider the coupling efficiencies to Gaussian beam antennas here. In the case where we only end up in the fundamental mode and the beam shape is fully given by this mode, we can achieve very good coupling efficiencies. In the case where the total power also carries higher modes, like in the 80 disk calculation in figure 8.19, coupling to such a Gaussian antenna one can essentially only receive the power provided by the fundamental mode. This contribution is still significant ($\gtrsim 70\,\%$ due to the coupling of the axion-field to the fundamental mode), although higher modes have changed the beam shape notably, as shown on the right. However, small couplings of the higher modes to the Gaussian may even interfere destructively when coupled to the antenna, further decreasing the received power. In principle it is possible, to design an antenna which is matched to a more

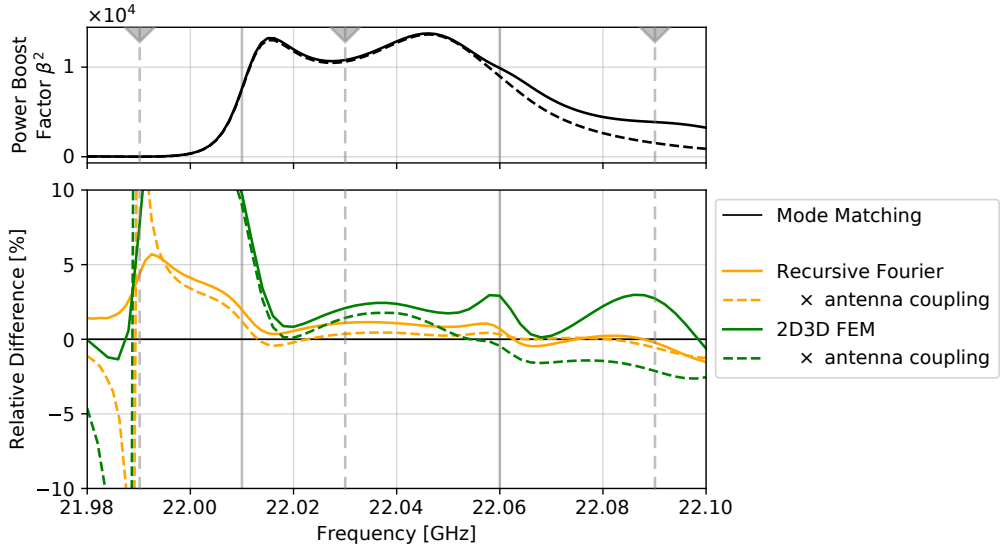

Figure 8.20: Comparison of boost factors and boost factors times antenna coupling calculated with the three different numerical methods for the boost factor with a bandwidth of 50 MHz for the idealized prototype setup as in the middle row of figure 8.18. The upper sub-panel shows the boost factor calculated with the Mode Matching method for orientation. The lower sub-panel shows the relative difference between the result from Mode Matching and either the result from Recursive Fourier Propagation (yellow) or 2D3D FEM (green). The FEM result has been obtained by our collaborators [10]. The vertical dashed markers indicate the frequencies at which we compare the beam shape in figure 8.21.

optimal combination of modes, as long as their relative phase stays roughly constant over the boost factor bandwidth – or in other words the total beam shape does not change drastically with frequency. For the initial stage of dielectric haloscopes this may already be a too costly and elaborate approach. In summary, as long as the boost factor bandwidth is smaller than the difference between the frequency shifts of the first two modes, the optimal antenna is one, that couples only to the fundamental mode.

Not considered here, but crucial for a final experimental realization, will be possible reflections on the antenna, especially those of the higher modes, which may interfere destructively with the fundamental mode. For MADMAX we will come back to such reflections in the context of the proof of principle setup described in part IV of this thesis.

Verification with other methods

In order to confirm these results, we compared the result from Mode Matching obtained above with the corresponding results from the Recursive Fourier Propagation and 2D3D FEM methods in figure 8.20. The lower panel shows the relative difference between their results and the result from the Mode Matching method, for the 20 disk benchmark boost factors over a bandwidth of 50 MHz, while in the upper panel the boost factor obtained with Mode Matching is shown for orientation. The boost factor from Finite Element methods (2D3DFEM) has been obtained by

our collaboration partners [10]. The differences follow a systematic pattern and are therefore likely due to the simplifying assumptions of the Recursive Fourier and Mode Matching methods. Most prominently, the boost factors obtained by Recursive Fourier Propagation and FEM are typically higher than then results from Mode Matching. This is expected, since the Mode Matching method neglects higher modes which may carry additional power. The differences are largest in the regions where the boost factor itself is small. The boost factors are consistent up to percent level within the boost factor bandwidth. This does not significantly affect sensitivity and therefore is sufficient for this study.

Moreover, we show the comparison of beam shapes obtained from the different methods in figure 8.21 in the xy-plane, corresponding to three different example frequencies for the boost factor in the middle row in figure 8.20, indicated by the dashed markers. Here the matching ratio between two beam shapes quantifies the amount of power received by an antenna perfectly matched to one beam, when actually the other beam is the physical beam shape. In particular the match is very good in the range of the boost factor, where only the fundamental mode is boosted. Typically deviations between the methods are on the percent level or below, insignificant for sensitivity estimates. Notice that the largest deviations indeed are outside the 50 MHz range of the boost factor, where higher modes contribute. Analogous results have been obtained for the MADMAX prototype within its designated frequency range at $\nu = (18, 20, 22, 24)$ GHz and at 22 GHz for different boost factor bandwidths $\Delta\nu_\beta = (5, 10, 20, 50, 100, 250)$ MHz. In addition, the comparison has also been performed for the full-scale MADMAX setup for the $\Delta\nu_\beta = 50$ MHz boost factor at 22 GHz shown in figure 8.19, also leading to analogous results. The agreement shows that in particular for ideal dielectric haloscopes consisting of multiple disks tuned to a boost factor over a bandwidth $\sim 10^{-3}\nu$ the simplifying physics assumptions of the Mode Matching and Recursive Fourier Propagation methods are valid, i.e., a relatively low number of modes (in our case 4) is sufficient to approximate the fields inside the system and a scalar diffraction theory neglecting near field effects is sufficient.

In short. The power contributed to the boost factor by different modes is shifted in frequency due to their different transverse momenta. In the case where the frequency shift of the second mode compared to the first mode ($\sim$ 50 MHz for the MADMAX prototype) is higher than the boost factor bandwidth, the boost factor amplitude within the considered bandwidth is reduced with the coupling-efficiency of the axion-induced field to the fundamental mode of $\sim 70\,\%$. In this case the optimal antenna would only couple to the fundamental mode of the system. For the MADMAX prototype this means in particular, that the antenna system should couple to a Gaussian beam with beam waist ~ 10 cm at the front disk of the booster independent of frequency. These results are consistently obtained with all three numerical methods introduced in section 6.

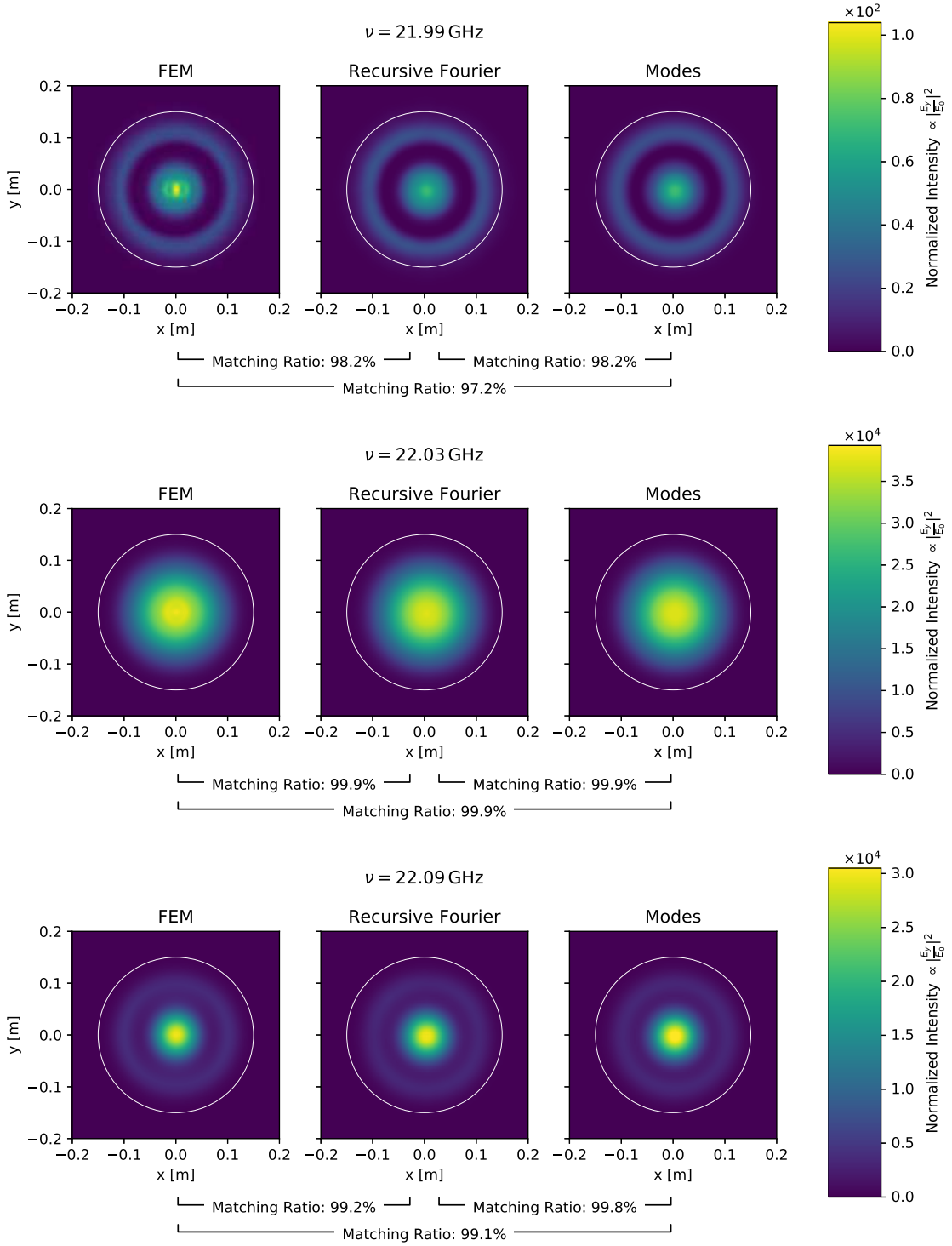

Figure 8.21: Comparison of beam shapes 15 cm in front of the booster calculated with the three different numerical methods for the boost factor for the idealized prototype setup in the middle row of figure 8.18 at three different example frequencies. The FEM results have been obtained by our collaborators with COMSOL and making use of the azimuthal symmetry [10]. The matching ratio quantifies the amount of power received by an antenna from one beam shape, if it is perfectly matched to the alternative beam shape.

8.4 Non-Ideal Booster

8.4.1 Axion Velocity and B-Field Inhomogeneity

Let us now study various systematic uncertainties from 3D effects on the boost factor. We begin with deviations caused by the axion-induced field E_a itself. The field emitted from the dielectric disks follows the axion-induced electric field E_a on the disk surface, since the emission compensates the discontinuity of the axion-induced field here. As described in section 2.1 the axion-induced field is $\propto \boldsymbol{B}_e\, \epsilon^{-1}\, a$. Spatial inhomogeneities of these quantities will therefore affect the boost factor. In this section we will survey those effects.

In the picture of modes this means that we change how the axion-induced field excites the modes, i.e., the power coupling of the axion-induced field to the modes. This is quantified in equation (6.17), which after inserting the axion-induced field E_a from equation (2.3) explicitly reads

$$\eta_{m\ell} = -\frac{g_{a\gamma}}{\mathcal{N}_a} \int_{\text{disk}} E^*_{m\ell}(r,\phi)\ \hat{\boldsymbol{e}}_y \cdot \frac{\boldsymbol{B}_{\text{e}}(\boldsymbol{x})}{\epsilon(\boldsymbol{x})}\, a(\boldsymbol{x})\ \mathrm{d}A, \tag{8.7}$$

where the normalization $\mathcal{N}_a = \int_{\text{disk}} |E_a|^2\, \mathrm{d}A$ simply ensures $\sum_{m,\ell} |\eta_{m\ell}|^2 = 1$. We will first survey velocity effects, which modify the complex phase of a. Afterwards we study the effect of a inhomogeneous magnetic field. Small relative inhomogeneities in ϵ are analogous, but the effects that this inhomogeneity would have on a propagating wave are more dominant on resonance, as discussed later.

Transverse Axion Velocity

With non-zero axion velocity $\boldsymbol{v}_a$ the axion-field a and therefore also the axion-induced electric field E_a acquire a spatial phase factor over the setup, i.e.,

$$a \approx a_0 \exp(-i m_a t) \exp(i m_a \boldsymbol{v}_a \cdot \boldsymbol{x}), \tag{8.8}$$

where again only the real part of this field is the physical field. Thus, a velocity along the booster axis causes phase differences between the disks, which has been studied already in [1, 91]. A transverse velocity tilts the direction of the emissions from the individual disks, where the angle of the emitted electromagnetic radiation is directly given by the axion velocity parallel to the disk $v_\parallel$ [164–166]. We can study the effect of this tilting by decomposing the axion-induced field into modes and observe how the coefficients $\eta_{m\ell}$ change with transverse velocity. Figure 8.22 shows the dependency of the power coupling efficiency $|\eta_{m\ell}|^2$ as a function of the product of the axion momentum parallel to the disk with disk diameter. This quantity corresponds to the phase change of the axion-field along the disk diameter. Each differently colored hatched band corresponds to the squared power coupling coefficient of different mode indices m. The coupling coefficients of the different modes are stacked on top of each other. The sum of all power coupling efficiencies is unity. Different shades of the same color correspond to higher ℓ modes. For each $\ell \neq 0$ there is a mode with positive and negative ℓ. In order to distinguish between them, the modes with negative ℓ are shown below the $\ell = 0$ band, the modes with positive ℓ above. The velocity effect starts having significant impact on the mode decomposition when the transverse de Broglie wavelength of the axion

$$\lambda_{\text{dB},\parallel} = \frac{2\pi}{m_a v_{a,\parallel}} \tag{8.9}$$

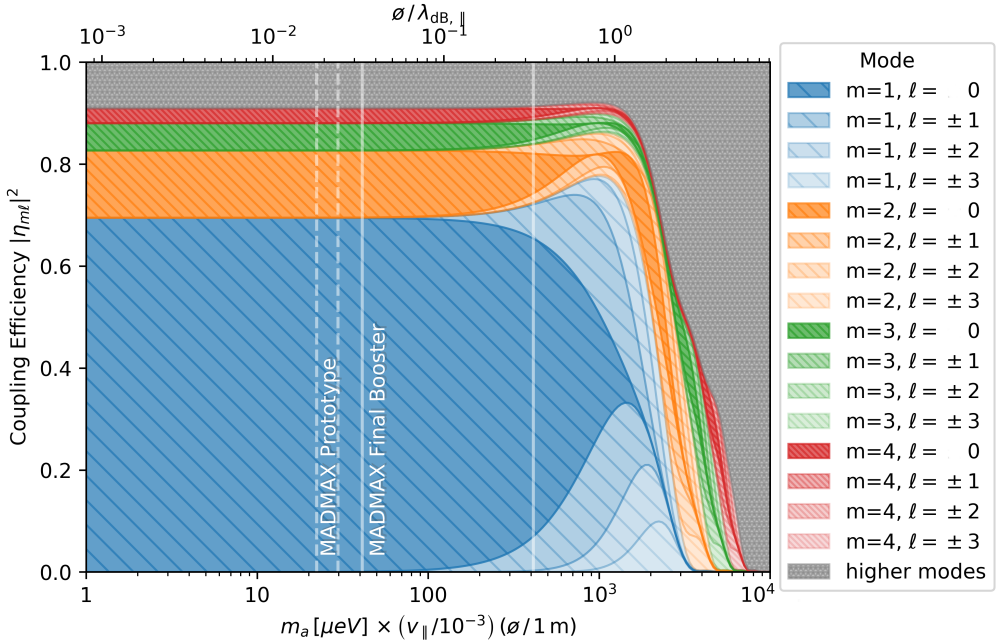

Figure 8.22: Velocity effect on the mode-coupling coefficients between axion-induced field and modes $\eta_{m\ell}$. We show the dependency of the power coupling efficiency $|\eta_{m\ell}|^2$ on the product of axion-mass m_a, axion-velocity parallel to the disks $v_\parallel$ and disk diameter ø (bottom axis) corresponding to a ratio between the diameter ø and axion de Broglie wavelength parallel to the disks $\lambda_{\mathrm{dB},\parallel}$. The vertical dashed white lines indicate the range for the MADMAX prototype, the vertical solid white lines indicate the range for the full-scale MADMAX experiment.

is becoming comparable to the disk diameter ø. Notice that for realistic axion-velocities $\sim 10^{-3}$ in the mass range $40-100\,\mu$eV the effect on a setup like MADMAX with ø $\sim 1\,$m would be negligible. For the higher mass band of MADMAX $100-400\,\mu$eV the effects may become more relevant, but still leave sufficient power in the fundamental mode. Notice that when velocity effects become relevant $\ell \neq 0$ modes are excited. This is expected, since the $\ell = 0$ modes have a plane phase front, i.e., their phase is constant in the xy-plane. Thus, $\ell \neq 0$ modes are needed to describe the aforementioned phase change over the disk.

The effect on the boost factor is explicitly demonstrated on the benchmark boost factor for the MADMAX prototype in figure 8.23 and for the 80 disk MADMAX booster in figure 8.24. An axion velocity that causes significant changes to the mode decomposition first of all takes power out of the fundamental mode in favor of higher modes. Therefore, the antenna coupling degrades while the total power emitted by the haloscope still remains almost unchanged, but is in the wrong mode to be 'seen' by the antenna. Higher modes have smaller propagation constants and therefore appear at larger frequencies. Hence, the boost factor shifts to higher frequencies when increasing the axion velocity. Higher modes are also more prone to diffraction losses and the inaccuracies such as surface roughness described later, so eventually even the total power emitted by the haloscope will be reduced. For the prototype booster the frequency shifts are larger compared to the final booster due to the smaller disk size, as we have also seen before in figures 8.18 and 8.19. On the

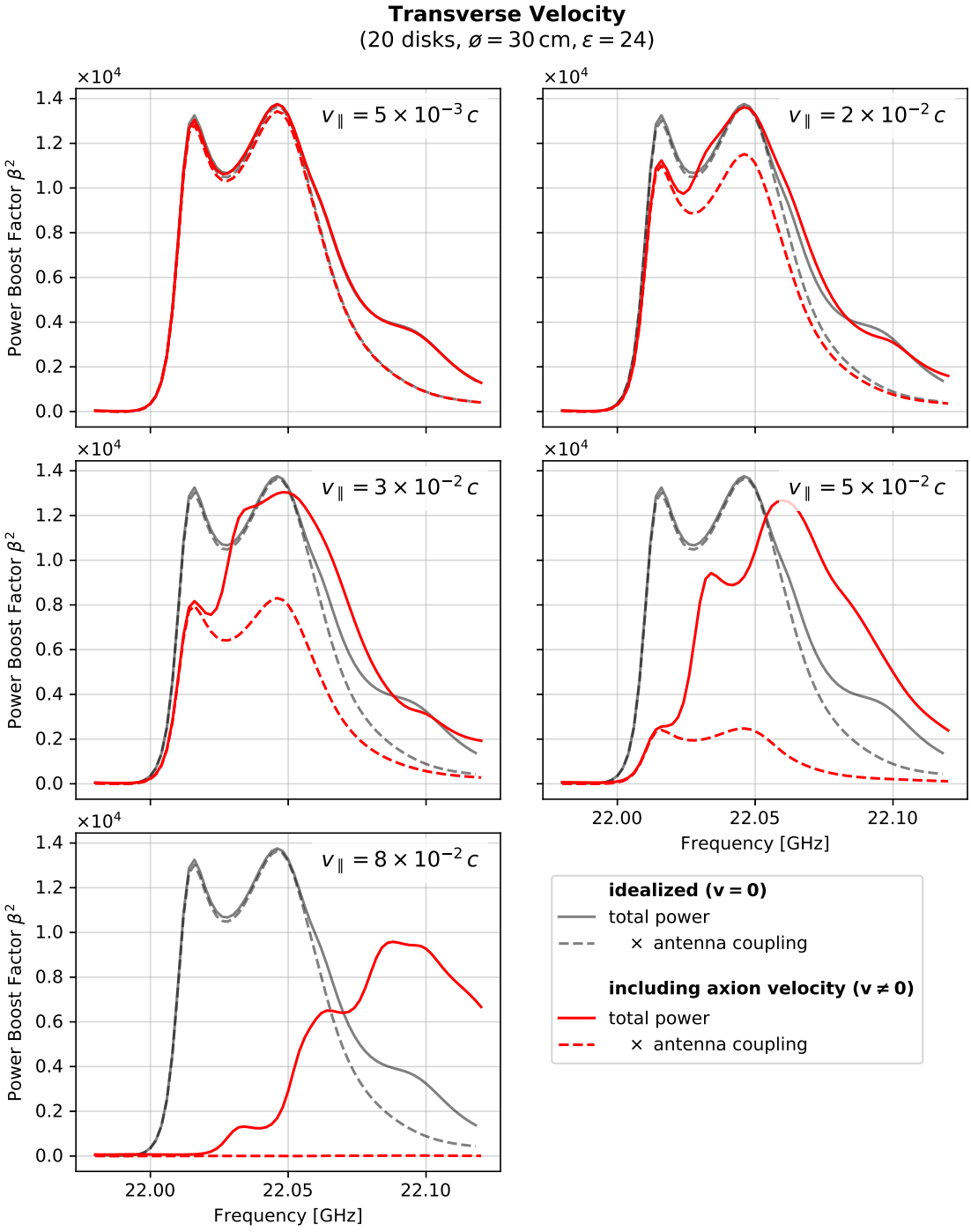

Figure 8.23: Effect of a transverse axion velocity on the benchmark boost factor for the 20 disk MADMAX booster. Each panel shows the boost factor for another transverse velocity $v_\parallel$. The solid red curves show the power boost factor corresponding to the total emitted power of the booster, while the amount which can be coupled to a $w_0 = 10\,\text{cm} = ø/3$ Gaussian beam is indicated by dashed lines. For comparison, each panel also contains the same curves for zero axion velocity indicated by the gray shaded lines.

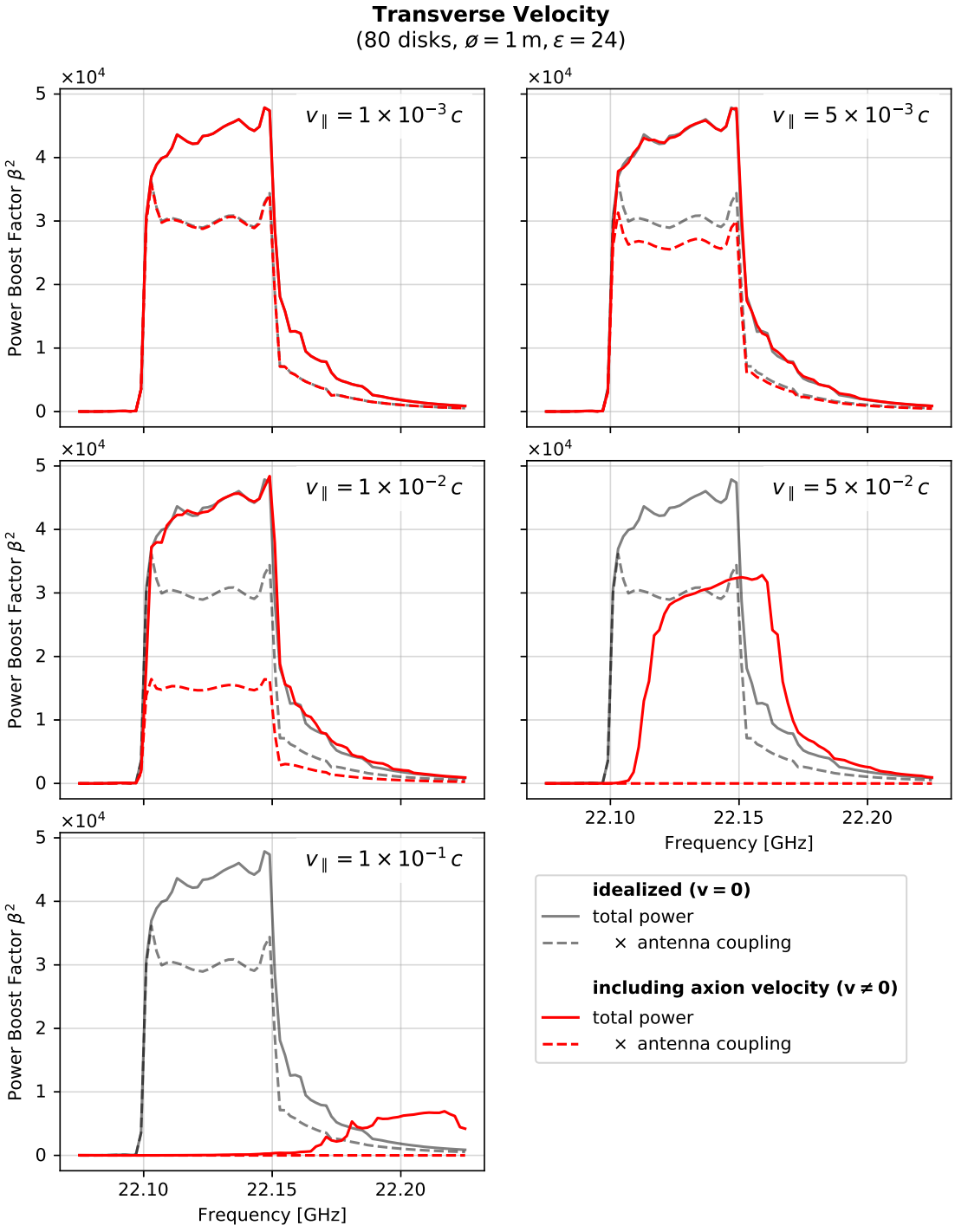

Figure 8.24: Effect of a transverse axion velocity on the benchmark boost factor for the 80 disk MADMAX final booster; analogous to figure 8.23.

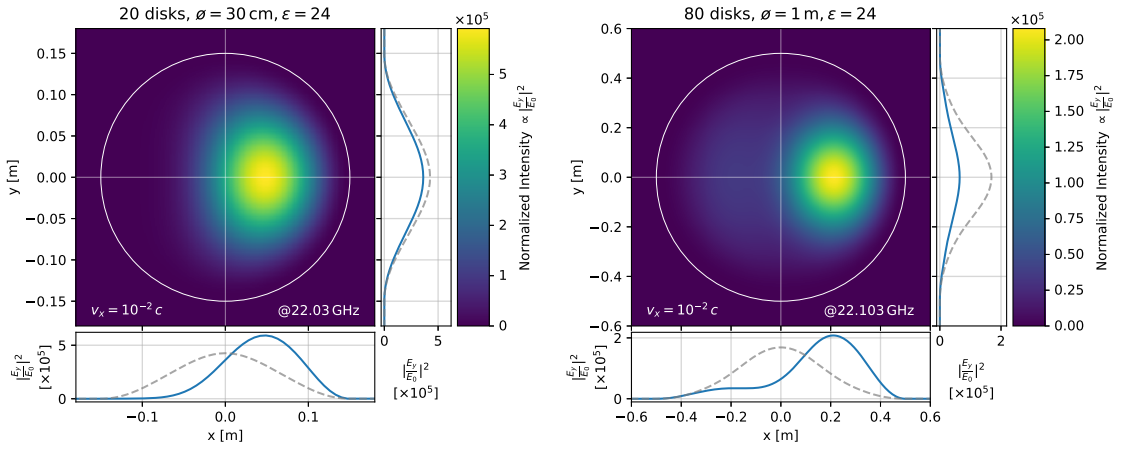

Figure 8.25: Beam Shape of the outpropagating wave from the booster for an exaggerated transverse axion velocity of $v_x \approx 1 \times 10^{-2} c$. The left panel shows the beam shape corresponding to the boost factor in the top right panel in figure 8.23 at a frequency of 22.03 GHz. The right panel shows the beam shape corresponding to the boost factor in the top right panel in figure 8.24 at a frequency of 22.103 GHz. The sidepanels show the fields along the x and y axes as a blue line and the fields when setting the velocity to zero as a dashed gray line.

other hand, the prototype is more robust against velocity effects, because a smaller disk diameter covers less of the transverse axion de Broglie wavelength. Nevertheless, for realistic CDM velocities $v \sim 10^{-3}\,c$ the changes to our benchmark boost factors are well below the percent level.

While the mode decomposition allows us to quantify the effect of the velocity, it is worth remembering that the emissions from each individual disk are simply slightly tilted due to the velocity effect. Therefore, the center of the beam shifts away from the center of the disk as shown in figure 8.25. The center is shifted in the direction of the velocity due to momentum conservation. We can naively estimate the shift of the beam center with the mean optical length a ray must propagate before leaving the booster, when assuming it is emitted at an angle $v_\parallel$. One finds for the shift in the presented cases $\sim (\nu/\Delta\nu_\beta)\,\lambda\,v_\parallel \sim 10\,\text{cm}$, which is consistent with the order of magnitude of observed shifts in the simulations. This estimate, however, assumes that the titled emission essentially propagates as plane waves, which is not the case.

In order to check the consistency of the different numerical methods, we did the same calculation for the MADMAX prototype also with Recursive Fourier Propagation. Note that for 80 disks this calculation would have been too numerically expensive using Recursive Fourier Propagation, and the calculation is not possible using 2D3D FEM since the velocity breaks the azimuthal symmetry. The results are consistent up to percent level differences in the power boost factor, as explicitly shown in figure 8.26 for a transverse velocity of $v = 3 \times 10^{-2}\,c$.

At last, let us briefly point out that the actual velocity effect on the boost factor is not given by a fixed, stationary velocity vector, since the coherence time of the axion-field is much smaller than the signal integration time of a typical haloscope. Hence, the effect on the boost factor needs to be calculated by taking the average power boost factor over the whole integration time of the experiment. Since the earth is rotating, the axion dark matter wind impinges the experiment

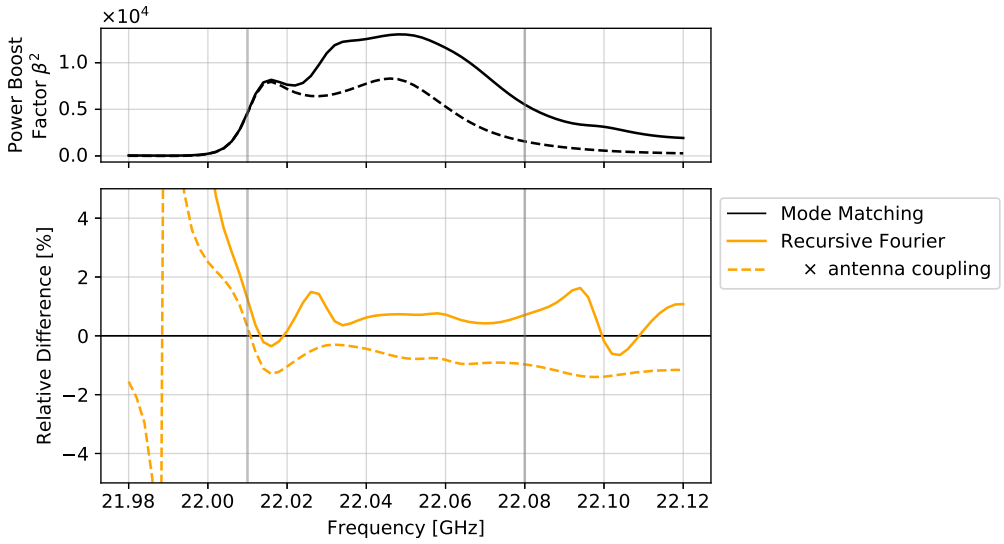

Figure 8.26: Comparison of boost factors and boost factor times antenna coupling calculated with Recursive Fourier Propagating and Mode Matching, corresponding to the boost factor shown in the middle left panel in figure 8.23. The upper sub-panel shows the boost factor calculated with the Mode Matching method for orientation. The lower sub-panel shows the relative difference between the result from Mode Matching and the result from Recursive Fourier Propagation.

from different sides. This gives rise to the changes to the measured axion power spectrum as discussed in part II and can in principle be used to infer properties of the axion dark matter velocity distribution. For the boosters considered above the reduction in received power would be symmetric for positive and negative velocities and the coupling efficiency of a Gaussian beam to a displaced beam degrades quadratically with the displacement, i.e., this setup corresponds to a q-type experiment in part II. On the other hand, if one has the freedom to choose the alignment of the experiment, one could try to suppress effects from the transverse velocity by aligning the disks as much as possible orthogonal to the dark matter wind. In contrast to the transverse velocity effects, the effects of an axion velocity in z-direction [91] are the same at different scan frequencies, because the length of the booster scales proportional to the de Broglie wavelength of the axion field.

In short. The effects from a transverse axion velocity are negligible for MADMAX in a mass range below $\sim 100\,\mu$eV. For the range above this limit the fundamental mode couples less to the axion-induced field, which may slightly reduce sensitivity.

Magnetic Field Inhomogeneity

In addition, a transverse inhomogeneity of the magnetic field implies the same inhomogeneity in the axion-induced field E_a. Therefore, we can treat such an inhomogeneity analogous to an axion velocity, i.e., it changes the amount of power coupled into the different modes. For example, a magnetic field which would follow the beam shape of the first mode $m = 1, \ell = 0$ would cause the coupling coefficient of the first mode to be $|\eta_{10}|^2 = 100\,\%$. To realize such a magnet is, however,

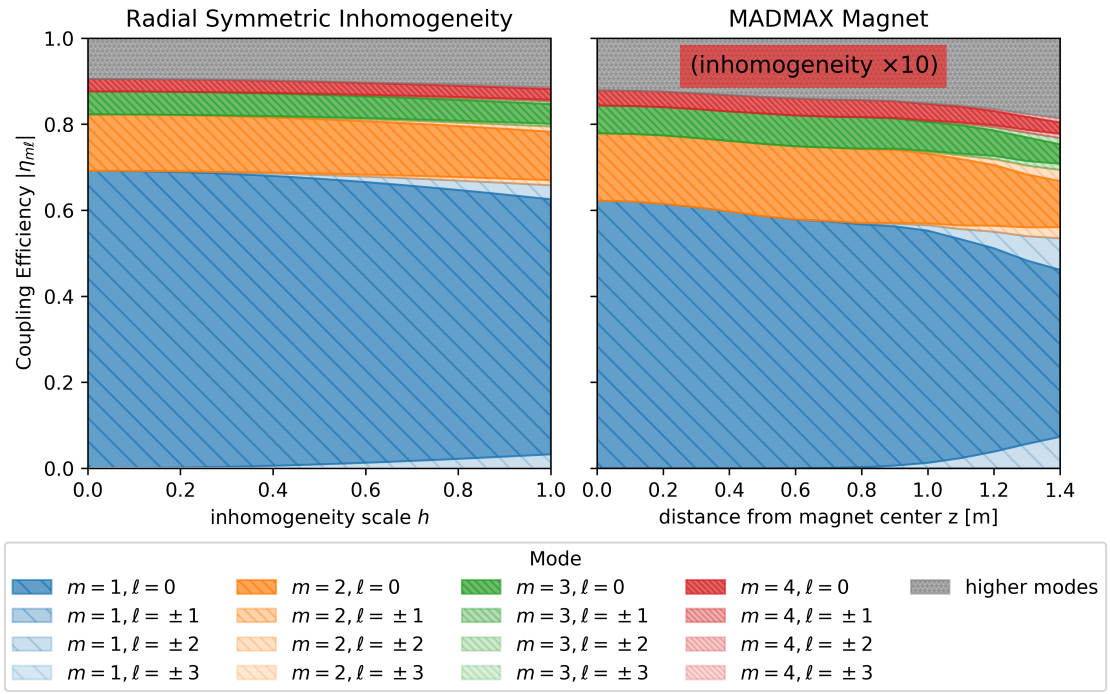

Figure 8.27: Inhomogeneity effects of the external magnetic field on the mode-coupling coefficients between axion-induced field and modes $\eta_{m\ell}$. **Left:** Dependency of the coefficients $|\eta_{m\ell}|^2$ as a function of inhomogeneity scale h for the radially symmetric external magnetic field defined in equation (8.10). **Right:** Dependency of the coefficients $|\eta_{m\ell}|^2$ as a function of the position inside the magnet z for the magnetic field in the current magnet design [105]. The inhomogeneities have been multiplied with a factor of 10 to make the effect visible.

technically challenging and likely to increase magnet cost significantly.

Another instructive example is a magnetic field with a radially symmetric inhomogeneity. Depending on the design such an inhomogeneity can be common for large scale dipole magnets such as the one used for MADMAX. Let us consider such a magnetic field parameterized by

$$\boldsymbol{B}_e(r,\phi) = B_0 \left[1 + h\sin(k\phi)\frac{r^2}{R^2}\right] \hat{\boldsymbol{e}}_y, \tag{8.10}$$

where B_0 is the magnetic field amplitude, h is the maximum scale of the inhomogeneity on the disk and $R = \text{ø}/2$. k is a non-zero positive integer corresponding to the angular spatial frequency of the magnetic field inhomogeneity, i.e., $k = 1$ corresponds to a linear inhomogeneity along the y-axis, $k = 2$ corresponds to a situation in which the fields on the left and right are smaller than on the top and bottom, etc. Notice that this parametrization is general for different disk radii R and can thus be applied to both the 30 cm disks of the prototype and 1 m disks of the full-scale MADMAX experiment in full analogy.

We show the dependency of $|n_{m\ell}|^2$ on h explicitly in figure 8.27 (left) analogous to figure 8.22. Each differently colored hatched band corresponds to the squared power coupling coefficient of different mode indices m. The coupling coefficients of different modes are stacked on top of each other, as the sum of all power coupling efficiencies is unity. Also here, different shades of the same

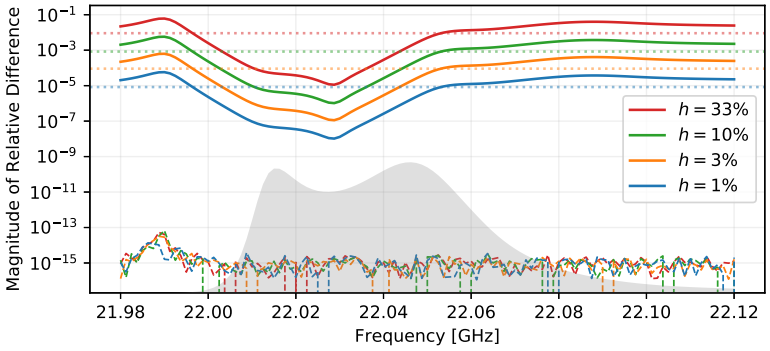

Figure 8.28: Magnitude of relative difference between boost factor where the magnetic field is set as in equation (8.10) and where the magnetic field is perfectly homogeneous. The straight lines show the difference in total power, the dashed lines which are at around $\sim 10^{-15}$ the numerical value after taking the antenna coupling into account. The straight dotted lines indicate the estimate from equation (8.11). Different colors refer to different values of h. The gray area shows the ideal boost factor curve for better orientation along the frequency axis.

color correspond to higher ℓ modes and in order to distinguish between positive and negative ℓ, the modes with negative ℓ are shown below the $\ell = 0$ band, the modes with positive ℓ above.

Remember that for constant magnetic field along z these coupling efficiencies of the axion-induced field to the modes is the same at all disks, i.e., the disk number is irrelevant for this calculation. For small h one can show that the relative change in the coupling coefficients of the $\ell = 0$ modes happens only at second order in h and is given by

$$\frac{\Delta|\eta_{m0}|}{|\eta_{m0}|} \sim -\frac{1}{12}h^2, \tag{8.11}$$

i.e., radial symmetric transverse inhomogeneities at the 10 % level leave the mode coupling coefficients unchanged below the percent level. Also notice that this is independent of k as the $\ell = 0$ modes have azimuthal symmetry.

Besides this analytical parametrization, we also consider the coupling coefficients $|n_{m\ell}|^2$ for the magnetic field provided by the conservative short magnet from the current MADMAX magnet design studies [105] with typical inhomogeneities on the ~ 5 % level. Since the magnetic field in fact changes along z, we computed the coupling efficiencies separately for different z along the booster axis. The result is shown in figure 8.27 (right). This magnetic field leaves the coupling efficiencies unchanged below the percent level. In order to make the changes visible, the inhomogeneity of the magnetic field has been multiplied by a factor of 10, where the inhomogeneity is the residual field after subtracting the spatially averaged field.

In addition, the above analytical estimate for the coupling efficiencies has been explicitly tested for the prototype setup, different inhomogeneity scales h and $k = 2$ using Recursive Fourier Propagation. Notice that $k = 2$ corresponds to the symmetry of the magnetic field e.g. naively expected for the final MADMAX magnet when considering the position of magnet coils in figure 2.7 in section 2.2. We show the relative difference in power boost factor between the ideal case and various scales h figure 8.28. The straight lines indicate the total power while the dashed lines the differences after taking the antenna coupling into account. The boost factor is defined here

as the power compared to the power emitted by only the mirror under a homogeneous magnetic field B_0. Since the inhomogeneity in equation (8.10) does not couple to the $\ell = 0$ modes, the total power contained in the $\ell = 0$ modes must be the same as without the inhomogeneity. Because the antenna does only couple to these modes, the boost factor after taking the antenna coupling into account is essentially unaffected by the magnetic field inhomogeneity. Therefore, we see only numerical noise in figure 8.28 for the boost factor after taking into account the antenna coupling. For the total power, where the $\ell \neq 0$ modes are relevant, we see a small effect on the boost factor, confirming the quadratic dependency on h estimated in equation (8.11). Also remember that the $\ell \neq 0$ modes have larger diffraction losses, so their contribution is expected to be damped in the resonant range of the boost factor. Even for $h = 33\,\%$ the inhomogeneity only has an effect on the boost factor below the percent level.

In short. The effects of percent-scale transverse inhomogeneities of realistic external magnetic fields are negligible for MADMAX.

8.4.2 Disk Surroundings

Besides the effects of the axion-induced field, let us now focus on geometrical imperfections of the booster which will mainly affect the propagation of electromagnetic waves inside the system. We start with the discussion of surroundings of the booster. Here we only refer to surroundings which are radially placed besides the disks. Other surroundings of the booster including the optical system, antenna and receiver have to be treated separately.

First remember that the modes which are boosted by the system drop to zero at the rims of the dielectric disks. Therefore, we expect disk surroundings and small perturbations at the rims of the disks to have little impact on the power boost factor. Another way to motivate this is to consider the diffraction angle θ introduced in equation (8.3). Although it defines the angle into which radiation is diffracted in the far field, we can still use it as an order-of-magnitude estimate in the vicinity of the disk, neglecting near field effects. A beam extending over a radius r will, after propagating for the typical distance between two dielectric disks of $\sim \lambda/2$, extend over a radius $r + \Delta r$ with

$$\Delta r \sim \frac{\lambda}{2}\theta \sim 0.6\frac{\lambda^2}{2R} \sim 3\,\mathrm{mm}\left(\frac{40\,\mu\mathrm{eV}}{m_a}\right)^2\left(\frac{20\,\mathrm{cm}}{2R}\right), \tag{8.12}$$

where λ is the photon wavelength, m_a is the axion mass and R is the radius of the disk. Thus, everything placed much farther away from the rims of the disks than this value is expected to have little impact on the boost factor. Since the diffraction angle decreases with increasing frequency, it is less relevant for higher axion masses. However, for small-scale prototype experiments with disk diameters smaller than 20 cm the effects could become relevant.

It is easy to check this estimate using Recursive Fourier Propagation. When constraining the spatial domain for the discrete Fourier transformation, one gets reflections at the boundaries. We show the result of an example 2D calculation for a 20 disk boost factor with sapphire disks in figure 8.29. We compare the free space solution with the solution from a waveguide surrounding with $\Delta r = 1.2\,\mathrm{cm}$. The large boost factor bandwidth makes the system less resonant and higher modes important, which extend closer to the rims of the disks. We also use a disk diameter

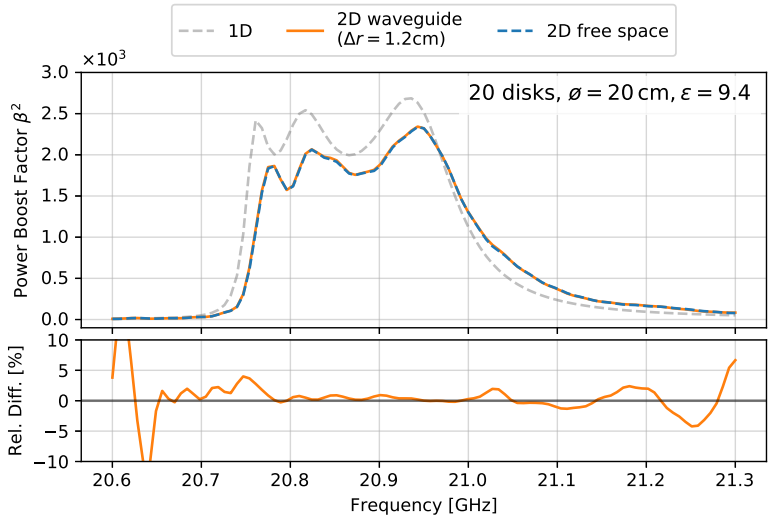

Figure 8.29: The upper panel shows a power boost factor with $\Delta\nu_\beta \sim 250\,\mathrm{MHz}$ for a 20 disk sapphire disk booster in 1D (gray dashed), in 2D assuming the booster is inserted in a waveguide (orange line) and in 2D assuming a free space surrounding (blue dashed). The 2D results within the waveguide and in free space lay on top of each other. The lower panel shows the relative difference between the two 2D cases. The disks have a diameter of 20 cm, the walls of the waveguide are 1.2 cm apart from the rims of the disk.

of 20 cm which corresponds to the proof of principle setup discussed in part IV of this thesis. This diameter is still smaller than for the MADMAX prototype, i.e., we expect the diffraction effects of surroundings to be more dominant here for the $\varnothing = 20\,\mathrm{cm}$ case. The boost factors with and widthout surrounding almost lay on top of each other in figure 8.29 (top). Therefore, we show the relative difference on the bottom revealing differences at the level of a few percent in the considered case. Figure 8.30 shows the beam shapes at the front disk of the booster. The differences between the different beam shapes are at the percent level. In both cases the electric fields emitted from the booster drop to zero at the rims of the dielectric disks at $x = \pm 10\,\mathrm{cm}$, i.e., also for the waveguide case the fields between the rims of the disks and the waveguide boundaries at $x = \pm 11.2\,\mathrm{cm}$ are small. This explicitly confirms that surroundings at this distance have only small effect on the sensitivity.

For clarity, we reemphasize that the above arguments only hold assuming that fields overshining the disks are absorbed and net charges $\rho = \nabla \cdot \boldsymbol{E}$ are negligible. The first assumption has been confirmed in more detail in [146]. The latter has been verified by 2D3D FEM simulations by our collaborators, which assume a waveguide surrounding in full 3D [10], leading to consistent conclusions than above. Moreover, we have neglected axion-induced radiation from the sides, such as from the cryostat walls, which is at the order of the axion-induced field $\sim E_0$ much smaller than the boosted electric fields. Since this radiation essentially comes in with only transverse momentum, it is not resonantly enhanced by the booster as long as the emitting walls are not placed at a resonant condition. It can therefore be neglected as also explicitly confirmed by [10]. Lastly, for a beam back-reflected on the antenna, the electromagnetic fields impinging the booster

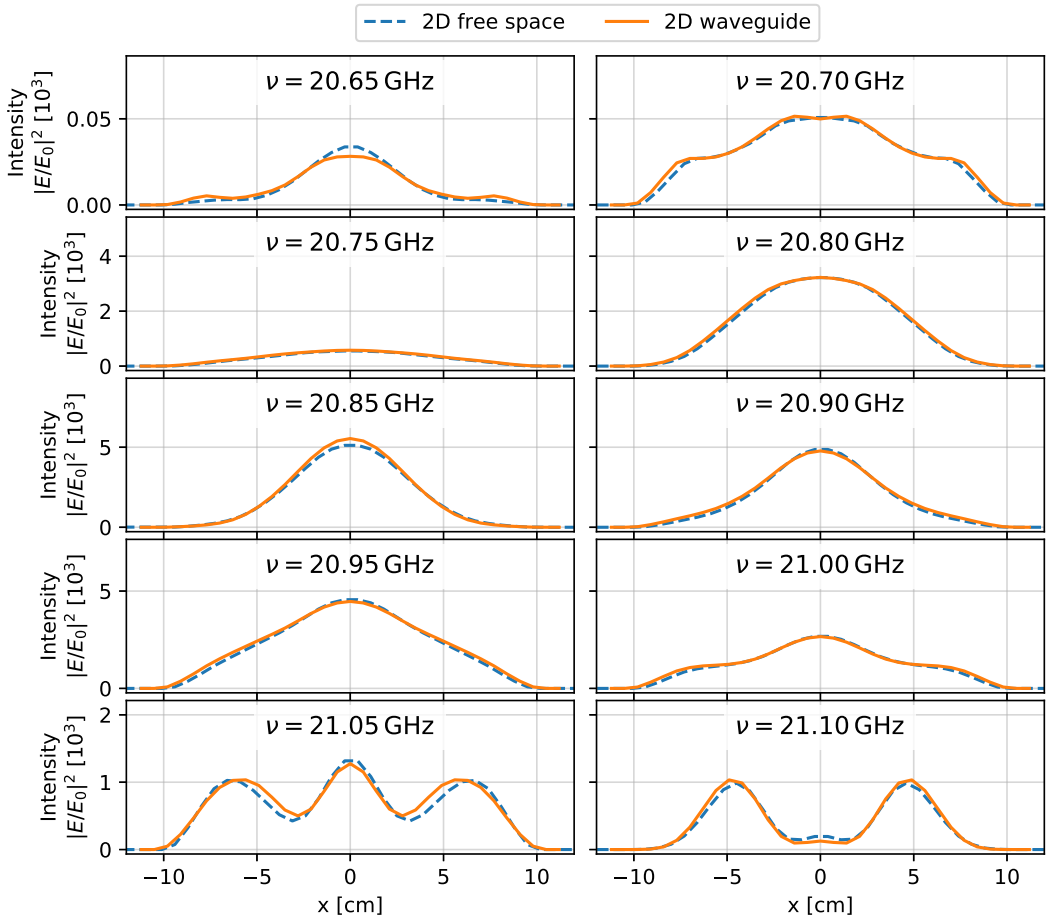

Figure 8.30: Beam shapes at the front disk of the 2D boost factors shown in figure 8.29 at different frequencies; i.e., assuming a free space surrounding (blue dashed) and in 2D assuming the booster is inserted in a waveguide (orange line). The disks extend from $x = -10\,\text{cm}$ to $x = +10\,\text{cm}$ and the waveguide walls are at $x = \pm 11.2\,\text{cm}$.

may stretch also over the surrounding structures and may be scattered there. Again, these fields do not match the resonance conditions of the booster. It is, however, a reasonable choice to place an absorber ring in front of the booster to absorb such unwanted reflections and avoid additional standing waves from these structures. We will discuss such effects later in more detail for our proof of principle setup in section 10.3.

In short. Surroundings placed more than a few mm away from the disks have small impact on the power boost factor for large enough disks.

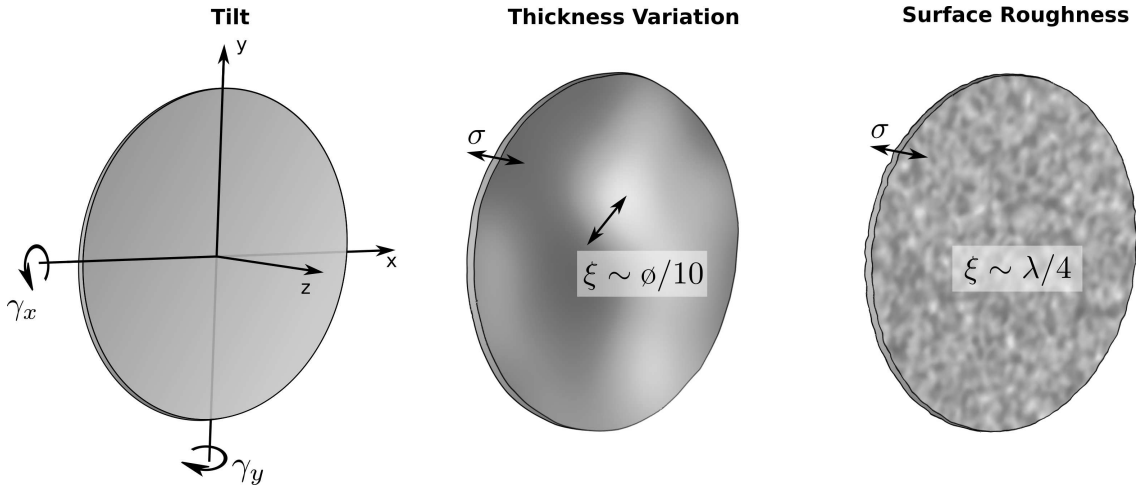

Figure 8.31: Different transverse inhomogeneities of the dielectric disks. **Left:** Tilt of the dielectric disk parameterized by γ_x, γ_y. **Center:** Transverse thickness variation of the disk. The root-mean-square of the variation is given by σ. The bumps and sinks caused by the variation stretch over transverse length scales given by the correlation length parameter ξ. **Right:** Surface roughness corresponding to a thickness variation with small correlation length parameter $\xi \sim \lambda/4$.

8.4.3 Non-Ideal Disks

In contrast to the surroundings of the booster the electromagnetic fields of the eigenmodes are much larger near the center of the dielectric disks. Therefore, changes in boundary conditions here are more prone to affect the propagation of electromagnetic waves. In this section we consider the effects from transverse inhomogeneities of the dielectric disks, such as a tilt of the disk and transverse variations of the thickness or the dielectric constant. We will first introduce our parametrization of these effects. We will then consider how these impact the benchmark boost factors with a bandwidth of 50 MHz and afterwards comment on how these results scale with boost factor bandwidth. At the end, we will show how these results can be understood in terms of Mode Matching and derive opportunities for improvement.

We consider the following distortions from an ideal disk, as sketched in figure 8.31.

- *Transverse Thickness Variation*

  Transverse thickness variations $\Delta z(x, y)$ are parameterized with the thickness standard deviation over the disk σ and a correlation length parameter ξ. Explicitly, we obtain a sample for $\Delta z(x, y)$ by sampling normal distributed random numbers on our (x, y) grid and applying a convolution with a Gaussian distribution of standard deviation ξ. We normalize the obtained points such that the root-mean-square of Δz over (x, y) is σ.

- *Tilt*

  Tilts are described by the rotation of a dielectric disks around the x and y-axis γ_x, γ_y. In this definition the tilts leave the mean distance between dielectric disks unchanged. Notice that a relative tilt between two disks is a special case of a transverse thickness variation in the air gaps where Δz is linear in x and y.

- *Surface Roughness*

  For thickness variations with a small correlation length parameter at the order of $\xi \sim \lambda/4$ we will also more specifically refer to as 'surface roughness'.

- *Transverse Variations of the Dielectric Constant*

  Transverse changes of the dielectric constant $\epsilon(x, y)$ over the disk can be treated analogously to transverse thickness variations, i.e., we parameterize them with the root-mean-square σ_ϵ of the variation $\Delta\epsilon(x, y)$ and correlation length parameter ξ as defined above.

Remember the phase factor of a plane wave propagating in z-direction evolves as $\exp(in\omega z)$ with the refractive index n and the propagation length z. The variations above change n and z as a function of (x, y) and thus at first order add a (x, y) dependent phase to the propagating electromagnetic wave, as argued previously in section 6.2. By comparing the phase shifts caused by the thickness variations and inhomogeneity in the dielectric constant, thickness variations at a scale σ correspond to variations σ_ϵ in the dielectric constant ϵ according to equation (6.10) of

$$\frac{\sigma_\epsilon}{\epsilon} \hat{=} 2\left(\frac{\sigma}{d}\right) \approx 1\,\% \left(\frac{\sigma}{5\,\mu\text{m}} \frac{1\,\text{mm}}{d}\right), \tag{8.13}$$

where d is the thickness of the dielectric disk. The presented results for thickness variations therefore directly apply to transverse variations of the dielectric constant.

Consistency of Numerical Methods

Here we use the Mode Matching method for being able to calculate a large set of boost factors for differently deformed boosters within a short time. Nevertheless, we have checked that the results obtained with Recursive Fourier Propagation are consistent with this method, if taking sufficiently many modes into account. Figure 8.32 shows the comparison of the total emitted power and power coupled to the antenna between the two different methods for an example 20 disk booster with 30 cm diameter $LaAlO_3$ disks with random thickness variations of $\sigma = 10\,\mu\text{m}, \xi = 35\,\text{mm}$ for all disks, leading to the boost factor shown previously in figure 7.3 in section 7.3. Figure 8.33 shows the corresponding beam shapes at frequencies indicated in figure 8.32. The results are consistent up to a few percent.

Numerical Results for Benchmark Cases

First we investigate these effects for the benchmark boost factors with a bandwidth of 50 MHz both for the 20 disk MADMAX prototype and 80 disk full MADMAX setup. For each setup we calculated the boost factors for a large set of deformations at varying scales, as detailed below. If not stated otherwise, we present the results obtained with the Mode Matching method, since it allowed to do significantly more calculations in the same amount of time. Consistent results for the 20 disk case have been obtained also with Recursive Fourier Propagation with less statistics. Since the full scale system takes at the order of ~ 100 times longer than the 20 disk system with Recursive Fourier Propagation, 80 disk calculations were not feasible with this method.

In order to predict the impact of tilted disks, for different maximum tilts in a range from 1 μrad to 3 mrad we sampled random tilts γ_x, γ_y from a uniform distribution for each dielectric disk in

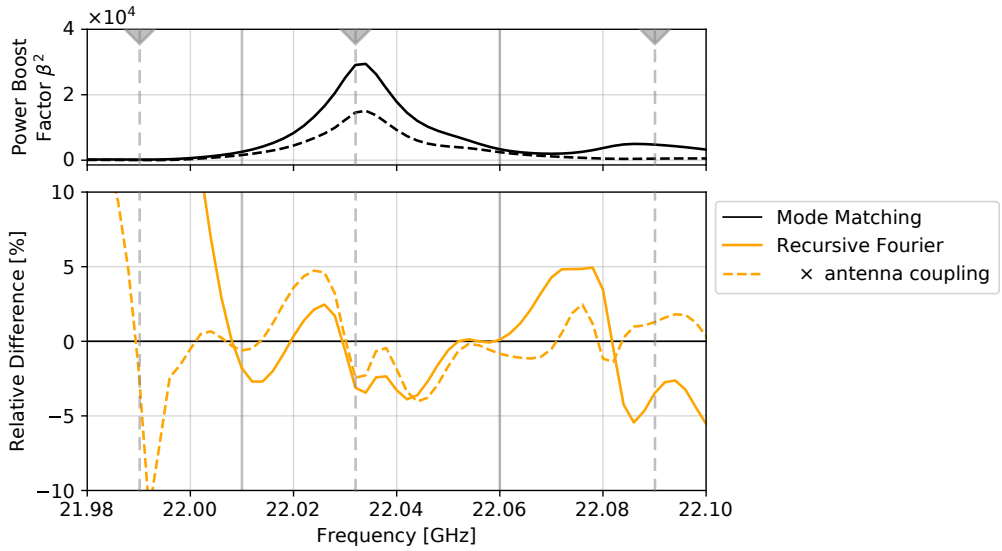

Figure 8.32: Comparison of boost factors and boost factor times antenna coupling calculated with Recursive Fourier Propagating and Mode Matching, corresponding to a boost factor from the 20 disk MADMAX prototype originally corresponding to the 50 MHz benchmark case, but now with random thickness variations of $\sigma = 10\,\mu\text{m}, \xi = 35\,\text{mm}$ for all disks. The upper sub-panel shows the boost factor calculated with the Mode Matching method for orientation. The lower sub-panel shows the relative difference between the result from Mode Matching and the result from Recursive Fourier Propagation. The vertical dashed markers indicate the frequencies at which the beam shape is compared in figure 8.33.

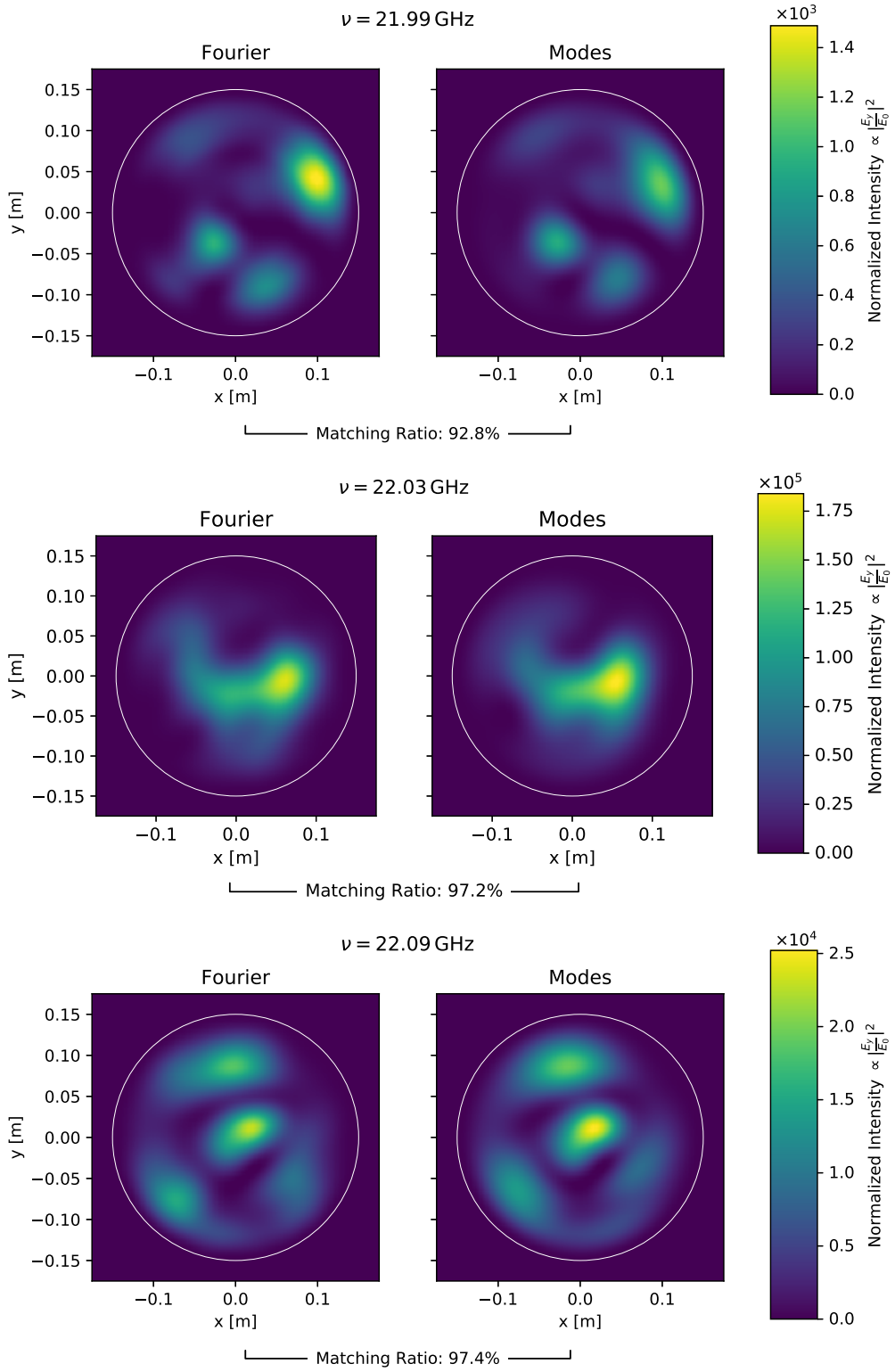

Figure 8.33: Comparison of beam shapes obtained with the Recursive Fourier Propagation method and Mode Matching for the boost factor from figure 8.32. The matching ratio quantifies how much power an antenna would receive from one beam, if the antenna is perfectly matched perfectly to the other beam in the comparison.

the dielectric haloscope. The resulting power boost factors multiplied with antenna coupling are shown in the top row of figure 8.34, for the prototype booster on the left and full scale MADMAX on the right. For each maximum tilt, a large set of random samples were generated, corresponding to the lines of identical color in the figure.

We find that tilts of 0.3 mrad start to become relevant at the $\mathcal{O}(10\,\%)$ level for the shape of the boost factor curve of the small scale 20 disk prototype and 0.1 mrad for the large scale 80 disk system. This corresponds to approximately $100\,\mu$m/30 cm for the prototype and $100\,\mu$m/1 m for the large scale system, i.e., absolute positioning of the disks is much more important than tilts, cf. section 5.3. Also notice that the disks in the large scale system have a 3 times larger diameter, so the phase changes over the disk for the large scale system with 0.1 mrad tilt are the same than the phase changes caused by a 0.3 mrad tilt in the small scale system. In this sense we see again, analogous to the 1D studies in chapter 5, that the amount of distortion we can accept does approximately not depend on the number of disks actually installed.

In order to predict the impact of transverse thickness variations, we applied the same procedure but for different scales of thickness variations σ. Here we consider a correlation length $\xi \sim \emptyset/10$. This gives surface elevation patterns similar to the ones previously measured by our collaborators [167]. Also notice that this corresponds to similar length scales relevant for the beam shapes of the first four m-modes. Hence, those modes are essentially sufficient for this calculation.

The results of these calculations are shown in the middle row of figure 8.34. The dark green lines, corresponding to a thickness variation of $2\,\mu$m are still very close to the case of an ideal disk, while $5\,\mu$m already give deviations of approximately 20%, for both the 20 and 80 disk systems. Considering the relative phase change caused by the effect, cf. equation (6.10), $10\,\mu$m thickness variations for a 1 mm thick disk are analogous to a variation the dielectric constant ϵ at the order of 2 % over the same correlation length. Also explicitly notice that thickness variations with the same scale σ again lead to a comparable effect on the boost factor, when comparing the 20 and 80 disk cases, i.e., the tolerable thickness variation is approximately independent of the number of actually installed dielectric disks.

Shorter correlation lengths $\xi \sim \lambda/4$ ('surface roughness') have been studied with the Recursive Fourier Propagation method for 20 disks. The same calculation using Mode Matching would require a significantly larger number of modes, which makes this calculation numerically unstable.

We show the corresponding results in the bottom row of figure 8.34. Compared to the transverse thickness variation considered before the requirement for σ is relaxed by at least a factor of 3, and the power boost factor is reduced much more uniformly and predictably. This is intuitive, since the length scales relevant for the dominating modes are more comparable to the larger correlation lengths. Here we considered small correlation lengths $\xi \sim \lambda/4$ which are well below the relevant length scale for the lower booster eigenmodes. Thus, the effect on the modes is approximately the same for different samples of surface roughness – in contrast to the thickness variations above, where the same scale σ leads to much more variance in the power boost factor.

Besides the effect on the power boost factor we show the impact on the beam shape of these effects in figure 8.35. It is evident that the different deformations alter the beam shapes on a similar scale than the size of distortions of the disks in the booster.

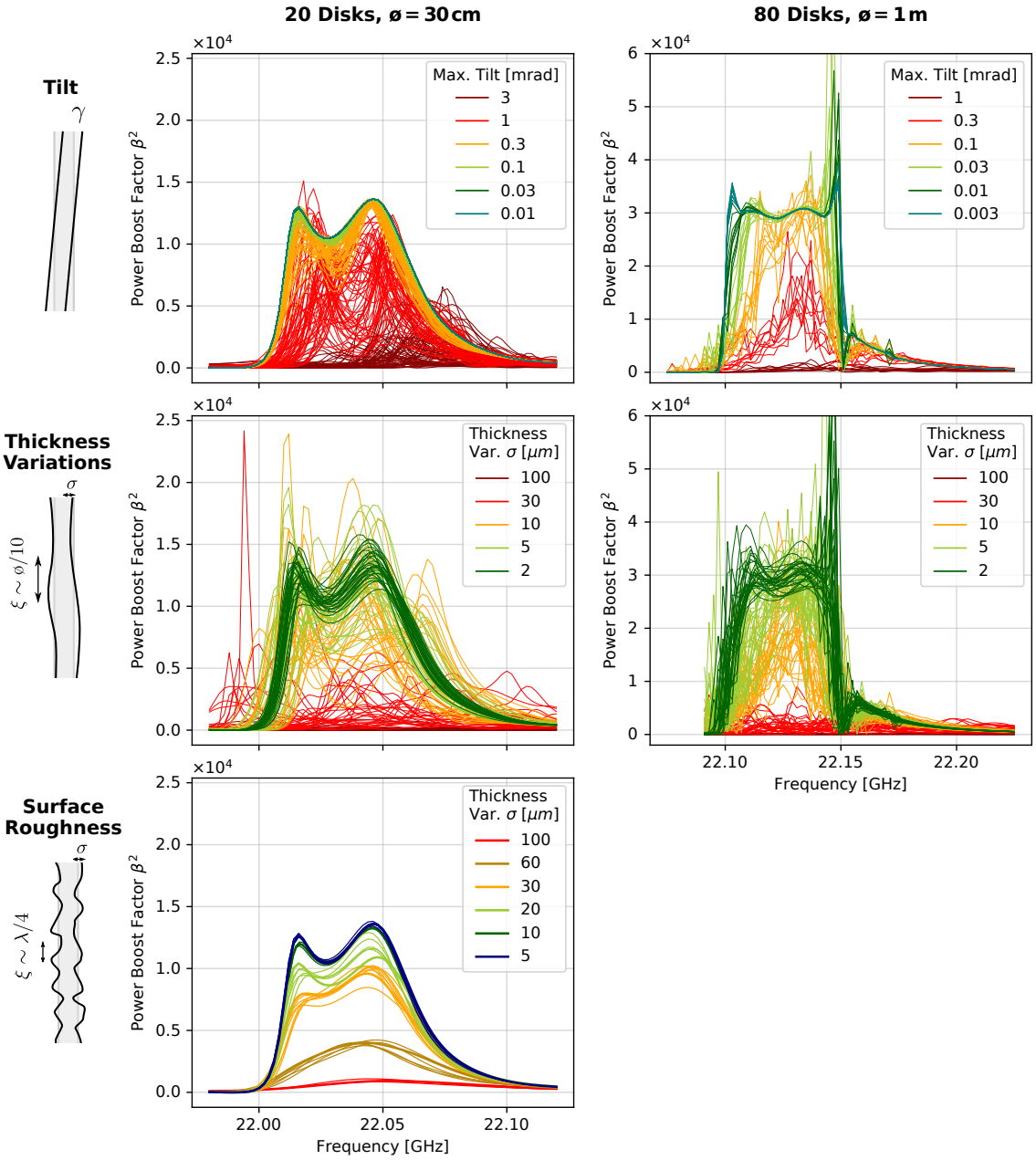

Figure 8.34: Effect of different transverse thickness variations on the power boost factor times antenna coupling. The left column shows the results for a 20 $LaAlO_3$ disk booster with 30 cm disk diameter, the right column shows the results for a 80 $LaAlO_3$ disk booster with 1 m diameter, both for the previously discussed benchmark boost factors with a bandwidth of about 50 MHz. The top row shows randomly tilted disks, where the maximum tilt in both x and y direction of each disk is as indicated in the legends. The middle row shows transverse thickness variations of the dielectric disks with a correlation length of $\xi \sim \phi/10$ and the scale σ of the thickness variation as indicated in the legends. The bottom row shows the same but for a correlation length of $\xi \sim \lambda/4$.

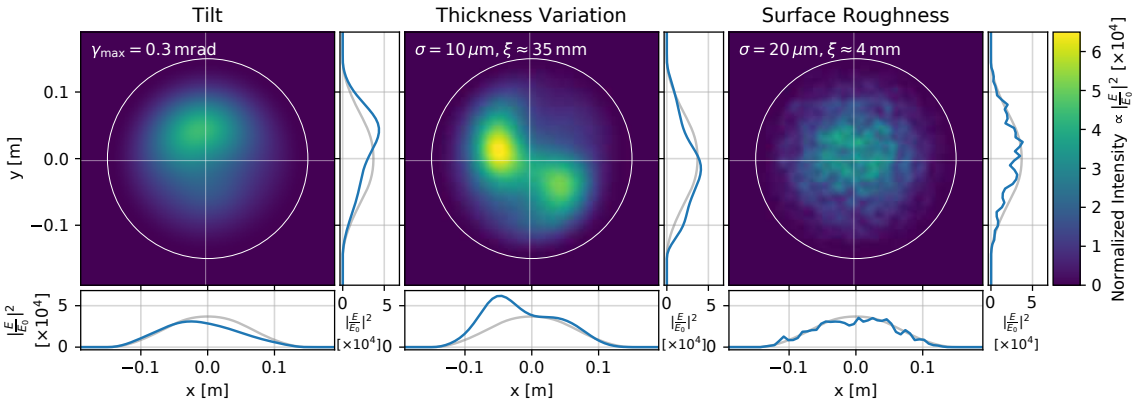

Figure 8.35: Effect of different transverse thickness variations on the beam shape. We show an example for the deterioration of the beam shape for the 20 disk prototype booster as in figure 8.34 at a frequency of 22.03 GHz. The effect of a maximum disk tilt of 0.3 mrad is shown on the left, the effect of a thickness variation ($\sigma = 10\,\mu\mathrm{m}, \xi = 35\,\mathrm{mm}$) is shown in the middle, and the effect of a surface roughness ($\sigma = 20\,\mu\mathrm{m}, \xi = 4\,\mathrm{mm}$) on the right. The main panels show the intensity profile, while the sub-panels show cuts through the x and y-axes. The blue curve shows the intensity profile of the plotted case, while the light gray curve show the ideal case without any distortion of the booster.

Numerical Results for Scaling

For the final operation of a dielectric haloscope like MADMAX it is important to understand how these results scale with the boost factor bandwidth, as well as other parameters like the number of disks, dielectric constant, and others. A full numerical study covering a broad range of these dimensions would be enough material for a separate thesis. However, we conducted some first studies confirming some basic expectations.

In order to estimate the effect of changing the bandwidth, we conducted the same study for thickness variations with the 20 disk setup as above for a set of bandwidths between 5 MHz and 250 MHz. We chose $\xi = 35\,\mathrm{mm}$, since this had the largest effect in the results presented above. For each bandwidth and thickness variation scale σ an ensemble of ~ 50 boost factors (multiplied with antenna coupling) corresponding to different randomly deformed boosters has been obtained. The boost factor which can be used in an experimental setup is given by the minimum boost factor from the ensemble at each frequency. We therefore consider the reduction of the area under the power boost factor which is still enclosed by all boost factor curves. In order to estimate a statistical uncertainty, we consider the reduction when only taking into account half of the obtained cases compared to the previous result when taking into account the full ensemble.

The result of this calculations is shown in figure 8.36. The area under the boost factor curve is reduced in a similar manner than for losses as in section 5.4. Thus, thickness variations set a similar limit to the minimal feasible boost factor bandwidth depending on the scale of thickness variations. A parametrization as in section 5.4 is hard to extract from the amount of data available, but we can roughly estimate for a reduction of less than 25 % the bandwidth cannot be below

$$\Delta\nu_{\mathrm{crit}} \sim 50\,\mathrm{MHz}\left(\frac{\sigma}{2\,\mu\mathrm{m}}\right), \tag{8.14}$$

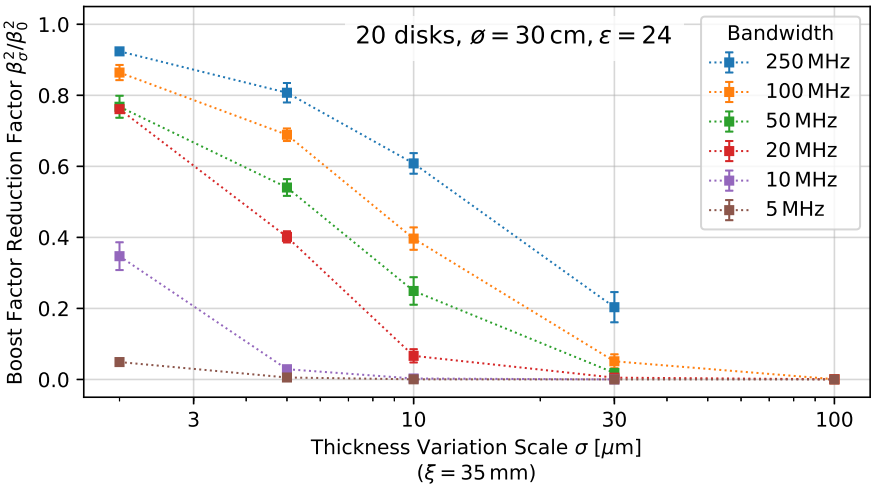

Figure 8.36: Reduction of the usable area under the power boost factor curve as a function of thickness variations σ for a correlation length $\xi = 35\,\text{mm}$. The data points indicate the results from 3D simulations, while different colors correspond to different boost factor bandwidths. The straight dotted lines are interpolations solely to guide the reader's eyes.

for $\xi \sim \text{ø}/10$ at a frequency of 22 GHz where these simulations have been performed. Unlike the 1D studies, this does not take into account that a given set of deformed dielectric disks may be readjusted to optimize the boost factor curve again (reoptimization). We will discuss this possibility briefly below.

A more quantitative understanding of the bandwidth dependency can be gained by performing faster 2D simulations. As an example we performed 2D simulations using the Recursive Fourier Propagation method for tilted disks. Unlike above, here we used booster configurations with sapphire disks ($\epsilon = 9.4$) and 20 cm diameter, in which all disks had a distance of 8 mm to each other. This is comparable to the experimental setup discussed in part IV of this thesis. Instead of reoptimizing the disk positions, we simply increase the number of dielectric disks to make the system more resonant. Thus, a higher number of disks corresponds to a different boost factor bandwidth. For each number of dielectric disks we optimized the scale of maximum tilt in the system until the minimum boost factor from 20 randomly sampled boosters approached an area of 80 % of the ideal boost factor. We call this the allowable tilt scale. Errors on this value can be estimated from the convergence of the optimization.

The result is presented in figure 8.37. The obtained allowable tilt scales as a function of disk number are shown as squares in the upper panel. Since here the bandwidth decreases with disk number, the allowable tilt scale also decreases with disk number. Remembering that the tilt essentially affects the phase of the propagating waves proportional to the amount of tilt, we naively expect the allowable tilt to scale like allowable phase errors in the 1D case. We have discussed in section 5.3 that tolerable phase errors should scale as $\propto 1/\sqrt[4]{\beta^2}$. A curve following this law is indicated as a green dashed line in the figure, the residual in terms of the ratio to this estimate is shown in the lower panel. Since the area law fixes the area under the boost factor curve, this does also parameterize the bandwidth dependency, i.e., the allowable scale is approximately

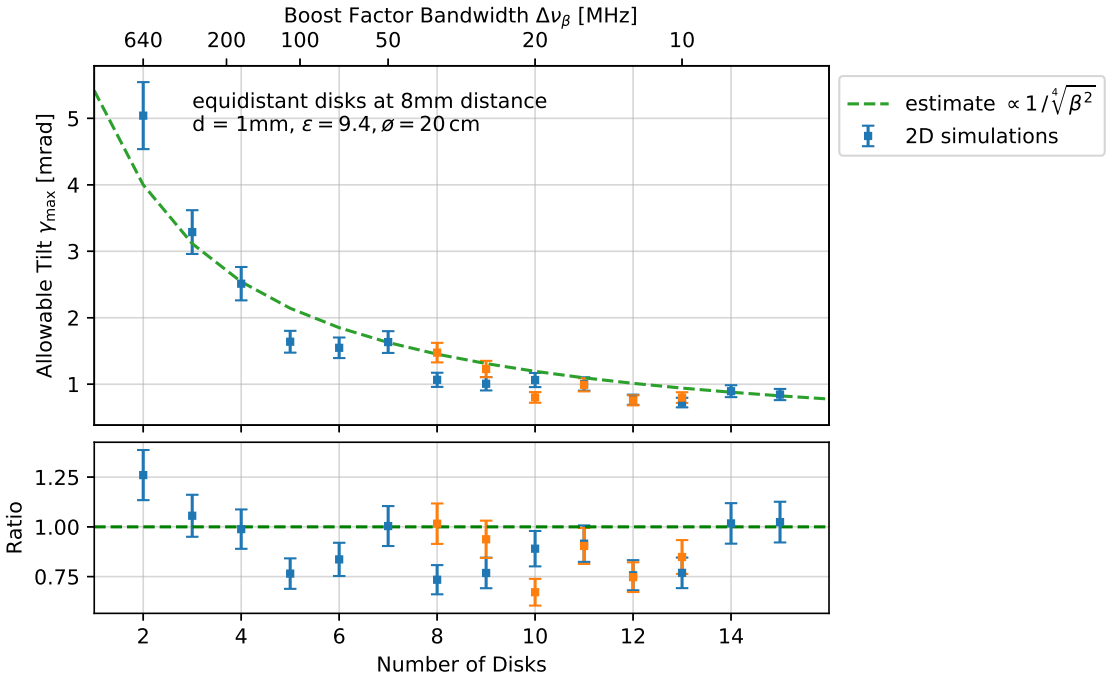

Figure 8.37: Scaling of acceptable tilt against number of disks for equidistant Sapphire disks with a diameter of 20 cm at a distance of 8 mm each, in 2D using Recursive Fourier Propagation. The upper panel shows the tilt which leads to a reduction of the usable boost factor at the order of 20 %, as defined in the text. The squares denote the data points from simulations with 10 MHz resolution (blue) and 2.5 MHz resolution (orange), while the green dashed line is an estimate inversely proportional to $\sqrt[4]{\beta^2}$. The secondary axis on the top indicates the corresponding boost factor bandwidths $\Delta\nu_\beta$. The lower panel shows the ratio of the data points with the estimate.

$\propto \sqrt[4]{\Delta\nu_\beta/N}$ with N the disk number. Notice that unlike losses these phase errors do not scale independently of disk number. However, changing the disk number in MADMAX by one order of magnitude gives a change in the constraint on the phase errors by less than a factor of two, i.e., in practice the dependence on the disk number is rather weak and can be treated as constant at zeroth order.

Analytical Understanding in Terms of Mode Mixing

We can gain a deeper understanding of these results by considering the structure of the mode mixing matrix P as defined in section 6.3. Only taking into account the mode mixing effect from the variations $\Delta z(x, y)$ without further propagation, it is given according to equation (6.15) by

$$P_{m\ell}^{m'\ell'} = \int_{\mathbb{R}^2} E_{m\ell}^*(r,\phi) E_{m'\ell'}(r,\phi) \exp\left[ik_0 \Delta z(r,\phi)\right] \mathrm{d}A, \tag{8.15}$$

with $k_0 = n\omega$. Remember that P is defined for the propagation within one specific disk or air gap in the booster, cf. section 6.3, i.e., in a realistic booster we have a different P for each disk and air gap. The off-diagonal elements in $P_{m\ell}^{m'\ell'}$ directly give the amplitude at which the mode (m', ℓ') is excited, if the amplitude in mode (m, ℓ) was unity before encountering the thickness variation.

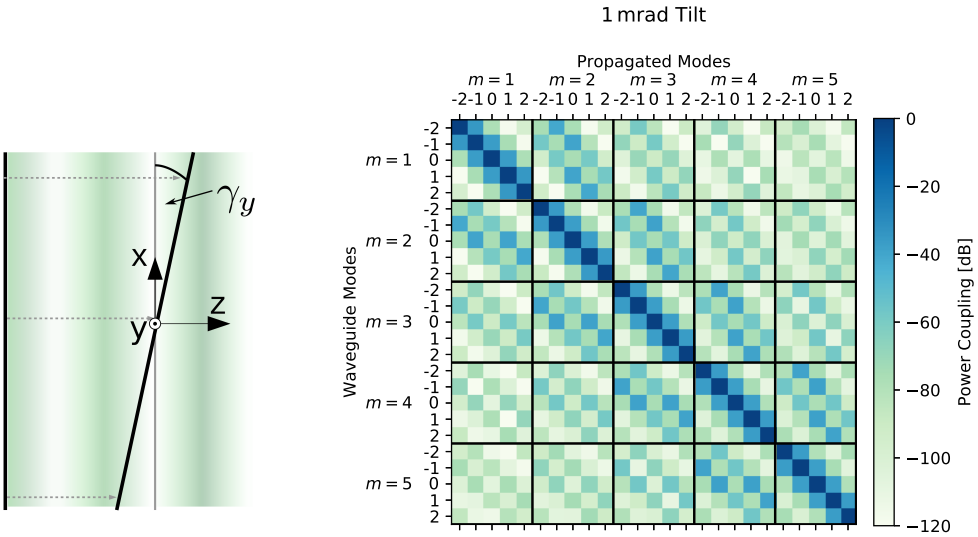

Figure 8.38: **Left:** Effect of a relative tilt γ_y of two disks to a propagating wave, linearly changing the phase depth of the gap between the disks. Tilts γ_x around the x-axis are analogous. **Right:** Result of a numerical calculation of the mode mixing matrix elements $|P_{ml}^{m'l'}|^2$ caused by a 1 mrad tilt. For the MADMAX prototype setup, i.e., $\varnothing = 30\,\text{cm}$, and at a frequency of 20 GHz. The sub-blocks are the mixing matrices for a fixed m.

Notice that if there is no thickness variation, $\Delta z = 0$, equation (8.15) is simply the overlap integral between the individual orthogonal modes, which gives a diagonal mode mixing matrix, i.e., $P_{m\ell}^{m'\ell'} = \delta_{m\ell}^{m'\ell'}$ by definition. For $\Delta z \neq 0$ the matrix can have off-diagonal elements. Thus, the transverse phase differences of the propagated field induce an additional coupling between the modes.

Let us first look at two specific examples. For the case of a propagation between two tilted disks we illustrate the expected phase change on the left side of figure 8.38. It is linear over the tilted disk surface. On the right side of figure 8.38 we show an example for the resulting mode mixing matrix P taking a 1 mrad tilt into account for a disk diameter of 30 cm. The resulting matrix is still close to a diagonal matrix, while a tilt essentially couples neighboring modes with similar mode indices.

In contrast, transverse thickness variations add more random phases as illustrated on the left in figure 8.39. On the right we show the mode mixing matrix for the 30 cm diameter disks as before with a transverse thickness variation of $\sigma = 10\,\mu\text{m}, \xi = 35\,\text{mm}$ in vacuum. Compared to the tilt the couplings are lower but much more spread among the neighboring modes. This is intuitive since these thickness variations induce changes over smaller length scales than the tilt, and therefore excite higher modes more easily.

We can quantitatively understand these observations by considering analytical properties of the mixing matrix P in more detail. First of all, the exponential phase factor is only relevant at places (r, ϕ) on the disk where both $E_{m\ell}^*(r,\phi)$ and $E_{m'\ell'}(r,\phi)$ are large. In particular for the diagonal elements $(m,\ell) = (m',\ell')$ we have $E_{m\ell}^*(r,\phi)E_{m'\ell'}(r,\phi) = |E_{m\ell}(r,\phi)|^2$, i.e., the phase factor is most important at places with the highest power in the booster. Another consequence

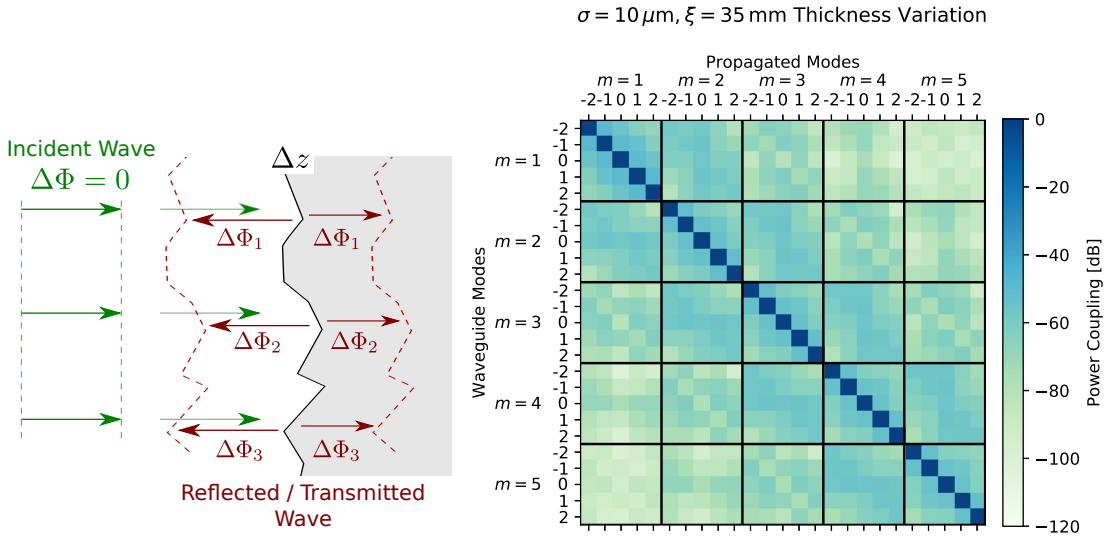

Figure 8.39: **Left:** Effect of a thickness variation to a propagating wave, randomly changing the phase depth of the gap between the disks along the disk surface. **Right:** Result of a numerical calculation of the mode mixing matrix elements $|P_{ml}^{m'l'}|^2$ caused by a 10 μm surface roughness over correlation lengths of $\xi = 35$ mm. For the MADMAX prototype setup, i.e., $\varnothing = 30$ cm, and at a frequency of 20 GHz. The sub-blocks are the mixing matrices for a fixed m.

can be seen by comparing the length scale ξ over which the phase factor varies with the length scale $k_{c,m\ell}^{-1}$ over which the fields of the modes are changing.

- $k_{c,m\ell}^{-1} \ll \xi$: If ξ is much larger than the length scales of the modes, the phase factor becomes effectively constant and can be pulled out of the integral in regions where Δz is approximately constant. We then have

$$P_{m\ell}^{m'\ell'} \sim \exp(ik_0\Delta z)\ (P_0)_{m\ell}^{m'\ell'}, \tag{8.16}$$

  where P_0 is the mixing matrix for the unperturbed system. Thus, this limit corresponds to a constant phase error, directly comparable to a mispositioning of the disk or overall thickness error at the order of Δz.

- $k_{c,m\ell}^{-1} \gg \xi$: If ξ is much smaller, we can divide the integration domain in pieces i on which the modes are piece-wise constant. Taylor expanding[1] up to second order in $k_0\Delta z$ and rewriting the remaining integral over the phase factor as an average over $\boldsymbol{x}_i$, we arrive at

$$P_{m\ell}^{m'\ell'} \approx \sum_i E_{m\ell}^*(\boldsymbol{x}_i)E_{m'\ell'}(\boldsymbol{x}_i)\ \left[1 - \tfrac{1}{2}k_0^2\langle\Delta z(\boldsymbol{x})^2\rangle_{\boldsymbol{x}_i} + ik_0\langle\Delta z(\boldsymbol{x})\rangle_{\boldsymbol{x}_i}\right]\ \Delta\boldsymbol{x}_i \tag{8.17}$$

$$\sim (1 - \tfrac{1}{2}k_0^2\sigma^2)\ (P_0)_{m\ell}^{m'\ell'}, \tag{8.18}$$

  where in the last line we used $\langle\Delta z(\boldsymbol{x})\rangle_{\boldsymbol{x}_i} = 0, \langle\Delta z^2\rangle_{\boldsymbol{x}_i} = \sigma^2$ independent of the individual patch i when integrating over a sufficiently large area. We see that the oscillations in the phase factor average out any additional phase factor while integrating over regions where

[1] This is justified since the scale of the deformations is much smaller than the photon wavelength, i.e, $k_0\Delta z \ll 1$.

the modes are approximately constant. Therefore, there is no net phase error. However, the oscillations in the phase factor amount to partial cancellation of the field with itself. Therefore, in this limit we effectively have an additional loss mechanism. Comparing the prefactor in equation (8.18) with the same effect of a $\tan\delta$ loss in the air gaps (phase depth π, $\epsilon = 1$), this corresponds to losses at the order of

$$\delta_{\Delta z} \sim 4\pi \left(\frac{\sigma}{\lambda}\right)^2 \sim 5 \times 10^{-5} \left(\frac{\sigma}{30\,\mu\text{m}}\right)^2 \left(\frac{\nu}{20\,\text{GHz}}\right)^2, \tag{8.19}$$

and more generally within a dielectric disk with arbitrary dielectric constant ϵ and thickness d

$$\delta_{\Delta z} \sim 2\pi \left(\frac{\sqrt{\epsilon}\sigma^2}{\lambda d}\right) \sim 2 \times 10^{-3} \left(\frac{\epsilon}{24}\right)^{\frac{1}{2}} \left(\frac{\sigma}{30\,\mu\text{m}}\right)^2 \left(\frac{1\,\text{mm}}{d}\right) \left(\frac{\nu}{20\,\text{GHz}}\right). \tag{8.20}$$

Thus, the effects within the disks are dominant. This result is consistent when compared with the numerical results in the bottom left panel in figure 8.34 and the 1D estimates in section 5.4, when taking into account that the 1D estimates assume a phase depth of π of the lossy regions (the disks here have phase depth ~ 2).

- $k_{c,m\ell}^{-1} \sim \xi$: In the intermediate range, where both scales are comparable, the phase variations modify the propagated fields on length scales of the modes. Here both phase change and loss is relevant. Moreover, while in the above two cases we had $P_{m\ell}^{m'\ell} \approx 0$ for $(m,\ell) \neq (m',\ell')$, this does not hold anymore. In practice, this means that during propagation the modes can excite each other, i.e., mixing between the relevant modes dominates. Notice that this happens for both the tilt effect in figure 8.38 and thickness variation in figure 8.39. However, for the tilt the correlation length is larger than for the thickness variation, leading to off-diagonal elements more close to the diagonal.

Notice that for a given ξ it depends on the specific mode (m,ℓ) which of the above regimes apply, i.e., unless $\xi \gtrsim \text{ø}$ there are always modes for which $\xi \sim k_{c,m\ell}^{-1}$ and mode mixing is relevant. Therefore, we see changes in the beam shape for all three correlation lengths corresponding to the cases in figure 8.35. However, power which is coupled to higher modes, that are not resonantly enhanced at the considered frequency or have high diffraction loss, will generally reduce the power boost factor.

We can verify above estimates by calculating P numerically for many realization of thickness variations and observing how it changes with ξ. Figure 8.40 shows the result of such a calculation for $\sigma = 10\,\mu$m. Other σ give analogous results. Here we used $\sim 10^3$ samples for the thickness variation at each scale. Each sample corresponds to one realization of thickness variation. Higher number of samples make the lines in the figure smoother. The top panel shows how the phase error for a single mode, $\Phi_m = \text{Arg}\left[P_{m,0}^{m,0}\right]$, changes with ξ. We also show the corresponding propagation length z in free space, related to the phase via $\Phi = k_0 z$ with $k_0 = 2\pi/\lambda$. We see that the phase errors increase when increasing ξ and approaches the value expected from $\sigma = 10\,\mu$m when the correlation length matches the disk diameter $\xi \sim \text{ø}$. The middle panel shows the lost power in a single mode, $1 - \left|P_{m,0}^{m,0}\right|^2$, as a function of ξ. Here the secondary axis shows the effective loss parameter $\delta_{\Delta z}$ in free space as defined above. We see that losses are large for low ξ. Lastly, the bottom panel shows how the magnitude of the mixing between two neighboring m-modes, $\left|P_{m,0}^{m+1,0}\right|^2$, behaves as a function of ξ. It is maximized near the region where ξ is comparable to

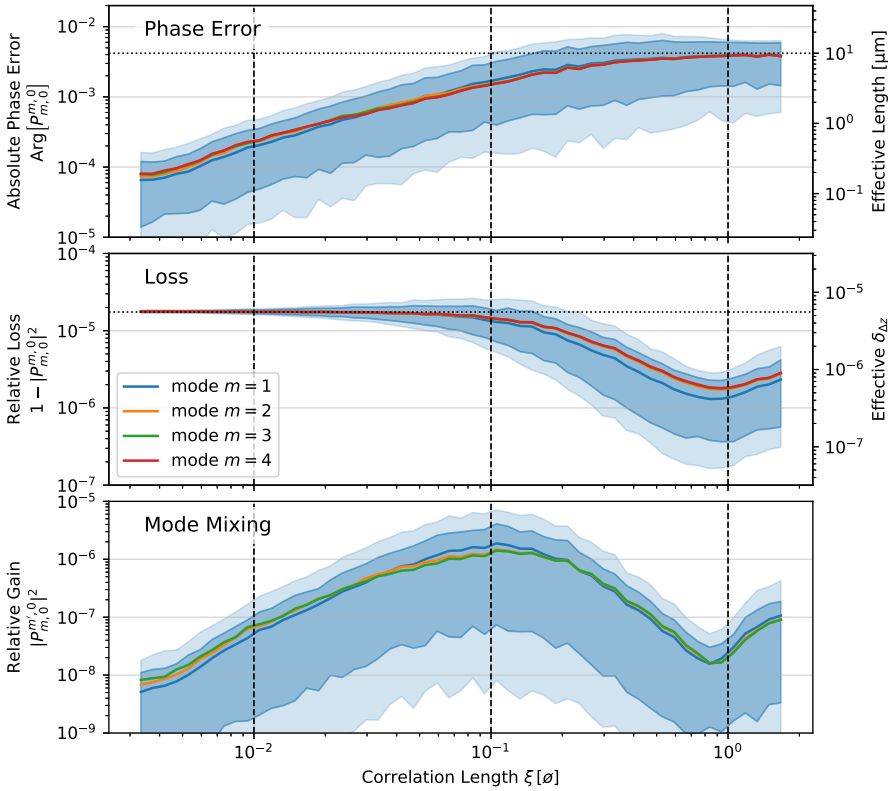

Figure 8.40: Behavior of various properties of the mixing matrix P as a function for the correlation length ξ of a 10 μm thickness variation in a vacuum gap. The top panel shows the phase shift in the self-coupling of the modes $P^{m,0}_{m,0}$. The secondary vertical axis shows the corresponding effective propagation length in free space. The middle panel the lost power in $P^{m,0}_{m,0}$, while the secondary axis shows the corresponding effective loss parameter $\delta_{\Delta z}$. The lower panel the magnitude of off-diagonal couplings $P^{m',0}_{m,0}$ with $m' = m+1$. The different colors correspond to different modes m. The lines correspond to the expectation value after averaging over many realizations of thickness variations. The dark blue regions correspond to the range of 70 % of the realizations of such thickness variations, the light blue to 95 %, respectively. For simplicity we only show the lowest mode here. The bands for the higher modes are analogous. The vertical dashed lines correspond to $\xi = ø/100, ø/10, ø$, comparable to the scales used for example in figure 8.34. The horizontal dotted lines correspond to the phase error expected from a uniform thickness error Δz (upper panel), and loss factor from a small correlation length $\xi \ll k_{c,m\ell}$ (middle panel). More details cf. main text.

the length scale of the modes. For a dielectric haloscope the relevant modes are in particular the lower modes $m = 1 \dots 4$ to which the axion-induced electric field couples most efficiently. Since they live on similar length scales, also the scales of ξ at which phase errors, mode mixing or effective losses are dominating are the same and approximately only given by the diameter of the disks $\varnothing$.

Disk Position Reoptimization

While it is hard to think of a mechanism to prevent losses apart from engineering more flat disks, the absolute position of the disks in MADMAX can be changed with μm accuracy, i.e., the phase depth of each free space gap can be adjusted on the level $\sim \mu\text{m} \times 2\pi/\lambda$ corresponding to phase shifts of $\sim$ few $\times 10^{-4}$ at 20 GHz. Notice that typical phase errors considered in figure 8.40 (top) are above this value. Hence, aligning the disks to more optimal positions may give a handle to compensate phase errors and potentially also mode mixing effects to some extent.

We consider the phase errors $\Phi^r_m = \text{Arg}\left[(P_r)^{m,0}_{m,0}\right]$ separately in different regions r with the same dielectric constant of the dielectric haloscope, i.e., each region corresponds to either a disk or free space gap. The phase errors in the fundamental mode $\Phi^r_1 = \text{Arg}\left[(P_r)^{1,0}_{1,0}\right]$ can be compensated by realigning the dielectric disks such that the thickness of region r is changed by $-k^{-1}_{z;1,0}\Phi^r_1$. Applying this to all regions, effectively sets the phase error for the fundamental mode in the whole haloscope to zero.

Notice that in our tilt studies the phase errors are automatically compensated, because we tilt around axes through the disk center, i.e., $\Phi^r_1 = 0$ due to symmetry. This is one reason, why tilts corresponding to up to 100 μm relative displacement of the disk edges are still acceptable, while the disk positions have to be adjusted an order of magnitude more accurate.

In addition, we also studied the compensation of the phase error for the above thickness variation studies with $\xi = \varnothing/10$. For simplicity, here we just multiplied all mixing matrices P_r for of all regions r with these phase factors, i.e., $P_r \to \exp\left(-i\Phi^r_1\right) P_r$ for all r. This procedure does the same than adding a corresponding length to the regions for small enough phase errors. The results for the power boost factor are presented in figure 8.41. Comparing to figure 8.34, we see that the acceptable thickness variation range can be improved by roughly a factor at the order of ~ 2, if one can compensate the phase errors in all regions. For surface roughness corresponding to short correlation lengths $\xi \sim \varnothing/100$ the loss effect is dominating, as argued above. Thus, realigning the disks cannot help to improve the boost factor for surface roughness.

In practice, such a compensation needs to happen by only realigning the disks, i.e., changing the phase depths of the air gaps. It is reasonable to assume that this way also small phase errors inside the disks can be compensated, since we can obtain similar optimized boost factors in the 1D model also with disk thicknesses randomly varied by a few μm around 1 mm. However, in 3D this is still to be demonstrated with dedicated simulations running optimizations using the 3D model, left for future studies. Also note that in addition the phase errors for higher modes $m \neq 0$ are different, i.e., mode mixing changes the optimal disk positions to maximize the boost factor. Hence, maybe even better results could be obtained by optimizing the boost factor with the 3D model.

Also note that another caveat on this reoptimization is that the boost factor in the experimental setup cannot be directly measured. Therefore, it has to be inferred from correlated quantities such as the reflectivity of the booster. We discuss the implications later in section 8.6.

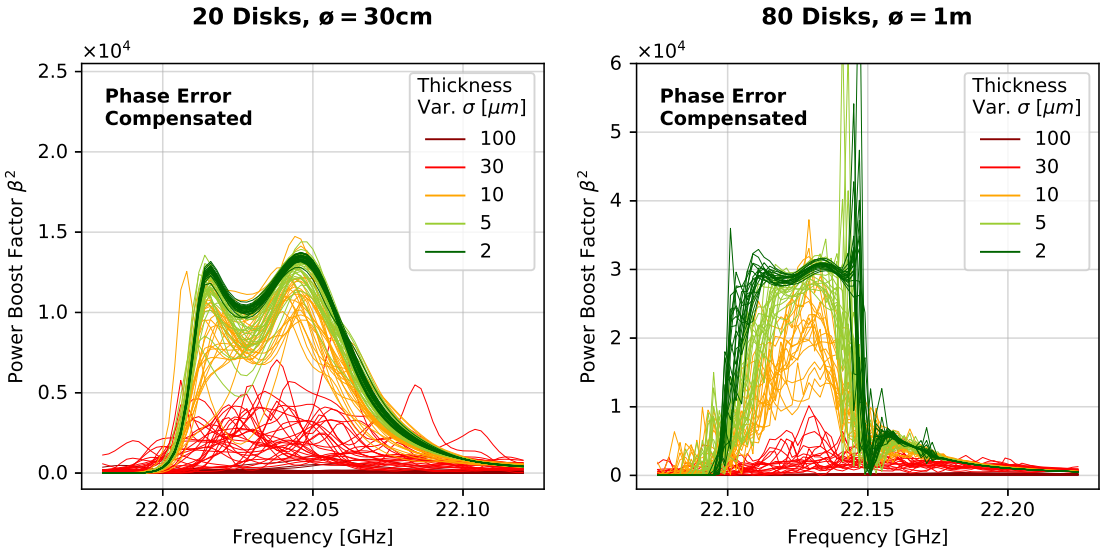

Figure 8.41: Effect of random thickness variations with a correlation length $\xi \sim \text{ø}/10$ analogous to the middle row of figure 8.34, but after compensating the phase errors $\Phi_1^r = \text{Arg}\left[(P_r)_{1,0}^{1,0}\right]$ in each region r, as described in the text.

In short. In order to have an impact on the benchmark power boost factors of less than 10 %, the following constraints need to be fulfilled: Tilts need to be kept smaller than 0.1 mrad (0.3 mrad) for the large-scale MADMAX booster (MADMAX prototype). Thickness variations over correlation lengths of $\sim$ ø/10 need to be at the order of $\sim$ 2 μm or smaller. Surface roughness, i.e., the thickness variation over small correlation lengths, needs to be not larger than 10 μm. These constraints can be translated to analogous requirements for the homogeneity of the dielectric constant over the disk by dividing twice the constraint with the disk thickness. For example, 2 μm thickness variations correspond to variations of ϵ of $\sim$ 4 μm/1 mm = 0.4 %. These constraints become tighter when decreasing the bandwidth or increasing frequency. The relative changes to the boost factor are approximately the same when keeping the bandwidth fixed, independent of disk number. The possibility of realigning the dielectric disks to more optimal positions can help to relax these constraints.

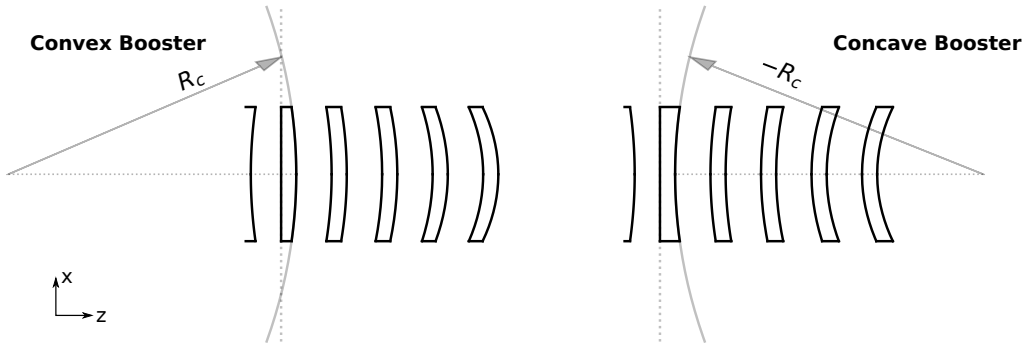

Figure 8.42: Sketch of a booster in which all free space gaps and disks are convex (left) or concave (right). R_c is the curvature radius of the disk surface if the other side of the disk is flat. R_c is measured from within the disk. The transverse thickness dependence of the other disks and free space gaps is chosen such that the effect on the phase of an electromagnetic wave traveling along z is the same for all disks and free space gaps during propagation. More details cf. main text. With an exaggerated curvature and not to scale.

8.5 Alternative Design Ideas for Booster

In this section we discuss some ideas to deliberately modify the boundary conditions of the ideal finite-size booster discussed before, in order to improve its 3D properties. In the picture of modes the goal is to change the eigenmodes of the booster, such that they do have more favorable properties in terms of coupling to the axion-induced field than the ones we found for the idealized booster with finite, but perfectly flat and parallel disks in section 8.3.1.

Lens-Shaped Booster

Convex lens-shaped disks have been initially thought of in order to reduce diffraction losses within the booster by focusing the electromagnetic power back inside the booster. However, we have seen that the diffraction loss of perfectly parallel disks is relatively small compared to the allowed range of $\tan\delta$, cf. section 5.4. Conversely, it may be possible to employ concave disks that slightly defocus the beam with still acceptable diffraction loss. In this section we present a preliminary calculation showing how such a booster could be designed and how it impacts the fundamental mode of the system. We consider a booster in which all regions have a convex or concave thickness variation, as outlined in figure 8.42.

In order to obtain the fundamental eigenmode of such a s system, we followed the same calculation as in section 8.3.1, i.e., we started with the axion-induced field over the disk surface and propagated it iteratively through air and disk multiple times. R_c is the curvature radius of the total thickness variation of the lens-shaped disks as seen from inside the disk, i.e., the thickness variation in polar coordinates is explicitly given by

$$\Delta z(r,\phi) \approx -\frac{1}{R_c} r^2. \tag{8.21}$$

The transverse thickness variation of the free space gaps was set analogously such that the effect on the phase front of the propagating wave $\mathrm{Arg}\,[E(x,y)]$ inside the disks and within the free space

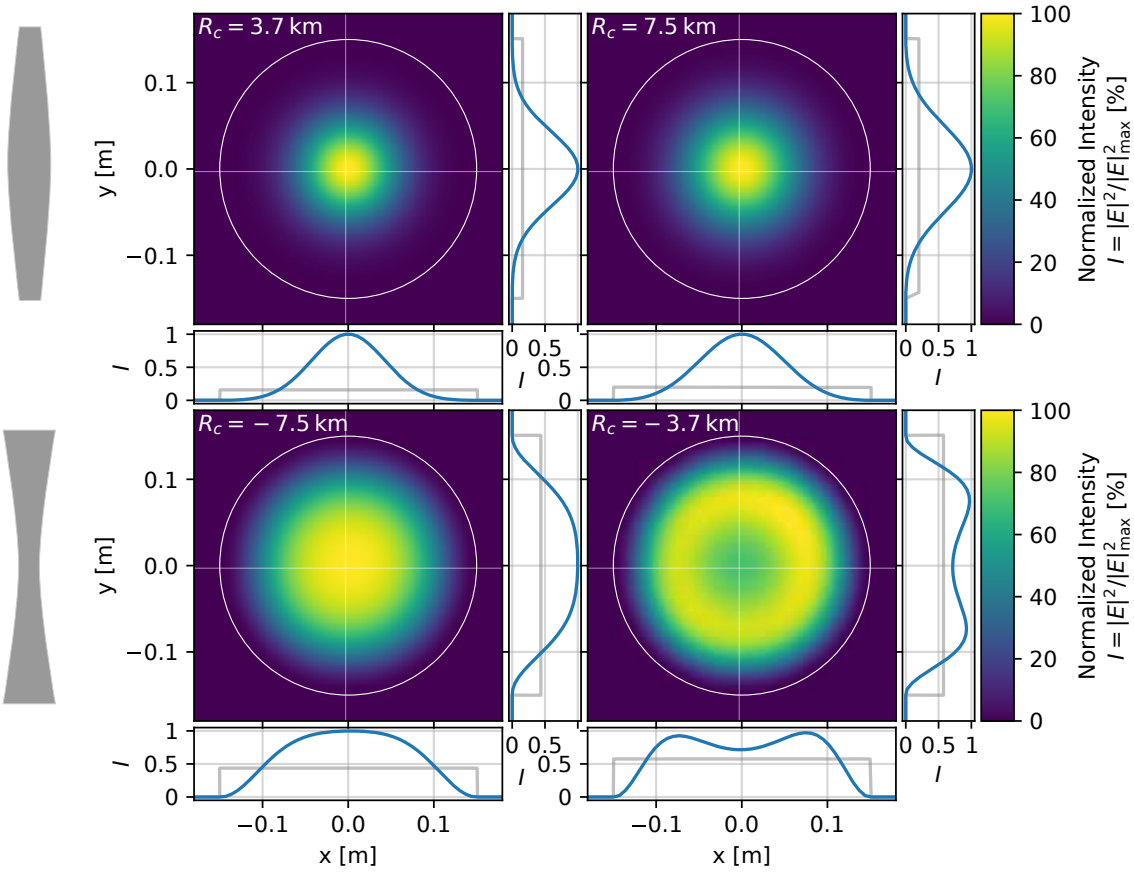

Figure 8.43: Beam shapes of the fundamental eigenmodes of a dielectric haloscope with disk diameter 30 cm for different lens-shaped gaps obtained with Fourier Propagation. R_c is the curvature radius of the lens-gaps as detailed in the main text. The main panels show the intensity distribution normalized to the maximum value. The sub-panels show cuts along the x and y-axes. The blue curves show the intensity profile of the mode, the gray curve the intensity profile of the axion-induced field, normalized to the same total power as the mode.

gaps is the same, cf. equation (6.8), i.e., for the free space gaps R_c in equation (8.21) is about one order of magnitude smaller leading to a more significant transverse thickness variation for the air gaps compared to the disks. We show the intensity profiles of the obtained fundamental modes in figure 8.43. As expected, if all regions are convex, the mode is focused, and if all regions are concave power is spread out more uniformly over the disk. Table 8.2 summarizes the properties of the obtained modes. While for more concave disks, the diffraction losses δ_d go up, this happens at an order of magnitude that may be still acceptable for a dielectric haloscope setup. On the other hand, the coupling $|\eta|$ to the axion-induced field improves as we go to more concave disks, leading to up to $\sim 10\,\%$ more power in the fundamental mode. Lastly, also the transverse momentum k_c goes down with more concave disks. This is intuitive, since a more spread out beam shape corresponds to a longer transverse wavelength.

Apart from defocusing the beam, we can understand the behavior by considering how the original waveguide eigenmodes introduced in section 6.3 behave in a region with convex transverse

Geometry		Axion Coupling	Propagation	
	R_c	$\lvert\eta\rvert^2$	k_c	δ_d
convex	3.7 km	55 %	$22\,\mathrm{m}^{-1}$	$\sim 6 \times 10^{-6}$
	7.5 km	52 %	$19\,\mathrm{m}^{-1}$	$\sim 1 \times 10^{-5}$
flat	∞	71 %	$16\,\mathrm{m}^{-1}$	$\sim 3 \times 10^{-5}$
concave	−7.5 km	79 %	$12\,\mathrm{m}^{-1}$	$\sim 5 \times 10^{-5}$
	−3.7 km	86 %	$1.8\,\mathrm{m}^{-1}$	$\sim 1 \times 10^{-4}$

Table 8.2: Properties of the fundamental eigenmodes of a dielectric haloscope with disk diameter 30 cm for different lens-shaped gaps obtained with Fourier Propagation. R_c is the curvature radius of the lens-gaps as detailed in the main text. $|\eta|^2$ denotes the coupling of the uniform axion field to the mode, k_c its transverse momentum, and δ_d the diffraction loss parameter between the dielectric disks as defined in the text.

thickness variation. If we want to increase the coupling to the axion-induced field, we need to be resonant also for higher modes. The fields of higher modes are located more at the outer regions of the disks. In order to compensate the smaller propagation constant k_z of the higher modes in the phase factor $\exp(ik_z z)$, the outer regions of the disks have to be slightly thicker, in order to give a resonance at the same frequency, corresponding to a concave transverse thickness variation.

This calculation demonstrates that in principle a better coupling of the fundamental mode to the axion-induced field is possible by changing the geometry of the booster disks in a controlled way on the level of several μm. The exact realization has to be tested with full 3D simulations of a booster in further studies taking into account also the feasibility of manufacturing such disks from an engineering perspective.

Others

As we have seen above, deliberate controlled changes to the boundary conditions can change the eigenmodes of the booster. Lens-shaped disks are one option to improve the coupling efficiency to the axion-induced field. In addition, one could imagine using different dielectric constants in the inner and outer region of the disks to achieve a similar effect. Using disks which have perturbations like slits in the outside regions, would increase diffraction loss in particular for the higher modes. Lastly, tiling the dielectric disks can have a crucial impact on their eigenmodes. Thus, understanding how the transverse design of the disks impacts the eigenmodes might allow us to optimize it for maximal boost factor. This kind of optimization is, however, very preliminary at the current stage, since it helps to slightly increase sensitivity at the $\sim \mathcal{O}(10\,\%)$ level – which is small compared to the $\mathcal{O}(1)$ impacts a too high loss mechanism might have on the boost factor. In addition, the feasibility of various disk types remains an open challenge for engineering.

In short. Lens-shaped disks or disk with other optimized designs may change the fundamental eigenmode of propagation within the booster and thus may be used to increase the coupling efficiency of the axion-induced field to this mode.

8.6 Boost Factor Calibration

Until now we have discussed the impact of systematic effects on the boost factor from a booster design perspective to set quantitative requirements for the experimental setup. Ultimately, the uncertainty on the power boost factor itself is what is relevant for the axion dark matter search. In particular we have assumed that the boost factor is a quantity deducible from known quantities which simply needs to be adjustable accurately enough. However, it is impossible to directly measure the power boost factor. In this section we hence investigate to which extent it is possible to derive constraints on the power boost factor and its systematic uncertainty from reflectivity measurements on a realistic booster including tilt and thickness variations of the disks. We thereby suggest a first procedure to obtain this uncertainty by a fit with a more simplified model. This study should be understood as a first step towards this important direction for the realization of a dielectric haloscope like MADMAX, and in order to pave the way for more detailed studies including further systematic uncertainties and more refined measures for the relevant errors.

This study is premature to give conclusive results for a large scale 20 or 80 disk system. Such systems have not yet been built within the MADMAX collaboration such that the final design and the resulting governing systematic uncertainties are still open. Here we consider a smaller scale system with only five dielectric sapphire disks, which can be directly compared to the experimental proof of principle setup we are going to discuss in the next part of this thesis.

A Simple Small-Scale Booster

Five dielectric disks allow to find disk positions to adjust the boost factor bandwidth quite freely within a range between $\sim$ afew MHz and $\sim$ 500 MHz respecting the area law. We show two examples in figure 8.44. The more narrowband boost factor on the right has several advantages: First of all, the frequency shift of the second mode compared to the fundamental mode is already at the order of $\sim$ 50 MHz. Thus, the narrowband boost factor contains significant contributions of the fundamental mode only within its main frequency range. It makes the results in general more easy to understand in terms of the effects of phase errors, mode mixing and loss on only the fundamental mode. Since in the ideal case the modes propagate independently within the booster according to the eigenmode approximation, it also justifies comparing to a 1D model in the ideal case. Moreover, the group delay clearly maps out the frequency position of the boost factor, while in the broadband case the correlation is less clear. Apart from this, the bandwidth of this boost factor equals roughly the one from the currently available receiver system of 50 MHz, cf. section 2.2, and therefore maximizes the achievable power boost within the receiver bandwidth. Lastly, the narrowband case is comparable to the benchmark cases with equidistant disk spacings that we will study in the experimental part of this thesis. For these reasons, in this section we will consider the $\sim$ 50 MHz configuration shown on the right of figure 8.44.

Figure 8.45 shows the correlation of the same boost factor as in figure 8.44 (right) with the group delay over a broader frequency range. It is worth to point out that the axion-induced field only couples dominantly to one of the resonances inside the system, i.e., only one of the resonances contributes significantly to the boost factor curve. When correlating a reflectivity measurement with the boost factor it is therefore important to correctly map the peaks in the reflectivity spectra with the boost factor.

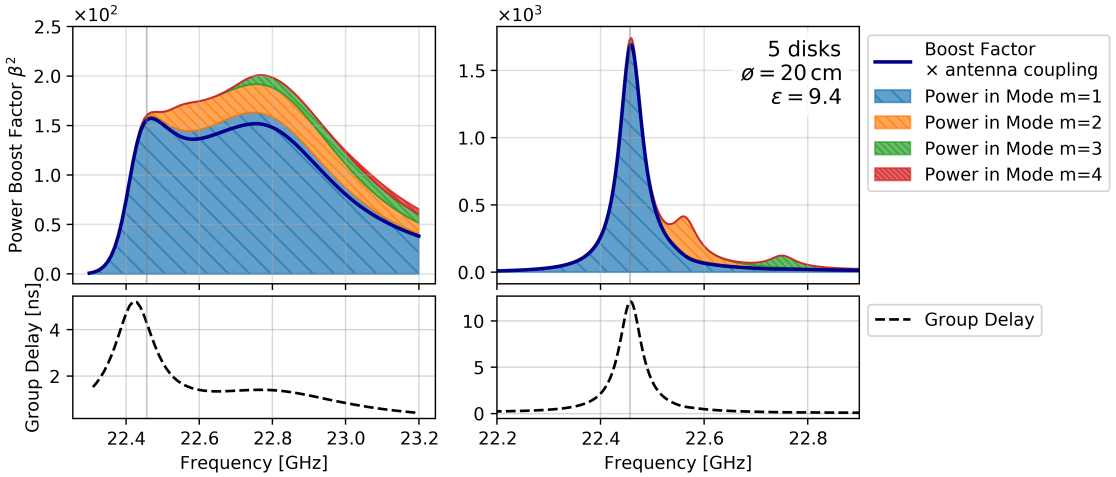

Figure 8.44: Two example boost factors with the corresponding group delay for a small scale 5 disk booster. The panels on the left resemble the same underlying disk spacings for a broadband boost factor configuration over $\sim$ 250 MHz. The upper panel shows the power boost factor in terms of the power contributed by the various modes. The bold blue line indicates the power times the coupling to a Gaussian beam antenna with a beam waist of $\sim$ 6.5 cm. The lower panel shows the group delay signal reflected on the booster using this antenna. The right panels are analogous but for a configuration corresponding to a $\sim$ 50 MHz boost factor bandwidth.

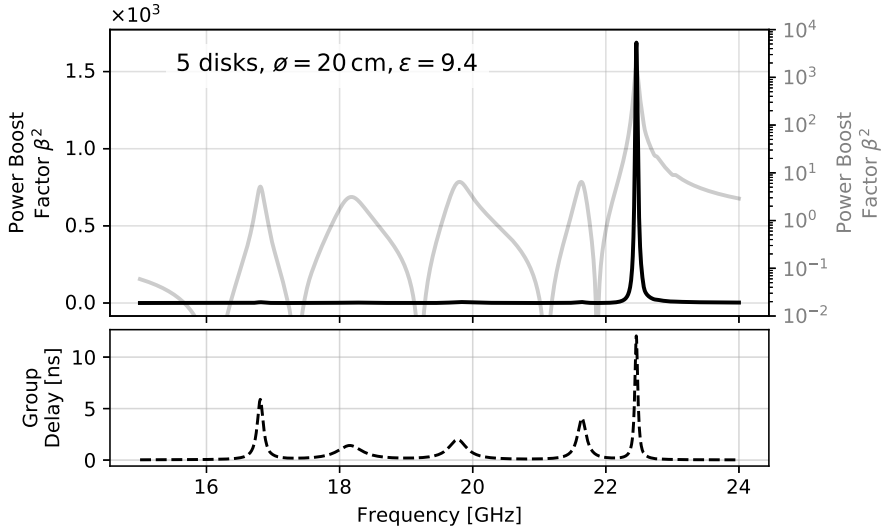

Figure 8.45: Correlation of the example boost factor (upper panel) with the corresponding group delay of the reflectivity (lower panel) as in figure 8.44 (right) but over an enlarged frequency range of 9 GHz. The black curve in the upper panel corresponds to the power boost factor in linear scale, the gray curve to the power boost factor in log-scale.

Monte Carlo Setup

Let us first assume that we have put the disks at exactly the positions predicted by the ideal model. Since our system is not ideal, but contains tilts and thickness variations, the measured reflectivity will be slightly different from the one predicted by the model. We call this difference the error on the reflectivity measurement. In this section we will investigate how this (measurable) error correlates with the equivalent (not measurable) error on the boost factor. To this end, we calculated the boost factor and reflectivity of the booster for a random set of over 2500 systems with random tilts and thickness variations.

We used Recursive Fourier Propagation since this approach needs to make less assumptions than Mode Matching, but still allows for computation of a large sample of 5 disk systems within a reasonable time. For the simulations we considered the frequency range from 22.2 GHz to 22.7 GHz with 7 MHz resolution. These values have been chosen as a trade-off between computation time and gaining sufficient information on the electromagnetic response. We considered an antenna that matches to a Gaussian beam with a beam waist located at the front disk surface of $w_0 = 6.5\,\mathrm{cm}$. All presented results take the antenna matching into account but neglect possible back reflections from the antenna back into the booster. We discuss the impact of antenna reflections later into account, when discussing our proof of principle setup in part IV, see section 10.3.

In order to study the correlation in the whole needed range, we set the scale for the tilts and thickness variations larger than what we expect in a realistic setup. For the thickness variation we consider a correlation length parameter $\xi = 3.5\,\mathrm{cm}$, which is similar than what we expect in our proof of principle booster discussed in part IV from previous disk thickness measurements. It is also at the same order of magnitude than $\xi \sim \varnothing/10$ which gave to strongest impact on the power boost factor in the simulation studies in section 8.4.3. The maximum scale for the tilt between two disks $\gamma_{\max}$ and the maximum scale for the thickness variation standard deviation $\sigma_{d,\max}$ have been set to

$$\gamma_{\max} = 10\,\mathrm{mrad}, \tag{8.22}$$

$$\sigma_{d,\max} = 100\,\mu\mathrm{m}. \tag{8.23}$$

Notice that these values are at least one order of magnitude beyond the requirements we found in the previous sections. In addition, for the experimental setup discussed in the next part of this thesis, tilts can be adjusted at the $\sim$ mrad level and we expect thickness variations at the order $\sim 10\,\mu$m, both values are respectively one order below the considered scale here. In order to uniformly 'scan' over differently strong perturbations of the setup, we sampled tilt scales s_γ and thickness scales s_d such that the total geometrical perturbation scale s_{tot}, defined by

$$s_{\mathrm{tot}} = \sqrt{\left(\frac{s_\gamma}{\gamma_{\max}}\right)^2 + \left(\frac{s_d}{\sigma_{d,\max}}\right)^2}, \tag{8.24}$$

is approximately uniformly distributed between 0 and 1. For each sampled (s_γ, s_d) we simulated the response of a corresponding booster. The maximum tilt between any two disks in both x and y direction is each s_γ, and the standard deviation of thickness variations in any region is s_d.

Figure 8.46 shows example results from about every fivehundredth run, selected in order to represent different total geometrical perturbation scales. We see that we have cases that are close

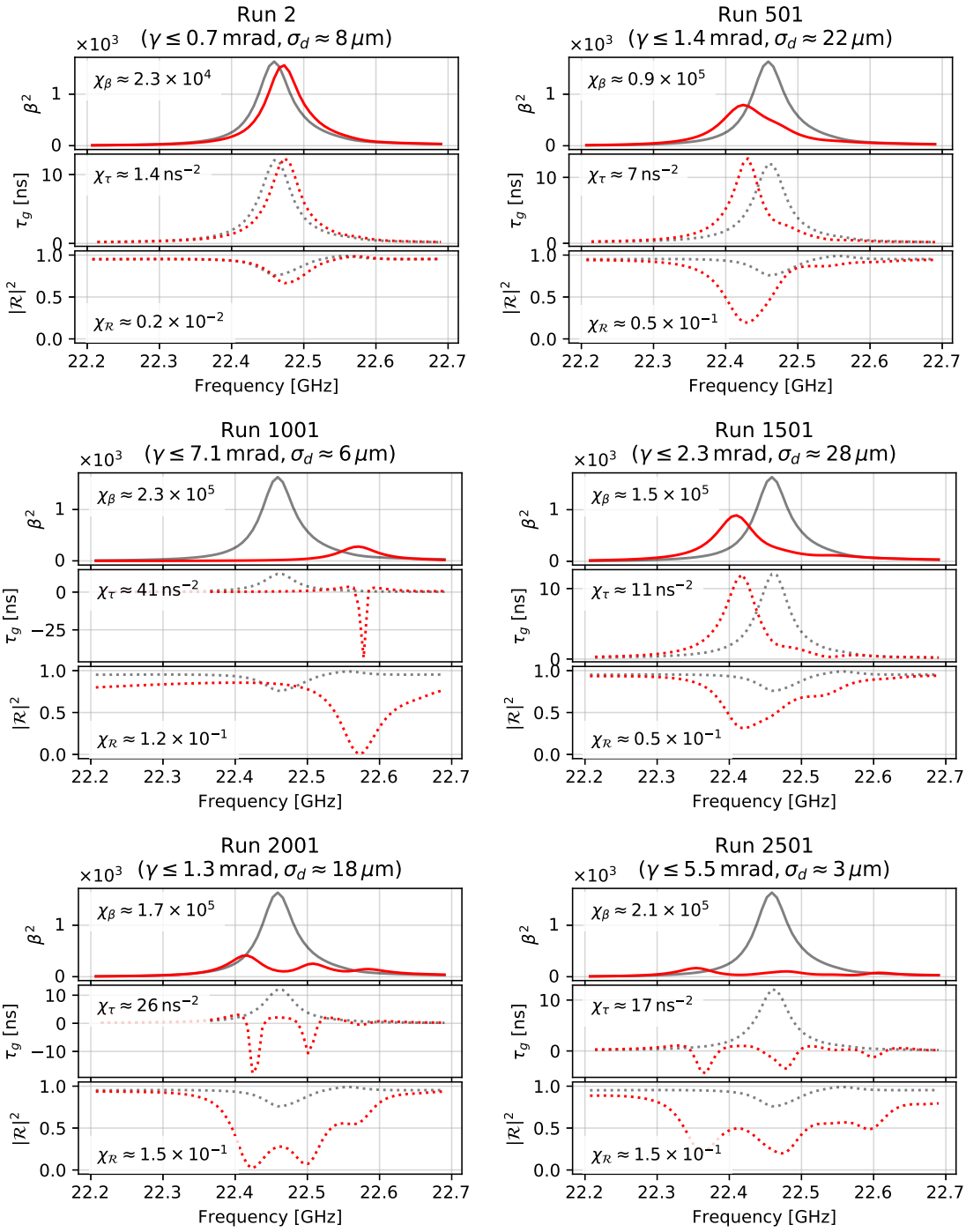

Figure 8.46: Example electromagnetic responses for six geometrically perturbed systems from the complete set of more than 2500 simulated boosters. The gray curves show the ideal case for orientation corresponding to figure 8.44 (right). The red curves show the results of the simulation for the perturbed systems. For each run the upper panels show the power boost factor, the middle panels the group delay and the lower panels the magnitude of the reflectivity. The χ^2-values denote the squared differences averaged over all shown frequencies between the simulated and ideal case.

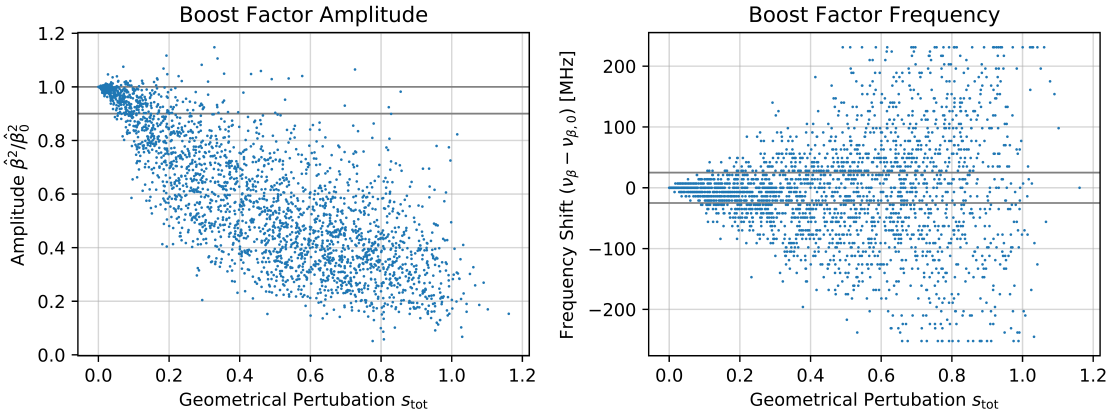

Figure 8.47: Scatter plot of various samples of more than 2500 perturbed boosters showing the correlation between resulting boost factor perturbations and the geometrical perturbation of the setup s_{tot} as defined in equation (8.24). **Left:** Power boost factor amplitude times antenna coupling relative to the same quantity from the ideal case. The horizontal gray lines show the band in which the power boost factor is reduced by less than 10 %. **Right:** Shift of the boost factor curve maximum with respect to the ideal case. The horizontal gray lines show the band in which the boost factor is shifted by less than half of its bandwidth.

to the ideal boost factor and reflectivity and some which are far away, i.e., we can study the full range. As expected, we can also already qualitatively see that there indeed is a correlation between the power boost factor and the reflectivity measurement. We study this quantitatively below. Also take note of the fact that the scale of the perturbation is similar for two runs this does not necessarily imply that the deviations in the electromagnetic response are comparable, cf. for example runs 501 and 2001. This illustrates again that some of the systematic effects can compensate each other to some extent, as we already argued at the end of section 8.2.3.

Boost Factor of the Non-Ideal Small-Scale Booster

Before studying the correlation of the boost factor with reflectivity, let us only look at the power boost factor and check the consistency with previous results. Figure 8.47 shows how the boost factor changes due to these perturbations of the system. On the left we show the effect on the amplitude. We consider the relative amplitude reduction $\hat{\beta}^2/\hat{\beta}_0^2$, where $\hat{\beta}^2$ is the maximum of the perturbed power boost factor curve and $\hat{\beta}_0^2$ the maximum of the unperturbed boost factor curve. Thickness variations and tilts introduce in general additional diffraction loss in the system and therefore reduce the power boost factor amplitude in nearly all cases. We see that the reduction is roughly linearly correlated with s_{tot}. As s_{tot} takes s_γ and s_d as independent, see equation (8.24), this is an indication that the thickness scale s_{d} and tilt scale s_γ increase the loss in a statistically independent manner, i.e., the mean systematic reduction of the boost factor expected from both effects and can be added in quadrature. This is confirms the physical intuition that both effects happen at different transverse length scales, as discussed in section 8.4.3, and are therefore independent.

On the right we show the effect on the boost factor frequency position. The difference $\nu_\beta - \nu_{\beta,0}$

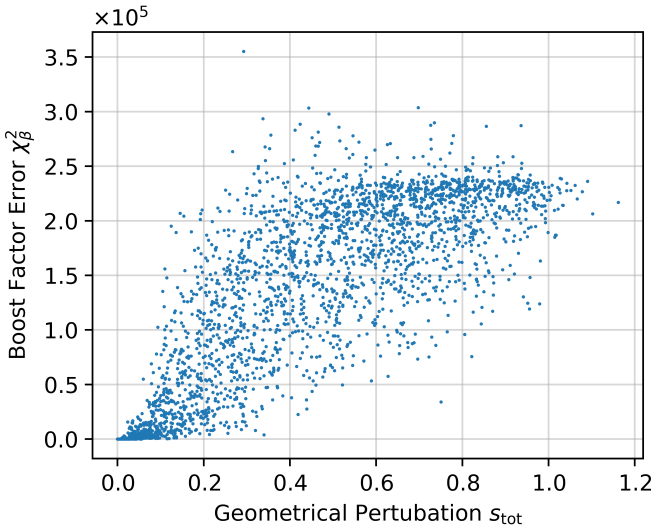

Figure 8.48: Same as figure 8.47 but showing the correlation of s_{tot} with the more general error on the boost factor χ^2_β which takes into account the whole simulated boost factor curve.

quantifies the shift between the frequency of the maximum from the perturbed boost factor curve ν_β and the frequency of the maximum from the unperturbed boost factor curve $\nu_{\beta,0}$. Besides the losses, the perturbations change the phase depths of the dielectric disks and air gaps in the booster and therefore may change the frequency position of the boost factor. However, opposing phase errors can average out, such that there remain many cases in which the frequency shift is still within the bandwidth of the ideal boost factor itself. The discretization in frequency is due to the 7 MHz resolution of the simulation. We see again, that for low enough s_{tot} the maximal frequency shift this effect causes, increases linearly with s_{tot}.

Notice that $s_{\mathrm{tot}} \gtrsim 0.1$ leads to a reduction in the boost factor amplitude considerably worse than 10 % and shift of the frequency position by more than half the bandwidth. This corresponds to less than about 1 mrad tilt and less than about 10 μm thickness variations. Therefore, this result is roughly consistent with the 20 and 80 disk values obtained in section 8.4.3 where we have argued that these values only have a weak dependency on disk number for a fixed boost factor bandwidth.

Besides the frequency shift and amplitude reduction, we may employ a more general measure for the error on the power boost factor taking into account all available data. Here we use the averaged squared difference defined as

$$\chi^2_\beta = \frac{1}{\nu_2 - \nu_1} \int_{\nu_1}^{\nu_2} \left|\beta^2(\nu) - \beta_0^2(\nu)\right|^2 \, \mathrm{d}\nu, \tag{8.25}$$

where (ν_1, ν_2) is the considered frequency range corresponding to all frequencies shown in figure 8.46, β_0^2 is the ideal power boost factor and β^2 is the power boost factor of the perturbed system for which we want to calculate the error. The corresponding χ_τ and $\chi_\mathcal{R}$ are defined analogously for the group delay τ_g and the magnitude of the reflectivity $|\mathcal{R}|^2$, respectively. Notice that the definition of the same quantity over the degrees of freedom, χ^2/ndf, is not useful here, since the calculation of χ^2 does not take into account any uncertainties and is in general not dimensionless. Hence, different values for χ^2 have to be compared to each other in order to define what

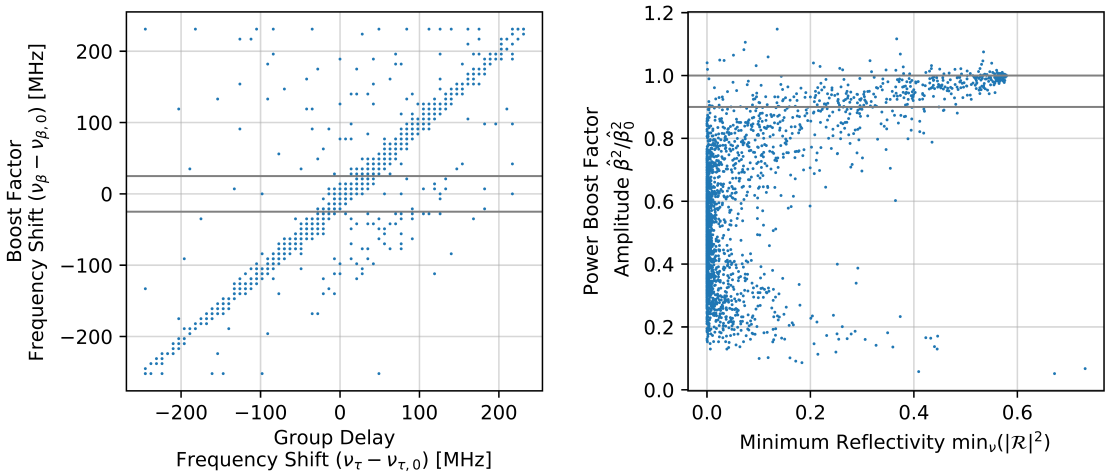

Figure 8.49: Scatter plot of various samples of the boosters with random tilts and thickness variations showing the correlation between the frequency shift of the group delay peak and boot factor peak (left), and the the correlation between the minimum reflectivity magnitude and the amplitude of the power boost factor peak (right).

corresponds to a good or bad match between both considered curves. Figure 8.48 shows how χ^2_β depends on the perturbation s_{tot} of the system. As expected, decreasing perturbations generally lead to a decrease in χ^2_β.

Correlation with Reflectivity

In the next step we study how the reflectivity measurement can give us information on the perturbation of the power boost factor. First, we consider again intuitive quantities such as frequency shift and magnitude reductions. As an example we show in figure 8.49 (left) how the frequency shift of the group delay correlates with the frequency shift of the boost factor peak. Notice that in some lossy systems the group delay can be negative, such as for example in runs 1001, 2001 and 2501 in figure 8.46. We will discuss negative group delays later in more detail in section 10.2. Due to the negative group delay peaks, here we determine the frequency of the group delay peak ν_τ as the frequency of the maximum from the squared group delay curve. It is evident that the group delay frequency position is correlated to the central boost factor frequency. Though, for very lossy runs the group delay can have many peaks, such as for example in run 2501. For these runs the correlation of the frequency position is obviously lost. This explains the outliers. In addition, the magnitude of the minima in the absolute reflectivity can give an indication of the losses inside the system as shown in figure 8.49 (right). Note that in the ideal system still some power is lost in the reflectivity measurement due to diffraction losses and antenna mismatch. These effects are already taken into account for the ideal power boost factor corresponding to the unperturbed booster. Hence, the full power boost factor including this loss is realized when the absolute reflectivity has a minimum with $\min_\nu(|\mathcal{R}|^2) \sim 0.6$.

We show in figure 8.50 how the amplitude of the power boost factor (upper panels) and the frequency shifts of the boost factor peak (lower panels) correlate with the errors obtained from a

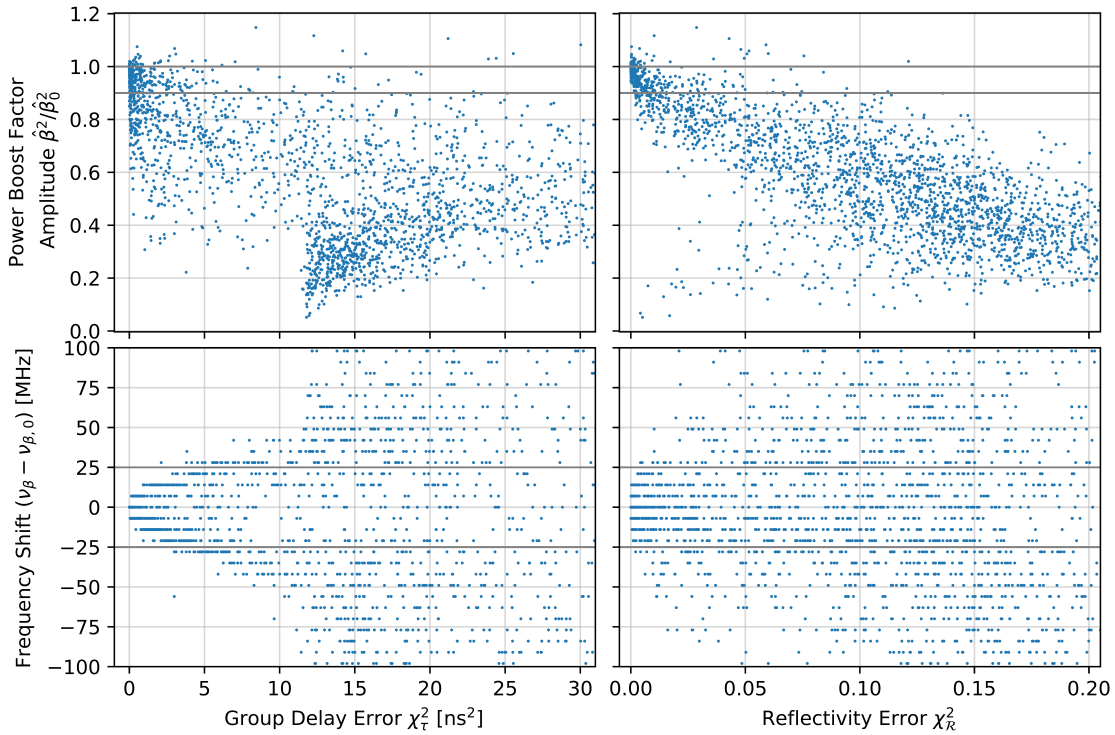

Figure 8.50: Scatter plot of various samples of the boosters containing random tilts and thickness variations showing the correlation between resulting boost factor perturbation and the deviations in group delay χ^2_τ (left) or the deviation in the magnitude of the reflectivity $\chi^2_\mathcal{R}$ (right). The upper panels show the power boost factor amplitude times antenna coupling relative to the same quantity from the ideal case. The lower panels show the shift of the boost factor curve maximum with respect to the ideal case.

Figure 8.51: Correlation between error on the reflectivity measurement χ^2_R and boost factor χ^2_β. The colors denote the probability density in χ^2_β (vertical axes) for a given χ^2_R (horizontal axes). Assuming the distribution is approximately Gaussian, the contours show where the probability density drops to the values corresponding to $1, 2$ and 3 standard deviations.

reflectivity measurement χ^2_τ (left) and $\chi^2_\mathcal{R}$ (right). We can clearly see that even for a good match of the group delay the amplitude of the boost factor peak can be reduced by a significant amount. However, the frequency shift of the boost factor peak can be well constrained with the group delay requiring $\chi^2_\tau \lesssim 10\,\mathrm{ns}^2$ (bottom, left). It depends quadratically on χ^2_τ as naively expected. For $\chi^2_\tau \gtrsim 10\,\mathrm{ns}^2$ the frequency shift can be larger than the FWHM of the power boost factor peak. In this case χ^2_τ cannot constrain the frequency position of the boost factor anymore. On the other hand, we see that the error on the reflectivity magnitude $\chi^2_\mathcal{R}$ can give us information on the amplitude reduction of the boost factor (top, right). However, it is less powerful to constrain the boost factor frequency position. This demonstrates that in a lossy system it is necessary to consider both, the group delay and the absolute reflectivity.

For this reason, we define a combined measure for the error on the reflectivity χ^2_R as

$$\chi^2_R = a_0 \chi^2_\mathcal{R} + 1\,\mathrm{ns}^{-2} \chi^2_\tau, \tag{8.26}$$

where a_0 is a dimensionless configuration dependent scaling parameter. Since both $\chi^2_\mathcal{R}$ and χ^2_τ have different dimensions and are not directly comparable, a_0 has to be set to an empirical value making them comparable. Here we set $a_0 = 25$ which brings the two summands to the same order of magnitude.

What will be important in the experiment is the probability that χ^2_β is smaller than a given value, given a χ^2_R. Therefore, we show the correlation between χ^2_R and χ^2_β in figure 8.51 in terms of the probability density $p(\chi^2_\beta|\chi^2_R)$. It can be calculated by using a bivariate Gaussian kernel density estimator [168] on the distribution of (χ^2_R, χ^2_β) combinations obtained from all simulations and normalizing accordingly. We see that there exists a correlation between both quantities for $\chi^2_R \lesssim 12$. The jump around $\chi^2_R \sim 12$ is because larger errors are typically generated from a

frequency shift larger than the FWHM of the power boost factor. In this case χ^2_β does not change much if the frequency shift is further increased. For $\chi^2_R = 0$ we constrain $\chi^2_\beta \lesssim 2.5 \times 10^4$ at the level of one standard deviation. This would be comparable to the deviations in run 2, as shown figure 8.46 (top, left). This demonstrates that the reflectivity measurement can be used to constrain the boost factor. This is roughly consistent with the fact that $\chi^2_R = 0$ (implying $\chi^2_\mathcal{R} = \chi^2_\tau = 0$) does not necessarily lead to zero boost factor reduction, as we have seen for example in the upper right panel of figure 8.50.

Fit with a 1D Model

Unlike in the above study, in the final MADMAX experiment one will not align the disks to fixed positions given by the model and then simply measure the reflectivity to constrain the boost factor. Instead, the disks will be realigned following similar optimization schemes as for the boost factor described in section 5.1, until the measured reflectivity matches best the predicted reflectivity. On one hand, one could argue that such a reoptimization could be problematic. Because we optimize the match between measured and simulated reflectivity we might end up in local minima that correspond to a good match in reflectivity, but still a bad match for the power boost factor. Those local minima would appear as outliers in the plots of the previous subsections. However since we did not run any optimization so far, it is not clear that these cases were encountered in the study above. On the other hand, this optimization process allows for example to compensate some of the phase errors introduced by 3D effects by changing the disk positions. While the random perturbations of the booster above are very likely to have an adverse effect on the power boost factor, the optimization should find those disk positions that minimize the adverse effects and make use of the aforementioned compensation effects as much as possible. Therefore, this should allow to improve the systematic uncertainty on the boost factor. It is therefore important to take the reoptimization of the disk positions into account for this study.

The computation time for a single optimization within the 3D model using Recursive Fourier Propagation and the available resources were not sufficient to optimize a large set of systems at the time this study was conducted. Therefore, we did not optimize the disk spacings in the full 3D model. Instead, we optimized the disk spacings in the ideal case until its reflectivity best matched the results for each of the different runs above. For the ideal case we can make use of the eigenmode approximation of the booster, cf. equation (6.21) in section 6.3 and the discussion of its validity in section 8.3.1. Since the antenna is essentially coupled to only the fundamental mode, we only need to take this mode into account in our calculation, i.e., the problem is reduced to a 1D model. Strictly speaking this does not correspond to the realignment of the actual disks anymore. It however corresponds to a procedure to predict the power boost factor from a reflectivity measurement and subsequent fit with a simplified 1D model. Both, the optimization of the setup and the optimization of the model, should however undergo similar systematic effects and the above arguments still hold.

We consider two different fitting methods: In method A only the match for the group delay is optimized assuming a lossless system. In this case, the quantity that is being optimized is χ^2_τ, but now between the perturbed 3D result from above and the ideal case obtained from the 1D eigenmode model. Method B optimizes both group delay and reflectivity and includes a free parameter for losses δ_p into the model. Tilts and thickness variations should naively increase the

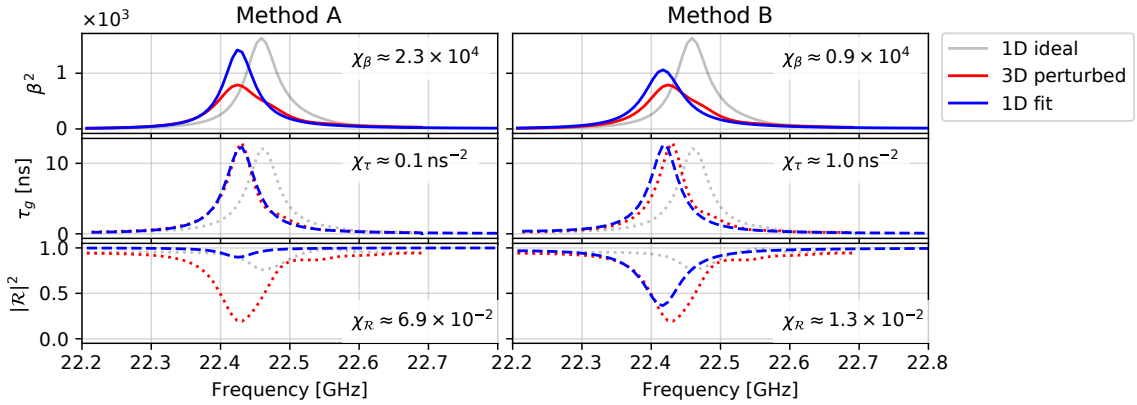

Figure 8.52: Example fits of the electromagnetic response from run 501 for two different fitting techniques. We show the fits of a 1D model in blue, the other colors are analogous to figure 8.46. The quoted χ^2 values now correspond to the frequency-averaged squared difference between the fitted response (blue) and the previously simulated response (red). **Left:** Only change disk spacings in the 1D model to best match the group delay (method A). **Right:** Change disk spacings and uniform loss parameter δ_p to best match group delay and reflectivity magnitude simultaneously (method B).

diffraction losses in the air gaps, while the disks themselves are less affected. Notice also that the ideal model already contains some diffraction loss δ_d (fixed by the disk geometry). Therefore, we set the total loss in the air gaps to the sum $\delta_d + \delta_p$. Since the losses are a priori unknown, this is an additional parameter to the optimization besides the disk spacings. In this case the quantity that is optimized is χ^2_R as defined above but now between the perturbed 3D result and the new ideal 1D result. We used the Nelder-Mead [116] algorithm to do the optimizations. Since this method is gradient-free, it is a viable option also for the optimization of the actual disk spacings in an experimental setup, as discussed in more detail in section 11.2.

The group delay has peaks at lower frequencies that do not correspond to a significant boost factor peak at this frequency. Therefore, the optimization could end up reducing all disk spacings such that all peaks are shifted upwards in frequency and the considered group delay peak is fitted with one that does not correspond to a boost factor at the same frequency. To avoid convergence to such local minima, we assume the group delay of the 3D responses is zero from 22.7 GHz to 30.0 GHz. Thus, if the optimization algorithm proposes disk spacings leading to a peak in this range, it will have a large χ^2_τ.

An example for such fits can be seen in figure 8.52, where we show the fit from method A on the left and method B on the right. Even for a very good match of the group delay the boost factor amplitude can be significantly off, which is consistent with the findings above. When taking into account the loss and reflectivity magnitude, we can achieve an improved prediction for the boost factor.

Eventually we are interested on the effect of the fitting procedure on the correlation between reflectivity and boost factor. This is illustrated in figure 8.53, where we plot the correlation of the error on the group delay for method A (left) and the combined error of the reflectivity for method B (right) against the error on the boost factor. First of all, we see that reoptimizing the

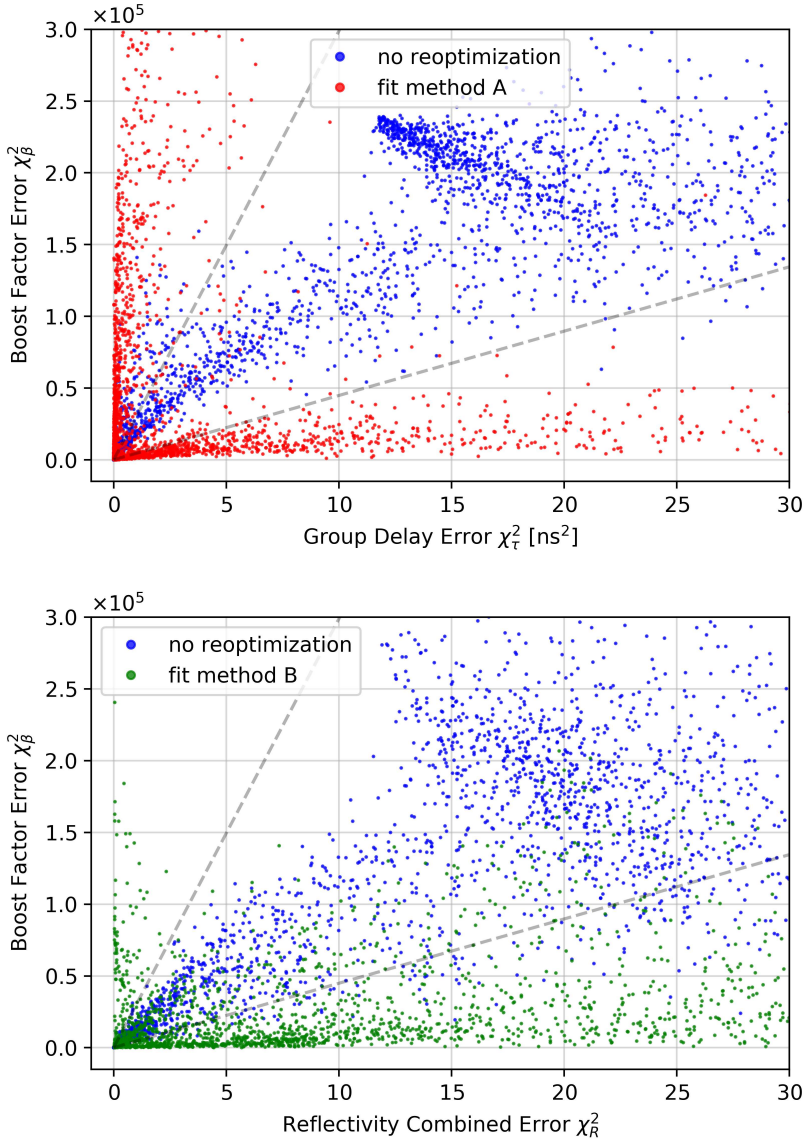

Figure 8.53: Effect of reoptimizing the disk spacings on the correlation between reflectivity and boost factor. In both panels the blue dots are obtained by comparing the initially defined ideal case and the perturbed 3D simulation. The gray dashed lines are only for orientation and referred to in the main text. **Top:** Correlation between the error on the group delay χ^2_τ and error on the boost factor χ^2_β. The red dots are obtained by comparing the perturbed 3D simulation with the reoptimized ideal model using method A, i.e., only the group delay is taken into account. **Bottom:** Correlation between the combined error on the reflectivity χ^2_R and the error on the boost factor χ^2_β. The green dots are obtained by comparing the perturbed 3D simulation with the reoptimized ideal model using method B, i.e., both group delay and reflectivity are taken into account.

disk positions has the potential to significantly decrease the systematic uncertainty on the boost factor, i.e., the boost factor error χ^2_β is significantly lower after applying the fit for the same group delay error or combined error, respectively (points under the lower dashed line). However, if one only takes the group delay into account, we see that for very good matches in the group delay the error on the boost factor can be significantly larger than without reoptimization (points above the upper gray dashed line). We can understand this, by taking a closer look at some of the cases that lead to a high boost factor error despite a low error on the group delay. In most of these cases the boost factor was significantly overestimated from the fit, because there is no loss taken into account. In fact, the example in figure 8.52 (left) belongs to these cases. For this reason, this effect can be much improved by using method B and correlating to the combined error on the reflectivity χ^2_R. Here only 5 % of the studied cases ended up in this region. We can take a closer look at these remaining cases by only considering cases which are above the upper gray dashed line, which corresponds to $\chi^2_\beta = 2 \times 10^4 \chi_\mathrm{R}$. This reveals that in all of these cases the boost factor is in fact underestimated, which increases the error on the boost factor in this parametrization. The sensitivity estimated from such fits would therefore be rather too conservative.

Summary and Outlook

In this section we considered the systematic effects of tilts and thickness variations on the reflectivity of the booster. We have demonstrated numerically that also for such a system the correlation between reflectivity and power boost factor can be used to constrain the the systematic uncertainty on the power boost factor. To harness the full predictive power of a reflectivity measurement the magnitude of the reflectivity should be taken into account as well. This holds in particular for the correct prediction of the boost factor amplitude for a lossy system in which the losses are not known a priori. Assuming no other significant systematic effects other than tilts and thickness variations, fitting a simplified 1D eigenmode model to reflectivity measurements can give a sufficient prediction of the power boost factor. For an accurate prediction this model needs to include a parameter for losses. The model needs to be compared to both the magnitude of the reflectivity and the group delay.

The considered values in this section (frequency shifts, amplitude reductions and χ^2) should be understood as first proposals to quantify the relevant errors. It is left for more detailed studies to extend these to more specific measures and compare their specific performance in terms of how strongly they can constrain the boost factor. Possible extensions could be for example the correlation of errors in individual subsets of the whole frequency band. These could be sensitive to the sign of the deviation at a particular frequency.

In short. We have demonstrated a basic calibration procedure to derive systematic uncertainties on the power boost factor from reflectivity data. Comparing to a 1D model is sufficient to constrain the boost factor for the presented system. While the group delay can be used to constrain the frequency position of the boost factor well when including a sufficient frequency range, using in addition the absolute reflectivity significantly improves the constraints on the power boost factor amplitude.

Part IV

Experimental Validation

Chapter 9

Proof of Principle Setup

In the previous part of this thesis we have discussed simulations of systematic effects in dielectric haloscopes. In additon, it is important to demonstrate experimentally that such a booster system with the desired electromagnetic properties can actually be built. The performance of a realistic setup will be limited by the obtainable mechanical accuracy and other systematic effects, such as unwanted reflections on the receiving antenna. Moreover, it is essential to understand the implications of tuning the disk positions, for example by employing optimization schemes to match the predicted electromagnetic responses and hence to a desired boost factor as discussed above in section 8.6. Here we present the implementation of such a first proof of principle booster setup. We evaluate systematic uncertainties and demonstrate basic tuning algorithms, as well as their impact on the power boost factor.

We first introduce the details of our experimental booster setup containing at present up to five sapphire disks in front of a copper mirror. After discussing systematic limitations, we describe the tuning of the setup and consequences of the systematic uncertainty on the power boost factor. Finally, we describe first measurements indicating deviations from the 1D model in the proof of principle setup which can already be understood in terms of more sophisticated 3D models.

9.1 Setup and its Components

We show our experimental realization of such a booster in figure 9.1. The proof of principle booster consists of up to five sapphire disks placed in front of a copper mirror. The disks have a dielectric constant of $\epsilon \approx 9.4$ perpendicular to the beam axis (crystal C-axis), a thickness of $1\,\mathrm{mm} \pm 10\,\mu\mathrm{m}$, and a diameter of 20 cm. Each disk is mounted on a holder connected to its own DC motor (*PI L-220.70DG* [170]). The motors are equipped with a position encoder. The disk positions can be changed with a precision of less than a μm. The tilts of the disks are adjusted at the mrad level by using manual tilting stages on the disk holders. The tilts are manually optimized by maximizing the measured absolute reflectivity of the booster. The disk holders slide on rails which have been aligned such that they are parallel up to $\sim 100\,\mu\mathrm{m}$ over a length of $\sim 0.5\,\mathrm{m}$ [8]. To determine the temperature of the setup, Pt-100 sensors are placed at the metal frame, on the backside of the copper mirror, and in the air above the disks.

To determine the electromagnetic response of this booster we measured the phase and ampli-

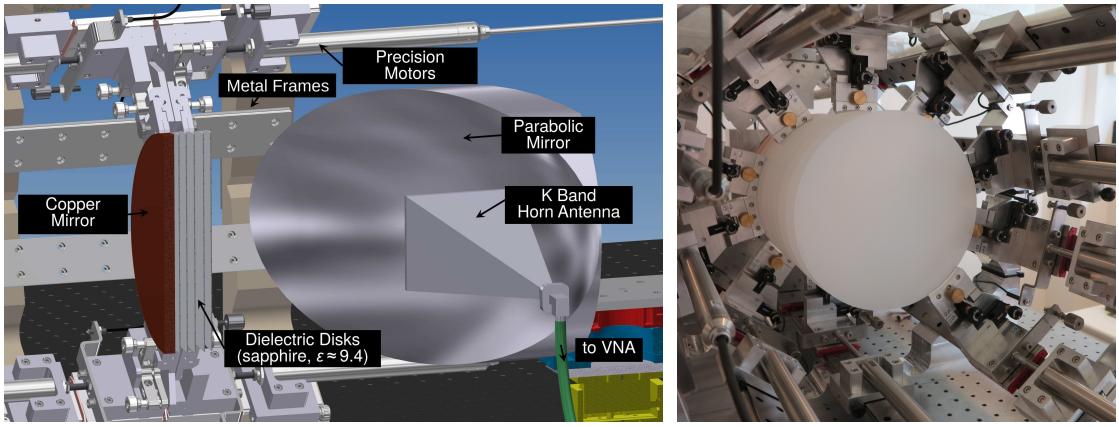

Figure 9.1: **Left:** Schematic drawing of the proof of principle setup. Up to 5 sapphire disks are mounted in front of a plane copper mirror and can be moved using precision motors. Test beam reflections are studied via the parabolic-mirror-antenna assembly and measured with a vector network analyzer (VNA). For clarity we only show a cross section orthogonal to the disk surfaces. **Right:** Photo of the proof of principle booster extended to 20 disks taken from the antenna side. The dielectric disks are placed in front of the copper mirror.

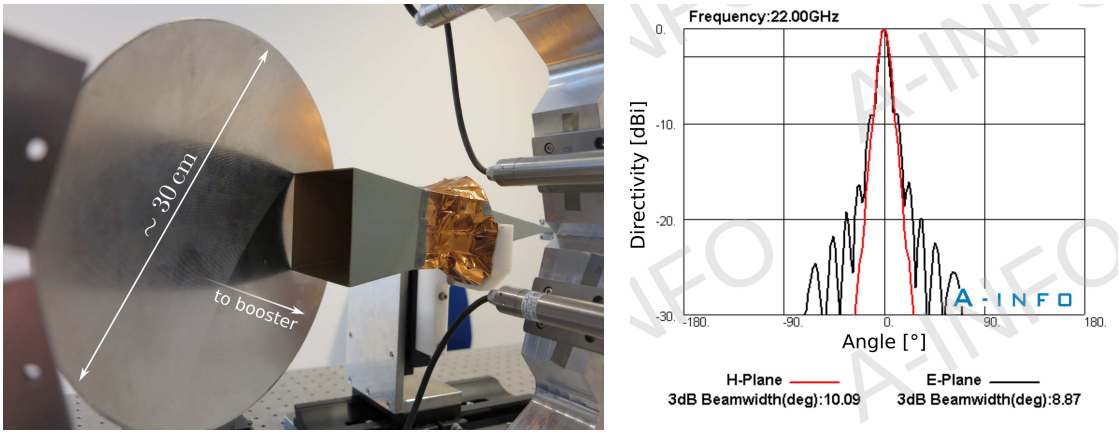

Figure 9.2: **Left:** Photo of the antenna-parabolic-mirror assembly taken from the booster side. The holders of the antenna are screened in part by reflective copper foil to reduce reflections. **Right:** Manufacture's specification of the far-field pattern of the antenna, adapted from [169]. The red line shows the pattern in the H-plane (horizontal) and the black line in the E-plane (vertical).

tude of a reflected microwave signal in the frequency range of $10 - 30\,\mathrm{GHz}$ using a Vector Network Analyzer (VNA, *Anritsu MS4647B* [171]). It is connected to a rectangular horn antenna (*A-INFO LB-42-25* [169]) facing a 90-degree off-axis parabolic aluminum mirror with a diameter of $\sim 30\,\mathrm{cm}$ as shown in figure 9.2 (left). The effective focal length of this mirror given by the supplier is $\sim 15\,\mathrm{cm}$, such that the focal point lies within a few cm at the antenna waist. The far-field pattern of the horn antenna is shown in figure 9.2 (right). The E-plane has the typical side-lobe structure expected from a rectangular horn.

We applied the following procedure to make sure the resulting beam shape is centered on the disks and impinges orthogonal to the disks. To this end, we take reflectivity measurements with the VNA without any dielectric disks installed, but insert a rectangular metal reflector with an area of a few cm^2 parallel to in front of the copper mirror. This causes additional diffraction from the metal reflector and thus alters the measured reflectivity. If the metal reflector is placed in the xy-plane (parallel to the disks) at the same radius r with respect to the beam axis, the changes in reflected signal are expected to be the same, even if the metal reflector is inserted at different angles, i.e., from different sides, into the beam path. From the perspective seen in figure 9.1 (left) we hence inserted the reflector from the front, back and top roughly at the place where the dielectric disks shown, as well as in front of them at other places along the z-direction towards the parabolic mirror. We afterwards changed the tilt and position of the parabolic mirror in order to improve the beam position and repeated the measurement above, until the changes in measured reflectivity are matched best when inserting the reflector from different sides. By comparing measurements in which the metal reflector is displaced slightly, we conclude that the accuracy of this method is better than $\sim$ cm scale for the transverse position of the beam.

The VNA takes reflectivity measurements including phase and amplitude of the reflected signal with respect to a previously defined reference plane, for more details cf. [172]. This reference plane has been calibrated to the coax-connector end of the horn antenna. By taking a reflectivity measurement without any dielectric disk installed, we measured the transmission-coefficient between the coax-connector end and the copper disk, including diffraction losses and the transmission factors of the antenna-parabolic-mirror assembly. Assuming a lossless copper mirror, we obtained the reflectivity of a booster, i.e., a system including disks, by dividing its measured complex reflectivity phasor with this factor.

9.2 Supplementary Material for Measurement of 3D Effects

In order to improve the antenna reflectivity discussed in section 10.3 and to extend the presented studies further to include 3D effects after performing the measurements with the setup described above we have put the following improvements in place.

A custom-made Gaussian horn antenna together with a large ellipsoidal mirror from *Thomas Keating Ltd. (TK)* shown in figure 9.3 (left) has been installed. The goal is to further reduce over-shining losses on the focusing mirror, match the antenna better to the fundamental mode of the booster and minimize its reflection coefficient. A *WG20 (WR42) near field probe* has been used to measure its beam shape in front of the booster. The result is displayed in figure 9.3 (right) relative to the transverse position of the dielectric disks denoted as a circle. The beam shape is compared to the expected beam shape from the manufacturer data sheets. After correction of

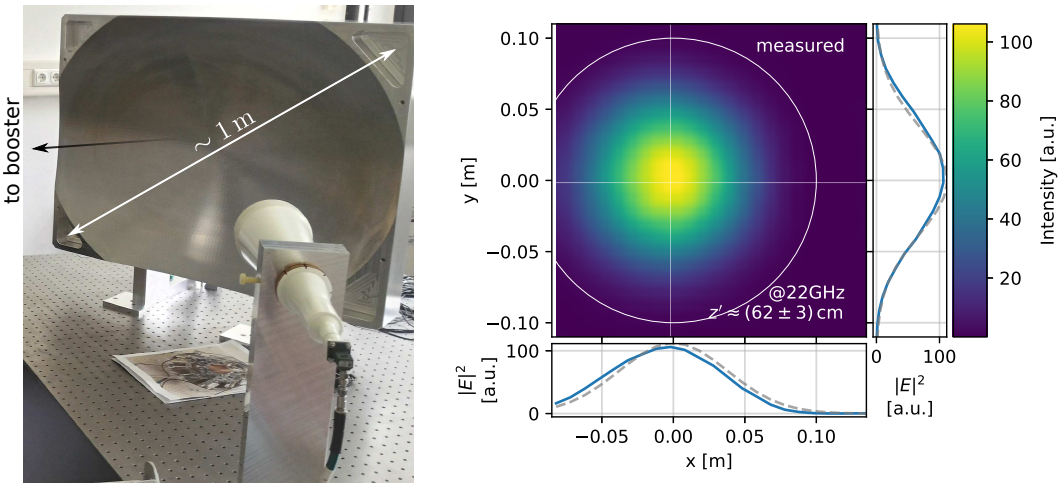

Figure 9.3: **Left:** Custom-made Gaussian horn antenna and ellipsoidal mirror. **Right:** Result of beam shape measurement $z' \approx (62 \pm 3)\,\mathrm{cm}$ in front of ellipsoidal mirror. The main panel shows the measurement. The sub-panels show the measurement as a blue line and the expectation from the manufacturer's data sheet as a gray dashed line.

small obvious shift, the matching ratio between the measured beam shape (main panel and blue lines) and the Gaussian beam shape specified by the manufacturer (gray dashed lines) is $97^{+3}_{-5}\,\%$. At this position the beam has a beam waist of $w \approx (7 \pm 1)\,\mathrm{cm}$.

In order to quantify the real positions, tilts and thickness variations of the disks independent from a microwave measurement, a low-coherence interferometer *SOFO V* by *SmarTec* has been acquired. By shining a broadband infrared beam through the disk stack, the disk positions can be determined by mapping out their reflections in time domain, for more details cf. [173]. First measurements showed that the relative tilt acceptance for the interferometer between the dielectric disks is $\approx \pm 5\,\mathrm{mrad}$. Comparing position measurements to the motor positions lead to consistent values within a standard deviation of $7\,\mu\mathrm{m}$. The full version of this device is currently still being installed and commissioned.

Chapter 10

Systematic Limitations

The precision at which the system described in the previous chapter can be adjusted to a certain boost factor is limited by the mechanical precision of the setup and systematic microwave effects, such as unwanted reflection and losses. In this chapter we survey these effects.

10.1 Mechanical Stability

The mechanical stability of the system is limited by vibrations from the surrounding, as well as long term displacement effects during measurement caused, for example, by temperature changes.

We investigated the long-term mechanical stability of our proof of principle setup by observing a resonant group delay peak of a single disk and mirror system. Figure 10.1 shows the result of a long-term measurement where the sapphire disk was placed $\sim 5\,\mathrm{cm}$ apart from the mirror without any motor movements. (a) shows the mean of all measured temperatures as a function of measurement time. (b) shows the frequency position of the group delay peak of the 7th harmonic from the resonance between the sapphire disk and copper mirror at $\sim 21\,\mathrm{GHz}$. (c) shows the hour-scale short-term fluctuations in (b). We obtained the residual short-term fluctuation by subtracting a smoothed version of (b), which has been obtained by applying a Gaussian filter with one hour standard deviation. The frequency stability is mainly limited by temperature effects of $\sim 2\,\mathrm{MHz\,K^{-1}}$, corresponding to a dependency of the disk position of $(-5 \pm 3)\,\mu\mathrm{m\,K^{-1}}$ [9]. This value slightly varies for individual motors and motor position, which leads to the conservative systematic uncertainty. Frequency analysis of the displacements over time reveal that the residual variations, i.e., the variations in (c) after subtracting the long-term temperature effects, can be attributed to vibrations such as table movements. They leave the group delay peak stable well below the MHz scale. The accuracy of the disk alignment is limited by the precision of the motors and the mechanics of the disk holders. We determined the reproducibility of positioning individual disks by repeatedly placing the single sapphire disk to a predefined position now $\sim 8\,\mathrm{mm}$ apart from the mirror. The measurement revealed a mechanical hysteresis on the order of $\sim 2\,\mu\mathrm{m}$ positioning difference depending whether the motor is placed from a higher or lower position. When mitigating this effect by placing the disk always from the same side, the group delay peak position was reproduced within a standard deviation of $\sim 1.5\,\mathrm{MHz}$. This corresponds to position errors of the order of $\sim 0.7\,\mu\mathrm{m}$ in this case. This is still well within the needed accuracy even for

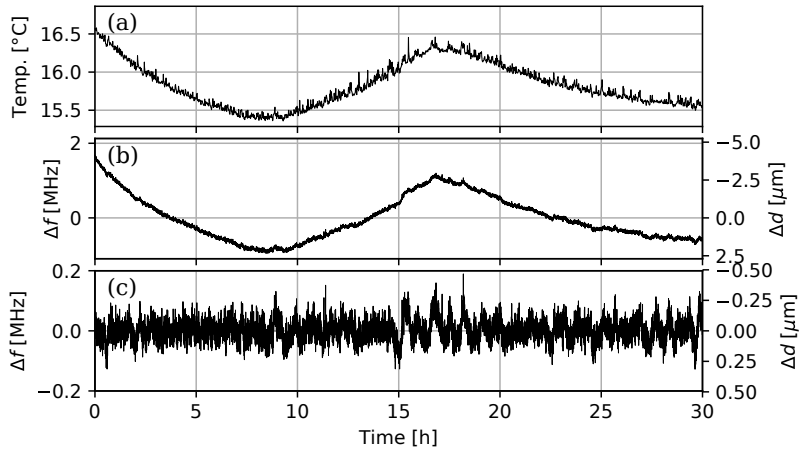

Figure 10.1: Effect of mechanical deformation of the proof of principle setup over a long-term measurement with a single disk and mirror. (a) Average measured temperature as a function of time. (b) Measured frequency of the 7th harmonic of the group delay peak as a function of time. The secondary axis shows the corresponding positioning error of the dielectric disk. More details are given in the text. (c) Residual of the measured group delay peak frequency and corresponding position after subtracting variations on the time scale of more than an hour.

a boost factor bandwidth of 50 MHz where $\sim 3\,\mu$m is required, cf. section 5.3.

10.2 Losses

In the previous part of this thesis we have seen various ways electromagnetic power can dissipate in a dielectric haloscope, including dielectric loss, diffraction, tilts, and surface roughness of the disks. For small losses we can parameterize those using the usual loss tangent $\tan\delta$ in the 1D model. To first order these reduce the total power in the system, i.e., the power boost factor and the absolute reflectivity. Therefore, the absolute reflectivity may be used in a later stage to calibrate the losses in the system and predict their impact on the power boost factor. This will in particular lead to a more realistic estimate of the boost factor amplitude, as we have seen in section 8.6.

In addition, losses affect the phase of a propagating electromagnetic wave. For high enough losses this effect can even change the sign of the phase and hence reverse how the phase evolves with frequency. This leads to negative group delay peaks. For a more detailed theoretical explanation why this happens cf. e.g. [174,175]. An example of this effect is demonstrated in figure 10.2. Here we show group delays corresponding to a system with 4 sapphire disks in front of the copper mirror each at a distance of 8 mm apart from each other, similar to the one considered in section 8.6 for five disks as in figure 8.45. On the left of figure 10.2 we show the group delay from a 1D calculation for different losses $\tan\delta$ in air. For more lossy, and thus less resonant, systems the group delay peaks, counter-intuitively, become more narrow in frequency and eventually 'flip' to negative values. On the right, we have applied a time gate ranging from -1.5 ns to a variable maximum time $t_{\max}$ to our four disk measurement shown in figures 10.3 and 10.4. If the time gate ranges beyond 5 ns, it encompasses the reflection on the antenna and we see additional ripples, which will be the subject

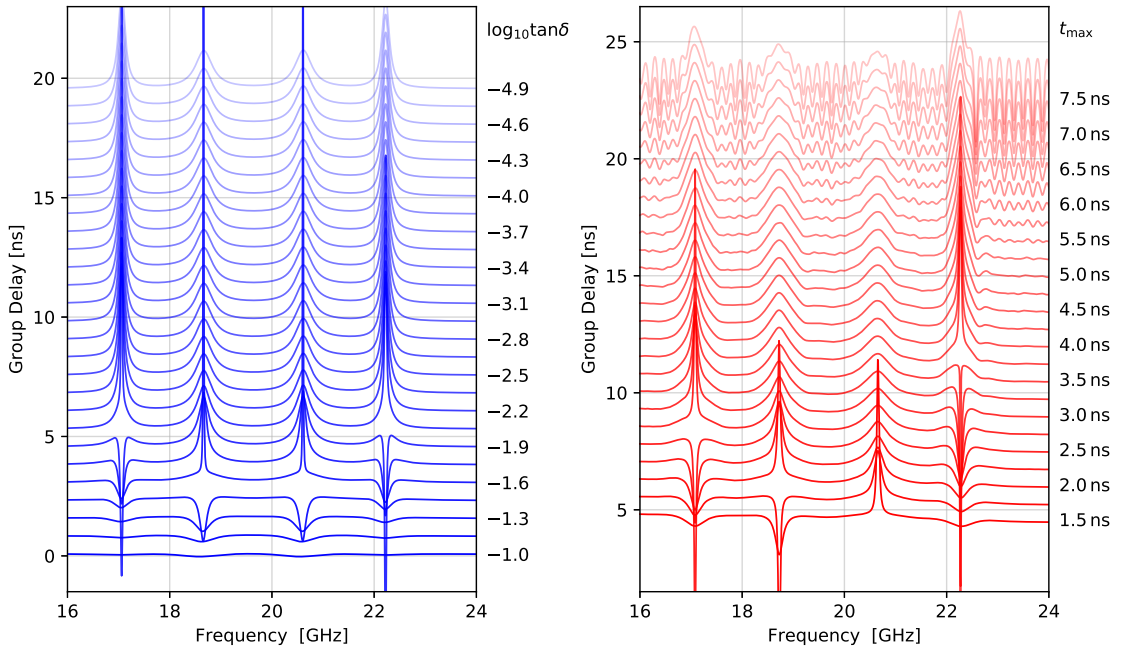

Figure 10.2: Effect of losses on the group delay of a booster with 4 dielectric disks. The left panel shows group delays in the ideal 1D model after applying different losses $\tan\delta$ in the air gaps. Each curve corresponds to a group delay with either different $\tan\delta$ as indicated by the labels on the right. The right panel shows the group delay after applying different time gates to the data from the measurement shown in figure 10.3. Each curve corresponds to a group delay with different maximum times for the gate $t_{\max}$ as indicated by the labels on the right. For clarity all curves are shifted by less than a nanosecond with respect to each other, without any shift all of them have their baseline at $\sim 0\,\text{ns}$. The upper more light lines correspond to less loss and longer time domain gates respectively. The lower more dark lines correspond to more loss and shorter gates, respectively.

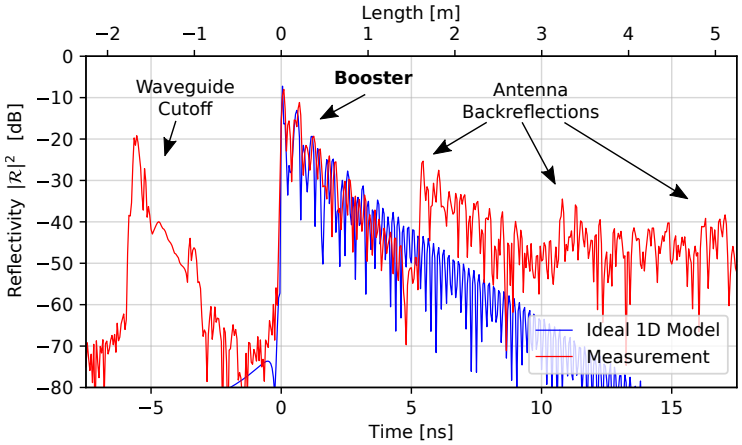

Figure 10.3: Reflectivity in time domain for a setup with the copper mirror and 4 sapphire disks from measurement (red) and ideal 1D model (blue). The corresponding length assumes free space propagation.

of the next section. If the time gate, however, is too short, it artificially 'breaks down' the resonance after some time and thus introduces an effective loss mechanism, which results in negative group delay peaks. Notice that the $\tan\delta$ or maximum time $t_{\max}$ at which a specific peak in the group delay spectrum becomes negative, is different for the different resonances. This is because the resonances at different frequencies correspond to different electromagnetic field configurations in the system which are in general affected differently by the same loss.

By minimizing losses from tilts and only considering a system with up to five sapphire disks, we ensured the above losses are small enough such that the lossless model can still approximately reproduce the measured group delays, i.e., we see no negative group delay peaks. In the following we will not consider the systematic effects caused by various loss mechanisms and focus on the task to tune the booster, i.e., we will compare our measurements to an ideal lossless model. For this purpose it is sufficient to only consider the group delay of the reflected signal, since the lossless 1D model predicts unity for the magnitude of the reflectivity independent of frequency. While this does not take into account systematic effects in 3D and from losses, it is sufficient to evaluate the alignment reproducibility of the real setup. It also lets us assess to what extent the behavior of the electromagnetic response as a function of disk spacings is as expected from the idealized model.

10.3 Unwanted Reflections

An important systematic effect on the measurement of the electromagnetic response results from unwanted reflections on the antenna. Figure 10.3 shows the reflectivity in time domain for a setup with four disks in front of the mirror. The booster reflectivity is essentially described by an exponential decay in time domain corresponding to its resonant behavior. The time scale for the exponential decay increases when making the system more resonant, e.g. by adding dielectric disks. The time domain data is shifted such that the reflection on the front disk of the booster happens at $t_0 = 0$. The other peaks can be identified according to the time they occur. The time between two such peaks is $\sim 6\,\mathrm{ns}$. This roughly corresponds to twice the distance between the

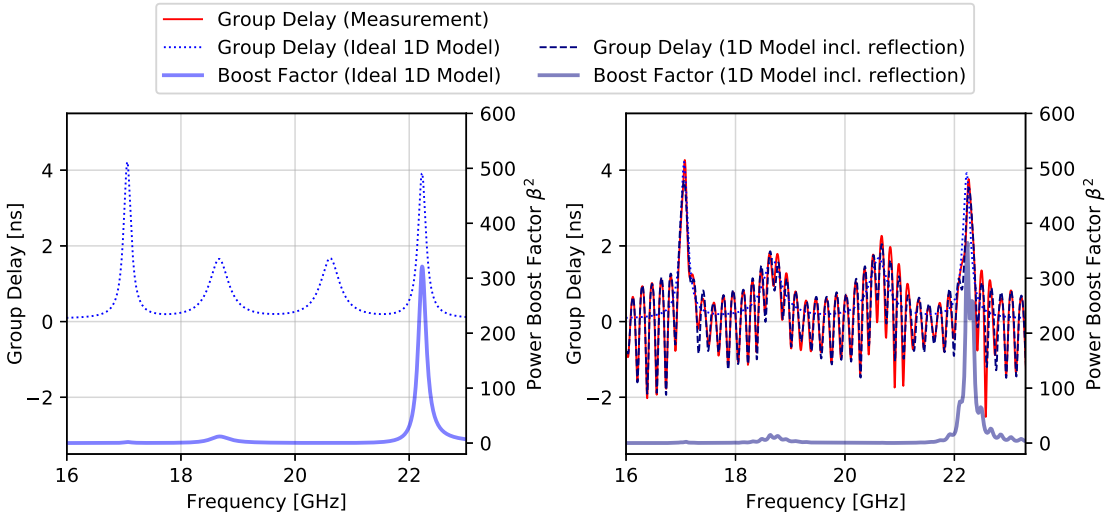

Figure 10.4: **Left:** Group delay (blue dotted line) and boost factor (bold light blue line) for a setup with 4 sapphire disks, each separated by 8 mm, in the ideal 1D model with 50 % antenna efficiency but without antenna reflections. **Right:** The same group delay but including antenna reflection from measurement (red straight line), without antenna reflection in idealized loss-less model (blue dotted line) and after including the antenna reflection (dark blue dashed line), as well as the corresponding power 1D boost factor including the antenna reflection (bold dark blue line). We only show a subsection of all recorded frequencies containing the resonant group delay peaks of the booster.

antenna and the booster and increases accordingly, if the booster is moved farther away from the antenna. The peak at ~ -6 ns corresponds to an internal reflection inside the antenna back to the VNA, mainly arising from the cutoff frequency of the waveguide section at around ~ 14 GHz. The peak at ~ 6 ns corresponds to the reflection off the antenna back to the booster. This reflection repeats every ~ 6 ns since a reflected signal may be back-reflected again. For a low number of disks we can filter out this higher order reflections in time domain by simply multiplying with a window function (time gating), cf. e.g. [176]. For more resonant systems the main peak stretches over a longer time period and begins to overlap with the peaks arising from the unwanted reflection. In addition, the axion-induced signal may also be affected by the reflection. However, time gating can only be done with a reflected signal, which can be related to the phase of the input signal over a broad frequency range. The axion signal cannot be time gated since it is continuous in time, oscillates in a narrow frequency band within a few kHz and its phase is unknown.

Figure 10.4 compares the group delay of the ideal 1D model without antenna reflection (left) with the model and measurement of the same booster but including the first order reflection (right). Note that we still apply a time gate, but include the first antenna reflection peak in time domain, i.e., the time gate stretches until $t_{\mathrm{max}} \sim 10$ ns in figure 10.3. The longer runtime of the reflected signal compared to the main signal causes a phase difference between them, which changes linearly with frequency. Depending on frequency, the interference is constructive or destructive, which adds an additional sinusoidal structure (ripples) to the frequency spectra of the group delay and the

boost factor. When fitting the group delay of an ideal 1D model with the disk positions as free parameters to such data, the predicted boost factor would therefore end up at the wrong frequency due to the ripples. The distance between the antenna and the front disk of the booster defines the frequency difference between neighboring ripples and thus the maximum frequency shift this effect may cause. For our distance of around $\sim 70\,\mathrm{cm}$ this shift is at the order of $\sim 200\,\mathrm{MHz}$. In the following we therefore discuss strategies to avoid reflections and include them into the electromagnetic response model, if needed.

Minimizing Reflections

The methods below can be applied to the design of the experimental setup to reduce the effect of the reflections.

- *Change the Distance to the Antenna.*

  The distance between the ripples $\Delta\nu_{\mathcal{R}}$ in frequency domain caused by antenna reflections is given by

  $$\Delta\nu_{\mathcal{R}} = \frac{c}{2d_a}, \tag{10.1}$$

  where c is the speed of light and d_a is the distance of the front disk of the booster to the antenna. Increasing d_a could make $\Delta\nu_{\mathcal{R}}$ much smaller than the boost factor bandwidth, such that the error it causes on the determination of the boost factor frequency range would be negligible. However, the error on the boost factor amplitude will be harder to quantify. One could even consider making d_a longer than the coherence length of the axion signal, i.e., reducing $\Delta\nu_{\mathcal{R}}$ below the bandwidth of the axion signal. This, however, would require a distance at the order of $d_a \sim 100\,\mathrm{km}$, which is not feasible for MADMAX. This fact is the reason why astronomers do not have to care about such effects. Alternatively, decreasing the distance could make $\Delta\nu_{\mathcal{R}}$ much larger than the boost factor bandwidth. This makes modeling of the reflection effect on the boost factor amplitude easier. In a realistic setup like the final MADMAX there will be, however, a minimal distance set by practical issues, such as the magnet length and even just the size of the focusing mirror and antenna themselves. Due to the restricted feasibility of this method we have not explicitly applied this method for the proof of principle setup.

- *Screen Reflective Parts of the Optical System.*

  By screening reflective parts of the antenna and surroundings with absorbers the radiation which is not directly detected can be absorbed before it is reflected back. However, the absorbers have to be put at low temperatures to minimize their contribution to the thermal noise of the booster. An alternative is the use of crumbled copper foil, which instead scatters the radiation in random directions. This is seen in figure 9.2, where the antenna has been screened with copper foil.

  Before the parabolic mirror shown in figure 9.2 had been implemented, measurements with a smaller parabolic mirror had been attempted. The mirror is displayed in figure 10.5 (a,b) and has a diameter of $\sim 10\,\mathrm{cm}$. This small size led to additional reflections from the holding stage and the reflection peaks in time domain as shown in figure 10.5 (c). Different colored

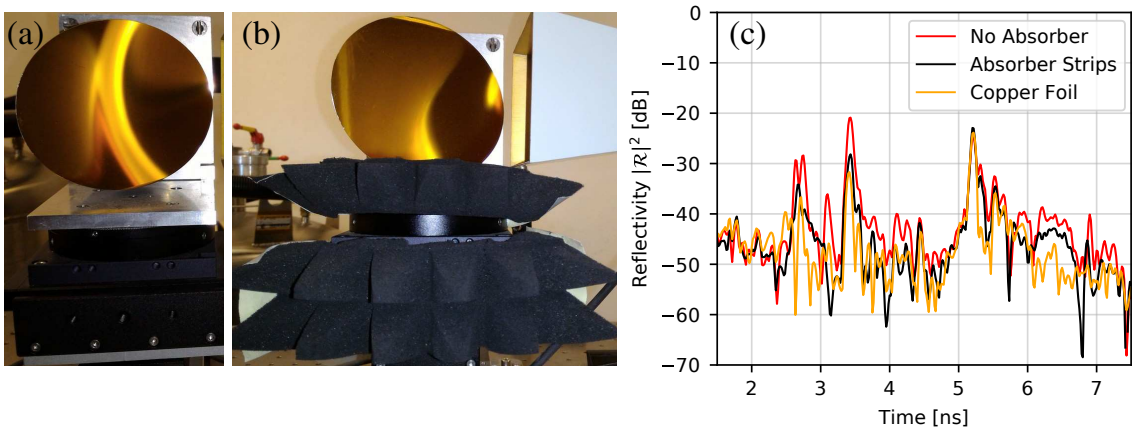

Figure 10.5: Strategies to reduce unwanted reflections. (a) Smaller parabolic mirror without absorber and reflective surfaces. (b) Screening the reflective surfaces with absorbers. (c) Reduction of reflection peaks in the measured time domain reflectivity when the mirror in (a) is installed (red), by screening the reflective surface as in (b) with absorbers (black) or crumbled copper foil (orange).

lines refer to different screening strategies to avoid the reflection at the holding stage. The red line corresponds to a measurement without any screening, the black line corresponds to a measurement with the absorber shown in (b) and the orange line corresponds to a measurement with crumbled copper foil. By employing the parabolic mirror with a larger diameter described in section 9.1 the first two reflection peaks become effectively negligible.

- *Improve Antenna Matching.*

  Lastly, a mismatch between the antenna beam shape and the booster modes cause additional reflections. In addition, the intrinsic mismatches, such as reflections at the antenna-waveguide interface, contribute to the reflections. These have to be minimized by careful antenna design. The new antenna described in section 9.2 is an attempt in this direction for the next generation of this setup.

Calibrating Reflections

If all options to minimize reflections have been implemented, the effect of the remaining reflection may still need to be included in the electromagnetic model in order to predict its effect on the reflectivity and boost factor. To this end, we perform a separate measurement during each calibration to determine the residual reflection coefficient of the antenna $\mathcal{R}_A$. It can be obtained by measuring the reflectivity only with the copper mirror and without dielectric disks installed. By applying a time gate around the peak of the antenna reflection at $\sim 6\,\mathrm{ns}$ to the measured reflectivity, we can infer the antenna reflectivity assuming the copper mirror is lossless.

This reflectivity can be directly included into the 1D model afterwards. We use the ADS circuit simulator as introduced in section 4.1. For simplicity, we only include the reflectivity as seen from outside the antenna rather than the reflectivity from inside and transmission factors as in a full antenna model. This is sufficient to describe the unwanted reflection on the antenna seen from

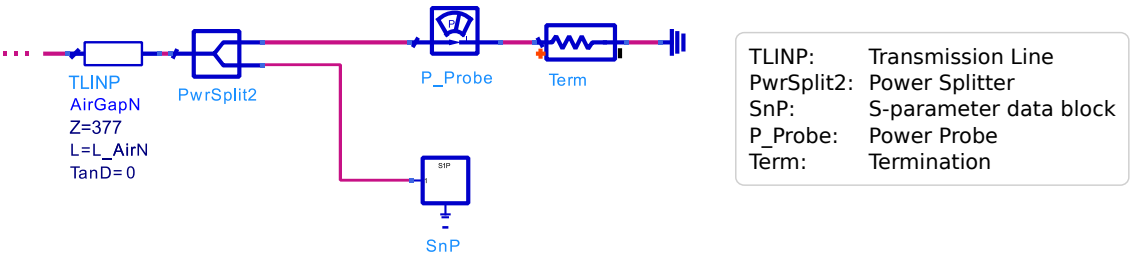

Figure 10.6: Extended antenna model in *Advanced Design System (ADS)* [112]. 'Z' is the impedance in Ω, 'L' is the length, and 'TanD' is the loss tangent of the respective element. For simplicity, we use a power splitter diverting some of the power received by the antenna to the S-parameter data block ('SnP') where the measured antenna reflectivity can be included in the model. See also figure 4.2 in section 4.1.

the outside which leads to the additional time domain peaks discussed above. The reflection effect is implemented by adding a power splitter that diverts some of the received power to a reflective S-parameter data block ('SnP') element, as shown in figure 10.6. We set the transmission factors of the power splitter $S_{21} = S_{31} = 1/\sqrt{2}$, which leads to an antenna efficiency of 50 % in the model, but can be easily adjusted to any other efficiency. Later, we will compare different boost factor amplitudes from this model relative to each other. Since the antenna efficiency is the same for all compared boost factors, the exact value for the antenna efficiency is irrelevant for comparison. Notice also that the reflectivity of the 'SnP' element is not directly the measured reflectivity, but scaled and phase shifted such that the total reflectivity of our antenna model in figure 10.6 is the measured $\mathcal{R}_A$ and happens without additional time shift.

We tested this model by measuring the group delay of the same booster, but at varying total distance of the booster from the antenna over more than the range of a few wavelengths. Afterwards, we fit the measured group delays with the model including the 'SnP' element, i.e., the effect of unwanted antenna reflections. The differences in the boost factors obtained from these fits determine the systematic uncertainty on the boost factor remaining after applying this model in order to predict the boost factor.

This procedure was done for boosters with one to four disks each. The total distance between the booster and parabolic mirror was changed by moving all dielectric disks and the copper mirror by the same amount in the same direction. Figure 10.7 (a) shows the relative disk spacings obtained from the fits of the model as a function of the total distance to the antenna for the example of the four disk booster. We see long range changes of the fitted disk positions at the order of around a few $\times 10\,\mu$m. This value is consistent with expectations from other independent alignment measurements of the setup. In addition, we see periodic changes which repeat after $\sim (8 \pm 3)$ mm, i.e., around half a wavelength at 20 GHz. This effect is expected from reflections that are not included properly in the model. This is because the distance to the antenna determines the frequency position of the additional ripples in the reflectivity spectra as discussed above, i.e., increasing the distance by half a wavelength shifts them by one period.

For this reason, from the inferred relative disk spacings in figure 10.7 we first determined the long range trends using a convolution with a Gaussian of standard deviation 20 mm. The standard deviation corresponds to more than a full wavelength above 15 GHz. These long range trends are

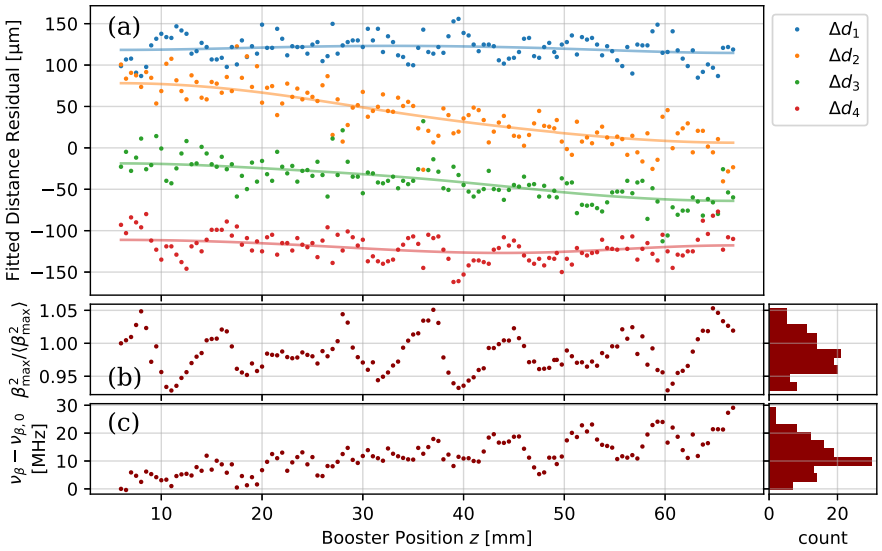

Figure 10.7: Results of fitting the group delay from a model including reflections to data from the same booster at varying distances to the antenna z. (a) Relative disk spacings between dielectric disks obtained from the fits. We show the residual to the mean; the data set for each spacing is shifted by up to 120 μm to make the individual dependencies on z more apparent. The dots show the results from the fits, while the light curves show the result after convolving with a Gaussian of standard deviation 20 mm. (b,c) Changes in the power boost factor of the booster without antenna when calculated with the disk spacings obtained from (a) after removing long term trends as described in the main text. We show the changes in relative power boost factor amplitude in (b) and changes in the maximum power boost factor frequency position in (c). The right sub-panels show histograms of the respective deviations obtained from these data points.

Booster	Standard deviation of...	
	$\beta^2_{\mathrm{max}}/\langle\beta^2_{\mathrm{max}}\rangle$ [%]	$\nu_\beta - \nu_{\beta,0}$ [MHz]
1 disk	0.1	16
2 disks	0.7	9
3 disks	2	7
4 disks	3	6

Table 10.1: Standard deviation of the power boost factor amplitude and frequency position from the ensemble of boost factors obtained from reflectivity measurements on the same booster but at varying distance to the antenna as described in the main text.

shown as pale lines among the data points in figure 10.7 (a). Afterwards we subtracted the long range trend to only obtain short range changes in the fitted disk spacings. Using these corrected distances in the model we calculated the corresponding boost factors from the ideal 1D model. Remember that when changing the total distance between booster and antenna, the reflections change the boost factor. However, the boost factor without antenna is expected to stay constant, since we did to not change the relative distances between the disks within motor position accuracy. Therefore, we used the ideal 1D model in this step. Thus, any observed change must arise from systematics not covered by the model including the antenna effect, such as misalignments in the setup or additional unaccounted reflections.

We show the changes in the relative power boost factor amplitude and frequency positions of the boost factor maximum in figure 10.7 (b,c). The results clearly reveal the periodic structure expected from reflections which have not been fully taken into account in the fitted model. For four disks the effect changes the boost factor amplitude at the order of 5 % and the frequency position at the order of 10 MHz. Table 10.1 summarizes the standard deviations of these quantities over the full observed range and for all different booster configurations for which this test has been performed. Since these are systematic deviations, the standard deviation is only a rough estimate for the systematic uncertainty which is caused by the failure of the model to include all systematic effects. We conclude that when using the improved electromagnetic response model including the reflections, a residual systematic uncertainty of 5 % on the power boost factor amplitude and 20 MHz on the boost factor frequency position needs to be taken into account. The latter is still much smaller than the full-width-half-maximum (FWHM) of, for example, the boost factors shown in figure 10.4, which has a FWHM of ~ 170 MHz. However, it may need further improvement for more narrowband configurations as envisioned in the final MADMAX setup.

In short. The presented proof of principle setup has the mechanical accuracy and repeatability to align the dielectric disks to control the frequency of the electromagnetic response to better than MHz level. However, unwanted antenna reflections need to be taken into account when determining the response of the booster, inducing a uncertainty of up to 20 MHz on the boost factor frequency and up to 5 % on the boost factor amplitude with up to four disks in this setup. Effects on the group delay due to loss can be observed when e.g. time gating the reflectivity measurement.

Chapter 11

Tuning and 1D Model Validation

Since different axion masses correspond to different frequencies, the boost factor needs to be tuned over the frequency range of interest during an axion search. In the following we develop a general procedure to do this tuning for the proof of principle setup. The central goal is to demonstrate that the booster can be tuned to a desired frequency range and that the electromagnetic response behaves as expected from the model, while here we consider first only the 1D model. This will give first indications how long tuning will take and how this time could possibly be reduced. Finally, we derive systematic uncertainties on the boost factor arising from our tuning procedure.

11.1 Tuning Scheme

We demonstrated that such tuning can be achieved with up to five equidistant disks using the following general tuning procedure:

1. *Define Goal Boost Factor in Model.*

   First, the disk positions corresponding to the desired boost factor center frequency and bandwidth are calculated with the 1D model, along with the corresponding group delay of the reflectivity.

2. *Align Experiment to Reproduce EM Response from Model.*

   Then, the disk positions in the setup are adjusted to approximately the calculated distances from the model. Afterwards, the distances are fine-adjusted using an iterative optimization algorithm in order for the measured group delay to match the prediction from the 1D model.

3. *Constrain Boost Factor with the Model.*

   In the last step we test the tuning procedure by fitting the model to the measured data. This allows to infer the systematic uncertainty on the boost factor arising from tuning.

In the first step, we adjust the boost factor to the right frequency band only within the model. This can be done numerically by optimizing the disk spacings in the simulation such that the desired boost factor is obtained. For simplicity here we did not optimize the disk positions, but considered configurations where all disks are at the same distance d. Figure 11.1 shows how the

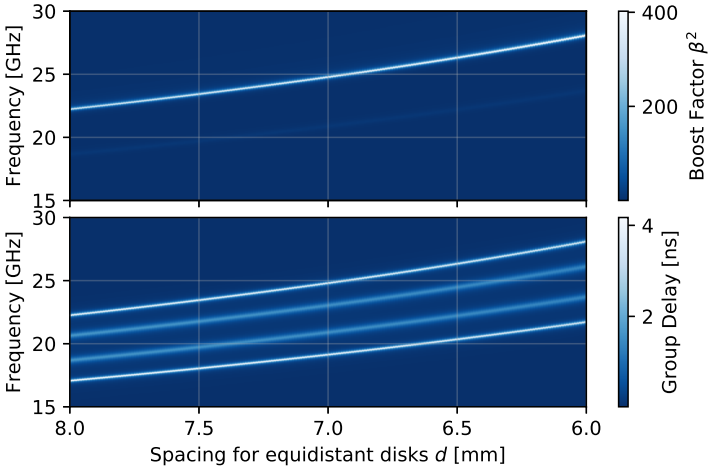

Figure 11.1: Simulated boost factor (top) and group delay (bottom) as a function of frequency (vertical axes) and separation between the sapphire disks (horizontal axes) for a system of four equidistant disks.

boost factor and group delay change for a four disk booster as a function of d. By tuning d between 6 mm and 8 mm the boost factor can be tuned over a frequency range between 22 GHz to 28 GHz. These configurations correspond to a boost factor bandwidth full-width-half-maximum (FWHM) between 170 MHz and 190 MHz, giving a ratio of boost factor central frequency over boost factor bandwidth $\nu_\beta/\Delta\nu_\beta \sim 140$ which is constant over the whole tuning range up to 5 %.

11.2 Setup Optimization

In the second step we aim for aligning the real disk positions in the experimental setup such that it reproduces the simulated boost factor. Simply placing the disks at the distances predicted from the 1D model and relying on the simulated boost factor is not the most feasible solution. Effects such as disk bending, surface roughness or variations in the dielectric constant may change the phase depths of each region and therefore contribute to the systematic uncertainty of the boost factor. Here we conservatively assume that the model still predicts positions which are do not differ from an optimal configuration by more than $\sim 100\,\mu$m which is much more than one would for example expect from the effect of $\sim 10\,\mu$m thickness variations of the disks. After moving to this position, it is more straightforward to optimize the electromagnetic properties of the system directly, after placing the disks at the positions approximately predicted by the ideal 1D model. Since the boost factor itself cannot be measured, we align the disk positions such that the measured group delay matches the simulated group delay. It is related to the boost factor as described in section 4.4.3.

The cost function for such an optimization is the sum of the squared differences (goodness of fit) between the measured and desired group delay data points over frequency χ^2_τ analogous as in section 8.6. In order to evaluate the cost function, the disk positions need to be realigned and the reflectivity needs to be measured. This corresponds to one trial of the iterative optimization scheme. In order to minimize the total time needed, we use gradient-free optimization algorithms

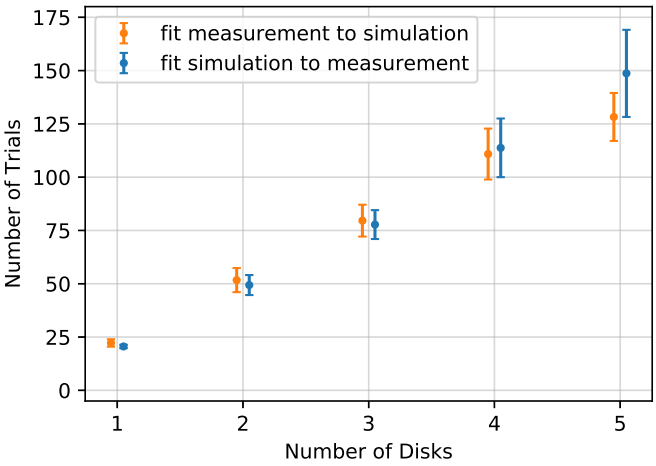

Figure 11.2: Number of trials needed for the optimization when using the Nelder-Mead algorithm as a function of disk number. The orange data points correspond to optimizing the disk spacings in the experimental setup until the measured group delay matches best the simulation. The blue data points correspond to optimizing the disk spacings in the simulation until the simulated group delay matches best the measurement.

that minimize the number of trials, while trying to be robust against local minima. In this work we consider custom implementations of the genetic [117] and simulated annealing [118] algorithms, as well as the Nelder-Mead algorithm [116]. As a convergence criterion we require changes of all motor positions of less than a μm between subsequent iterations. We evaluate the reproducibility of the system response by repeatedly performing the optimization using uniformly distributed randomized starting positions within 100 μm. We investigate the dependence on the used algorithm with three dielectric disks installed and the disk number dependency using the Nelder-Mead algorithm. Both investigations have been performed at different times during the year with their own respective calibrations and possibly slightly different environmental conditions.

Before discussing the resulting reproducibility of disk spacings and electromagnetic responses from this optimization, let us comment on its performance. During the realignment of the disks the search for an axion signal is paused. Thus, the time needed for the realignment needs to be minimized. We have seen differences in the number of trials the algorithms need until convergence depending on how specific parameters of the algorithms are adjusted, such as the probability distribution for sampling the next step in the genetic algorithm. However, non of them was significant enough to draw a conclusion on which algorithm provides the best convergence time.

Besides the dependency on the used algorithm, it is important to keep in mind how the the number of trials scales with the number of disks. This relation is shown in figure 11.2 for Nelder-Mead. We find an approximate linear dependency. The highest number of trials corresponded to realignment times of approximately $\sim$ 10 min in our setup, so naively extrapolating to 20 disks one arrives at 600 trials or a realignment time of less than an hour. This is, however, still quite speculative, since the dependency can change for a higher number of disks and the realignment time may also depend on the boost factor bandwidth. Nevertheless, the worst case scenario with readjustment times of one day as assumed for the previous sensitivity estimates e.g. in section 2.2

seems sufficiently conservative. Also notice that if the initial guess is closer to the optimum than the assumed spread of 100 μm, the required number of trials would be reduced. The difference to the optimal position roughly decreases exponentially during the optimization and we require 1 μm for convergence. Hence, starting for example with positions that are spread $\sim 10\,\mu$m around the optimum instead would roughly half the needed number of trials.

Let us turn our attention to the reproducibility of disk spacings. Figure 11.3 (top) shows a scatter plot of the final motor position differences when running the tuning procedure for ~ 200 times. All runs correspond to the same calculated boost factor function with four disks and 8 mm disk spacings in the ideal 1D model. Figure 11.3 (bottom) shows the same but when optimizing disk spacings in the ideal 1D model instead. The correlations show that there exists degeneracy in the disk position phase space. Both measured and simulated position distributions show the same features. The final positions are scattered more narrowly around zero when only using the model. This is expected from additional systematic disk position noise sources in the setup. Typical temperature fluctuations are at the order of 1 K and can already lead to a broadening of $\sim 5\,\mu$m, as discussed in section 10.1.

The degeneracy can be understood by realizing that the group delay and boost factor maxima frequencies are at first order unchanged when changing the disk spacings along the correlation, i.e., when moving along the gray lines indicated in figure 11.3. We demonstrate this explicitly in figure 11.4 for the correlation between the first and last disk spacing, as well as the correlation between the second and third disk spacing in the four disk setup. The changes in frequency position happen at second order, i.e., they are at first order unchanged. Thus, the degeneracy is a property expected from the ideal 1D model. Also remember that the optimization procedure of the experimental setup only tries to reproduce a desired group delay, but does not use any further information from the 1D model, i.e., how this group delay depends on the disk spacings. Therefore, the agreement between simulated and measured degeneracies explicitly confirms that the measured group delays as a function of disk spacings behaves as expected from the 1D model in the vicinity of the optimization minimum.

11.3 Boost Factor Reproducibility

To quantify the systematic uncertainty on the boost factor arising from this tuning procedure, we optimize the disk positions in the 1D model until the calculated group delays best match the measured ones. Afterwards, we calculate for each realization the corresponding boost factor. The systematic uncertainty on the obtained maximum of the boost factor can then be extracted from this ensemble, thus taking into account the effect of disk spacing degeneracy. Figure 11.5 shows a scatter plot of the obtained relative power boost factor amplitudes against the shift of the boost factor frequency for the same 4 disk case corresponding to the results in figure 11.3. The boost factor amplitude $\hat{\beta}^2$ is obtained as the maximum boost factor over the considered frequency range, and the boost factor frequency ν_β as the frequency at which the boost factor was maximized. The disk spacing degeneracy does not lead to a degeneracy in the boost factor frequency and amplitude phase space.

Based on this result we can quantify the systematic uncertainty within which the tuning procedure leads to the same boost factor. We now may take into account that it is possible to

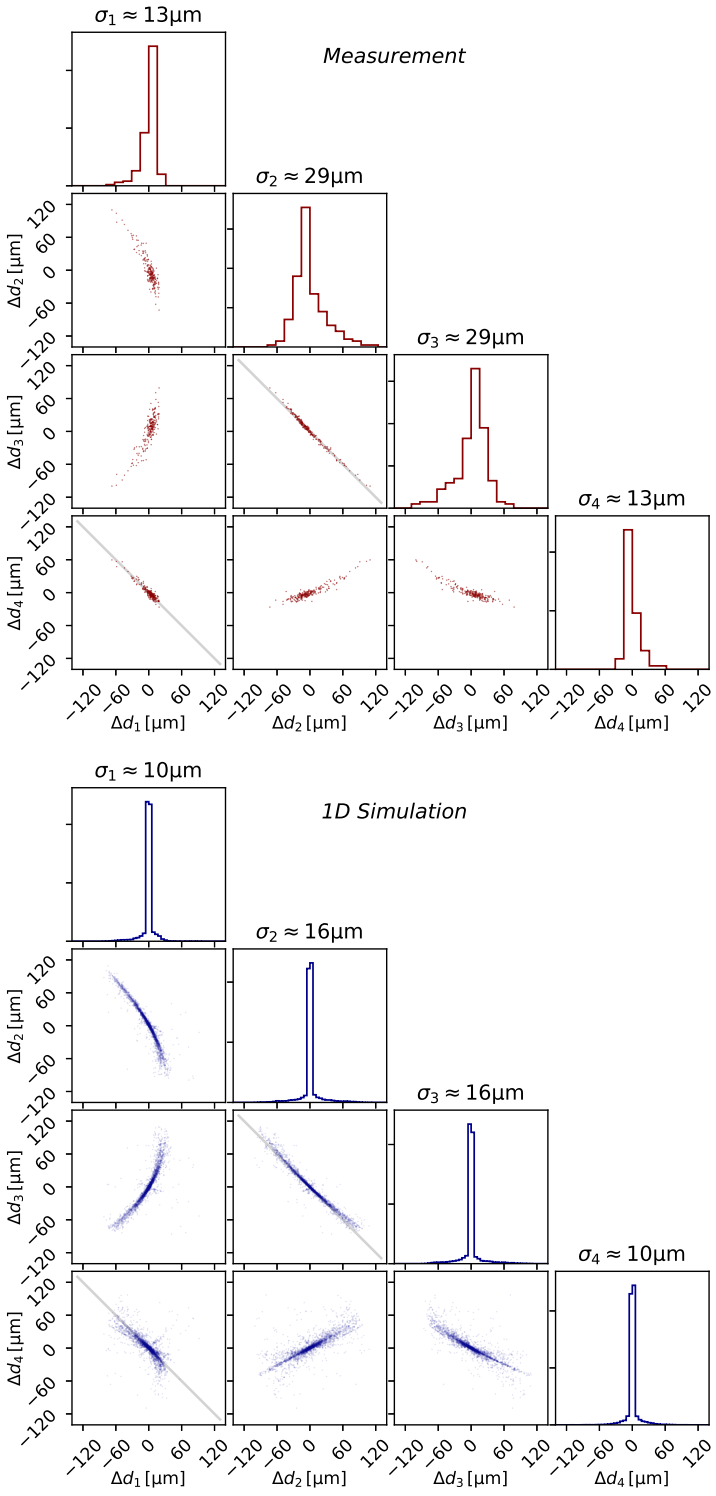

Figure 11.3: **Top:** Final disk spacings after optimizing the actual disk positions in the four disk setup for ~ 200 times. d_1 refers to the spacing between the copper mirror and the first disk, d_2 the following spacing, and so on. Δd_i is the difference of the final spacing i compared to its mean. The diagonal subplots show the histogram of final disk spacings, the off-diagonal subplots show scatter plots illustrating the correlation between different gaps. The gray lines indicate $\Delta d_2 = -\Delta d_3$ and $\Delta d_1 = -\Delta d_4$. **Bottom:** Same as on the top but doing the same optimization for $\sim 10^4$ times only within the ideal 1D model.

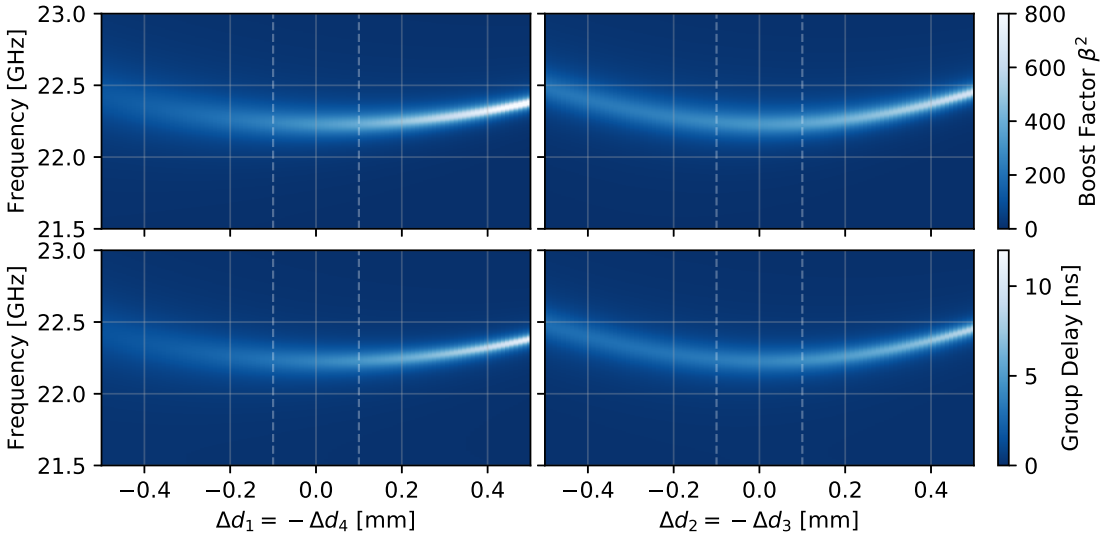

Figure 11.4: Simulated boost factor (top) and group delay (bottom) as a function of frequency (vertical axes) and separation between different disks Δd_i. **Left:** Both as a function of the distance between the mirror and first disk Δd_1 and changing the separation between the third and fourth disk as $\Delta d_4 = -\Delta d_1$, i.e., following the gray line in the rightmost subplot in the bottom row of figure 11.3. The vertical dashed lines indicate the $\pm 100\,\mu$m range comparable to the range of the correlations in figure 11.3. **Right:** Analogous to the left panels but for $\Delta d_3 = -\Delta d_2$.

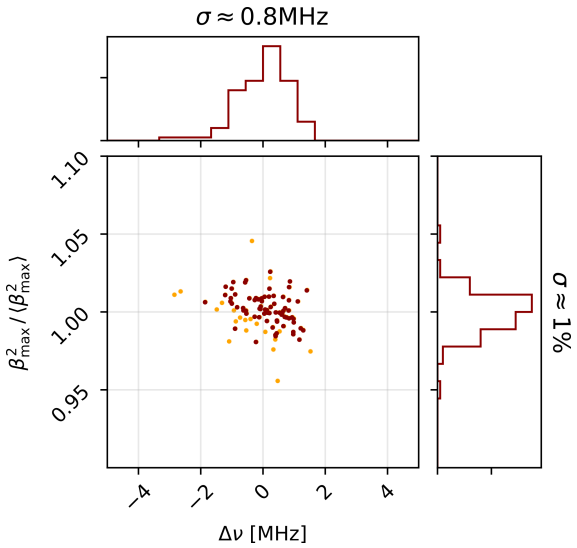

Figure 11.5: Scatter plot of the obtained power boost factor frequency positions and amplitudes after fitting the model to the measured group delays corresponding to the physical disk positions shown in figure 11.3. The horizontal axis shows the frequency shift of the boost factor maximum frequency compared to the mean of the considered ensemble. The vertical axis shows the relative boost factor amplitude deviation compared to the mean of the ensemble. The orange points correspond to solutions with large χ^2_τ and can be rejected, more details cf. main text.

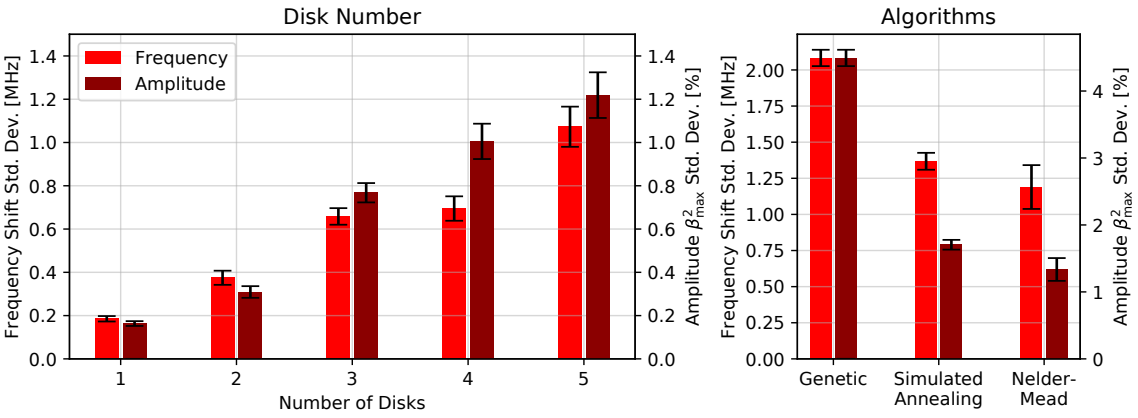

Figure 11.6: Standard deviation on frequency position (left bars, light red) and standard deviation on amplitude relative to the ideal amplitude (right bars, dark red) of the boost factor after fitting the model to the measured group delays corresponding to the physical disk positions. **Left:** For one to five disks when using the Nelder-Mead algorithm. **Right:** For different algorithms and 3 disks.

accept or reject a solution based on the agreement between the two group delays. Thus, we can neglect obvious outliers, such as fits that converged to local minima with only a subset of the group delay peaks fitted correctly. Here we do this by rejecting all solutions for which the cost function χ^2_τ is larger than a standard deviation above the mean of χ^2_τ for the whole ensemble. Notice that this corresponds to a fixed threshold in χ^2_τ which does not take any information on the boost factor into account other than how well the group delay matches the prediction. Hence, such a threshold can always be set in any booster setup to reject bad solutions. Points filtered by this threshold are marked in orange in figure 11.5 and are rejected for the subsequent analysis.

Figure 11.6 shows the resulting uncertainties as a function of the number of disks for a measurement for setups resulting in a boost around 22 GHz as shown in figure 10.4 on the left. For this case, the frequency uncertainty ($\lesssim 2$ MHz, i.e., $\lesssim 2\,\%$ FWHM) and the amplitude uncertainty ($< 2\,\%$) would have an acceptable impact on the sensitivity of the booster. Note that for a fixed disk number the width of the boost factor peak is approximately inversely proportional to the boost factor amplitude according to the area law in [89], i.e., the relative uncertainty on the FWHM is approximately the same as the relative uncertainty on the boost factor amplitude. This result does not contain possible systematic uncertainties due to losses and 3D effects which are not covered by the lossless 1D model. The dependency on the used optimization algorithms is shown on the right of figure 11.6. We see that the choice of the algorithm influences the achievable boost factor uncertainty.

Similar results have also been obtained for other equidistant configurations in the frequency range between 22 GHz to 28 GHz but using the smaller parabolic mirror at a larger distance to the booster and time gating only the main reflection peak.

In summary, we have demonstrated a basic tuning procedure of the proof of principle setup. During this tuning the experimental setup behaves as expected from the 1D model. In addition, the correlations in disk spacings and the resulting boost factors illustrate that different disk spacing configurations can still result in the same electromagnetic response. This shows that phase errors

can be compensated by corresponding phase errors resulting from other disk spacings. This can be an advantage for tuning since it reduces the effective degrees of freedom of the system and thus may help to find optimal positions more quickly. In addition, the differences between the compared optimization algorithms indicate that convergence time and/or systematic boost factor uncertainty may be further improved by using another optimization algorithm. Since the setup behaves as expected from the 1D model, future optimization algorithms could include more information on the disk spacing dependency predicted by the 1D model. This would speed up convergence since the algorithm can propose spacings which are most likely to be optimal according to the model rather than just randomly guessing.

In short. We have demonstrated that the electromagnetic response of the proof of principle booster in terms of group delay behaves like expected from the 1D model and can be tuned to a desired frequency with small systematic uncertainties due to the repeatability of the tuning procedure. The convergence time for tuning the dielectric disk positions to move the boost factor to a preset frequency band seems feasible.

Chapter 12

3D Effects

In the previous chapter we have demonstrated that with the proof of principle setup the expected electromagnetic responses in terms of group delay from a 1D model can be reproduced. In contrast, in this chapter we show first results from measurements that cannot be properly described by the 1D model. We give first indications on their understanding by qualitatively comparing to 3D simulations.

12.1 Diffraction

As pointed out already in section 6.2 the transverse momentum of the electromagnetic wave increases the phase depth of the regions between the dielectrics due to diffraction. Here we test how this depends on the number of disk in the proof of principle booster. To this end, we iteratively remove dielectric disks from a four disk booster while leaving all remaining disks at the same positions. After removing a disk we take a reflectivity measurement. Each measurement is subsequently fitted by the 1D model. Assuming the 1D model is sufficient to derive the disk spacings from the reflectivity measurement, the obtained spacings estimated from each fit are expected to remain the same independent on how many additional disks are installed. Remember, this is equivalent to a 3D situation in which the eigenmode approximation holds, the antenna only couples to the fundamental mode and there is no dominant mode mixing because of thickness variations or tilts.

We can compare the result of this procedure to the result from a 3D simulation to obtain the group delay for each booster configuration. We use Recursive Fourier Propagation for the 3D simulation and assume a Gaussian beam shape with a beam waist of $w_0 \sim 10\,\mathrm{cm}$ for the antenna beam at the front disk (disk closest to the antenna). For simplicity, we do not include the antenna reflection effect in the 3D calculation and thus also do not take it into account when fitting the 1D model to the simulated group delays. Since the measurement still contains the effect of the antenna reflection, we fit the measured data instead with a 1D model taking the reflection effect into account as described in section 10.3.

We show the result of this procedure in figure 12.1. For the simulation, the obtained spacings are compared to the ones set in the simulation, i.e., Δd_i is the difference between spacing i in the 1D model fit and the 3D simulation. For the measurement, the absolute position of the disks

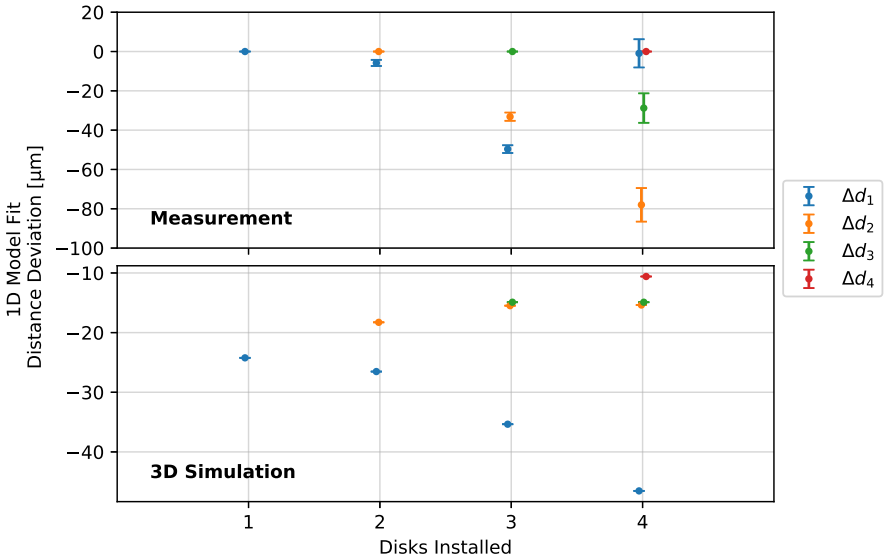

Figure 12.1: Relative prediction for the disk spacings when fitting the group delay of a one to four disk booster from a measurement (top) or 3D simulation (bottom) with the 1D model. When installing disks the already installed disks are not moved. More details cf. text.

is unknown. Hence, we only show how the fitted spacings change relative to each other when inserting disks, i.e., Δd_i is the spacing obtained from the 1D model fit relative to same value obtained when the i^{th} disk has been first installed. The error bars indicate the range of disk spacings when repeating the fit for multiple times. We repeated the same procedure about a month later and saw the the same qualitative effects though the observed differences changed. This is expected since the disks have not been inserted again at the same positions, might be tilted differently and environmental conditions such as temperature have likely changed. We also verified that when doing the same procedure but first adding and later removing disks the results while adding and removing disks are the same. This shows that the mechanical act of adding or removing disks actually has insignificant impact on the position of the other disks.

First notice that the predicted distances from the 1D fit are all lower than the set distances in the 3D simulation. This is expected since the boost factors in the 3D simulations are typically shifted upwards in frequency due to the transverse momentum of the modes. For the 1D model to predict the resonance at the same frequency, it requires therefore smaller distances between the disks. In addition, the predicted distances change when inserting more disks both for the setup and the simulation. This is also expected, since a more resonant system only resonates with fewer modes, thus changing the effective phase depths between the dielectrics. For the experimental setup these effects are expected to be stronger than in our simulation, since tilts and thickness variations may introduce additional transverse momentum and mode mixing making higher modes more relevant.

This result shows that the 1D model is not sufficient when describing the reflectivity over a larger range than only in the vicinity of an optimal position as we have done in the previous chapter. According to the eigenmode approximation the 1D model is sufficient if the antenna is

only coupled to the fundamental mode and there is no dominant mode mixing in the system, i.e., tilts and thickness variations are sufficiently small, cf. section 8.4.3. Hence, the fact that the 1D model fails to predict the same spacings for each inserted disk, shows that at least one of these conditions is not fulfilled.

12.2 Tilts

Another comparison has been performed for the tilt of dielectric disks using the tilting stages on the disk holders in the proof of principle setup. The tilt induced by one turn of the adjustment screw was determined with a ruler measurement of the top displacement of the dielectric disk when turning the screw for 8 revolutions, leaving a relative uncertainty on the tilts at the order of 3 %.

We show the results from a measurement for a booster with one dielectric disk in figure 12.2. We tilted the disk around vertical axis going through the disk holder to leave the mean distance to the copper mirror as much as possible unchanged as indicated in the sketch on the left in the figure. The left panel shows the measured group delays, while the right panel shows group delays from a 3D simulation with a Gaussian antenna beam with $w_0 = 5\,\mathrm{cm}$. We see the same features in both plots, i.e., the group delay is slightly reduced due to the tilt and seems to broaden. Note that a more quantitative comparison is not very meaningful at this point of time, since the 3D simulation lacks information on the exact disk position and its transverse thickness variation.

In addition, in figure 12.3 we also show the measured and simulated reduction of the reflectivity magnitude integrated over the whole measured frequency range $(16-29)\,\mathrm{GHz}$, as well as quantities obtained from a fit with the 1D model analogous to the previous section. It is intuitive that tilts induce losses and therefore reduce the integrated reflectivity (left panels). When fitting the group delays with the 1D model the disk position obtained from the 1D model changes (middle panels). In addition, the value of the cost function χ^2_τ (right panels) tends to increase for larger angles. This shows as expected that the 1D model describes the data better when decreasing the tilts. The χ^2_τ however has a plateau-like feature for low tilts both in simulation and measurement.

We see again that measurements and simulations show the same qualitative features. Notice that the exact position of zero tilt in the experimental setup is a priori unknown and was estimated manually by maximizing the reflected power. Hence, we see that the extrema corresponding to zero tilt are slightly shifted in the measured data. This may potentially be useful to help guiding the alignment. We also point out that a quantitative match between measured and simulated data is difficult in this case. On the one hand, the losses predicted from the simulation are higher than in the measurement. On the other hand, the fit of a 1D model to the 3D simulation data seems to predict less shift in the fitted spacing between disk and mirror. Moreover, we see that these effects depend strongly on the assumed antenna beam shape. This is intuitive if we remember that the beam shape determines to which modes of the booster the antenna couples, while (mode mixing) effects of the tilt are individual for each mode. Hence this kind of measurement can constrain the antenna beam shape. Conversely, a more quantitative comparison requires a more precise independent measurement of the antenna beam. This has only been performed for the new antenna described in section 9.2. We describe a first measurement with this antenna in the next section.

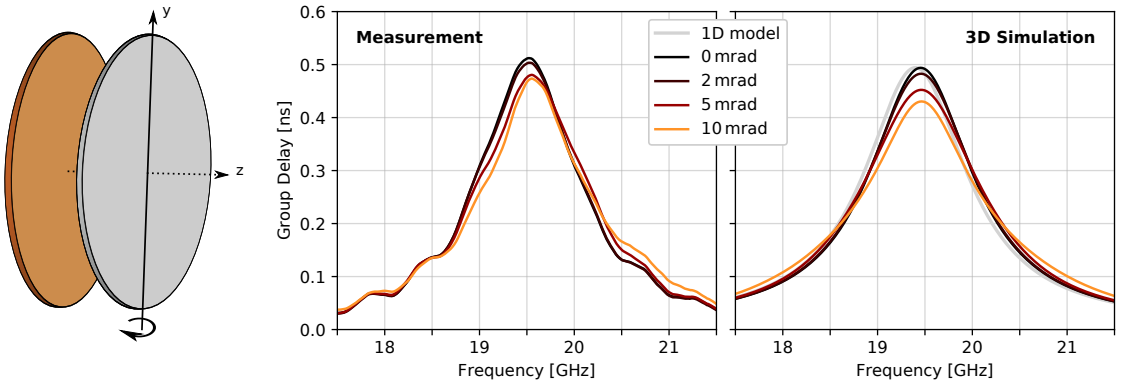

Figure 12.2: Effect on the group delay of tilting the dielectric disk in the proof of principle setup with one one sapphire disk around 8 mm apart from the mirror. We show a sketch of the situation on the left. The disk (gray) is tilted along its central axis such that the mean distance to the copper mirror (orange) is unchanged. Not to scale. The plots show the group delay of the proof of principle booster for different tilts of the dielectric disk. We show group delays measured with the proof of principle setup in the left panel and group delays predicted from 3D simulations in the right panel.

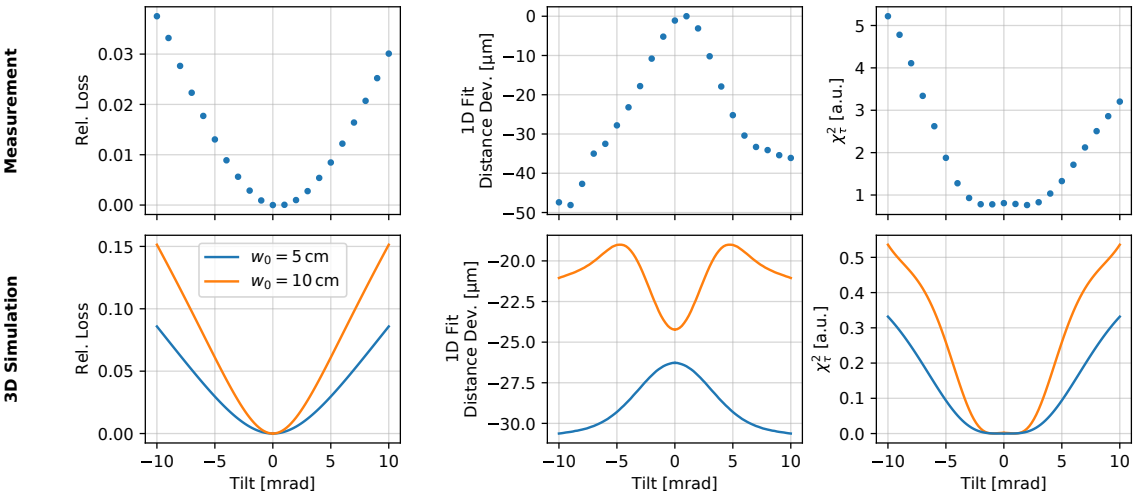

Figure 12.3: Comparison of measurements of the proof of principle booster (top row) with one dielectric disk as a function of disk tilt with corresponding 3D simulations (bottom row). The 3D simulation assumes a Gaussian antenna beam shape with a beam waist of $w_0 = 5\,\text{cm}$ (blue) and $w_0 = 10\,\text{cm}$ (orange) located at the front most disk of the booster. The panels on the left show the relative reduction of the integrated reflectivity in the frequency range $(16 - 29)\,\text{GHz}$. The panels in the middle and on the right show quantities derived from fitting the simulated or measured group delay using the 1D model. The middle panels show the resulting relative distance of the disk from the mirror predicted from the 1D model. The right panels show the χ^2_τ to which the fits converged.

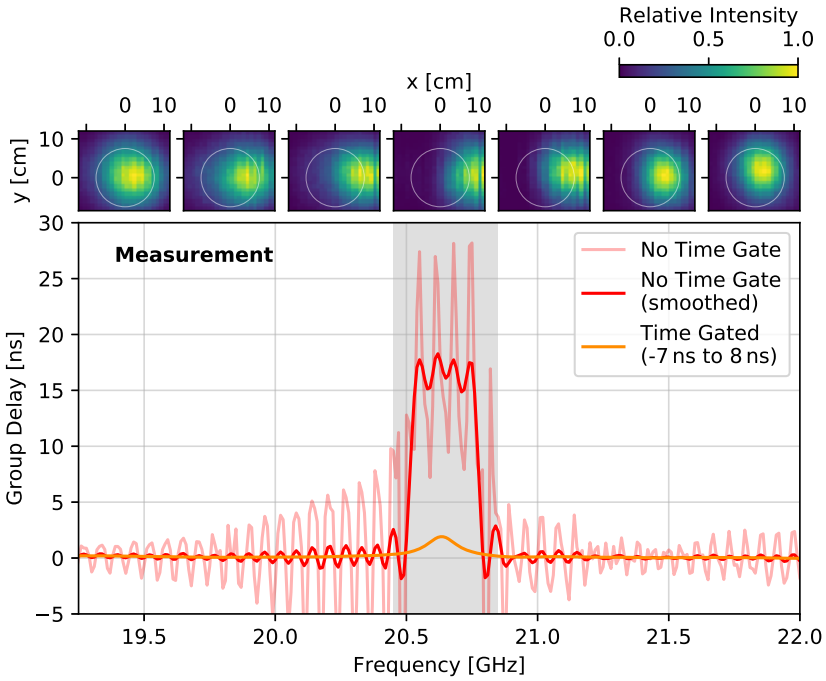

Figure 12.4: Group delay measurement of a one disk booster with the TK antenna displayed in figure 9.3 (left). The pale red curve shows the measurement without time gating, the dark red curve shows the same curve but smoothed with a Gaussian filter of 20 MHz standard deviation. The orange curve shows the same measurement but after applying a time gate from −7 ns to 8 ns. The upper sub-panels show beam shape measurements of the reflected beam measured at the center of the corresponding frequency range in the main panel. The gray range shows the region for the frequency gate used in figure 12.5

12.3 Antenna Coupling

Besides the impacts of 3D effects on the electromagnetic response of the booster itself, its coupling to the antenna system is important. This becomes for example apparent when considering one of the first measurements with the new TK antenna setup described in section 9.2 with a booster configuration containing one dielectric disk. We show the measured group delay in figure 12.4, as well as the response in time domain in figure 12.5. We see two jump of the un-gated group delay baseline in the vicinity of the resonance frequency of the system, specifically at around 20.5 GHz to a higher baseline and at around 20.8 GHz back to the original baseline. The group delay difference between both baselines corresponds to approximately the distance between the two reflection peaks in time domain. When gating only the main peak in time domain, the plateau-like jump of the baseline disappears while the expected group delay peak of only the booster resonance becomes visible. Its amplitude is approximately given by the length of the resonant ring down of the main peak in time domain. A reason for this can be found by frequency gating the affected region and considering the signal in time domain again. We find that in this frequency range the signal received by the antenna after it has been reflected once on the antenna and passed through the booster twice is higher than the signal directly received from the booster.

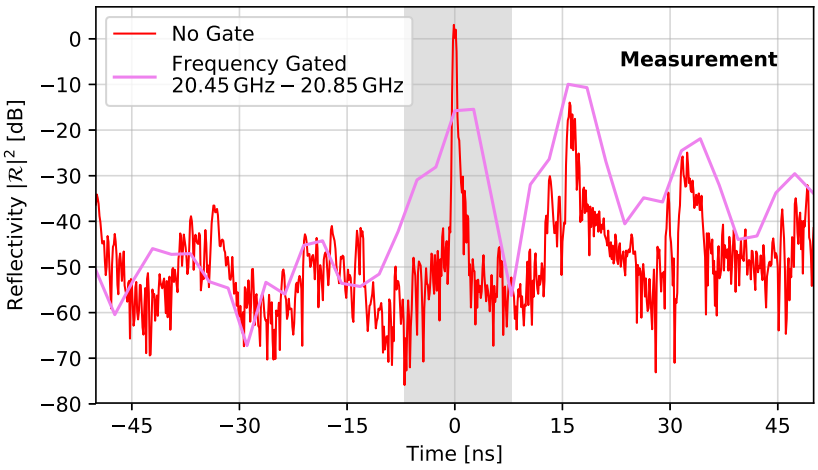

Figure 12.5: Reflectivity measurement of a one disk booster with the new TK antenna displayed in figure 9.3 (left) in time domain. The red curve shows the obtained time domain data for the frequency range of the TK antenna $(18 - 26)$ GHz, while the violet curve shows the same data but only for the frequency range between 20.45 GHz and 20.85 GHz. The gray range shows the region for the time gate used in figure 12.4.

Our understanding is that on resonance a slight tilt between the dielectric disk and the copper mirror can 'rotate' the beam reflected by the booster such that it has a bad coupling to the antenna. Since the ellipsoidal mirror still focuses it onto the antenna, it gets mainly reflected there. If it has left the booster under an angle α, after the reflection on the antenna it impinges the booster again under the angle $-\alpha$, such that the booster rotates it back to around zero angle, which couples well to the antenna. We tested this by inserting a glass plate as a beam splitter in the beam path between antenna and booster around ~ 0.5 m at a 45° angle in front of the booster. We then measured the beam shape of the beam after its reflection on the booster using the WB20 near field probe at a distance of ~ 0.5 m in front of the glass plate. The obtained beam shapes are shown in the top row of figure 12.4. Each sub-panel corresponds to a measurement of the beam shape at different frequency. The frequency is given by the central frequency under the respective sub-panel. The circle indicates the mean position of the beam without any dielectric disk installed. The shift of the beam center near the resonance is consistent with the explanation given above.

Besides the measurement, we conducted 3D simulations to verify that this behavior can be achieved with a tilted disk. We assumed a one disk booster as in the proof of principle setup, with a tilted dielectric disk. The antenna beam was adjusted to match the data sheet value from TK and its Gaussian beam waist was set to the front disk of the booster. We assume that all fields which are not received by the antenna are reflected back towards the booster. After passing a 2^{nd} time through the booster, we further assume that higher order reflections on the antenna are negligible. Here we used the Mode Matching method ($\hat{m} = 5, \hat{\ell} = 2$). When only including the tilt, 30 mrad reproduce the observed group delay baseline jump. This, however, changes the beam shape much stronger than we observed. It is possible that another loss mechanism contributes

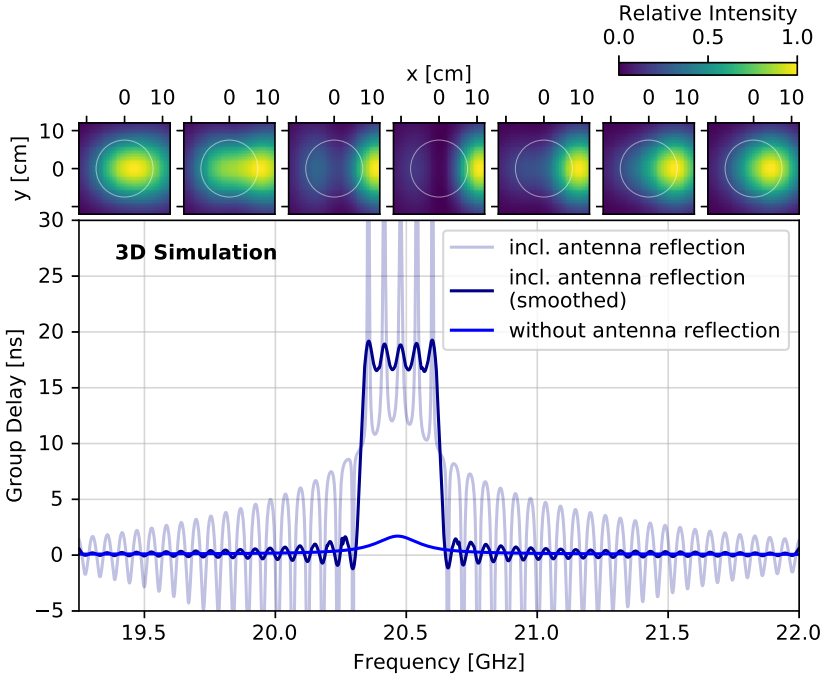

Figure 12.6: 3D Simulation of a one disk booster with a tilted disk of 12 mrad. The pale dark blue curve shows the simulated group delay including one additional reflection on the antenna, the dark blue curve shows the same curve but smoothed with a Gaussian filter of 20 MHz standard deviation. The light blue curve shows the same simulation but neglecting the antenna reflection. The upper sub-panels show the reflected beam shape 80 cm in front of the booster for the corresponding frequencies.

which has less impact on the beam shape. Hence, we show the result of such a simulation in figure 12.6 analogous to figure 12.4 for a tilt of 12 mrad and an additional loss at the order of $\tan\delta \sim 4 \times 10^{-2}$ within the air gap. Notice that this loss corresponds to a 1D effect and does not change the beam shape and thus the antenna coupling. Therefore, a 1D loss alone cannot explain the higher antenna reflection and thus the baseline jump in the group delay.

These results show the importance of antenna coupling for the whole booster system. Although a huge amount of power arrives at the antenna, it could not be received due to the relative tilt within the booster. Since time gating is not available for the axion signal, one needs to make sure that such effects are small for the boost factor. In addition, we see that relative tilts between the disks and mirror within the booster are more important than the relative tilt of the booster with respect to the antenna, since on resonance the effect of an internal tilt on the beam shape is enhanced. Lastly, the presented results qualitatively agree with 3D simulations, which is a first validation using measurements and a tool to gain better understanding of the booster.

In short. We have discussed first measurements of 3D effects from diffraction and tilt including antenna coupling, which qualitatively agree with 3D simulations.

Part V

Closure

Chapter 13

Sensitivity Estimate for Proof of Principle Setups

As physicists we strive to detect dark matter. In this chapter we thus conservatively estimate sensitivities for small-scale prototype dielectric haloscopes to search for hidden photon and axion dark matter with currently available technology and based on findings from this thesis. Such a measurement could be an interesting glance into unexplored regions of the hidden photon or axion-like particle parameter spaces and could lead to surprises. The projected sensitivities presented here will also give a quantitative indication where on the way to the full scale MADMAX experiments the current proof of principle experiment is located and how it compares with other similar efforts.

First, we detail our assumptions on the receiver system. The already available proof of principle detection system [2] using HEMT amplifiers inside liquid Helium bath achieves a total system noise temperature better than 10 K including the noise temperature of the signal source. Its bandwidth is $\Delta\nu_r = 50\,\mathrm{MHz}$. Here we neglect the possibility to rescan observed excesses and require a signal-to-noise ratio of 10. Already a signal-to-noise ratio of 6 leads to a probability to see a false positive within 1 GHz total scanned bandwidth of $\sim 5 \times 10^{-5}$. The value of $S/N = 10$ conservatively takes into account that we may encounter other systematic noise sources at some frequencies leading to additional unexpected candidates. For the signal power to which the system is sensitive we find thus, according to the radiometer equation (2.7),

$$P_{\mathrm{sens}} = \frac{S}{N} k_B T_{\mathrm{sys}} \sqrt{\frac{\Delta\nu_a}{\tau}} = 3 \times 10^{-22}\,\mathrm{W} \left(\frac{S/N}{10}\right) \left(\frac{T_{\mathrm{sys}}}{10\,\mathrm{K}}\right) \left(\frac{\Delta\nu_a}{20\,\mathrm{kHz}}\right)^{\frac{1}{2}} \left(\frac{4\,\mathrm{d}}{\tau}\right)^{\frac{1}{2}}. \tag{13.1}$$

Next, we discuss the power provided by the booster. We assume systems with different number of sapphire disks with diameter of 10 cm, which would fit inside an available liquid helium bath cryostat. Figure 13.1 shows the result of boost factor calculations for different such configurations covering a bandwidth of 50 MHz at a frequency of $\sim 22\,\mathrm{GHz}$ ($m_a \sim 90\,\mu\mathrm{eV}$). The calculations are done for the fundamental mode of the booster, taking into account its $\sim 70\,\%$ coupling-efficiency to the axion-induced field and thus the respective reduction compared to the 1D model. Remember that going to a larger disk diameter of e.g. 20 cm would give approximately the same boost factor for the fundamental mode, since it does not change this coupling efficiency.

We also point out that the central frequency of this boost factor is an example. By changing

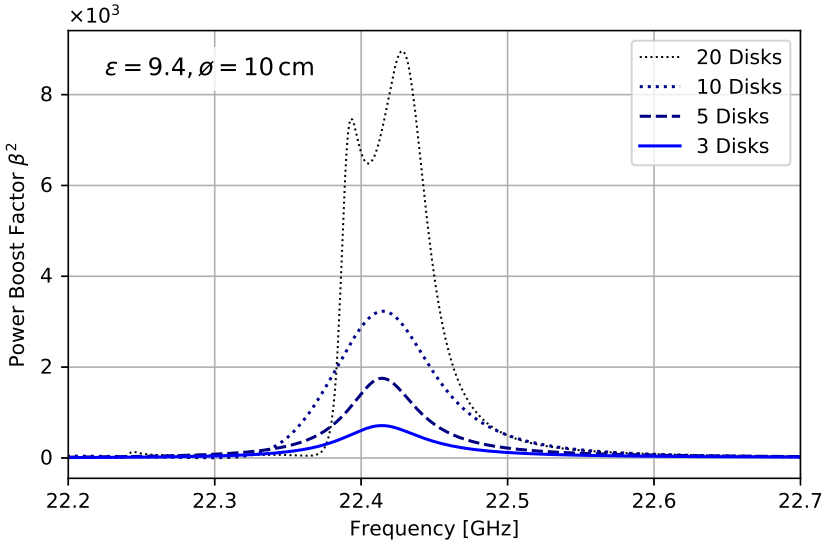

Figure 13.1: Optimized boost factors for different number of sapphire disks with a diameter of 10 cm in 3D assuming the antenna is coupled to the fundamental eigenmode of the idealized booster. The black dotted curve corresponds to 20 disks, the dark blue dotted curve to 10 disks, dark blue dashed to 5 disks and the blue continuous line to 3 disks, respectively.

the disk positions, the boost factor peak can be tuned in frequency as discussed in chapter 11. However, phase errors may shift the boost factor peak in frequency and and change its amplitude. Such phase errors may arise for example from thickness variations of the disks, cf. section 8.4.3, but also from thermal contraction when inserting the system into the cryostat. However, the studies in section 8.6 show that these changes can in principle be calibrated.

Before estimating the sensitivity in $g_{a\gamma}$ for axion-like particles and χ for hidden photons, we need to account for possible reductions of the boost factor due to the systematic effects surveyed in this thesis. Table 13.1 shows a summary of the various studied effects together with their potential impact on the power boost factor. The sapphire disks have a loss tangent of $\tan\delta \sim$ few $\times 10^{-5}$ at room temperature which improves drastically at cryogenic temperatures [177, 178]. We conservatively assume the room temperature value leading to a reduction of the boost factor by around $\sim 5\,\%$ according to section 5.4. Measurements of the thickness variations from the sapphire disks revealed that they are at the $\sigma \sim 10\,\mu$m level [121]. From our first measurements with the laser interferometer, as well as manually adjusting the tilt in section 12, it is reasonable to assume that the tilts can be controlled at the 1 mrad level. While the corresponding phase errors may shift the boost factor frequency, the simulation studies in chapter 8 indicate that the boost factor amplitude may be reduced at the level of $\mathcal{O}(10\,\%)$ for the five disk booster. The real impact might be further reduced when taking into account the possibility of reoptimizing the disk positions, as discussed at the end of section 8.4.3. In practice, however, when operating the system at cryogenic temperatures this is more difficult than in the proof of principle booster presented in this thesis. Also remember that the boost factor cannot be directly measured. Constraining the boost factor with simulations following the aforementioned calibration procedure in section 8.6 can constrain the power boost factor amplitude approximately at the 10 % level. This dominates over the repeatability of the

Source		Relative Reduction	See Chapter
Booster	Dielectric Loss ($\tan\delta \sim$ few $\times 10^{-5}$)	$\sim 5\,\%$	5
	Disk Tilt ($\sim 1\,\mathrm{mrad} \sim 100\,\mu\mathrm{m}/10\,\mathrm{cm}$)	$\sim 10\,\%$	8
	Disk Flatness ($\sim 10\,\mu\mathrm{m}$)	$\sim 10\,\%$	
	Boost Factor Calibration	$\sim 10\,\%$	
	Alignment Repeatability	$\sim 2\,\%$	11
Antenna	Antenna Coupling	$\sim 5\,\%$	6, 8
	Antenna Reflections	$\sim 50\,\%$	10
Total		$\sim 70\,\%$	

Table 13.1: Summary of conservative estimates for the relative reduction of the power boost factor from various systematic limitations in the proof of principle booster. The individual estimates are detailed in the main text. We also give references to the respective chapters with more details.

alignment of the proof of principle setup discussed in section 11, where we have experimentally demonstrated the aforementioned reoptimization. Besides the effects from the booster, we have to take into account systematic reductions from improper coupling to the antenna. As we have seen also in sections 8.3 and 8.6, the beam shape corresponding to the boost factor discussed here is dominated by the fundamental mode. Here we assume the diameter of the antenna beam is off by up to 5 mm and has a maximal transverse offset by 5 mm to the booster beam. These numbers are reasonable taking possibly asymmetric thermal contraction of the antenna and booster into account. In this case the coupling efficiency between the booster mode and antenna is deteriorated by at most $\sim 5\,\%$. While this value is comparable to the other reductions, we saw in section 10.3 that the reflection effect may shift the boost factor in the model compared to its actual location by up to 20 MHz. In our case this corresponds to half its FWHM such that the boost factor is reduced by 50 %. However, this is conservative, since we have obtained the above shift with only one dielectric disk, and the value improved for more disks. All effects taken together lead to a reduction of the power boost factor by almost up to one order of magnitude. This is conservative since the different systematic uncertainties are independent of each other. Nevertheless, due this result we assume a total efficiency of $\eta = 10\,\%$ for the following estimate.

Based on these assumptions we can calculate the sensitivity in the hidden photon mixing parameter χ and axion-photon-coupling $g_{a\gamma}$ by rearranging the emitted power in equation (2.6), see also [76, 89]. For hidden photons the sensitivity is given explicitly by

$$\chi = 3 \times 10^{-13} \left(\frac{P_{\mathrm{sens}}}{3 \times 10^{-22}\,\mathrm{W}}\right)^{\frac{1}{2}} \left(\frac{10\,\%}{\eta}\right)^{\frac{1}{2}} \left(\frac{1000}{\beta^2}\right)^{\frac{1}{2}} \left(\frac{10\,\mathrm{cm}}{\text{ø}}\right) \times \left(\frac{0.45\,\mathrm{GeV/cm^3}}{\rho_{\mathrm{HP}}}\right)^{\frac{1}{2}} \left(\frac{\sqrt{2/3}}{\alpha}\right), \tag{13.2}$$

where ø is the diameter of the disks, ρ_{HP} is the local dark matter density in hidden photons and α is a polarization parameter coming from the fact that only hidden photons polarized parallel to

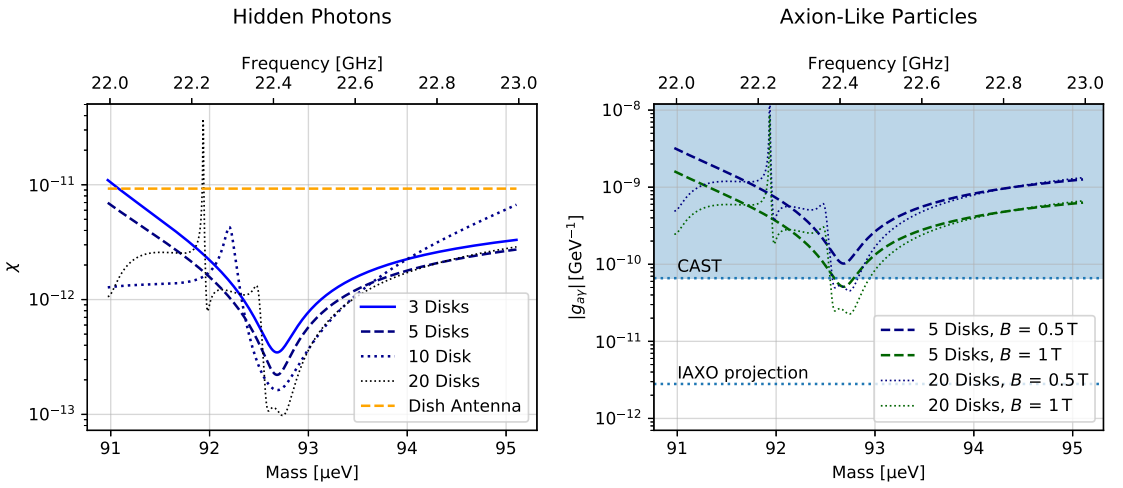

Figure 13.2: Sensitivities of boosters with sapphire disks of 10 cm diameter with the boost factors shown in figure 13.1 on hidden photon dark matter (left) and axions (right) in the coupling vs. mass plane. The upper axis denotes the corresponding photon frequencies. The limits assume $T_{\mathrm{sys}} = 10\,\mathrm{K}$, 4 days measurement time, a signal-to-noise ratio of 10 and an efficiency due to systematic uncertainties of 10 %. The blue to black curves on the left correspond to different number of disks, while the orange dashed line corresponds to the case where all disks are removed and only the mirror is left (dish antenna). The blue curves on the right assume 5 or 20 disks with a 0.5 T magnetic field, while the green lines assume a 1 T magnetic field. For axion-like-particles the presented range has been probed previously by CAST [78] denoted by the blue shaded region. We also show the projected sensitivity of its successor IAXO [35] as a blue dotted line.

the disk surfaces can be converted. For axion-like particles one finds in full analogy

$$|g_{a\gamma}| = 6 \times 10^{-11}\,\mathrm{GeV}^{-1} \left(\frac{P_{\mathrm{sens}}}{3 \times 10^{-22}\,\mathrm{W}}\right)^{\frac{1}{2}} \left(\frac{10\,\%}{\eta}\right)^{\frac{1}{2}} \left(\frac{1000}{\beta^2}\right)^{\frac{1}{2}} \left(\frac{10\,\mathrm{cm}}{\text{ø}}\right) \left(\frac{1\,\mathrm{T}}{B_e}\right) \times \left(\frac{m_a}{100\,\mu\mathrm{eV}}\right) \left(\frac{0.45\,\mathrm{GeV\,cm}^{-3}}{\rho_a}\right)^{\frac{1}{2}}, \tag{13.3}$$

where B_e is the external magnetic field strength parallel to the disk surfaces and ρ_a is the local dark matter density in axions. We show the resulting sensitivities for the booster configurations and detection system discussed above in figure 13.2. Notice that the limits improve with the square root of the disk number N_{disk} as expected. For axion-like particles the limits also improve proportional to the magnetic field in the case of axion-like particles. For axion-like particles the estimated sensitivity is comparable to the exclusion limit set by CAST [78], which we indicate as a blue shaded region. This existing limit could potentially be improved using a 20 disk setup.

For hidden photons previous exclusion limits could be improved by few orders of magnitude. Many pathfinder experiments typically first operate only as hidden photon searches, since no magnet is required. In order to compare our efforts to those experiments, we show a broader range of limits on the hidden photon parameter space in figure 13.3. Here we also assume that not only the previous 50 MHz range is scanned but a range of 1 GHz by repeating the same measurement at different frequency bands over around four months. This assumes that the time

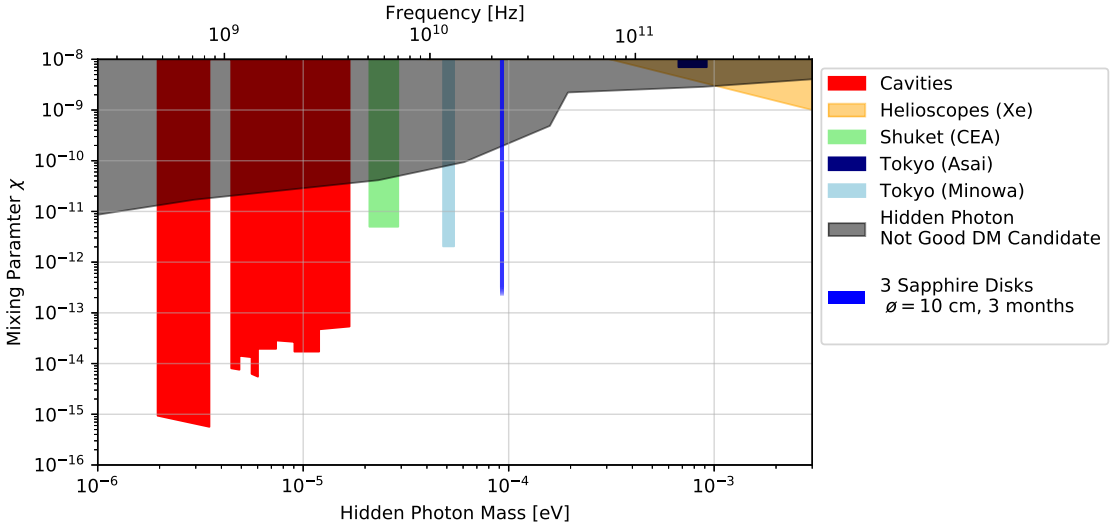

Figure 13.3: Sensitivity of a three disk proof of principle booster to hidden photon dark matter after four months of measurement time (blue line) compared with other limits, analogous to figure 13.2 but for a wider range of the mixing parameter χ and hidden photon mass. The various colored regions denote the limits from cavity experiments (red) [102,179], helioscope experiments (yellow) [180], as well as the SHUKET dish antenna [104] and dish antenna experiments in Tokyo (light blue [103], dark blue [181]). The gray region denotes the range where cosmological arguments suggest that hidden photons are not a good dark matter candidate [76].

for one disk realignment is one day and thus still shorter than the 4 days of signal integration time. If this procedure is automated in the cryostat, using for example piezo-motors, the realignment could still be speeded up significantly to below the hour scale, comparable to the readjustment times of the proof of principle setup discussed in section 11. We see that already a small-scale proof of principle booster setup yields competitive limits on the hidden photon parameter space can be obtained. When comparing our estimated sensitivity with previous efforts, we see that the established cavity experiments [102,179] are much more sensitive, but only operate at lower hidden photon masses, for which the cavity concept is optimal. Turning our attention to the higher masses, notice that our estimated sensitivity is comparable to similar small-scale dish antenna experiments. Current limits are from groups in Japan [103, 181] and in particular the SHUKET experiment in France which has been performed by our collaborators [104]. While all these efforts rely on the dish antenna concept, i.e., a mirror without any dielectric disks, our proof of principle booster would take advantage from the boost factor which increases the emitted power by three orders of magnitude.

In short. In this chapter we estimated the sensitivity of small-scale proof of principle booster setups, comparable to the one discussed in part IV. We find that with conservative experimental parameters ($T_{\mathrm{sys}} = 10\,\mathrm{K}$, $S/N = 10$, efficiency $\eta = 10\,\%$, few sapphire disk booster with 10 cm diameter, $B_e = 1\,\mathrm{T}$, for more details see above) similar sensitivities than CAST [78] can be achieved for $m_a \approx 90\,\mu\mathrm{eV}$ axion-like particles, while for hidden photons at the same mass possible exclusions could be two to three orders of magnitude more stringent than existing limits.

Chapter 14

Conclusions and Outlook

In the ongoing quest to hunt for axion dark matter, the novel concept of dielectric haloscopes has recently been proposed in various variants [34, 92, 94, 95]. This concept is suited to probe the well-motivated mass range around $m_a \sim 100\,\mu$eV. Previous work such as [89] elegantly describes these systems in theory while using an idealized, lossless 1D model, leaving the experimental feasibility and understanding of unaccounted systematic effects to be demonstrated. In this work we have laid foundations to understand the electromagnetic response of dielectric haloscopes and its systematic uncertainties, using a range of different 1D and 3D simulations, including losses and other important subtleties, as well as an experimental proof of principle setup. We will first discuss the main results of these studies and show their impact on the MADMAX experiment. Afterwards, we give an outlook by exploring how these results apply to other haloscope experiments.

Taking on the challenge of bringing the dielectric haloscope to life, we outlined a range of 1D and 3D methods to calculate electromagnetic fields and their behavior in dielectric haloscopes. Previous work for resonant cavities focused on simulating cavity modes, assuming the axion-induced electric field as the driver of the resonance and power losses implicitly [82, 133, 134]. We generalized this to open systems by explicitly including the axion source term in our simulations and calculating the out-propagating power. We also employed and justified dedicated assumptions allowing to efficiently scale these simulations to systems stretching over $\mathcal{O}(100)$ photon wavelengths.

Based on these methods, this work presents the first rigorous discussion of possible systematic uncertainties within the MADMAX dielectric haloscope. First, these may arise from the driver of the system: the axion-induced field itself. It is proportional to the external magnetic field and to the axion field. As such it is important to quantify the acceptable scale of magnetic field inhomogeneities. A realistic transverse magnetic field homogeneity at the percent level is found to be insignificant for the sensitivity of dielectric haloscopes, while longitudinal inhomogeneities can be one order of magnitude larger when taken into account during tuning. In addition, previous calculations assumed zero axion velocity. However, typical CDM velocities can affect the boost factor and in particular also the emitted beam shape. For MADMAX we showed that these effects are negligible below $m_a \sim 100\,\mu$eV and that until $m_a \sim 400\,\mu$eV they are below the $\sim 10\,\%$ level.

However, the most significant impact on the boost factor in MADMAX emerges during the propagation of the emitted electromagnetic waves within the booster. The relevant effects can be

classified in phase errors, arising e.g. from misplaced disks, losses, such as a dielectric loss, and mode mixing, arising e.g. from transverse disk thickness variations. For example, for a boost factor bandwidth of 50 MHz phase errors are under control if the disks are placed with an accuracy better than 10 μm, confirming previous 1D studies [2, 89, 124]. Losses modify the area law [89], i.e., the fact that the area under the power boost factor curve is approximately proportional to the number of dielectric disks installed in the haloscope and stays approximately constant when changing the disk positions. Due to loss the area law breaks down below a critical boost factor bandwidth where the boost factor is significantly reduced. For a typical frequency of 20 GHz this bandwidth is $\sim 20\,\mathrm{MHz}\,(\tan\delta/10^{-4})$. Notice that this sets a minimum bandwidth at which the booster can be operated and thus will be important for the scan strategy of the experiment. Mixing between orthogonal eigenmodes of the propagating beam can only be treated with 3D simulations taking higher modes into account. This effect occurs for tilted disks, thickness variations and surface roughness. While tilts and thickness variations also lead to additional phase errors, the effect of surface roughness can be approximated with an effective loss. We find that for a 50 MHz boost factor bandwidth tilts of the dielectric disks around their central axes corresponding to less than 100 μm (~ 0.1 mrad) longitudinal displacements between their edges are acceptable for MADMAX. However, in order to have negligible effect on the same boost factor, the order of 2 μm or less is required for transverse disk thickness variations varying over length scales of a tenth of the disk diameter. This requirement is much more relaxed for surface roughness corresponding to disk thickness variations with a ten times shorter correlation length. Here 10 μm is sufficient. Importantly, the tolerable losses and inaccuracies do not show a strong dependence on the number of disks but rather on the boost factor bandwidth, i.e., the critical bandwidth mentioned above stays approximately constant when adding dielectric disks. Hence, for negligible loss, i.e., above this bandwidth, it is always advantageous to add dielectric disks, since it increases the area under the power boost factor curve. Moreover, since losses therefore affect the MADMAX prototype and final scale experiment in a comparable way, successful operation of the prototype will be a close demonstration that the needed accuracy can be met also for the full-scale MADMAX.

Aside from setting requirements on the dielectric disks and their positioning, the understanding of the working principle of the booster in 1D and 3D leads to critical impacts on the experimental design and operation. As the magnet is one of the main cost drivers for an experiment, it is worth investigating whether it is sufficient if only some of the disks are inside the magnetic field. However, we confirmed a generalized version of the area law, i.e., the area under the power boost factor is proportional to the number of magnetized disks. On the other hand, the studies on magnetic field inhomogeneities showed that for MADMAX a magnet with a significantly lower homogeneity in the longitudinal direction corresponding to a shorter straight section and than in the initial design [105] can be ordered. Moreover, the beam shape is a crucial parameter for the design of the optics system and the antenna in order to properly receive the emitted power [153]. The 3D studies presented in this thesis revealed for the first time the expected emitted beam shape of dielectric haloscopes and how it depends on its geometry, boost factor frequency and bandwidth. Moreover, the studies on phase errors and tilts inform the experimental design on the accuracy at which the disk positions and alignments need to be determined – a central input for the conceptualization of a device to measure these quantities [182]. Finally, we pointed out that the booster eigenmodes can be manipulated with controlled changes of the disk geometry, such as

lens-shaped disks. Thereby, the coupling efficiency of the mode to the axion-induced E-field could be increased by clever optimization of the disk geometry. Hence, the sensitivity of the experiment could be optimized.

Besides the implications for the experimental design, the requirements deduced in this thesis indicate that a position measurement of the disks alone is likely insufficient to reliably infer the boost factor. Since the boost factor cannot be directly measured, it has to be deduced from measurements of correlated quantities. To this end, we established a first quantitative procedure to calibrate the boost factor using the reflectivity of the booster and demonstrated its validity on a Monte Carlo data set obtained from 3D simulations with a five disk booster configuration. We find that in this case the comparison to a 1D model is sufficient to constrain the boost factor frequency. However, in order to not overestimate the power boost factor due to losses from 3D effects, the model needs to include a loss parameter.

Using the group delay of the reflected signal we applied this calibration procedure to an experimental proof of principle booster. It consists of a copper mirror and up to five movable sapphire disks with a diameter of 20 cm. It is tunable over the frequency range between 22 GHz and 28 GHz. Using this setup, we have surveyed various systematic effects which have adverse impact on the reflectivity measurement and boost factor. The mechanical stability of the system corresponds to a frequency stability at the order of MHz, which is sufficient for the concept of broadband dielectric haloscopes. A major limitation for the measurement of the group delay is due to unwanted antenna reflections. This effect induces a spurious frequency shift of the inferred boost factor from the model. By employing strategies to reduce those reflections and calibrate them within the model, we have shown how this frequency shift can be reduced to less than 20 MHz in our setup, which limits the minimal usable boost factor bandwidth. By utilizing an antenna with a smaller reflection coefficient and increasing the distance to the booster we expect that this effect can be further reduced.

Moreover, we have demonstrated that our system can be tuned to a previously defined desired electromagnetic response. The measured group delays follow the expected dependency on disk spacing from the 1D model. This confirms the previous finding from 3D simulations above indicating that a 1D model is sufficient for the boost factor calibration. In particular, we confirm the degeneracy of the group delay in the disk spacing phase space, which is expected by the model. Although the physical disk positions ended up in a range over more than 100 μm after our tuning procedure, the measured electromagnetic response always corresponded to a boost factor with its amplitude remaining unchanged up to a few percent and which was shifted in frequency by less than 2 MHz. This degeneracy allows for compensating misaligned disks on one side with slightly offset spacings on the other side. Hence, this effect shows that phase errors, arising for example from position errors or surface imperfections of the disks, can be compensated by corresponding phase errors resulting from other disks. Notice that the repeatability in boost factor shows that the repeatability of the tuning procedure is sufficient for frequency tuning. This does only include systematic effects covered by the lossless 1D model, i.e., losses from 3D effects still have to be taken as additional systematic uncertainty.

Like this we demonstrated that a stable, small-scale dielectric haloscope with electromagnetic properties expected from an 1D model could in fact be realized and achieve the necessary accura-

cies, which is an important milestone towards the realization of MADMAX. The setup is currently being extended with an independent disk position measurement, a better antenna and higher number of disks, which will be the next step before going to the MADMAX prototype with 20 disks. First measurements revealing discrepancies to the 1D model can already now be qualitatively understood using 3D simulations.

Finally, we presented first sensitivity estimates for a setup comparable to the proof of principle setup described above based on the findings within this thesis. This sets our efforts in relation to the work of other groups and shows that under conservative assumptions competitive limits, in particular for hidden photons, can be obtained.

In addition, this work went beyond the current state of axion searches by exploring the possibility of directional axion detection. We developed a general analytical formalism to parameterize the changes in the power spectrum from axion-photon conversion due to directional velocity effects. Using realistic experimental parameters we showed that annual and daily modulations can be detected. This should be a useful basis for the post-detection era of the axion, enabling precise measurements of the local CDM velocity distribution.

The interest in axion searches and beyond is shared by a broad community and it is a vivid time for new axion haloscope ideas and proposals. Many of these new approaches face similar challenges, i.e., still lack detailed 3D simulations or experimental verification. As such, the presented results do not only apply to MADMAX, but are useful for a broad range of other haloscope experiments.

For example, the discussion of diffraction effects applies to all dish antenna experiments operating in the GHz-range [103, 104, 144, 181, 183, 184]. In particular FUNK employs a $14\,\mathrm{m}^2$ optical mirror tiled from smaller, quadratic patches [184]. This may affect the diffraction pattern of the emitted radiation which has been studied also within this work. While these experiments search for hidden photons, the BRASS experiment aims to also search for axion-like particles by magnetizing the dish with a Halbach array [144]. This leads to non-negligible magnetic field inhomogeneities which can be treated with the 3D formalisms described in this thesis. We also like to point out the relationship of dielectric haloscopes with multi-cell cavities like for example pizza cavities [82] or RADES [83]. Here the separations between the cells is analogous to the disks in dielectric haloscopes. Thus, both concepts face similar issues of locating the resonant cavity modes coupling to the axion-induced E-field [185], or in other words, calibrating the boost factor. It is obvious that the same holds for other dielectric haloscope experiments, like ORPHEUS [92, 93], DALI [94] and LAMPOST [95]. ORPHEUS and DALI are both designed for similar axion masses as MADMAX. Interestingly, DALI also aims at explicitly implementing directional velocity sensitivity. By employing an antenna array it is sensitive to the directional beam shape changes discussed in this work. Moreover, this concept shares with MADMAX the idea to use tiled disks. Opposed to these haloscopes, LAMPOST is intended to operate at optical frequencies. Here unlike for MADMAX, the diameter is ~ 100 times larger than the de Broglie wavelength of the axion, which again makes the velocity effects relevant. In addition, the large diameter of the layers $\mathcal{O}(10\,\mathrm{cm})$ compared to optical wavelengths makes diffraction negligible. However, e.g. transverse thickness variations of the layers still lead to analogous uncertainties as discussed in this work, a property shared by all dielectric haloscope approaches. Hence, this work lays foundations useful to determine systematic

limitations for all dielectric haloscope experiments.

Beyond lab setups, an interesting opportunity to look for axion signals lays in the observation of radio signals from astrophysical objects such as neutron stars [186]. While a main challenge of these endeavors is the systematic uncertainty in the neutron star magnetosphere, it has also been questioned, whether 3D effects may impact previous sensitivity estimates with 1D calculations [187, 188]. Since these systems are also much larger than a few photon wavelengths, the techniques described in this work might be useful.

In summary, this work lays comprehensive foundations to derive systematic uncertainties of dielectric haloscopes using both simulations and experiment. This understanding has crucial impact on the design of the MADMAX apparatus, such as the required magnet, disk manufacturing accuracy and antenna design, but is also applicable to other axion haloscope experiments. In addition, we went beyond the current state of axion searches by exploring the possibility of directional axion detection. Thus, this work provides not only one of the cornerstones for a thorough understanding of the working principle of dielectric haloscopes including major systematic uncertainties, but also a glimpse into the era after the discovery of an axion-like particle.

Bibliography

[1] S. Knirck, A. J. Millar, C. A. J. O'Hare, J. Redondo and F. D. Steffen, *Directional axion detection*, *JCAP* **1811** (2018) 051, [1806.05927].

[2] MADMAX collaboration, P. Brun et al., *A new experimental approach to probe QCD axion dark matter in the mass range above 40 μeV*, *Eur. Phys. J.* **C79** (2019) 186, [1901.07401].

[3] S. Knirck, J. Schütte-Engel, A. Millar, J. Redondo, O. Reimann, A. Ringwald et al., *A First Look on 3D Effects in Open Axion Haloscopes*, *JCAP* **2019** (2020) 026, [1906.02677].

[4] J. Egge, S. Knirck, B. Majorovits, C. Moore and O. Reimann, *A first proof of principle booster setup for the MADMAX dielectric haloscope*, 2001.04363.

[5] S. Knirck for the MADMAX interest group, *MADMAX: A new way of probing QCD Axion Dark Matter with a Dielectric Haloscope – Foundations*, *J. Phys. Conf. Ser.* **1342** (2020) 012097, [1712.01061].

[6] MADMAX collaboration, S. Beurthey et al., *MADMAX Status Report*, 2003.10894.

[7] MADMAX collaboration, S. Beurthey et al., *Usage of the CERN MORPURGO magnet for the MADMAX prototype,* CERN-SPSC-2020-012. SPSC-P-366, Apr, 2020.

[8] A. Partsch, "Investigation of Loss Effects Influencing the Sensitivity of the Magnetized Disc and Mirror Axion Experiment - MADMAX." Master thesis, Munich, 2018.

[9] J. Egge, "Electromagnetic Properties of the Proof of Principle Booster Setup for the MADMAX Experiment." Master thesis, Munich, 2018.

[10] J. Schütte-Engel, "Axion direct detection in particle and condensed matter physics." PhD thesis, Hamburg (in preparation), 2020.

[11] G. Bertone, D. Hooper and J. Silk, *Particle dark matter: Evidence, candidates and constraints*, *Phys. Rept.* **405** (2005) 279–390, [hep-ph/0404175].

[12] Planck collaboration, N. Aghanim et al., *Planck 2018 results. VI. Cosmological parameters*, 1807.06209.

[13] R. Catena and P. Ullio, *A novel determination of the local dark matter density*, *Journal of Cosmology and Astroparticle Physics* **2010** (2010) 004.

[14] J. I. Read, *The Local Dark Matter Density*, *J. Phys.* **G41** (2014) 063101, [1404.1938].

[15] Q. Xia, C. Liu, S. Mao, Y. Song, L. Zhang, R. Long et al., *Determining the local dark matter density with lamost data*, *Monthly Notices of the Royal Astronomical Society* **458** (2016) 3839–3850.

[16] J. Buch, S. C. J. Leung and J. Fan, *Using gaia dr2 to constrain local dark matter density and thin dark disk*, *Journal of Cosmology and Astroparticle Physics* **2019** (2019) 026.

[17] R. D. Peccei and H. R. Quinn, CP *conservation in the presence of pseudoparticles*, *Phys. Rev. Lett.* **38** (Jun, 1977) 1440–1443.

[18] S. Weinberg, *A new light boson?*, *Phys. Rev. Lett.* **40** (Jan, 1978) 223–226.

[19] F. Wilczek, *Problem of strong p and t invariance in the presence of instantons*, *Phys. Rev. Lett.* **40** (Jan, 1978) 279–282.

[20] M. Dine and W. Fischler, *The not-so-harmless axion*, *Physics Letters B* **120** (1983) 137 – 141.

[21] J. Preskill, M. B. Wise and F. Wilczek, *Cosmology of the invisible axion*, *Physics Letters B* **120** (1983) 127 – 132.

[22] L. Abbott and P. Sikivie, *A cosmological bound on the invisible axion*, *Physics Letters B* **120** (1983) 133 – 136.

[23] R. Davis, *Cosmic axions from cosmic strings*, *Physics Letters B* **180** (1986) 225 – 230.

[24] D. H. Lyth and E. D. Stewart, *Constraining the inflationary energy scale from axion cosmology*, *Physics Letters B* **283** (1992) 189 – 193.

[25] M. Kawasaki, K. Saikawa and T. Sekiguchi, *Axion dark matter from topological defects*, *Phys. Rev.* **D91** (2015) 065014, [1412.0789].

[26] L. Fleury and G. D. Moore, *Axion dark matter: strings and their cores*, *JCAP* **1601** (2016) 004, [1509.00026].

[27] A. Ringwald and K. Saikawa, *Axion dark matter in the post-inflationary Peccei-Quinn symmetry breaking scenario*, *Phys. Rev.* **D93** (2016) 085031, [1512.06436].

[28] L. M. Fleury and G. D. Moore, *Axion String Dynamics I: 2+1D*, *JCAP* **1605** (2016) 005, [1602.04818].

[29] S. Borsanyi, Z. Fodor, J. Guenther, K.-H. Kampert, S. D. Katz, T. Kawanai et al., *Calculation of the axion mass based on high-temperature lattice quantum chromodynamics*, *Nature* **539** (Nov., 2016) 69–71.

[30] G. Ballesteros, J. Redondo, A. Ringwald and C. Tamarit, *Standard Model—axion—seesaw—Higgs portal inflation. Five problems of particle physics and cosmology solved in one stroke*, *JCAP* **1708** (2017) 001, [1610.01639].

[31] P. W. Graham, I. G. Irastorza, S. K. Lamoreaux, A. Lindner and K. A. van Bibber, *Experimental Searches for the Axion and Axion-Like Particles*, *Ann. Rev. Nucl. Part. Sci.* **65** (2015) 485–514, [1602.00039].

[32] I. G. Irastorza and J. Redondo, *New experimental approaches in the search for axion-like particles*, *Prog. Part. Nucl. Phys.* **102** (2018) 89–159, [1801.08127].

[33] Particle Data Group collaboration, M. T. *et al.* [Particle Data Group], *Review of particle physics*, *Phys. Rev. D* **98** (Aug, 2018) 030001.

[34] MADMAX Working Group collaboration, A. Caldwell, G. Dvali, B. Majorovits, A. Millar, G. Raffelt, J. Redondo et al., *Dielectric Haloscopes: A New Way to Detect Axion Dark Matter*, *Phys. Rev. Lett.* **118** (2017) 091801, [1611.05865].

[35] IAXO collaboration, E. Armengaud et al., *Physics potential of the International Axion Observatory (IAXO)*, *JCAP* **1906** (2019) 047, [1904.09155].

[36] M. Pospelov and A. Ritz, *Theta vacua, QCD sum rules, and the neutron electric dipole moment*, *Nucl. Phys.* **B573** (2000) 177–200, [hep-ph/9908508].

[37] J. M. Pendlebury et al., *Revised experimental upper limit on the electric dipole moment of the neutron*, *Phys. Rev.* **D92** (2015) 092003, [1509.04411].

[38] T. Chupp, P. Fierlinger, M. Ramsey-Musolf and J. Singh, *Electric dipole moments of atoms, molecules, nuclei, and particles*, *Rev. Mod. Phys.* **91** (2019) 015001, [1710.02504].

[39] D. Wurm et al., *The PanEDM Neutron Electric Dipole Moment Experiment at the ILL*, *EPJ Web Conf.* **219** (2019) 02006, [1911.09161].

[40] nEDM collaboration, C. Abel et al., *Measurement of the permanent electric dipole moment of the neutron*, *Phys. Rev. Lett.* **124** (2020) 081803, [2001.11966].

[41] R. D. Peccei and H. R. Quinn, *CP Conservation in the Presence of Instantons*, *Phys. Rev. Lett.* **38** (1977) 1440–1443.

[42] R. D. Peccei and H. R. Quinn, *Constraints Imposed by CP Conservation in the Presence of Instantons*, *Phys. Rev.* **D16** (1977) 1791–1797.

[43] S. Weinberg, *A New Light Boson?*, *Phys. Rev. Lett.* **40** (1978) 223–226.

[44] F. Wilczek, *Problem of Strong P and T Invariance in the Presence of Instantons*, *Phys. Rev. Lett.* **40** (1978) 279–282.

[45] G. Grilli di Cortona, E. Hardy, J. Pardo Vega and G. Villadoro, *The QCD axion, precisely*, *JHEP* **01** (2016) 034, [1511.02867].

[46] A. J. Millar. private communication.

[47] T. Hiramatsu, M. Kawasaki, K. Saikawa and T. Sekiguchi, *Production of dark matter axions from collapse of string-wall systems*, *Phys. Rev. D* **85** (May, 2012) 105020.

[48] V. B. Klaer and G. D. Moore, *The dark-matter axion mass*, *JCAP* **1711** (2017) 049, [1708.07521].

[49] M. Gorghetto, E. Hardy and G. Villadoro, *Axions from Strings: the Attractive Solution*, *JHEP* **07** (2018) 151, [1806.04677].

[50] M. Kawasaki, T. Sekiguchi, M. Yamaguchi and J. Yokoyama, *Long-term dynamics of cosmological axion strings*, *PTEP* **2018** (2018) 091E01, [1806.05566].

[51] C. Hogan and M. Rees, *Axion Miniclusters*, *Phys. Lett. B* **205** (1988) 228–230.

[52] B. Eggemeier, J. Redondo, K. Dolag, J. C. Niemeyer and A. Vaquero, *First simulations of axion minicluster halos*, 1911.09417.

[53] Y.-Y. Mao, L. E. Strigari, R. H. Wechsler, H.-Y. Wu and O. Hahn, *Halo-to-Halo Similarity and Scatter in the Velocity Distribution of Dark Matter*, *Astrophys. J.* **764** (2013) 35, [1210.2721].

[54] M. Lisanti, L. E. Strigari, J. G. Wacker and R. H. Wechsler, *The Dark Matter at the End of the Galaxy*, *Phys. Rev.* **D83** (2011) 023519, [1010.4300].

[55] J. Herzog-Arbeitman, M. Lisanti, P. Madau and L. Necib, *Empirical Determination of Dark Matter Velocities using Metal-Poor Stars*, *Phys. Rev. Lett.* **120** (2018) 041102, [1704.04499].

[56] C. A. J. O'Hare. private communication.

[57] A. M. Green, *Astrophysical uncertainties on direct detection experiments*, *Mod. Phys. Lett.* **A27** (2012) 1230004, [1112.0524].

[58] T. Piffl et al., *The RAVE survey: the Galactic escape speed and the mass of the Milky Way*, *Astron. Astrophys.* **562** (2014) A91, [1309.4293].

[59] N. Bozorgnia, F. Calore, M. Schaller, M. Lovell, G. Bertone, C. S. Frenk et al., *Simulated Milky Way analogues: implications for dark matter direct searches*, *JCAP* **1605** (2016) 024, [1601.04707].

[60] E. W. Lentz, T. R. Quinn, L. J. Rosenberg and M. J. Tremmel, *A New Signal Model for Axion Cavity Searches from N-body Simulations*, *ApJ* **845** (Aug., 2017) 121, [1703.06937].

[61] J. Herzog-Arbeitman, M. Lisanti and L. Necib, *The Metal-Poor Stellar Halo in RAVE-TGAS and its Implications for the Velocity Distribution of Dark Matter*, *JCAP* **1804** (2018) 052, [1708.03635].

[62] D. Stiff, L. M. Widrow and J. Frieman, *Signatures of hierarchical clustering in dark matter detection experiments*, *Phys. Rev.* **D64** (2001) 083516, [astro-ph/0106048].

[63] DES collaboration, N. Shipp et al., *Stellar Streams Discovered in the Dark Energy Survey*, *Astrophys. J.* **862** (2018) 114, [1801.03097].

[64] G. C. Myeong, N. W. Evans, V. Belokurov, J. L. Sand ers and S. E. Koposov, *The Shards of ω Centauri*, 1804.07050.

[65] C. A. J. O'Hare, N. W. Evans, C. McCabe, G. Myeong and V. Belokurov, *Velocity substructure from Gaia and direct searches for dark matter*, *Phys. Rev.* **D101** (2020) 023006, [1909.04684].

[66] M. Schaller, C. S. Frenk, A. Fattahi, J. F. Navarro, K. A. Oman and T. Sawala, *The low abundance and insignificance of dark discs in simulated Milky Way galaxies*, *Mon. Not. Roy. Astron. Soc.* **461** (2016) L56–L61, [1605.02770].

[67] P. Tinyakov, I. Tkachev and K. Zioutas, *Tidal streams from axion miniclusters and direct axion searches*, *JCAP* **1601** (2016) 035, [1512.02884].

[68] V. I. Dokuchaev, Y. N. Eroshenko and I. I. Tkachev, *Destruction of axion miniclusters in the Galaxy*, *Soviet Journal of Experimental and Theoretical Physics* **125** (Sept., 2017) 434–442, [1710.09586].

[69] P. Sikivie, *Experimental tests of the "invisible" axion*, *Phys. Rev. Lett.* **51** (Oct, 1983) 1415–1417.

[70] J. E. Kim, *Weak Interaction Singlet and Strong CP Invariance*, *Phys. Rev. Lett.* **43** (1979) 103.

[71] M. A. Shifman, A. I. Vainshtein and V. I. Zakharov, *Can Confinement Ensure Natural CP Invariance of Strong Interactions?*, *Nucl. Phys.* **B166** (1980) 493–506.

[72] M. Dine, W. Fischler and M. Srednicki, *A Simple Solution to the Strong CP Problem with a Harmless Axion*, *Phys. Lett.* **104B** (1981) 199–202.

[73] A. R. Zhitnitsky, *On Possible Suppression of the Axion Hadron Interactions. (In Russian)*, *Sov. J. Nucl. Phys.* **31** (1980) 260.

[74] J. Jaeckel, *A force beyond the Standard Model - Status of the quest for hidden photons*, *Frascati Phys. Ser.* **56** (2012) 172–192, [1303.1821].

[75] J. Jaeckel and A. Ringwald, *The Low-Energy Frontier of Particle Physics*, *Ann. Rev. Nucl. Part. Sci.* **60** (2010) 405–437, [1002.0329].

[76] D. Horns, J. Jaeckel, A. Lindner, A. Lobanov, J. Redondo and A. Ringwald, *Searching for WISPy Cold Dark Matter with a Dish Antenna*, *JCAP* **1304** (2013) 016, [1212.2970].

[77] Particle Data Group collaboration, M. Tanabashi et al., *Review of Particle Physics*, *Phys. Rev.* **D98** (2018) 030001, and 2019 update.

[78] CAST collaboration, M. Karuza, *The CAST Experiment: Status Report*, in *Proceedings, 13th Patras Workshop on Axions, WIMPs and WISPs, (PATRAS 2017): Thessaloniki, Greece, 15 May 2017 - 19, 2017*, pp. 39–42, 2018, DOI.

[79] P. Sikivie, *Detection rates for "invisible"-axion searches*, *Phys. Rev. D* **32** (Dec, 1985) 2988–2991.

[80] ADMX collaboration, T. Braine et al., *Extended Search for the Invisible Axion with the Axion Dark Matter Experiment*, *Phys. Rev. Lett.* **124** (2020) 101303, [1910.08638].

[81] HAYSTAC collaboration, L. Zhong et al., *Results from phase 1 of the HAYSTAC microwave cavity axion experiment*, *Phys. Rev.* **D97** (2018) 092001, [1803.03690].

[82] J. Jeong, S. Youn, S. Ahn, J. E. Kim and Y. K. Semertzidis, *Concept of multiple-cell cavity for axion dark matter search*, *Phys. Lett.* **B777** (2018) 412–419, [1710.06969].

[83] A. A. Melcon et al., *Axion Searches with Microwave Filters: the RADES project*, *JCAP* **1805** (2018) 040, [1803.01243].

[84] B. T. McAllister, G. Flower, L. E. Tobar and M. E. Tobar, *Tunable Supermode Dielectric Resonators for Axion Dark-Matter Haloscopes*, *Phys. Rev. Applied* **9** (2018) 014028, [1705.06028].

[85] J. Kim, S. Youn, J. Jeong, W. Chung, O. Kwon and Y. K. Semertzidis, *Exploiting higher-order resonant modes for axion haloscopes*, *J. Phys.* **G47** (2020) 035203, [1910.00793].

[86] B. T. McAllister, G. Flower, E. N. Ivanov, M. Goryachev, J. Bourhill and M. E. Tobar, *The ORGAN Experiment: An axion haloscope above 15 GHz*, *Phys. Dark Univ.* **18** (2017) 67–72, [1706.00209].

[87] D. Morris, *Electromagnetic detector for relic axions*, 5, 1984, DOI.

[88] J. Jaeckel and J. Redondo, *Resonant to broadband searches for cold dark matter consisting of weakly interacting slim particles*, *Phys. Rev.* **D88** (2013) 115002, [1308.1103].

[89] A. J. Millar, G. G. Raffelt, J. Redondo and F. D. Steffen, *Dielectric Haloscopes to Search for Axion Dark Matter: Theoretical Foundations*, *JCAP* **1701** (2017) 061, [1612.07057].

[90] P. Sikivie, *Experimental tests of the "invisible" axion*, *Phys. Rev. Lett.* **51** (Oct, 1983) 1415–1417.

[91] A. J. Millar, J. Redondo and F. D. Steffen, *Dielectric haloscopes: sensitivity to the axion dark matter velocity*, *JCAP* **1710** (2017) 006, [1707.04266].

[92] G. Rybka, A. Wagner, A. Brill, K. Ramos, R. Percival and K. Patel, *Search for dark matter axions with the Orpheus experiment*, *Phys. Rev.* **D91** (2015) 011701, [1403.3121].

[93] R. Cervantes et al., *Orpheus: Extending the ADMX QCD Dark-Matter Axion Search to Higher Masses*, *APS April Meeting* (2019) Z09–005.

[94] J. De Miguel-Hernández, *A dark matter telescope probing the 6 to 60 GHz band*, 2003.06874.

[95] M. Baryakhtar, J. Huang and R. Lasenby, *Axion and hidden photon dark matter detection with multilayer optical haloscopes*, *Phys. Rev.* **D98** (2018) 035006, [1803.11455].

[96] MADMAX collaboration, S. Beurthey, N. Böhmer, P. Brun, A. Caldwell, L. Chevalier, C. Diaconu et al., *Madmax status report*, 2020.

[97] T. R. Hunter and R. Kimberk, *Statistical topics concerning radiometer theory*, 1507.04280.

[98] J. D. Kraus, R. J. Marhefka and A. S. Khan, *Antennas and wave propagation*. Tata McGraw-Hill Education, 2006.

[99] F. Beaujean, A. Caldwell and O. Reimann, *Is the bump significant? An axion-search example*, *Eur. Phys. J.* **C78** (2018) 793, [1710.06642].

[100] L. Planat, A. Ranadive, R. Dassonneville, J. P. Martinez, S. Leger, C. Naud et al., *A photonic crystal josephson traveling wave parametric amplifier*, 1907.10158.

[101] ADMX collaboration, N. Du et al., *A Search for Invisible Axion Dark Matter with the Axion Dark Matter Experiment*, *Phys. Rev. Lett.* **120** (2018) 151301, [1804.05750].

[102] P. Arias, D. Cadamuro, M. Goodsell, J. Jaeckel, J. Redondo and A. Ringwald, *WISPy Cold Dark Matter*, *JCAP* **1206** (2012) 013, [1201.5902].

[103] J. Suzuki, Y. Inoue, T. Horie and M. Minowa, *Hidden photon CDM search at Tokyo*, in *Proceedings, 11th Patras Workshop on Axions, WIMPs and WISPs (Axion-WIMP 2015): Zaragoza, Spain, June 22-26, 2015*, pp. 145–148, 2015, 1509.00785, DOI.

[104] P. Brun, L. Chevalier and C. Flouzat, *Direct Searches for Hidden-Photon Dark Matter with the SHUKET Experiment*, *Phys. Rev. Lett.* **122** (2019) 201801, [1905.05579].

[105] M. W. Abdel. CEA-IRFU, Saclay, private communication.

[106] C. A. J. O'Hare and A. M. Green, *Axion astronomy with microwave cavity experiments*, *Phys. Rev.* **D95** (2017) 063017, [1701.03118].

[107] J. W. Foster, N. L. Rodd and B. R. Safdi, *Revealing the Dark Matter Halo with Axion Direct Detection*, *Phys. Rev.* **D97** (2018) 123006, [1711.10489].

[108] I. G. Irastorza and J. A. Garcia, *Direct detection of dark matter axions with directional sensitivity*, *JCAP* **1210** (2012) 022, [1207.6129].

[109] S. S. Wilks, *The large-sample distribution of the likelihood ratio for testing composite hypotheses*, *Ann. Math. Statist.* **9** (03, 1938) 60–62.

[110] G. Cowan, K. Cranmer, E. Gross and O. Vitells, *Asymptotic formulae for likelihood-based tests of new physics*, *Eur. Phys. J.* **C71** (2011) 1554, [1007.1727].

[111] L. L. Sánchez-Soto, J. J. Monzón, A. G. Barriuso and J. F. Cariñena, *The transfer matrix: A geometrical perspective*, *Physics Reports* **513** (2012) 191 – 227.

[112] "Advanced Design System (ADS), Keysight EEsof EDA, Santa Rosa, California, United States." http://www.keysight.com/find/eesof-ads (accessed 27 Aug 2019).

[113] "Quite Universal Circuit Simulator (Qucs)." http://qucs.sourceforge.net/ (accessed 3 Feb 2020).

[114] A. N. Ioannisian, N. Kazarian, A. J. Millar and G. G. Raffelt, *Axion-photon conversion caused by dielectric interfaces: quantum field calculation*, *JCAP* **1709** (2017) 005, [1707.00701].

[115] O. Zinke and H. Brunswig, *Lehrbuch der Hochfrequenztechnik*. Springer, 1986.

[116] J. C. Lagarias, J. A. Reeds, M. H. Wright and P. E. Wright, *Convergence properties of the nelder–mead simplex method in low dimensions*, *SIAM J. Optim* **9** (1998) 112–147.

[117] D. Whitley, *A genetic algorithm tutorial*, *Statistics and Computing* **4** (Jun, 1994) 65–85.

[118] P. J. M. Laarhoven and E. H. L. Aarts, eds., *Simulated Annealing: Theory and Applications*. Kluwer Academic Publishers, Norwell, MA, USA, 1987.

[119] D. van Ravenzwaaij, P. Cassey and S. D. Brown, *A simple introduction to markov chain monte–carlo sampling*, *Psychonomic Bulletin & Review* **25** (Feb, 2018) 143–154.

[120] D. P. Bertsekas, *Nonlinear Programming*. Athena Scientific, 2016.

[121] O. Reimann. private communication.

[122] J. Redondo, *Photon-Axion conversions in transversely inhomogeneous magnetic fields*, in *Proceedings, 5th Patras Workshop on Axions, WIMPs and WISPs (AXION-WIMP 2009): Durham, UK, July 13-17, 2009*, pp. 185–188, 2010, 1003.0410, DOI.

[123] J. Ouellet and Z. Bogorad, *Solutions to Axion Electrodynamics in Various Geometries*, 1809.10709.

[124] S. Khan, "Sensitivity of the MADMAX Boost Factor on the Disk Spacing Uncertainty." Master thesis, Tübingen, 2019.

[125] J. E. Mazierska, M. V. Jacob, D. O. Ledenyov and J. Krupka, *Complex Permittivity Measurements at Variable Temperatures of Low Loss Dielectric Substrates Employing Split Post and Single Post Dielectric Resonators*, 1209.0111.

[126] "Expected number of steps in a random walk with a boundary." https://math.stackexchange.com/questions/553690/expected-number-of-steps-in-a-random-walk-with-a-boundary (accessed 17 Jan 2020).

[127] U. S. Inan and R. A. Marshall, *Numerical electromagnetics: the FDTD method*. Cambridge University Press, 2011.

[128] S. D. Gedney, *Introduction to the finite-difference time-domain (FDTD) method for electromagnetics*, *Synthesis Lectures on Computational Electromagnetics* **6** (2011) 1–250.

[129] O. C. Zienkiewicz, R. L. Taylor, O. C. Zienkiewicz and R. L. Taylor, *The finite element method*, vol. 36. McGraw-hill London, 1977.

[130] "Elmer – finite element solver for multiphysical problems." www.csc.fi/web/elmer/elmer (accessed 7 Jul 2018).

[131] J. Szałatkiewicz, R. Szewczyk, M. Kalinowski, J. Kataja, P. Råback, J. Ruokolainen et al., *Open source elmer software based fem modeling of waveguides and resonant cavities for microwave heating and drying devices*, *Archives of Electrical Engineering* **66** (2017) 745 – 750.

[132] "COMSOL Multiphysics® v. 5.3.a COMSOL AB, Stockholm, Sweden." `www.COMSOL.com` (accessed 7 July 2018).

[133] P. L. Hoang, J. Jeong, B. X. Cao, Y. Shin, B. Ko and Y. Semertzidis, *Theoretical models of axion electromagnetism for haloscope searches*, *Phys. Dark Univ.* (2017) .

[134] F. L. Krawczyk, *Introduction to the Numerical Design of RF-Structures with Special Consideration for Axion Detector Design: A Tutorial*, *Springer Proc. Phys.* **211** (2018) 1–19.

[135] "Elmer models manual." `www.csc.fi/web/elmer/documentation` (accessed 7 Jul 2018).

[136] J.-P. Berenger, *A perfectly matched layer for the absorption of electromagnetic waves*, *Journal of Computational Physics* **114** (1994) 185 – 200.

[137] "Using perfectly matched layers and scattering boundary conditions for wave electromagnetics problems." `https://www.comsol.de/blogs/using-perfectly-matched-layers-and-scattering-boundary-conditions-for-wave-electromagnetics-problems/` (accessed 7 Jul 2018).

[138] R. Barrett, M. W. Berry, T. F. Chan, J. Demmel, J. Donato, J. Dongarra et al., *Templates for the solution of linear systems: building blocks for iterative methods*, vol. 43. Siam, 1994.

[139] R. W. Freund, *A transpose-free quasi-minimal residual algorithm for non-hermitian linear systems*, *SIAM journal on scientific computing* **14** (1993) 470–482.

[140] P. H. S.S. Antman and K. Sreenivasan, eds., *Computational Electromagnetics*, vol. 51. Springer, second ed.

[141] F. Pedrotti, *Introduction to optics*. Prentice Hall, Englewood Cliffs, N.J, 1993.

[142] "COMSOL: Corrugated Circular Horn Antenna." `https://www.comsol.com/model/corrugated-circular-horn-antenna-15677` (accessed 7 Jul 2018).

[143] J. D. Jackson, *Classical electrodynamics*. Wiley, New York, NY, 3rd ed. ed., 1999.

[144] "Brass website." `http://www.iexp.uni-hamburg.de/groups/astroparticle/brass/brassweb.htm` (accessed 6 Apr 2019).

[145] J. Goodman, *Introduction to Fourier Optics*. Roberts and Company Publishers, 2016.

[146] D. Bergermann, "Influence of outer fields on simulated MADMAX axion signals." Bachelor thesis, Aachen, 2019.

[147] A. Snyder and J. Love, *Optical Waveguide Theory*. Springer US, 1983.

[148] C. Yeh and F. I. Shimabukuro, *The essence of dielectric waveguides*. Springer, 2008.

[149] P. Goldsmith, *Quasioptical Systems: Gaussian Beam Quasioptical Propogation and Applications*. Wiley-IEEE Press, 1998, 10.1109/9780470546291.

[150] J. Kraus, *Antennas*. Wiley, 2nd ed., 1988.

[151] Y.-S. Lee, *Principles of Terahertz Science and Technology*. Springer Publishing Company, Incorporated, 1st ed., 2008.

[152] "Thomas keating ltd." `http://www.terahertz.co.uk/`.

[153] S. Heyminck and C. Kasemann, "Minimax optics (internal report)."

[154] S. Knirck, "Dish Antenna Searches for WISPy Dark Matter – Theory and Experiment." Master thesis, Heidelberg, 2016.

[155] J. Ruokolainen, M. Malinen, P. Råback, T. Zwinger, A. Pursula and M. Byckling, *ElmerSolver Manual*. CSC – IT Center for Science.

[156] "Julia manual." `https://docs.julialang.org/en/v1/stdlib/LinearAlgebra/` (accessed 9 Mar 2020).

[157] R. Rannacher, *Einführung in die Numerische Mathematik (Numerik 0)*. Heidelberg University Publishing, 2017, 10.17885/heiup.206.281.

[158] J. Stoer and R. Bulirsch, *Numerische Mathematik*, vol. 7. Springer, 1989.

[159] M. Beutter, A. Pargner, T. Schwetz and E. Todarello, *Axion-electrodynamics: a quantum field calculation*, *JCAP* **1902** (2019) 026, [1812.05487].

[160] M. Born and E. Wolf, *Principles of Optics*. Cambridge University Press, 7 ed., 1999.

[161] J. Stratton, *Electromagnetic Theory*. New York: Mc Graw-Hill, 1941.

[162] E. Garutti. Hamburg University, private communication.

[163] M. Halpern, H. P. Gush, E. Wishnow and V. D. Cosmo, *Far infrared transmission of dielectrics at cryogenic and room temperatures: glass, fluorogold, eccosorb, stycast, and various plastics*, *Appl. Opt.* **25** (Feb, 1986) 565–570.

[164] J. Jaeckel and J. Redondo, *An antenna for directional detection of WISPy dark matter*, *JCAP* **1311** (2013) 016, [1307.7181].

[165] J. Jaeckel and S. Knirck, *Directional Resolution of Dish Antenna Experiments to Search for WISPy Dark Matter*, *JCAP* **1601** (2016) 005, [1509.00371].

[166] J. Jaeckel and S. Knirck, *Dish Antenna Searches for WISPy Dark Matter: Directional Resolution Small Mass Limitations*, in *Proceedings, 12th Patras Workshop on Axions, WIMPs and WISPs (PATRAS 2016): Jeju Island, South Korea, June 20-24, 2016*, pp. 78–81, 2017, 1702.04381, DOI.

[167] F. Hubaut and P. Pralavorio. private communication.

[168] J. S. Simonoff, *Smoothing methods in statistics*. Springer Science & Business Media, 2012.

[169] "A-Info LB-42-25, Data Sheet, www.ainfoinc.com." `http://www.ainfoinc.com/en/pro_pdf/new_products/antenna/Standard%20Gain%20Horn%20Antenna/tr_LB-42-25.pdf` (accessed 6 Dec 2019).

[170] "PI L-220, Data Sheet, physikinstrumente.com." `https://static.physikinstrumente.com/fileadmin/user_upload/physik_instrumente/files/datasheets/L-220-Datasheet.pdf` (accessed 6 Dec 2019).

[171] "Anritsu MS4647B, Data Sheet, anritsu.com." `https://dl.cdn-anritsu.com/en-us/test-measurement/files/Brochures-Datasheets-Catalogs/datasheet/11410-00611AA.pdf` (accessed 6 Dec 2019).

[172] M. Hiebel, *Grundlagen der vektoriellen Netzwerkanalyse*. Rohde & Schwarz, 2006.

[173] D. Inaudi, B. Glisic, S. Fakra, J. Billan, S. Redaelli, J. G. Perez et al., *Development of a displacement sensor for the cern-lhc superconducting cryodipoles*, *Measurement Science and Technology* **12** (2001) 887.

[174] H. Takahashi, P. Carlsson, K. Nishimura and M. Usami, *Analysis of negative group delay response of all-pass ring resonator with mach-zehnder interferometer*, *IEEE Photonics Technology Letters* **16** (Sep., 2004) 2063–2065.

[175] R. Das and Q. Zhang, *Synthesis of negative group delay using lossy coupling matrix*, 2017.

[176] F. J. Harris, *On the use of windows for harmonic analysis with the discrete fourier transform*, *Proceedings of the IEEE* **66** (1978) 51–83.

[177] J. Krupka, K. Derzakowski, M. Tobar, J. Hartnett and R. G. Geyer, *Complex permittivity of some ultralow loss dielectric crystals at cryogenic temperatures*, *Measurement Science and Technology* **10** (1999) 387.

[178] X. Aupi, J. Breeze, N. Ljepojevic, L. J. Dunne, N. Malde, A.-K. Axelsson et al., *Microwave dielectric loss in oxides: Theory and experiment*, *Journal of applied physics* **95** (2004) 2639–2645.

[179] B. M. Brubaker et al., *First results from a microwave cavity axion search at 24 μeV*, *Phys. Rev. Lett.* **118** (2017) 061302, [1610.02580].

[180] H. An, M. Pospelov and J. Pradler, *Dark Matter Detectors as Dark Photon Helioscopes*, *Phys. Rev. Lett.* **111** (2013) 041302, [1304.3461].

[181] S. Knirck, T. Yamazaki, Y. Okesaku, S. Asai, T. Idehara and T. Inada, *First results from a hidden photon dark matter search in the meV sector using a plane-parabolic mirror system*, *JCAP* **1811** (2018) 031, [1806.05120].

[182] J. Jochum and C. Strandhagen. private communication.

[183] B. Döbrich et al., *The FUNK search for Hidden Photon Dark Matter in the eV range*, in *Photon 2015: International Conference on the Structure and Interactions of the Photon and 21th International Workshop on Photon-Photon Collisions and International Workshop on High Energy Photon Linear Colliders Novosibirsk, Russia, June 15-19, 2015*, 2015, 1510.05869.

[184] FUNK Experiment collaboration, D. Veberič et al., *Search for hidden-photon dark matter with the FUNK experiment*, *PoS* **ICRC2017** (2018) 880, [1711.02958].

[185] A. Melcón et al., *Scalable haloscopes for axion dark matter detection in the 30μeV range with RADES*, 2002.07639.

[186] A. Hook, Y. Kahn, B. R. Safdi and Z. Sun, *Radio Signals from Axion Dark Matter Conversion in Neutron Star Magnetospheres*, *Phys. Rev. Lett.* **121** (2018) 241102, [1804.03145].

[187] R. A. Battye, B. Garbrecht, J. I. McDonald, F. Pace and S. Srinivasan, *Dark matter axion detection in the radio/mm-waveband*, 1910.11907.

[188] M. Leroy, M. Chianese, T. D. P. Edwards and C. Weniger, *Radio Signal of Axion Photon Conversion in Neutron Stars: A Ray Tracing Analysis*, 1912.08815.